CRANFIELD UNIVERSITY at SILSOE

National Soils Resources Institute

Engineering Group

PhD

2005

Craig S Knight

An Investigation into Jet Assisted Submarine Cable Burial Ploughs

Supervisors: Professor R J Godwin & Dr D W Pullen

Submitted on 1st July 2005

IMAGING SERVICES NORTH
Boston Spa, Wetherby
West Yorkshire, LS23 7BQ
www.bl.uk

MISSING PAGE/PAGES HAVE NO CONTENT

Abstract

Fibre optic telecommunication cables laid across the seafloor are buried in shallow water depth (<2000m) for protection against hazards arising from commercial fishing and shipping activity. The cables are buried in a trench created by a sea plough, often jet assisted and towed from a ship, or by a ROV with jet legs straddling the cable and fluidising the soil around it. Recent trends in the industry require more versatile burial tools, so a sound understanding of their fundamental mechanics is required to enable their optimum design and performance. The aim of this research program was to study the mechanics of force reduction on jet assisted cable burial tools.

The experimental program consisted of two stages, both conducted in controlled submerged conditions. The first studied the effects of jet parameters, tool rake angle and pore pressure on tool force reduction. The second stage studied the action of a single horizontal buried jet on the surrounding soil, in which the first series of experiments studied a static jet nozzle in sand and clay, and the second a dynamic jet nozzle. The flow rate or nozzle velocity was varied in each respectively.

The first stage showed force reduction was caused by the reduced soil stress on the tool face in areas intersecting fluidised sand. The larger the fluidised area (FA), or the lower its intersection, the greater the force reduction. Evenly spaced nozzles gave greater FA coverage of the tool face. Interaction between jet and rake angle and force was complex, but upward angled jets and forward raked tools gave least force reduction. Results of the second stage showed cavity formation in sands characterised by shear erosion whereas in clay by pressure fracturing. The cavity size in sands was directly proportional to jet momentum flux and inversely proportional to tool velocity.

Mathematical models were developed from each stage, the first to simulate tool force reduction created by the jets, given knowledge of the FA, and the second to simulate the FA created by a single jet. The second over predicted cavity length by an average of 7% over the range of tool velocities tested. The combined models over predicted tool force, and suggested reasons for the discrepancies are given. Further research is required to refine the model and provide a useful tool for the design and operation of jet assisted cable burial tools in saturated sands.

Acknowledgements

I would like to thank Professor Dick Godwin and Dr. David Pullen for their supervision, inputs and guidance throughout the project, and Professor Peter Leeds-Harrison for his role as Chairman of the Thesis Committee. I also thank Professor Mike O'Dogherty for his help and consultation in modelling mathematical protocols, Simon Stranks, Roy Newland and Roger Swatland, of the Soil Dynamics Laboratory, and Phil Trolley, of the workshop, for their practical assistance.

I also express my appreciation to Global Marine Systems Ltd. for their sponsorship of the project.

Contents

List of Tables

List of Figures

Nomenclature

A	=	surface area of impingement zone (m^2)
A_J	=	total cross-sectional area of nozzles (m^2)
A_L	=	area of disturbed logarithmic spiral section (m^2)
A_R	=	rake angle effect factor (greater than one for aft rake)
A_T	=	area of tine face (m^2)
a, b	=	constant of parabola
$a_,$	=	factor of solution to quadratic equation. Suffixes: l = of l, q = of x_a and x_b, r = of r_b, η = of η
b_m	=	maximum disturbed width (m)
b_2	=	radial distance where $u = u_m/2$
$b_,$	=	factor of solution to quadratic equation. Suffixes: l = of l, q = of x_a and x_b, r = of r_b, η = of η
C, A	=	constant and exponent of cavity length power equation
C.S.A	=	cross sectional area of jet cone (m^2)
C_f	=	coefficient of friction
c	=	cohesion ($kN.m^{-2}$)
$c_,$	=	factor of solution to quadratic equation. Suffixes: l = of l, q = of x_a and x_b, r = of r_b, η = of η
D	=	soil particle diameter (m)
D_z	=	cavity depth fraction
d_h	=	maximum scour hole diameter (m)
d_j	=	diameter of jet (m)
d	=	depth of cavity (m)
E	=	sediment detachment rate per unit area
F	=	tine Force (kN)
FA	=	fluidised area (m^2)
F_J	=	jet force (N)
F_L	=	force reduction (kN)
F_{NET}	=	net force (kN)
F_o	=	coulombs passive earth pressure (kN)
F_P	=	tine passive force (kN)
G	=	cavity depth to length ratio (typically 0.45)

g	=	acceleration due to gravity (ms^{-2})
H	=	jet impingement height (m)
H_{ATM}	=	head of atmosphere (m)
H_{SEA}	=	head of sea water (m)
h	=	head of water in cavity (m)
h_d	=	maximum dynamic scour hole depth (m)
JMF,J	=	jet momentum flux (kg.m)
K_0	=	ratio of horizontal to vertical stress on soil at rest ($1-\sin\varphi$)
k	=	soil hydraulic conductivity (ms^{-1})
k_N	=	normalised factor constant
L	=	depth of cavity centre = length of flow path (m)
l	=	cavity length (m)
M	=	torque (Nm^{-1})
m	=	gradient of soil stress profile ($kN.m^{-3}$)
N'	=	dimensionless number. Suffixes: q = gravitational, c = cohesive
NA	=	normalised area
N_c	=	dimensionless strip footing bearing capacity factor. Suffices: c = cohesive (~7), q = frictional
NF	=	normalised force
NP	=	normalised pressure
NQ	=	normalised flow rate
$N\varphi$	=	terzaghi's passive earth pressure factor
n	=	number of jets on tine
n_g	=	generated porosity = $n_m - R_\sigma * (n_m - n_o)$
n_m	=	maximum (ASTM standard) porosity at $\sigma = 0$
n_o	=	initial porosity before ploughing
n_s	=	sample size
P	=	pressure (bar). Suffix: J = jet impingement pressure
p_o	=	exponent of depth/width ratio in static geometry factor
pv	=	exponent of depth/width ratio in drainage geometry factor
Q	=	jet flow rate (m^3s^{-1})
Q_F	=	horizontal force component from lateral section (kN)
Q_m	=	soil void volume generation rate (m^3s^{-1})

R	=	diameter of grouser plate. Suffixes: i = internal, o = external (m)
R_σ	=	stress ratio (square root) = $(\sigma_g / \sigma_{cr})^{0.5}$
r_a	=	vertical distance nozzle centreline to top of FA (m)
r_b	=	vertical distance nozzle centreline to base of FA (m)
r_j	=	radial distance from jet centreline (m)
S_u	=	effective undrained shear strength ($kN.m^{-2}$)
s	=	sample standard deviation
s_r	=	ratio of sand to water density
t	=	time (s)
U_b	=	cavity boundary velocity (ms^{-1})
U_j	=	jet velocity (ms^{-1}). Suffixes: ji = impingement, js = shear
U_m	=	velocity of centreline of jet at position 'x' from origin (ms^{-1})
U_n	=	nozzle and plough velocity (ms^{-1})
U_o	=	velocity of jet at source (ms^{-1})
U_p	=	pore water velocity (ms^{-1})
V	=	volume (m^3)
W_s	=	submerged weight of sediment ($kg.m^{-3}$)
w	=	tine width (m)
x	=	distance from jet at source (m)
x_a	=	horizontal distance from front of cavity to top of FA (m)
x_b	=	horizontal distance from front of cavity to base of FA (m)
$x_{s,\xi}$	=	constants of sediment detachment equation
Y	=	height from blade base (m)
z	=	depth (m)
z_a	=	depth to top of FA (m)
z_b	=	depth to base of FA (m)
z_c	=	critical depth (m)
z_m	=	maximum depth of tine (m)
α_o	=	effective fraction of blade depth where overburden acts
α_v	=	constant incorporating permeability-velocity-drainage effects
β	=	jet diffusion coefficient (typically 6.3)
γ	=	soil bulk weight density ($kN.m^{-3}$)

γ_s = buoyant weight density of soil (Nm^{-3})

γ_w = weight density of sea water (Nm^{-3})

ε_v = volumetric strain

η = dimensionless loss factor

μ = population mean

ρ_s = bulk density of soil ($kg.m^{-3}$)

ρ_w = density of water ($kg.m^{-3}$)

σ = soil stress acting on tine face ($kN.m^{-2}$)

σ_g = generated confining stress ($kN.m^{-2}$)

σ_{cr} = soil critical confining stress ($kN.m^{-2}$)

τ = shear stress (Nm^{-2})

τ_c = critical shear stress (Nm^{-2})

τ_e = excess shear stress (Nm^{-2})

φ = soil internal friction angle

ψ = ratio of σ_Y to σ_{AVG}

1 Introduction

1.1 The Need for Sub-sea Burial of Cable

Global communication is an essential element of today's society and requires highly technological and reliable systems. These systems often utilise fibre optic cables for the transmission of information between geographical locations. It is therefore necessary to lay fibre optic cables across large sections of the seafloor when the transfer of information between landmasses is required, and cable systems on the seafloor are now common place. However, it is an undesirable necessity, for since the first telecommunication cables were laid across the Atlantic in the 1950's they have been vulnerable to damage from both man made and natural causes. These hazards are from shifting ocean bottom conditions and ships anchors, but 95% of cable failures on the continental shelf have been due to commercial fishing activity (Messina *et. al.*, 2001). Damage is caused when heavy 'otter' boards used in bottom fishing are dragged over the cables. The results yielded unreliable systems with very high repair costs.

In attempts to improve the reliability of seafloor cable systems the cables were armoured and rerouted around areas of known high fishing activity. However, this proved expensive and unreliable, so a more reliable protection system was required. The solution was to bury the cable at the shore ends, in water depths of less than 2000 m. From the late 1960's this was accomplished using sled type cable burial ploughs. However, the typical designed burial depth of 1 m was often hard to achieve in dense sand and stiff clay. The draught force required for seafloor ploughing is often very large, up to fifty tonnes, because of the dilation properties of saturated sands. Consequently, large ships, with high operating costs, are required to pull the ploughs.

The Burial Protection Index (BPI), proposed by Global Marine Systems Ltd, suggests a burial depth based on seafloor soil type and strength. However, its suggested burial depths of 2.5 m in soft clay and 1 m is dense sand, are hard to achieve with passive ploughs. The solution is the jet assisted plough, which uses jets positioned on the plough blade or a vertically impinging jet in front of the blade. They have the ability to achieve greater burial depth at a reduced draught force, giving an economic

advantage since they provide increased protection at a reduced cost. This is because the reduced force enables the use of a smaller ship, or a greater ploughing speed for a given draught force.

Recent trends of reduced fishing stocks have driven fishing into deeper water, so heavier fishing tackle is used at greater water depth. Consequently, a greater cable burial depth is required at a greater water depth. Also the cable market is tending towards short, non-repeater regional networks, often using jetting tools on Remotely Operated Vehicles (ROV) to bury pre-laid cables. Therefore, the more recent requirements have been towards more versatile cable burial systems.

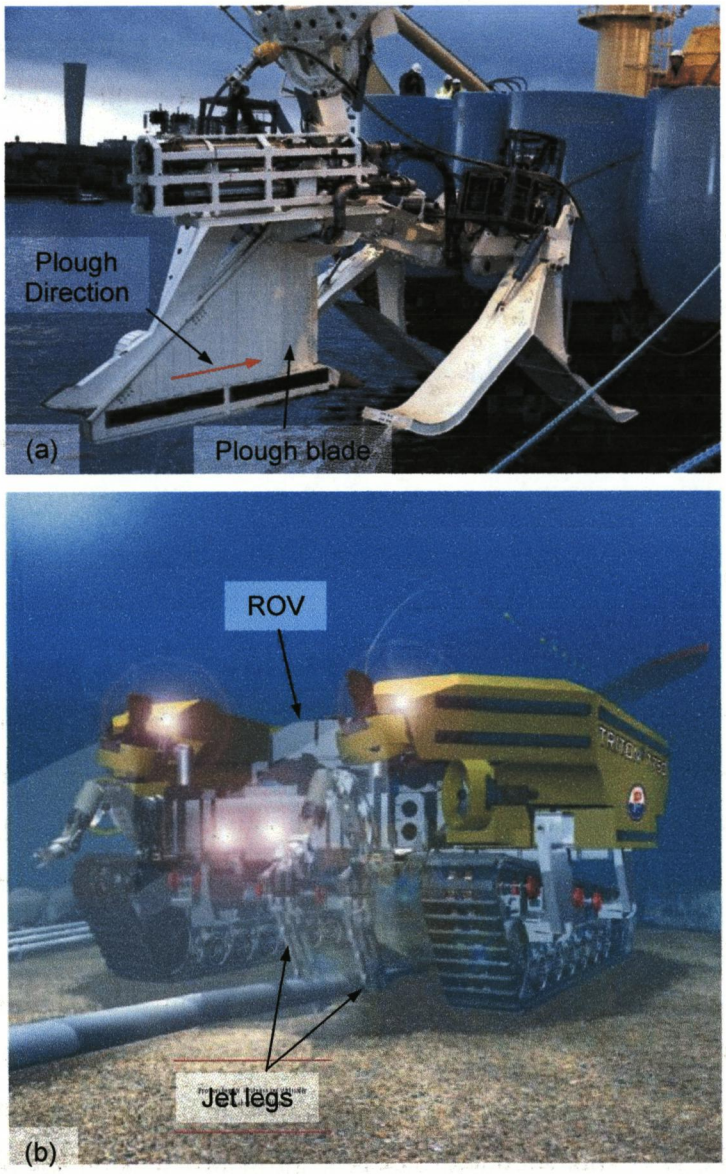

Figure 1.1 **Jet assisted sea plough (a), and ROV burying cable (b)**

To develop more versatile systems requires a sound understanding of jetting tool mechanics. Although cable burial techniques have been used for more than thirty years, and despite various development projects, little is understood of the fundamental jetting tool mechanics. A particular focus of interest is the mechanics of jets in reducing tool force, since the limited power supplied to ROV's requires the most effective use of jetting power to obtain optimum performance.

1.2 Project Aim

The aim of this project is to investigate jet assisted tools for the sub-sea burial of cables. The purpose is to increase the understanding of their mechanics and to develop a mathematical model simulating their behaviour, to assist in the design and operation of jet assisted tools.

1.3 Project Objectives

The two main project objectives were;

1. To study the effects of jetting parameters on tool force reduction.
2. To study the effects of jet parameters on the extent of the resulting fluidised cavity.

1.4 Project Methodology

A methodology was developed consisting of two stages;

1. The effect of jet flow rate (Q), pressure (P), nozzle distribution and jet angle (θ_J) on tool forces were examined in controlled submerged conditions. The distribution of soil pressure on the tool face was also investigated. A model was developed to simulate tool forces given knowledge of the fluidised areas created by the jets. This work is detailed in Chapters 2 and 3.
2. The effect of jet flow rate and nozzle velocity on the resulting fluidised cavity was examined in controlled submerged conditions, initially using a single static jet nozzle, detailed in Chapter 4, followed by a single dynamic nozzle, detailed in Chapter 5. A mathematical model is proposed to simulate the size of the fluidised cavity created and the extent of the fluidised area on the tool face.

3. An evaluation is made of the ability of the combined models to simulate the net soil force acting on jet assisted cable burial tools, detailed in Chapter 6.

The research plan and layout of the thesis is shown in Figure 1.2. Each Chapter deals with one element of the program and include, where relevant, a review of literature, experimental work conducted and the development of the mathematical models. Chapters are supported by appendices that contain further details of results and other appropriate material.

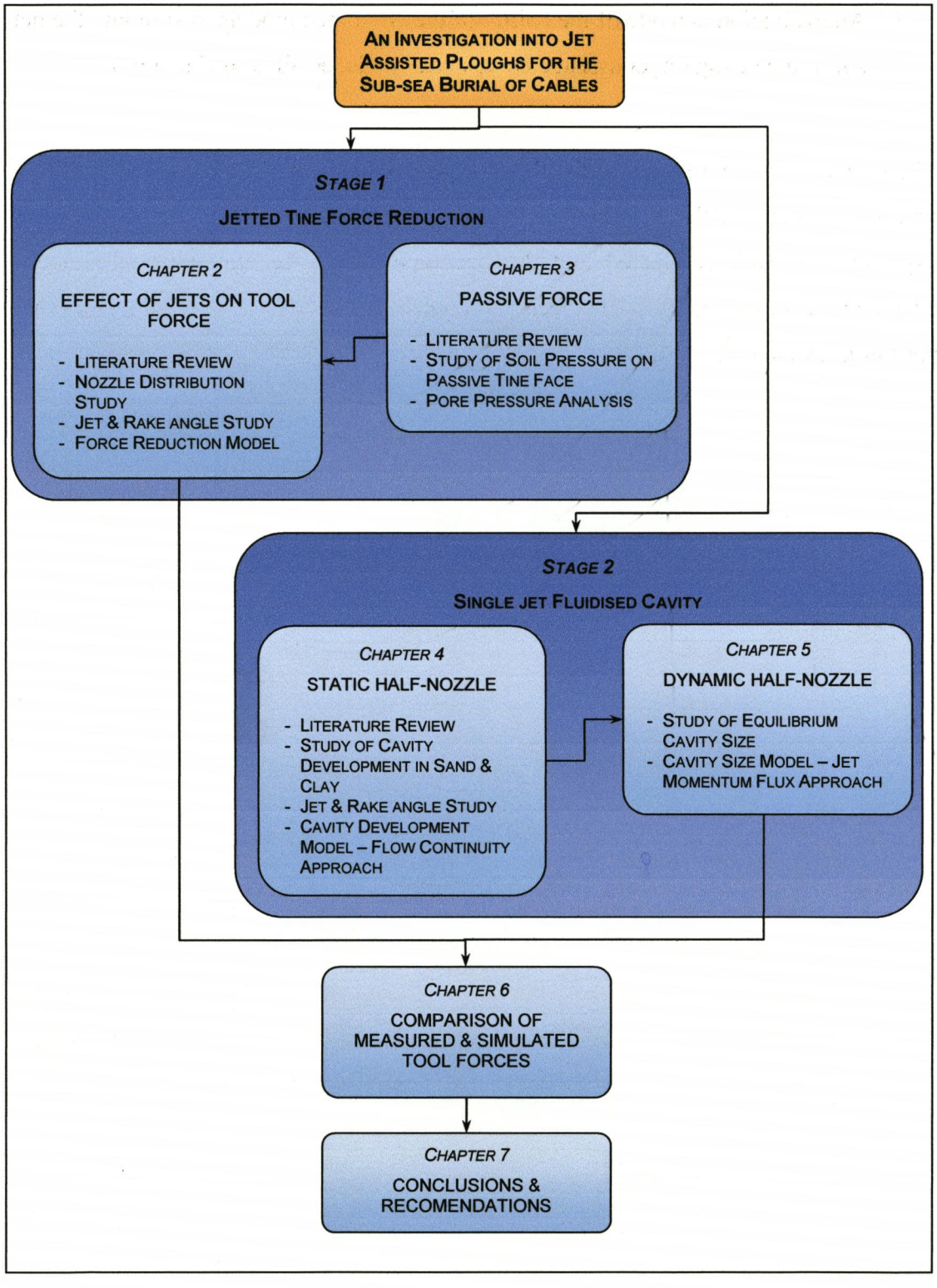

Figure 1.2 Structure of Research Program

2 Investigation into the Interaction between Water Jets and Soil Force on Jetted Tines

2.1 Introduction

Most research into the characteristics of jet-assisted cable burial tools has focused on the effect of jet and tool parameters on the resulting force reduction. Some research has touched on the causes of these effects, but knowledge of them has remained limited. The aim of this Chapter is not only to study the effects of jet and tool parameters on force reduction, but also to develop an understanding of the mechanics causing the effects. This understanding will enable the prediction of the force reduction for jet and tool combinations.

This Chapter contains the details of two investigations using jet-assisted tines in saturated sand. The first investigates the effect of the distribution of jet nozzle area across the tine face, and the second investigates the effect of jet and tine rake angle on force reduction. The understanding gained from these investigations is then used to develop a mathematical model simulating the force reduction, given certain jet and tine parameters.

2.2 Review of Jet-Assisted Cable Burial Plough Literature

Much of the literature on jet-assisted cable burial tools concerns testing the capabilities of newly developed tools; very little literature concerns the fundamental mechanics that give an understanding to their behaviour. There are two main categories of literature. Firstly, those that deal with vertically impinging jets external to the soil, often positioned immediately in front of the plough blade. This is generally concerned with clay soils and often develops some form of empirical equation or dimensional analysis relating jet parameters to the soil forces developed. This literature is reviewed in Chapter 4. The second category concerns jets internal to the soil and predominately relates to sand. This literature gives an indication of the effect of jet and tool properties on soil force reduction and is reviewed below.

Lewis and Messina (1998) report on the General Dynamics Advanced Technology Systems (GD-ATS) and Tyco Submarine Systems Ltd (TSSL) development of a high

speed low force cable burial tool for operation in compacted sands. The tool is based on their development of the Swept Flow Jetter (SFJ) concept, which was born from earlier work by Messina when he found that trenching performance was improved markedly when the jet flow was directed downwards. The SFJ concept uses a backward raked jetting tool with downward facing jets creating flow almost parallel to the tool, as shown in Figure 2.1. Their explanation for the improved performance over the more conventional vertical blades with horizontal jets is that the SFJ concept provides a mechanism for both soil erosion and removal, but no quantitative explanation is given.

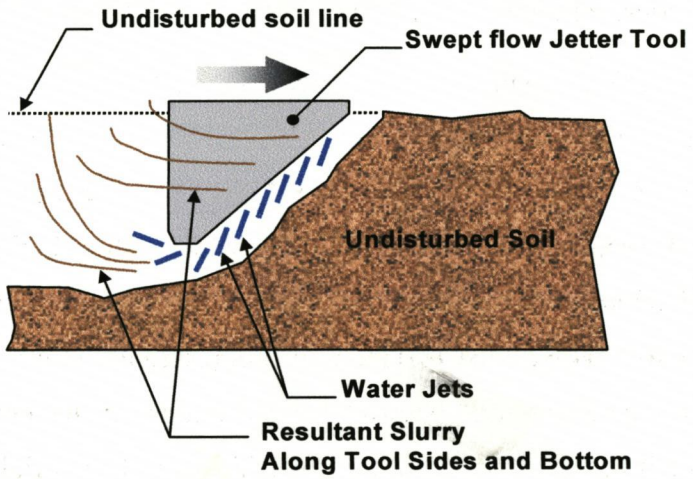

Figure 2.1 Operating principle of the Swept Flow Jetter (after Lewis & Messina, 1998)

The concept was tested using quarter scale tools, where a dimensionless number termed N_2 provided a relative measure of tool effectiveness by relating the fluid flow rate to the tool excavation rate (Q/(tool speed x width x depth)). They found an N_2 value of four was required to reduce the tool force to zero, although force reductions in excess of 50% were realised for N_2 greater than two. The zero force speed of the tool was also found to vary directly with the flow rate of the jets.

Full scale tests were conducted with a tool measuring 0.1 m wide by 1.09 m deep with a backward rake angle of 30° to the horizontal. Two nozzle configurations were tested, being thirty four 12.7 mm diameter nozzles at 63.5 mm spacing and seventeen nozzles at 127 mm spacing. They found the latter gave slightly better performance, and concluded this was due to either the result of a more efficient nozzle arrangement or the higher nozzle pressure. They also concluded the combined quarter and full

scale tests showed that key performance parameters scaled linearly with fluid flow rate.

The SFJ concept has been applied to commercial ploughs, being the GD-ATS Deep Venture Cable Plough (DVCP) and the TSSL Sea Plough VIII. The improved capabilities of these ploughs is reported in a number of papers by Hill *et.al.* (1999), Leifer *et.al.* (1999), Kober *et.al.* (2000), Messina, (2000) & Messina *et.al.* (2001). During sea trials showed the TSSL Sea Plough VIII had a three-fold reduction in tool force and a 50% increase in forward speed with jetting. The GD-ATS DVCP was found to have a two to three fold improvement in trenching speed compared to forward facing nozzles, for a given tool force.

Adamson and Kolle (1995) conducted experiments with a backward raked jetting arm and developed an ROV deployed post lay cable burial system in a joint venture between Perry Tritech, Inc. and Quest Integrated, Inc. Initial experiments in kaolin clay used two evenly spaced 5.5 mm diameter nozzles on a short jetting arm inclined at 40° to the horizontal, which oscillated through 100° along its longitudinal axis. With a jet pressure of 1.04 bar (151 psi) the arm progressed at 50 m/h in 50 kPa clay. Full scale tests conducted in sand showed the oscillation of the jet arms gave no advantage, but speeds in excess of 350 m/h were achieved at 1 m burial depths.

The investigations of Lewis (2002) had the objectives of determining the effect of jet angle and forward speed on force acting on the tine. His research, conducted at the National Soil Resources Institute at Cranfield University at Silsoe, used three $1/10^{th}$ scale tines measuring 30 mm wide and a working depth of 300 mm with three jets. Three jet angles, being horizontal, 30° upward and 30° downwards relative to the horizontal, were tested at 1.5 bar and at four tine speeds. His results showed that jet angle had a significant influence on force reduction, the mean draught force for the upward jets being six times greater than the downward jets. He also found, as Coyne & Lewis (1999) and True and Girard (1998) have, that increasing the forward speed caused the force to increase.

An investigation into the factors influencing the performance of jet assisted submarine cable ploughs was conducted by Knight (2002), also at the National Soil Resources Institute at Cranfield University at Silsoe. One of his objectives was to determine the

effect of jetting factors and forward speed on the forces acting on water jet assisted submarine ploughs. This was done using tines of similar design to Lewis (2002), measuring 30 mm wide with a working depth of 280 mm. Tests were conducted using the jet factors shown in Table 2-1.

Table 2-1 Jet factors used by Knight (2002)

Factor	Values
Jet Angles (x4)	70° & 35° downward, horizontal, 70° upward
Jet pressure (x4)	2, 4, 6 & 7 bar
Nozzle diameter (x3)	5, 6 & 7 mm

The experiments showed that;

1. Jet assistance reduced tine draught force considerably.
2. Draught force reduced with increasing jet pressure until a critical pressure was reached, above which further increases in pressure caused no further force reduction.
3. The critical pressure increased as the jet angle became more upward facing.
4. Downward facing jets had lower draught forces, but the 35° downward jets had slightly lower forces than the 70° downward jets. The draught force was least for the horizontal jets when above the critical pressure.
5. Increasing the flow rate reduced the draught force when below the critical pressure.

However, little explanation was given to the mechanical causes of the results. Knight developed a mathematical model simulating the relationships between jetting factors and tine force by normalising the jetting factors and tine force, shown by Eqs. 2.1 to 2.4.

$$NF = F / F_P \quad \text{= tine force relative to passive force} \tag{2.1}$$

$$NP = P / (F_P/A_T) \quad \text{= jet pressure relative to average soil pressure} \tag{2.2}$$

$$NQ = Q /(vA_T) \quad \text{= total jet flow rate relative to swept volume} \tag{2.3}$$

$$NA = A_J / A_T \qquad \text{= total nozzle area relative to tine face area} \tag{2.4}$$

$$NF = k_N{}^{NQ} \tag{2.5}$$

$$NP = f\left(\frac{1}{k_N} - 1\right) \qquad (0 \leq k_N \geq 1) \tag{2.6}$$

$$NF = \left(\frac{2.g.NA^2}{NQ^2 + 2.g.NA^2}\right)^{NQ} \tag{2.7}$$

The normalised flow rate (NQ) was then related to the normalised force (NF) by Eq. 2.5. Since the flow, pressure and nozzle area are all related (shown in Eqs. 2.6 & 2.7), a Normalised Factor Chart was drawn relating the normalised jetting factors to the normalised force, as shown in Figure 2.2. However, the chart only gives the form of the relationship between factors, not the exact values.

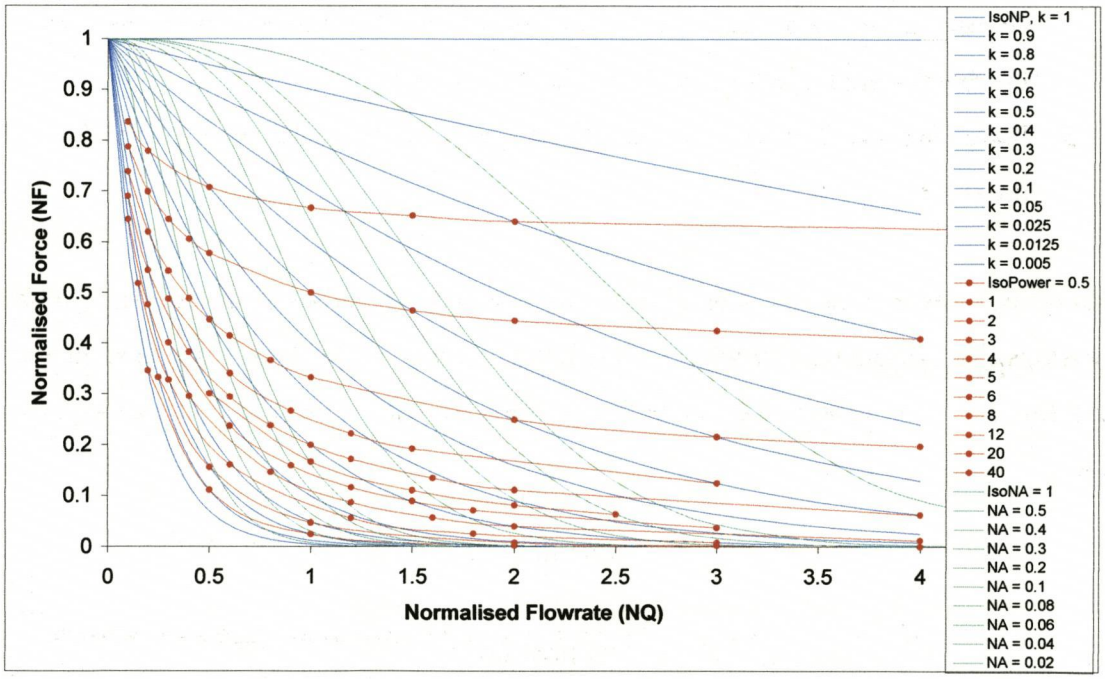

Figure 2.2 Normalised Factor Chart, according to Knight (2002). NP curves are blue, NA cures are green, isoPower curves are red.

The model relates jet factors, and then makes a logical assumption as to how the normalised flow relates to force. However, the model raises concerns in that it takes no account of jet angle, the rake angle or the distribution of the jet flow across the tine face. It has been shown experimentally that jet angle affects the force reduction. The model implies that the distribution or number of nozzles has no effect on the force, only the total cross sectional area of them, which is questionable.

Knight recommends further investigations into the effect of jet angle on force, and why the draught force ceases to decrease as the angle of the jet has a greater vertical downward component. He also suggests an experiment in which in which the soil and fluid dynamics are videoed through a window adjacent to the tine, enabling the effect of jet angle to be explained.

The existing literature gives little explanation for the jetting tool characteristics observed, but gives rise to the following questions.

1. Why do downward angled jets create greater force reduction?
2. How does the rake angle of the tool affect the force?
3. How does the distribution of jet nozzles on the tool face influence the force reduction?
4. Why does much of the literature define jet properties in terms of pressure and flow rate as opposed to the momentum flux of the jet, which is the force exerted by the jet on the soil?

Further investigations are required to establish the fundamental mechanics of jetting tools in order to understand their effect on force reduction.

2.3 Objectives

The objectives of this Chapter are;

1. To determine the behaviour of jets in reducing soil forces on a cable burial tool by investigating the effect of;
   a) Jet nozzle area distribution across the tine face on force reduction.
   b) Jet and tine rake angle on force reduction.
2. To use the above to develop a mathematical model simulating the force reduction gained from tine and jet combinations.

2.4 Methodology and Experiment Design

2.4.1 Effect of Jet Nozzle Area Distribution on Soil Force Reduction

An experiment was designed in which the forces acting on jet assisted tines were measured. Six tines were tested, each having a different number of nozzles, although the total cross sectional area of the nozzles was constant for all the tines. The nozzles were evenly spaced along the centreline of the tines. To investigate the effect of nozzle configuration on the forces two tines had the same number of nozzles, one with nozzles evenly spaced, the other with nozzles in three groups of four. Details of the number of nozzles on each tine and their corresponding diameters are given in Table 2-2.

The effect of nozzle distribution on force was initially examined using four jet pressures, creating four different total jet momentum fluxes. The jet pressures of 1, 1.5, 2 and 2.5 bar were selected after pilot tests had been conducted to establish a suitable range. The forces on a passive (non-jetted) tine were also examined. After the initial experiments had been conducted, additional experiments were conducted to extend the range of pressures (and thus jet momentum flux (JMF)) over which some of the tines were examined. Table 2-3 shows details of the additional pressures examined.

Table 2-2 Details of the nozzles in the nozzle distribution experiment

Tine	No. of Nozzles	Nozzle Diameter (mm)	Nozzle Spacing (mm)
1	1	10.32	135
2	3	6.0	90
3	6	4.25	45
4	9	3.45	30
5	12	3.0	22.5
6	12 (Grouped)	3.0	90 (group centres)
Total cross sectional area = 84.8 mm^2			

Table 2-3 Details of the additional jet pressures tested

Tine	Additional Jet Pressures (bar)
1	3.0, 3.5
2	3.0, 3.5
3	0.5

The tines were designed to have a forward velocity of 1 km/h, which was near the upper limit of capability of the equipment. A high velocity was used since the investigations of Knight (2002) showed that force differences between tines were accentuated at greater tine velocities.

All tests were conducted in medium sized sand from Cainhoe Quarry, Bedfordshire, having a D_{50} of 0.2 mm and a hydraulic conductivity (k) of 0.972 m/h. This sand is termed 'standard sand' (SS) in this study. The same sand was used by Knight (2002) and Lewis (2002). Details of the particle size distribution is in Appendix 2.

The experiments were conducted in a randomised block design, each test being replicated three times. The tests within each block were conducted in a randomised order. The exact order of experiments in the program is shown in Appendix 2.

2.4.2 Effect of Jet and Rake Angle on Soil Force Reduction

An experiment was designed in which the soil forces acting on tines of different rake and jet angles were measured. Three rake angles were tested, being forward, vertical and backward raked. Three jet angles were then examined for each of the rake angles. Details of the rake and jet angles are shown in Table 2-4 and Figure 2.3. Three nozzles of 6 mm diameter were evenly spaced down the centreline of each tine.

Table 2-4 **Combination of tine rake and jet angles tested**

Tine	Rake Angle (α)	Jet angle (relative to horizontal) (θ_J)
1	45°	90°
2	45°	45°
3	45°	0°
4	90°	45°
5	90°	0°
6	90°	-45°
7	135°	0°
8	135°	-45°
9	135°	-90°

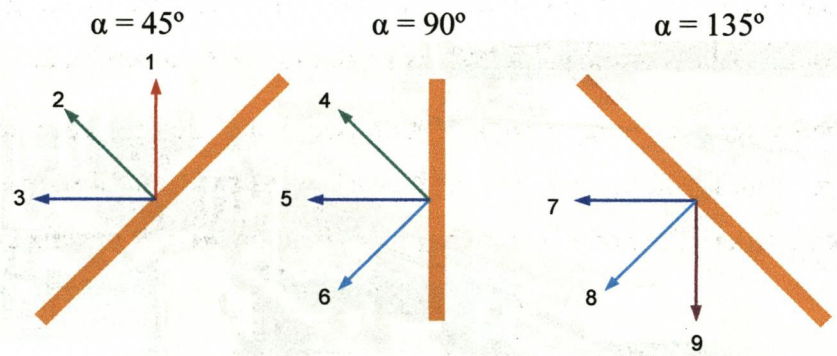

Figure 2.3 **Combination of tine rake and jet angles tested**

Each tine rake and jet angle combination was examined at four jet pressures (and thus JMFs). The results of the previous experiments on the jet distribution were studied to select appropriate jet pressures. The pressures were 1, 1.5, 2.25 and 3 bar. A passive (non-jetted) test was also conducted for each rake angle.

The tines were designed to have a forward velocity of 1 km/h and were conducted in sand from Cainhoe Quarry, the same as in the nozzle distribution experiments.

Experiments were conducted in a randomised block design, the experiments in each block being conducted in a randomised order. Each test was replicated three times, once in each block. The exact order of tests are recorded in Appendix 2.

2.5 Equipment and Measurement Technique

2.5.1 Jet-Assisted Tine Instrumentation Systems

The experiments were conducted in a fully instrumented soil bin facility in the soil dynamics laboratory at Cranfield University at Silsoe. The soil bin, measuring 6 m long, 1 m wide and 1 m deep, was equipped with an instrumented carriage fitted with an Extended Octagonal Ring Transducer (EORT) (Godwin, 1975) to which the tines were mounted, as shown in Figure 2.4. The EORT measured the horizontal and vertical forces and the moment acting on the tine independently, as shown in Figure 2.5. The drive sprocket for the chain pulling the carriage was instrumented with a proximity sensor, from which the velocity of the carriage was determined. A proximity switch at either end of the test section sensed when the carriage passed through it.

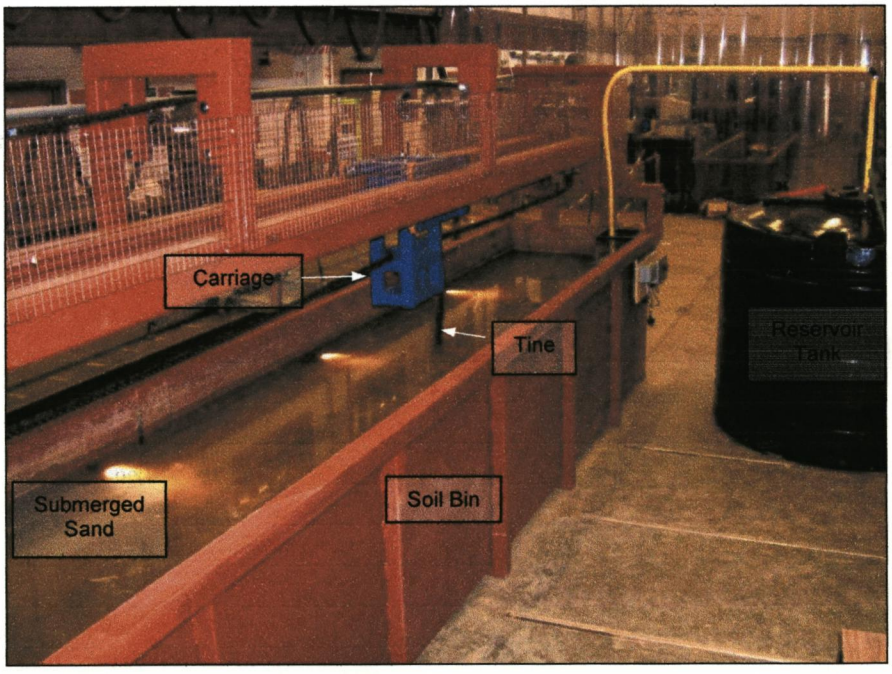

Figure 2.4 Soil bin used for experiments with jet-assisted tines

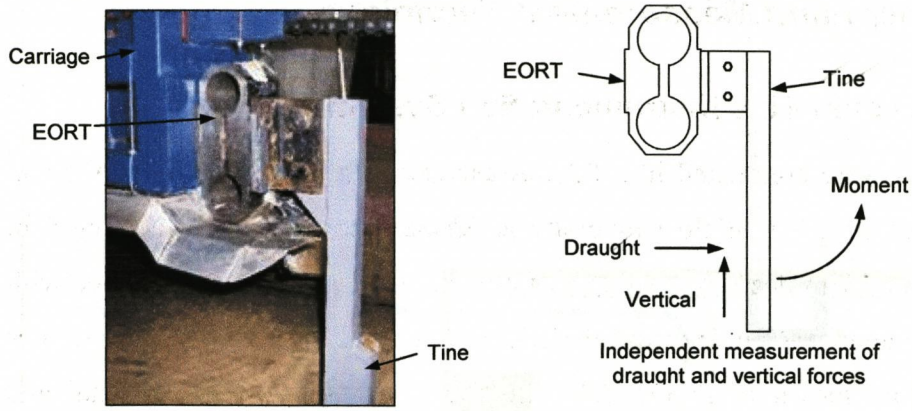

Figure 2.5 Tine mounted on EORT and carriage

Figure 2.6 shows the jet assisted tines in action. A Grundfos centrifuge pump (CR16) supplied water under pressure to the tine from a reservoir tank. Transducers measured both the flow rate and pressure of the water downstream of the pump, as shown in Figure 2.7.

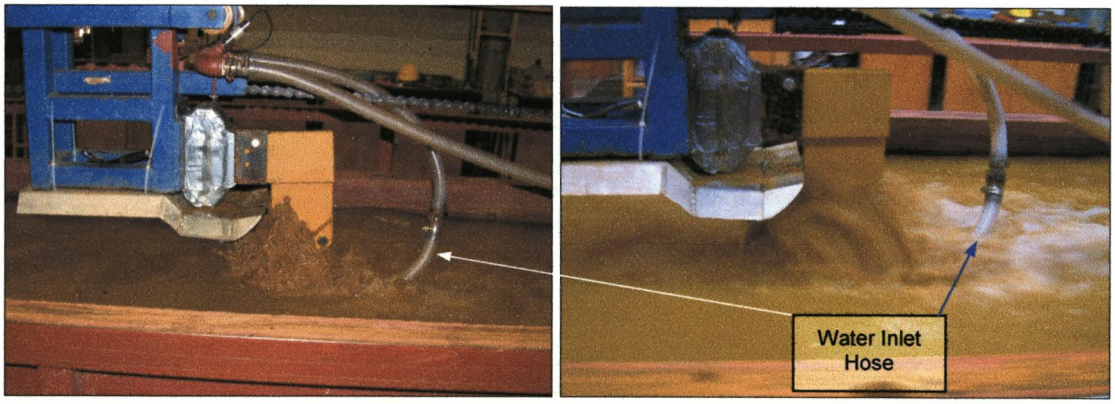

Figure 2.6 Forward raked jetted tines in action (direction of travel right to left)

Data from all the transducers was recorded onto a laptop computer using DasyLab v.7.0 software via a Flyde data acquisition module, as shown in Figure 2.8. The calibration details of the horizontal force, vertical force and moment from the EORT, the carriage velocity and the flow and pressure transducers are given in Appendix 3.

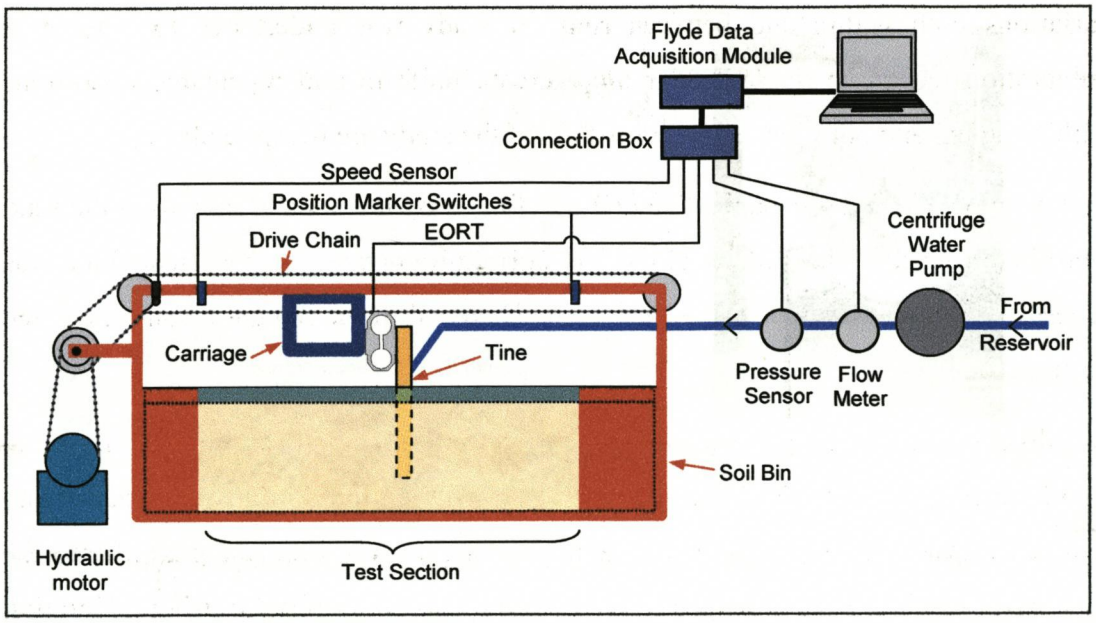

Figure 2.7 Diagram of the soil bin, water jet and instrumentation systems for the jet assisted tines experiments

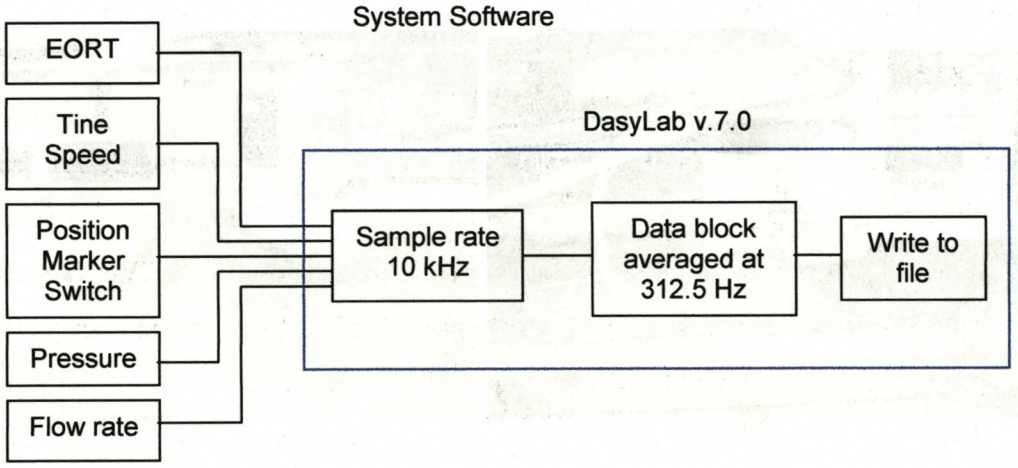

Figure 2.8 Details of instrumentation software system

2.5.2 Soil Preparation Method

The soil bin enabled the sand to be tested in fully saturated conditions and submerged with a headwater depth of up to 0.2 m. To ensure the experiments were conducted in the same soil conditions a preparation method was developed to create uniform and repeatable soil conditions. The preparation method used by Knight (2002) of manually mixing the sand after each test was inadequate and produce large force

variations both within and between runs. A study was undertaken to develop a preparation technique that would rapidly create uniform and repeatable conditions within the bin and between tests. Full details of the study are in Appendix 1.

In the study different mechanical, jetting and fluidizing methods of preparing the sand were investigated. The soil condition and uniformity created by each technique was accessed from the draught force generated when pulling a standard non-jetted tine through the bin.

Results showed fluidizing the sand was the most appropriate preparation technique. A small water upflow of 0.75 l/sec at 0.4 bar through the sand partially fluidized it and reduced its shear strength allowing manual mixing with a steel rod pushed into the sand at 0.15 m intervals. Compaction of the sand was then achieved using a vibrating plate pulled over the surface. The upflow water was dispensed through a manifold-lateral system of perforated pipes laid at the base of the soil bin. The mean coefficient of variation of force data for individual tests was 6%, and for all tests was <3%, demonstrating the method created uniform and repeatable soil conditions.

2.5.3 Design of Nozzle Distribution Tines

The tines used in the nozzle distribution experiment had the following design features;

1. The tine geometry was the same as that used by Knight (2002), having a working depth of 280 mm by 30 mm wide, giving an aspect ratio of 9.33. The same aspect ratio was used in the rake angle experiments. Details of the tine geometry are given in Figure 2.9, and CAD drawings are in Appendix 5.
2. The total cross sectional area of the nozzles on the tines was constant so that the total jet momentum flux of each tine was constant. A total nozzle cross sectional area of 84.8 mm^2 was used, being that of three 6 mm diameter nozzles, the same as used in the rake angle experiment. For each of the other tines the total nozzle area was divided evenly between the number of nozzles, giving the nozzle diameters shown in Table 2-2.
3. Nozzles were evenly spaced down the centre of the tine face with the distance between adjacent nozzles being twice that between the end nozzles and the tine base/soil surface, as shown in Figure 2.9. This was to enable the fluidised cavities

to cover the whole of the tine face without any overlap, assuming the cavities were symmetrical about the nozzle. Nozzle spacing is shown in Table 2-2.

4. The nozzle length/diameter ratio was kept the same for all nozzles, being 6.66, to minimise differences between the nozzles coefficients of discharges (which vary with l/d ratio). However, the length of the largest nozzle (10.32 mm diameter) was limited to 40 mm, giving a ratio of 3.88.

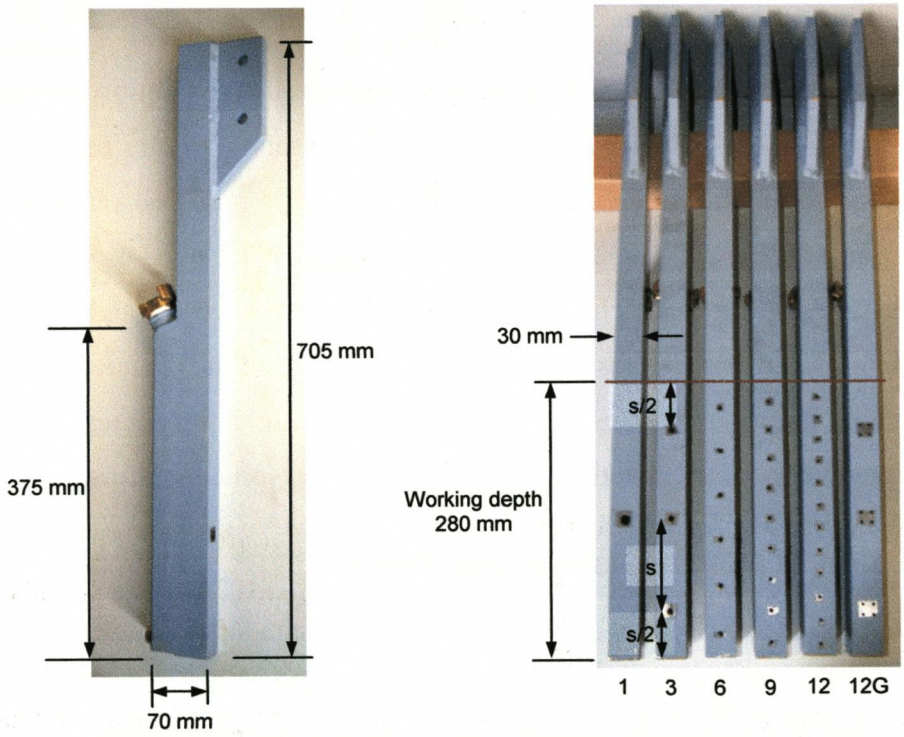

Figure 2.9 Details of tine geometry for nozzle distribution experiments

2.5.4 Design of Rake Angle Tines

The tines used in the rake angle experiments had the following design features;

1. The tines for all rake angles had the same depth/width ratio as the tines in the nozzle distribution experiments, having a working depth of 280 mm and a width of 30 mm.
2. The tine rake and jet angles are given in Table 2-4.
3. Each tine had three 6 mm diameter nozzles, with a vertical distance of 75 mm between adjacent nozzles with the top nozzle being 75 mm below the soil surface. Therefore the three nozzle depths were the same for all the rake angles.
4. The tines were manufactured from mild steel.

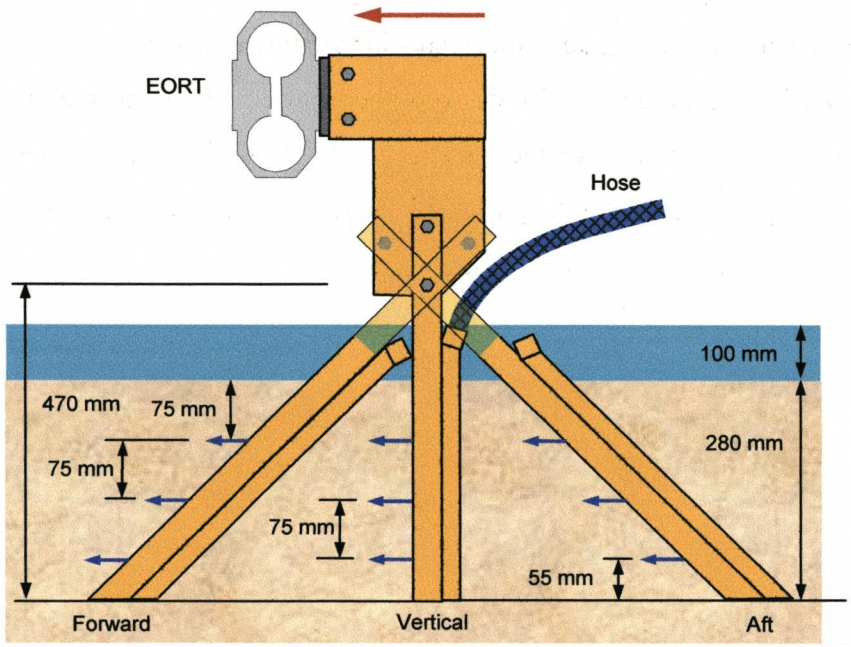

Figure 2.10 **Details of tine geometry for rake angle experiments**

2.5.5 Measurement Technique

The same experimental technique for both the nozzle distribution and rake angle experiment were used and was as follows;

1. The tine was put into the soil and attached to the carriage while the upwash system was operating.
2. The soil in the bin was prepared according to the method detailed in Appendix 1.
3. The water jets were turned on while the desired pressure was set, which also cleared the nozzles of sand.
4. The geostatic soil forces on the tine were recorded for ten seconds before the carriage pulled the tine through the soil at 1 km/h.
5. The water jets were stopped at the end of the run and the tine was taken from the bin with the upwasher system operating.

2.5.6 Measurement Analysis

The experimental data was exported into Microsoft Excel to be analysed. The mean of each factor (horizontal force, vertical force, moment, jet pressure, flow rate and tine velocity) was found over the tests section of the bin, which was designed to eliminate end effects from the results. The test section of the results was determined from the marker switches, which changed signal value when the carriage passed through the section. However, in the rake angle experiments the position of the tine in the soil bin as the carriage passed through the test section was different for each rake angle, due to the geometry of the tines. Therefore in order that the means were calculated over the same section of soil, the test section was altered individually for each rake angle, as shown in Figure 2.11.

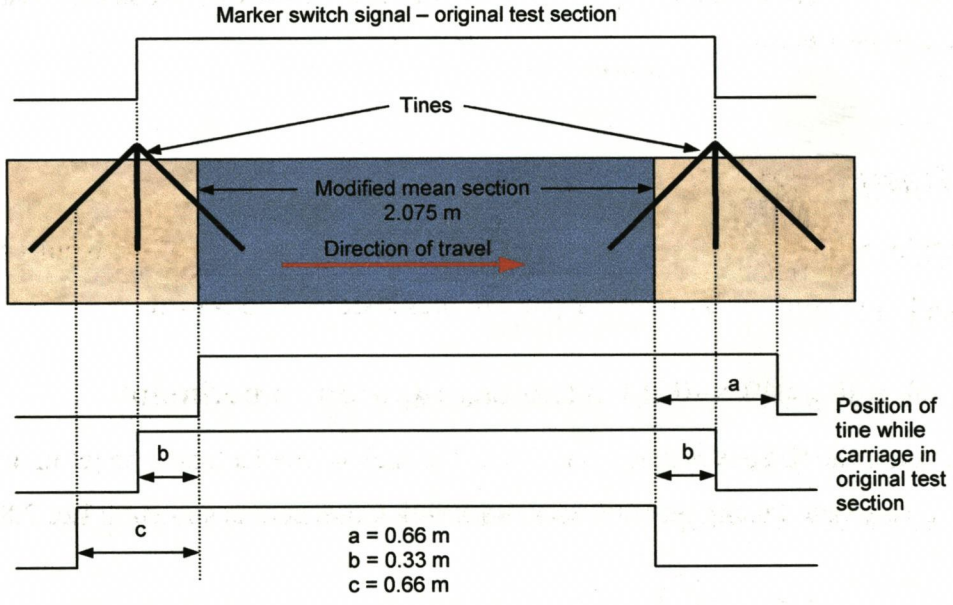

Figure 2.11 Modified test section for the rake angle experiments

The mean data was then used to determine the total JMF of each test. The horizontal force was examined against the JMF for both the nozzle distribution and rake angle experiments. The horizontal force was also examined against the rake and jet angle in the rake angle experiment.

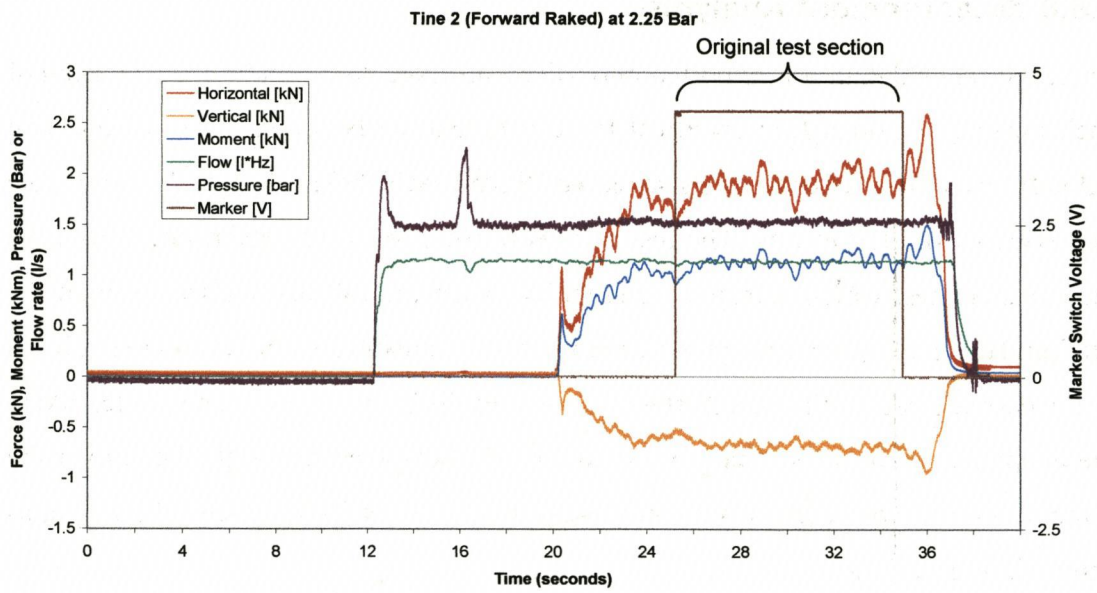

Figure 2.12 Typical data from jet assisted tine experiments showing section over which mean values were taken

2.6 Results and Discussion

Full results of each experiment are given in Appendix 4. Aspects of the results that are relevant to the objectives of the Chapter are presented and discussed.

2.6.1 Results of the Jet Nozzle Distribution Experiment

The mean of the three replicates was found for each of the factors. The jet momentum flux was calculated using jet flow data and nozzle diameter, as shown in Eq. 2.8.

$$JMF = \frac{4.Q^2.\rho_w}{\pi.d_j^{\,2}.n} \qquad \textbf{2.8}$$

The mean horizontal force is plotted in Figure 2.13 against the mean JMF for each of the tines and jet pressures tested. The nozzles on the tines with nine or twelve nozzles became blocked with sand on some tests, causing the flow rate to be reduced and the horizontal force to increase. Mean values including the 'blocked' data are shown by the dashed lines in Figure 2.13, and when they were excluded is shown by the solid lines. The data is connected by lines to help identify the data associated with each

tine, and show the general trends rather than expressing an accurate relationship between force and JMF.

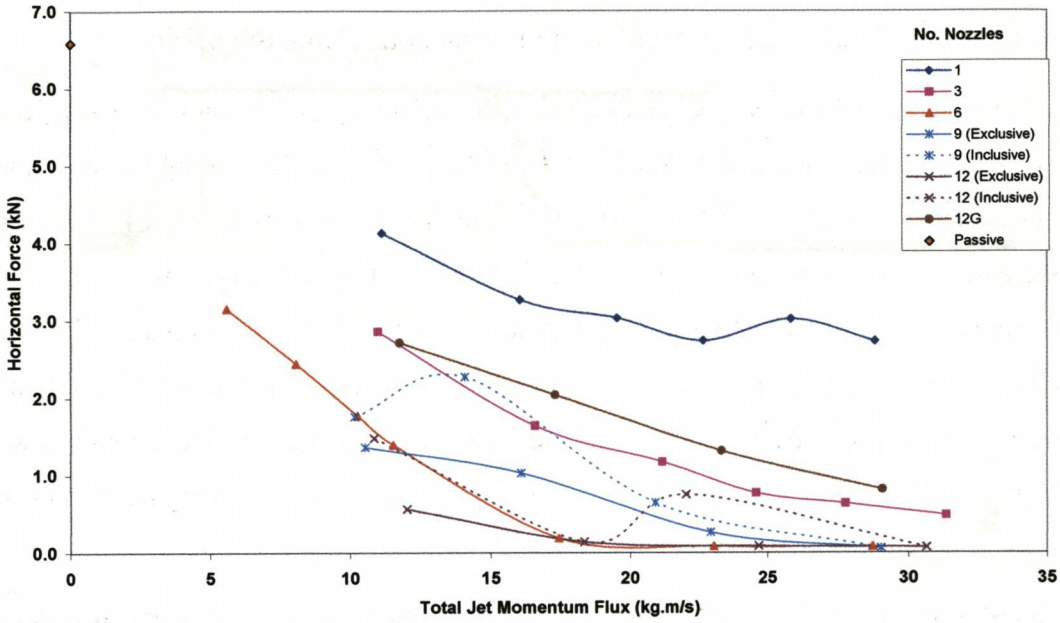

Figure 2.13 Horizontal force against total jet momentum flux for the jet nozzle distribution experiments. The mean non-jetted horizontal force was 6.58 kN

Figure 2.13 shows three important characteristics. Firstly, the horizontal force decreased as the JMF increased. This was true for all the tines. It occurred to such an extent that the forces on the 6, 9 and 12 nozzle tines were reduced to nearly 1% of the passive force at the higher JMF tested. Secondly, the smaller diameter nozzles, which were on the nine and twelve nozzle tines, sometimes became blocked with sand, with an increasing tendency to do so at lower JMF. This is shown by data on the dashed lines having spuriously high force values. Examination of the tine after these tests showed that the nozzles at the base of the tine became blocked while those higher up remained free. Thirdly, the tines with a greater number of nozzles evenly spaced down the tine face had much lower forces. This is seen in that the tines with six, nine and twelve nozzles had negligible force at a JMF of 30 $kg.ms^{-1}$ whereas the tine with only one large nozzle had a force of 2.7 kN (still 40% of the passive force) at the same JMF. This demonstrates that the more evenly the JMF is distributed across the tine face, the greater is its effectiveness at reducing soil forces. However, the tine with twelve nozzles in three groups of four had forces very similar to those of the tine with

only three nozzles. This shows that the group of four jets behaved effectively as one jet. The tine with twelve jets evenly spaced down the tine face had much lower forces than the tine with twelve grouped nozzles. Therefore it is not the number of jets, but the distribution of them that is important, if the total nozzle area is constant.

The above characteristics can be understood if the fluidising and erosion effects of the jet on the sand are considered. Knight (2002) found that a jet issuing from a tine creates a cavity around the jet by eroding the sand. Therefore increasing the JMF of a jet increases its ability to erode the sand, so creating a larger cavity. An area of tine face around the jet nozzle, namely the fluidised area (FA), will engage with the fluidised cavity rather than the original sand mass. Therefore, the soil forces on the tine are generated by the elements of the tine face still engaging the original soil mass. So, a greater JMF causes a larger FA, reducing the remaining soil engaging elements, resulting in lower soil forces.

The distribution of jets on the tine face is important since it determines the positions of the FAs. Evenly distributed jets result in a greater coverage of the tine face by FAs, whereas clustered jets effectively overlap their FAs reducing the total tine coverage. The tines that focussed all the JMF through one or three nozzles created jets with high erosive ability, so creating large cavities. However, because the cavities were wider than the tine, much of the energy from the jet fluidised sand that was not in the path of the tine, and was thus wasted. The smaller jets, on the tines with many nozzles, had a much smaller erosive power than the larger jets, so consequently the resulting cavities were much smaller. Nevertheless, the fluidising power of the jets was focussed on the sand immediately in front of the tine face, resulting in much more of it being covered by FAs. These principles are shown graphically in Figure 2.14.

A certain threshold JMF is required to create a cavity about a jet on a moving tine. Below the threshold JMF the jet has insufficient ability to erode and transport sand from in front of the nozzle as fast as the sand approaches the tine face. The study in Chapter 3 shows the soil pressure on the tine face is significantly greater than the jet pressure, thus when sand meets the nozzle it is forced into it, so blocking it. Since the soil pressure is greater at increasing soil depth, nozzles lower down the tine face became blocked while nozzles nearer the surface remained free.

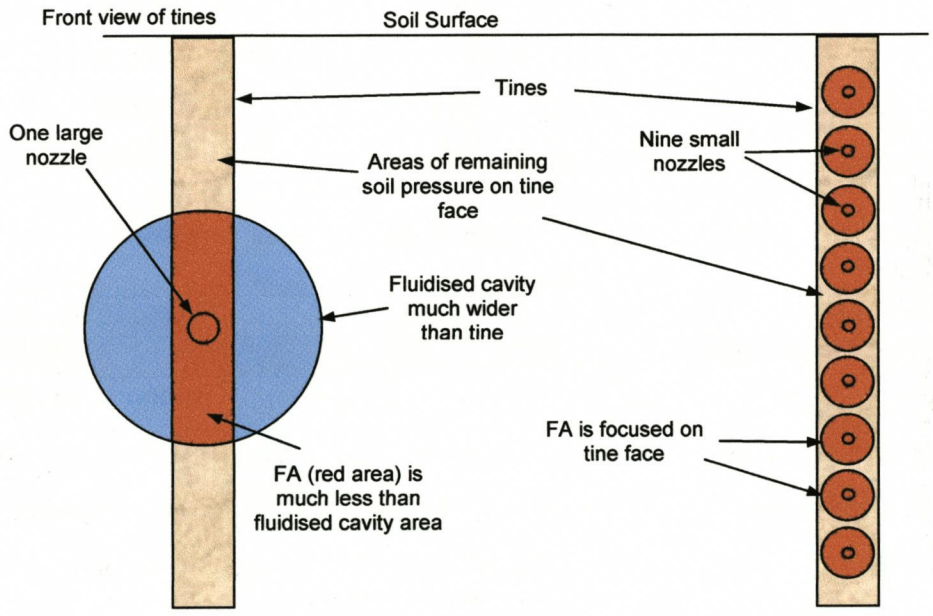

Figure 2.14 **Differences in the fluidised areas of one large nozzle and many smaller nozzles**

The percentage of the tine face area covered by the FAs may be determined for each test on the following basis.

1. Soil stress on the tine face increases approximately linearly with depth, as shown in Chapter 3.
2. Because the nozzles are positioned symmetrically about the mid depth of the tine, the mean soil stress can to apply to the whole of the tine face without causing error when determining the force eliminated by a particular FA.
3. It is assumed that the FA is symmetrical about the jet centreline.

The fraction of tine face engaging the soil is then determined as the ratio of the net force (F_N) to the passive force (F_P). Therefore the percentage of tine face covered by FAs is;

$$\% \text{ tine face covered by FA} = \left(1 - \frac{F_N}{F_P}\right) \times 100 \qquad \textbf{2.9}$$

The mean %FA was calculated for each of the tines and JMF tested and is displayed in Figure 2.15. It clearly demonstrates that the tests with the low forces (i.e. those with many jets evenly distributed on tine face) had most of the tine face covered by FAs, with little area left to engage the soil.

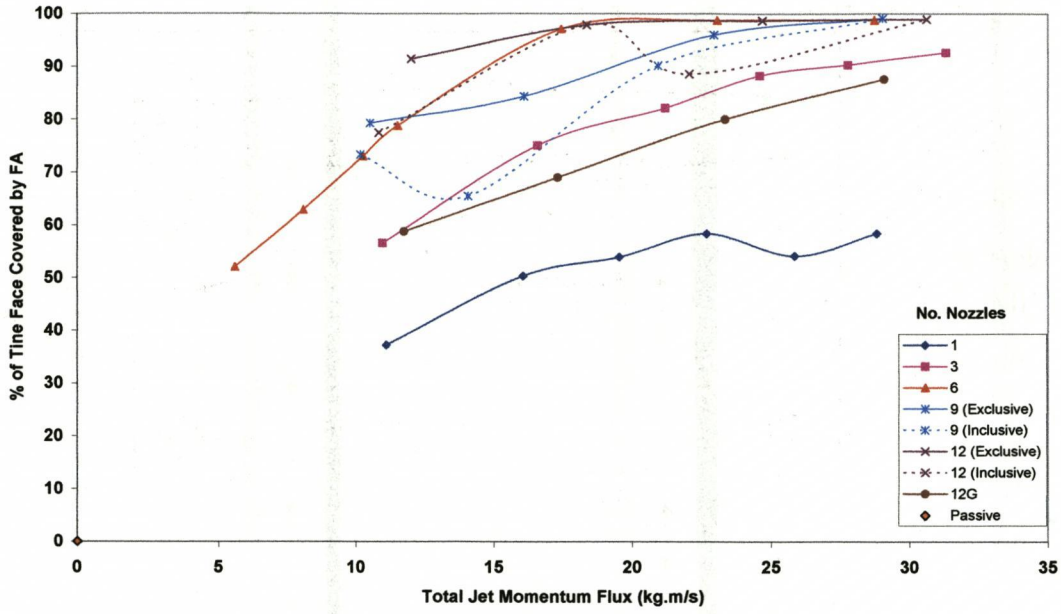

Figure 2.15 **Percentage of tine face covered by fluidised areas for each of the tests**

2.6.2 Results of the Jet Angle Experiment

I. Paint Wear Analysis

After completing the experiments the paint wear on the tines was studied to determine on the sections that experienced abrasion. The paint on some areas of the tine faces was completely worn off; in others the abrasion was less intense and took only the shine from the paint leaving a matt finish. The boundary between the gloss and matt finishes was occasionally clear, but often ill defined. The abrasion was often in the vicinity of the nozzles, indicating it was not caused by contact with the un- jetted sand mass but largely due to the sand blasting effect of sand transported in the jet flow impacting the tine. Many of the tines showed paint abrasion on their sides, thought to be caused by the non jetted sand mass, since it often covered large areas. The paint wear patterns on the tine faces were used to give an indication of the flow path of the jets, and thus the size of the resulting cavities, enabling estimates of the r_a or r_b dimensions (vertical distance from nozzle to top or base of FA respectively) to be made. The wear patterns on the forward and backward raked tines are presented and analysed in Figure 2.16 and Figure 2.17 respectively. There was very little paint wear on the vertical tines, so these were unable to be included in the analysis.

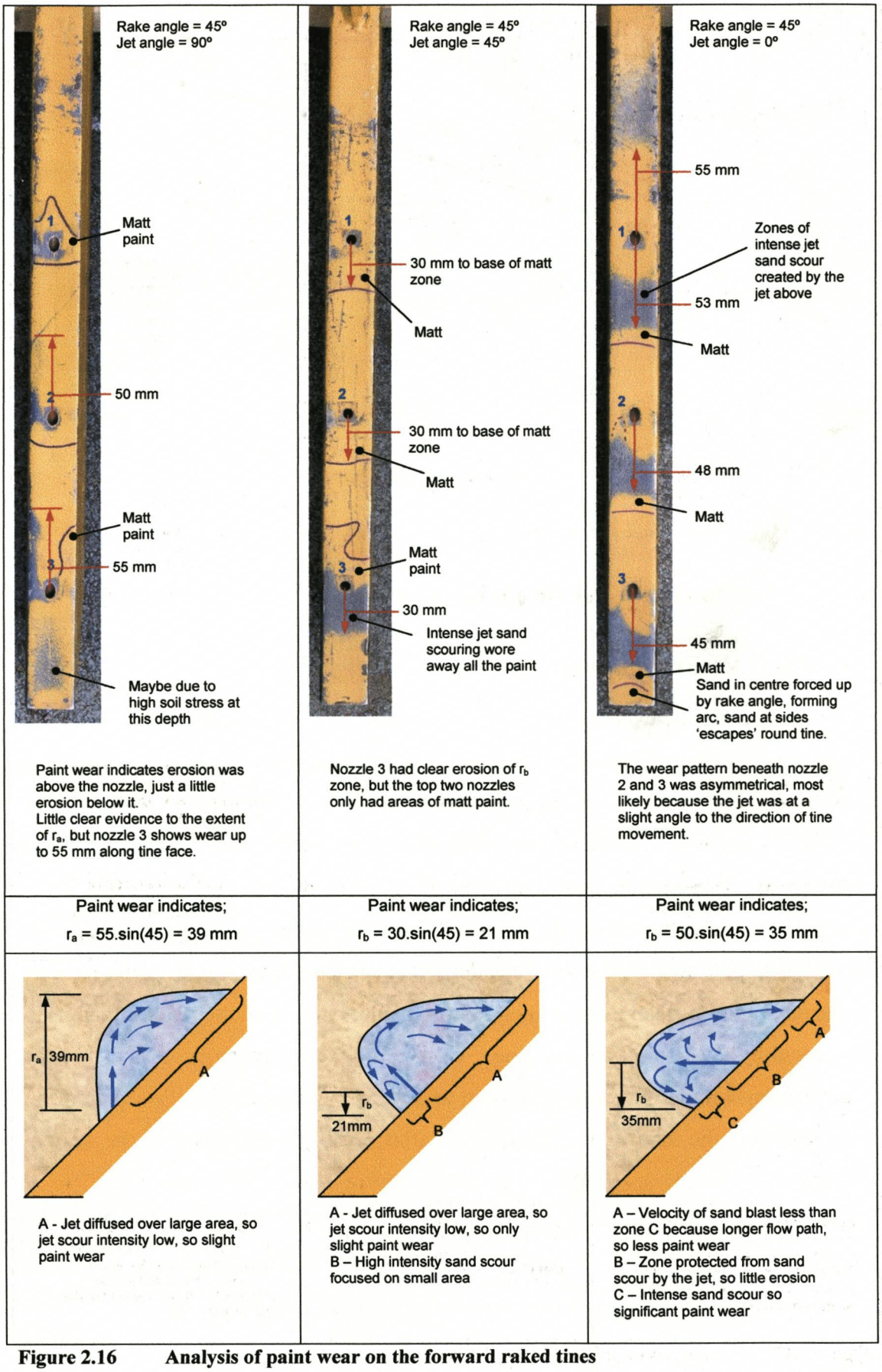

Figure 2.16 Analysis of paint wear on the forward raked tines

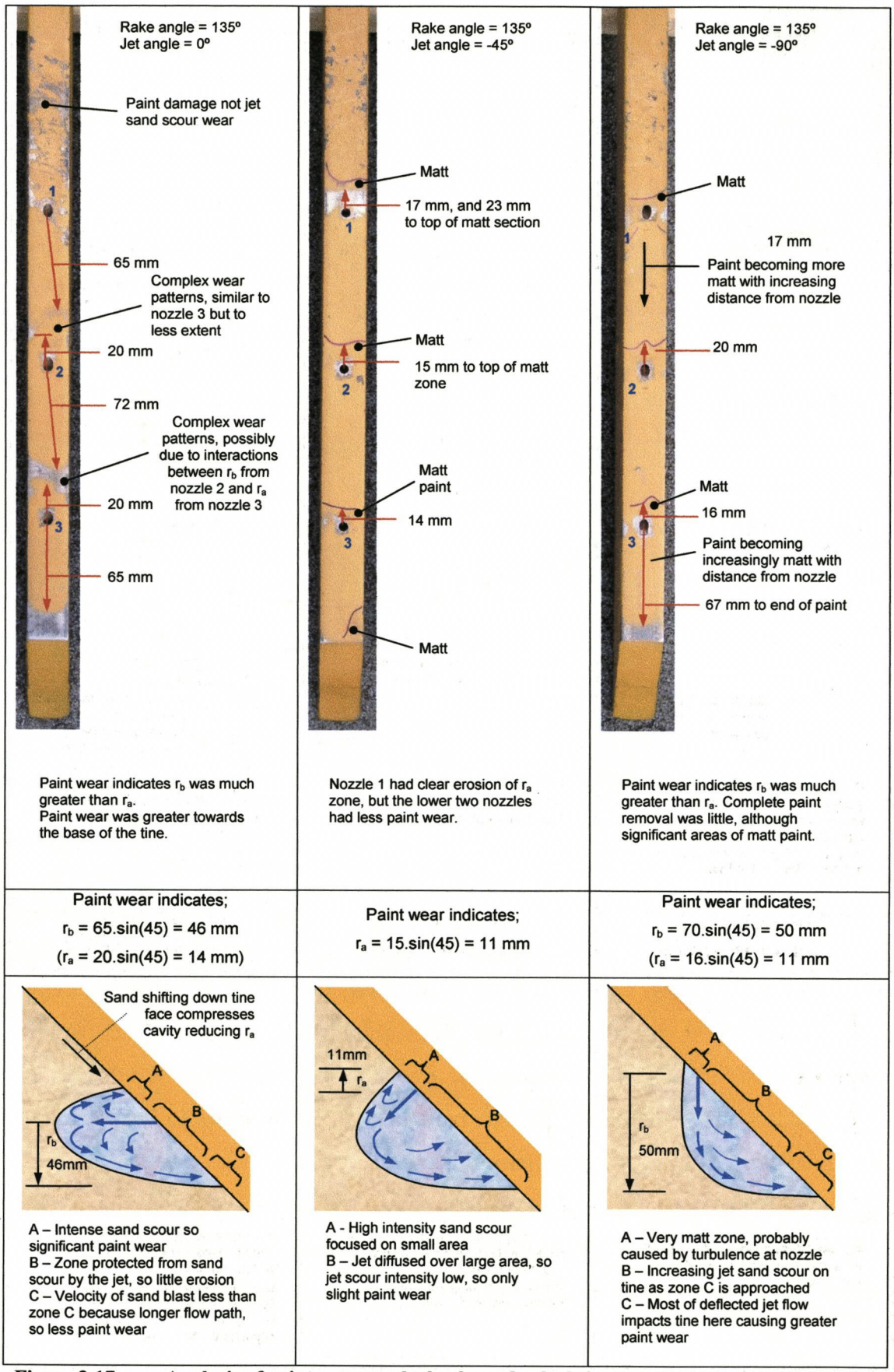

Figure 2.17 Analysis of paint wear on the backward raked tines

II. Force Analysis

The mean of the three replicates of each test was found for each of the factors. The jet momentum flux was calculated using Eq. 2.8. The mean horizontal force is plotted against the corresponding mean JMF in Figure 2.18 for each of the jet and rake angles tested. The data of each tine is connected by lines to aid their identification and show the general trends rather than their exact mathematical relationship between force and JMF.

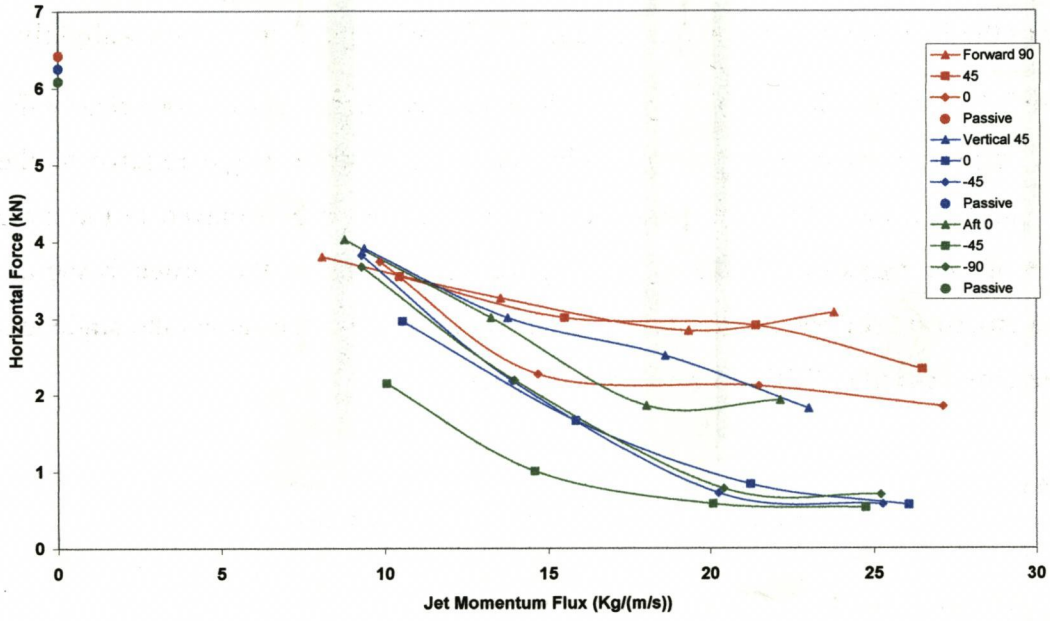

Figure 2.18 Horizontal force of the rake angle tines against jet momentum flux

The data in Figure 2.18 shows three important characteristics. Firstly, the passive forces for the forward, vertical and backward raked tines were very similar, being 6.42, 6.25 and 6.09 kN respectively. The force decreased slightly as the tine became more backward raked. This is because the forward raked tine had a slightly greater working depth than the backward tine, because a slight slackness in the mounting system allowed the tines to rotate rearwards by 2°. Because the forces were similar for all the rake angles it is concluded, in the context of the Godwin and Spoor (1977) narrow tine soil failure model, that the soil failed laterally around the tine, with no significant crescent type failure. This concept is developed further in Chapter 3.

Secondly, the horizontal force decreased with increasing JMF. This was true for all the jet and rake angles tested, and is in agreement with the findings of the JMF distribution experiment.

Thirdly, the effect of JMF on force was much greater for the vertical and backward raked tines than the forward raked tines. This is seen in that the forces in the vertical and backward raked tines were reduced as the JMF increased to about 20 $kg.ms^{-1}$, after which they remained constant at about 10% of the passive force. However, the force for the forward raked tines reduced to approximately only 33% of the passive force as the JMF increased to about 15 $kg.ms^{-1}$, after which it decreased only slightly.

Figure 2.19 displays the data of Figure 2.18 in another form to show more clearly the effect of jet and rake angle on the horizontal force. The jet angle relative to the horizontal is on the horizontal axis. The three rake angles are displayed in the three groups of data, the forward rake angle being the right hand side, the vertical being the centre group and the backward being the left group. Data for the same rake angle and jet pressure (and thus JMF) are connected by lines.

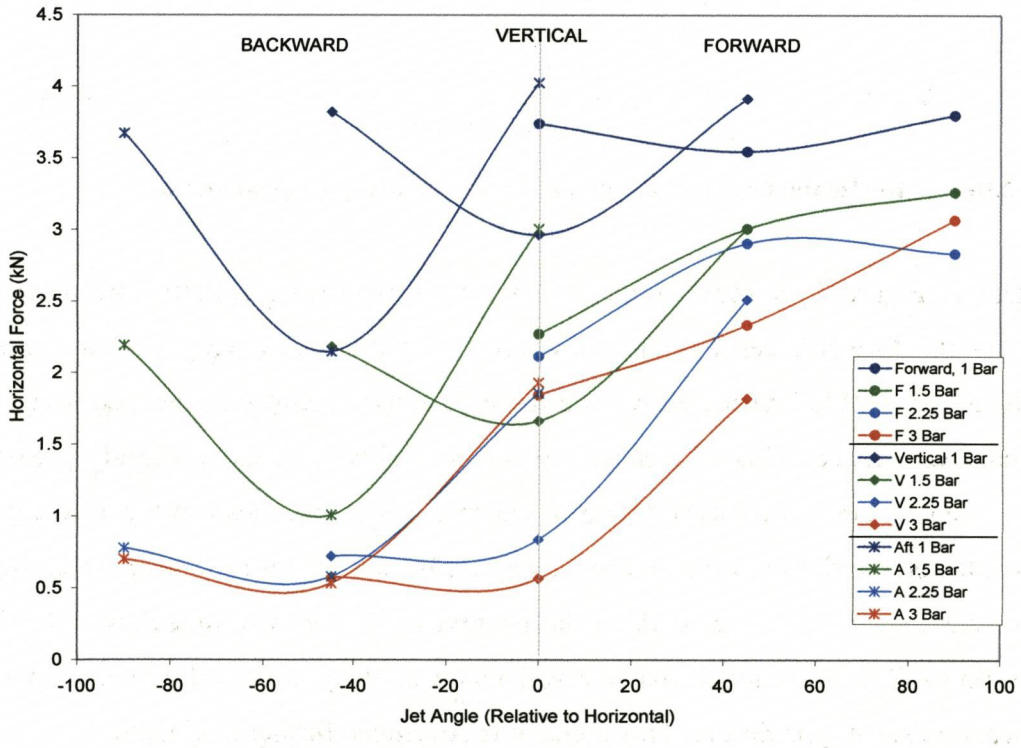

Figure 2.19 The effect of jet angle, rake angle and jet pressure on horizontal force

The data in Figure 2.19 shows the horizontal force decreased with increasing jet pressure (and thus JMF), as discussed above. It also shows complicated interactions between jet angle, rake angle and the force. The force was a function of both the jet and rake angle, since most jet angles had very different forces, for each of the rake angles. For example, the 1 bar jet at an angle of -45° gave a force magnitude of 2.15 kN with the backward raked tine, compared to 3.82 kN with the vertical tine. Because of the complicated nature of the results, the general effects of the jet and rake angles are discussed individually, with exceptions being noted and explained.

III. Effect of Jet Angle

The general characteristic of jet angle (θ_J) on the horizontal force was that the more downward facing the jets were, the lower the force was. This is seen by the force of the 90° jets tine (upward facing) at maximum jet pressure being equal to 3.07 kN, whereas for jets angled below the horizontal this was reduced to about 0.5 kN. The reason for this is that the jet angle alters the position of the FAs. The more downward angled the jets are, the lower down the tine face the eroded cavity is, and consequently, the FAs are lower too. If the jet angle only affects the position of the FAs and not their size, then downward jets have lower FAs and thus eliminate greater forces from the tine face, because soil stress increases with depth. Therefore, in general, downward angled jets create lower tine forces.

However, the data in Figure 2.19 shows that lowering the jet angle did not always reduce the force. This is seen at the lower jet pressures in the backward raked tine, where the forces of the -90° jets were considerably greater than with -45° jets. Similar characteristics are seen with the vertical tine. This is because the jet angle not only affects the position of the FAs, but their size also. Jets at an oblique angle to the direction of movement through the soil created a different shaped cavity to those that were normal to it, because a different aspect of the jet was exposed to the soil, and the path of the jet was deflected by the cross flow component of the sand. Consequently, the FA created by the jet on the tine face was of a different shape and most likely to be smaller than that created by a horizontal jet. Figure 2.19 also shows that the forces for the most downward angled jets on the backward and vertical tines reduced to similar values as for the less oblique angled jets. This was most likely due to the FAs

of the most downward angled jets increasing as the JMF increased until they eliminated the same force from the tine face as those of the less oblique jets (the -45° and 0° jets on the backward and vertical tines respectively).

Figure 2.19 shows that raising the jet angle resulted in greater forces. This is because the FA was shifted up the tine face and was most likely to be reduced in size, consequently creating higher forces.

IV. Effect of Rake Angle

The results show the forward and vertically raked tines generally had lower forces. This was accentuated at the greater jet pressures, by the difference between the forward and backward raked tines being greatest. The general explanation is that the rake angle affects the position of the FA on the tine face, and thus the force reduction. Assuming the cavity was symmetrical about the jet centreline and that its diameter increased with increasing distance from the front of the cavity, then the rake angle of the tine affects the position where the tine face intercepts the cavity, as shown in Figure 2.20. As the rake angle increases (becomes more backward raked), the upper boundary of the FA shifts towards the jet centreline, reducing r_a, and the lower boundary shifts further down, increasing r_b, so moving the FA down the tine face. The FA consequently eliminates a greater force, for reasons discussed previously. The reverse is true if the rake angle is decreased (becomes more forward raked).

However, the data in Figure 2.19 shows that the force did not always decrease with increasing rake angle. For example, the vertical tine always had significantly lower forces than the backward raked tine when using horizontal jets. Without measurement of the shape, size and position of the eroded cavities during the experiments it is difficult to give a conclusive explanation for this. However, the results of the experiment with a single dynamic nozzle in Chapter 5 showed that the cavity was not always symmetrical about the jet centreline, and in some cases the base of the cavity closed up to the nozzle, as shown in Figure 2.20. This indicates that a vertical tine may intersect the cavity at a section of greater depth, whereas an backward raked tine at a section of smaller depth. Consequently, the FA on the vertical tine would be larger than that on the backward raked tine, and thus, the vertical tine would have greater force reduction when using horizontal jets. However, when jets at oblique

angles are used, the size and position of the cavities are altered, as discussed earlier, such that with downward facing jets with sufficient JMF, the backward raked tine intersects the cavity at a section of greater diameter, creating greater force reductions than on the vertical tine.

In summary, the experimental data shows that the force was lowest when the combination of JMF, jet angle and rake angle created large FAs that were positioned low on the tine face.

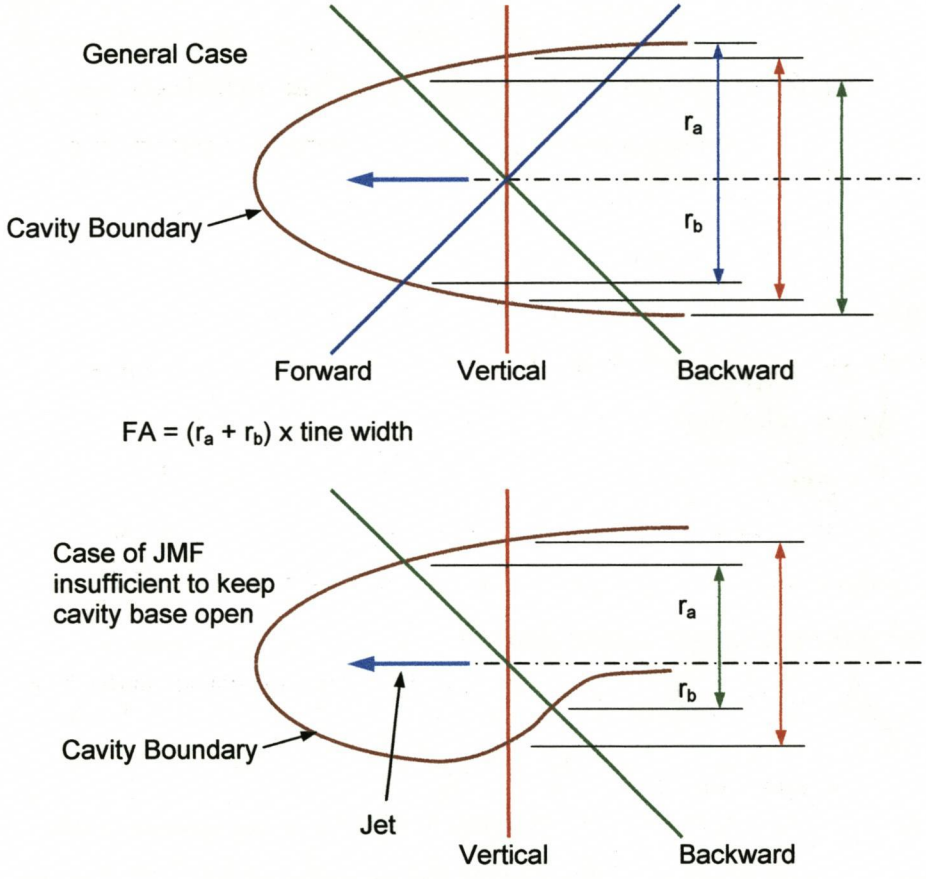

Figure 2.20 Effect of rake angle on the position of the FA

2.7 Development of a Mathematical Model Relating the Fluidised Area to the Tine Force Reduction

2.7.1 Stress Elimination by Fluidised Areas on Jet-Assisted Tines

A mathematical model was developed to relate the force reduction to the fluidised area created by the jets. It was developed by analysis of the stress profile on the tine face, as shown in Figure 2.21.

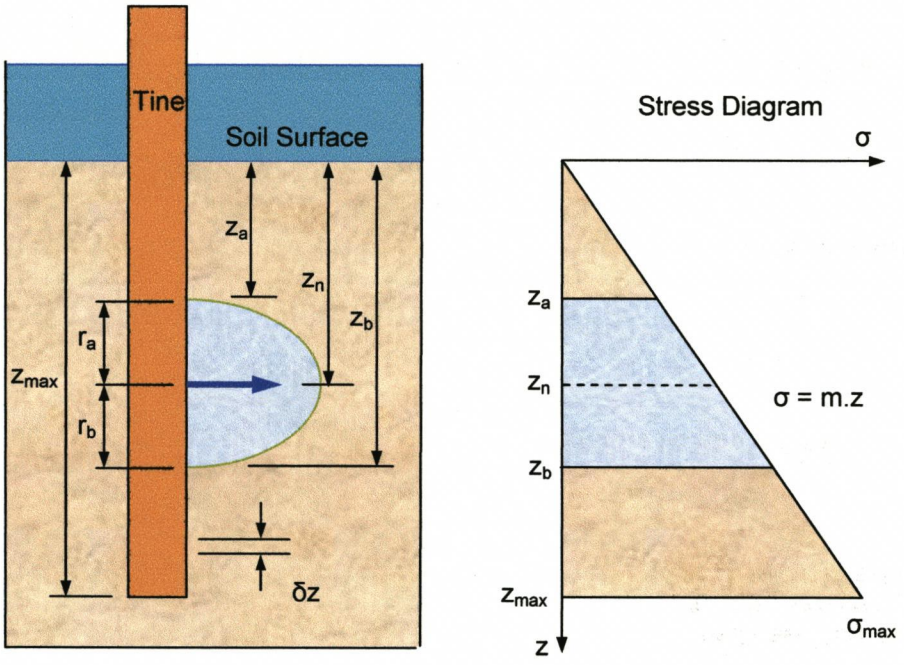

Figure 2.21 **Diagram of fluidised cavity and the resulting stress profile on the tine face**

The equation of the stress profile is;

$$\sigma = m.z \qquad 2.10$$

The stress on element δz is;

$$\sigma = \frac{Force}{Area}$$

Now, the element area is;

$$Area = Depth \times TineWidth = \delta z.w$$

Thus;

$$\sigma = \frac{F}{\delta z.w}$$

2.11

So the force on element $\delta.z$ is;

$$F = \sigma.\delta z.w$$

2.12

But if σ is substituted with Eq. 2.10 it gives the force as;

$$F = m.z.w.\delta z$$

2.13

The force over the fluidised section is therefore the integral of Eq. 2.13 between z_a and z_b;

$$F = \int_{za}^{zb} m.w.z.\delta z \quad = \quad \left[\frac{m.w.z^2}{2}\right]_{z_a}^{z_b}$$

$$F = \frac{m.w}{2}\left(z_b{}^2 - z_a{}^2\right)$$

2.14

The total force on a passive tine face is the integral of Eq. 2.13 between the soil surface and the base of the tine, giving;

$$F_P = \frac{m.w.z_m^2}{2}$$

2.15

And when rearranged for m gives;

$$m = \frac{2.F_P}{w.z_m^2}$$

2.16

Substituting Eq. 2.16 into Eq. 2.14 and simplifying gives,

$$F = \frac{F_P}{z_m^2}\left(z_b{}^2 - z_a{}^2\right)$$

2.17

Equation 2.17 gives the force loss over the fluidised area. However, if there are n jets on the tine face, then the total force loss from the jets is given by;

$$F_L = \frac{F_P}{z_m^2}\sum_{i=1}^{i=n}\left(z_{bi}{}^2 - z_{ai}{}^2\right)$$

2.18

Where from cavity geometry in Figure 2.21;

$$z_{ai} = z_{ni} - r_a$$

$$z_{bi} = z_{ni} + r_b$$

2.19 (a,b)

The net force on the tine is;

$$F_{NET} = F_P - F_L$$

2.20

2.7.2 Force Reduction with Forward or Backward Raked Tines

To determine the force loss with a jet issuing from a forward or backward raked tine, the values of r_a and r_b must be calculated at the point where the fluidised profile intersects the tine face. If it is assumed that the fluidised cavity profile is approximately parabolic, as the experimental results of Chapter 5 indicate, then the geometry of the fluidised profile and the tine face is as shown in Figure 2.22.

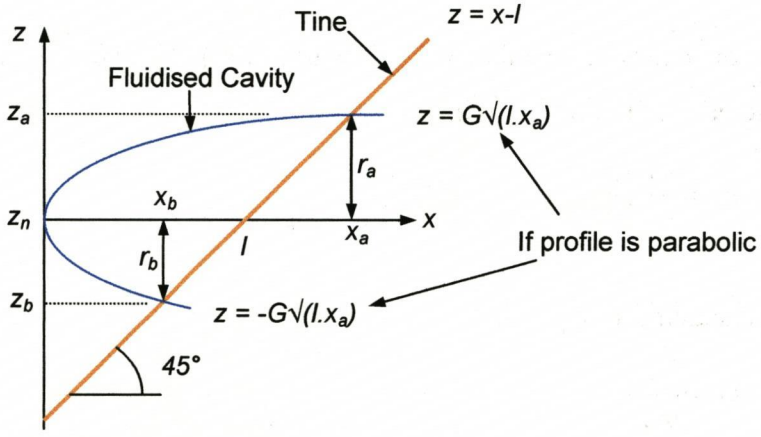

Figure 2.22 Profiles of fluidised cavity with forward raked tine

To determine the position of x_a, assuming that the cavity profile is parabolic, the intersection between the cavity profile and tine face is calculated;

$$G\sqrt{l.x_a} = x_a - l$$

$$G^2 l.x_a = x_a^{\,2} - 2l.x_a + l^2$$

$$0 = x_a^{\,2} - G^2 l.x_a - 2l.x_a + l^2$$

$$0 = x_a^{\,2} - x_a l.\left(G^2 + 2\right) + l^2$$

2.21

Equation 2.21 is of quadratic form, thus for forward raked tines with horizontal jets;

$$x_a = \frac{-b_q + \sqrt{b_q^{\,2} - 4.a_q.c_q}}{2.a_q}$$

2.22

$$x_b = \frac{-b_q - \sqrt{b_q^{\,2} - 4.a_q.c_q}}{2.a_q}$$

2.23

And for backward raked tines, this changes to;

$$x_a = \frac{-b_q - \sqrt{b_q^{\,2} - 4.a_q.c_q}}{2.a_q}$$

2.24

$$x_b = \frac{-b_q + \sqrt{b_q^{\,2} - 4.a_q.c_q}}{2.a_q}$$

2.25

Where,

$$a_q = 1 \qquad b_q = -l.\left(G^2 + 2\right) \qquad c_q = l^2$$

2.26 (a,b,c)

The depth of the cavity at the tine face is;

$$r_a = G.\sqrt{l.x_a}$$

2.27

$$r_b = G.\sqrt{l.x_b}$$

2.28

2.7.3 Determination of FA Size and Position from Force Data and Paint Wear Measurements

The model developed in Section 2.7.1 simulates the force reduction and net force acting on a tine, based on tine geometry, passive force and FA data. However, no direct measurements of FA were taken, only indirect estimates through paint wear measurements. Therefore, in order to evaluate the model it is rearranged to give simulated FAs based on force reduction data and measurements from the paint wear

analysis. The model is then evaluated by comparison of the simulated FAs with those discussed in Section 2.6.2. The model in Section 2.7.1 is rearranged as follows.

There are three nozzles on each of the tines in the jet angle experiment, at depths z_{n1}, z_{n2} and z_{n3}. From Eqs. 2.18 and 2.19 the force reduction is given as;

$$F_L = \frac{F_P}{z_m^2}\sum_{i=1}^{i=3}\left((z_{ni}+r_b)^2-(z_{ni}-r_a)^2\right)$$

2.29

When multiplied out it gives;

$$F_L = \frac{F_P}{z_m^2}\left[2.r_b.\sum_{i=1}^{i=3}z_{ni}+2.r_a.\sum_{i=1}^{i=3}z_{ni}+3.r_b{}^2-3.r_a{}^2\right]$$

2.30

Rearranging for r_b gives an equation of quadratic form, being;

$$0 = 3.r_b{}^2+2.r_b.\sum_{i=1}^{i=3}z_{ni}+2.r_a.\sum_{i=1}^{i=3}z_{ni}-3.r_a{}^2-\frac{F_L.z_m{}^2}{F_P}$$

2.31

So,

$$r_b = \frac{-b_r \pm \sqrt{b_r{}^2-4.a_r.c_r}}{2.a_r}$$

2.32

Where;

$$a_r = 3, \qquad b_r = 2.\sum_{i=1}^{i=3}z_{ni} \qquad c_r = 2.r_a.\sum_{i=1}^{i=3}z_{ni}-3.r_a{}^2-\frac{F_L.z_m{}^2}{F_P}$$

2.33(a,b,c)

If the jet is horizontal and the tine vertical, then assuming the cavity is symmetrical about the jet centreline, and $r_a = r_b$, Eq. 2.31 simplifies to;

$$0 = 4.r_a.\sum_{i=1}^{i=3}z_{ni}-\frac{F_L.z_m{}^2}{F_P}$$

$$r_a = \frac{F_L.z_m{}^2}{4.F_P.\sum_{i=1}^{i=3}z_{ni}}$$

2.34

Equation 2.32 gives r_b as a function of r_a, but r_a is unknown. However, there are limits to the possible value of r_a, for it cannot exceed the distance between the nozzles, otherwise the FAs from adjacent nozzles would overlap. (Overlap may have occurred in reality once the minimum force was reached, but the force analysis is limited to when there is no overlap.) There are further limitations; the depth of the FA cannot exceed the distance between nozzles, for the same reasons, thus the sum of r_a and r_b can be no greater than the nozzle spacing. Since the nozzles were spaced at 0.075 m, the limits of the FA are;

$$0.0 \leq r_a \leq 0.075$$

$$-0.075 \leq r_b \leq 0.0$$

$$r_a - r_b \leq 0.075$$

(r_b is negative)

Therefore, for a given force reduction there is, mathematically, a range of possible positions of the FAs that create the required force reduction. The range of positions is plotted in Figure 2.23, for each of the tests with the forward raked tines, and in Figure 2.24, for each with the backward raked tines, and in Figure 2.25 for the vertical tines using Eqs. 2.32 and 2.33(a,b,c) and the limits set above.

The vertical axes in the three Figures are the values of r_a (above the horizontal axis) and r_b (below the horizontal axis). The horizontal axis is the value of r_a used to generate the corresponding r_b value.

The estimated r_a or r_b value of each tine, measured from the paint wear analysis, is marked onto the corresponding plot. The rest of the FA is then determined by the curves generated by the model, as shown in the two Figures. Thus, the model defines the position and size of the FA based on a r_a or r_b value estimated from the paint wear analysis. The estimated r_a and r_b values from the paint wear analysis were assumed to be associated with the higher jet pressures, since the greater pressures would have created greater abrasion on the tine face, creating the visible wear patterns. Therefore the r_b values on the plots are always associated with the curve of the greatest jet pressure.

I. Discussion of the FA analysis with regard to JMF

The simulated FAs from the force analysis, displayed in the two Figures, show that the FAs increased with increasing jet pressure (and thus JMF), but to a diminishing extent as the pressure became larger, until there was no increase in FA with increasing jet pressure. This is seen clearly with all the backward raked tines in Figure 2.24, as the simulated r_b curves are the same for both 2.25 and 3 bar. This is because the minimum force had been reached at a jet pressure of 2.25 bar, so further increases in pressure reduced the force no further. This is in agreement with the discussion of the force results in Section 2.6.2.

II. Discussion of the FA analysis with regard to jet angle

Figure 2.23 shows there to be a large range of possible FA positions on the forward raked tines. When using the paint wear to define either the r_a or r_b value, the resulting FA positions are the same as that expected from the discussion of the force results in Section 2.6.2, that is, the more upward facing the jet, the higher were the FAs. For the vertically upward jets, the value of r_a was about three times greater than the value of r_b, yet as the jet angle reduced the FA became more central about the nozzle with r_a and r_b being about equal for the horizontal jet.

Figure 2.24 shows the range of possible FA positions for the backward raked tines to be only where the value of r_b is greater than r_a, except for the horizontal jets, where the range is greater. However, the estimated r_a or r_b values from the paint wear analysis define the FAs to be largely below the jet centreline, as expected. Yet the positions of the FAs are not as consistent with the discussion in Section 2.6.2 as they the forward raked tines were. Analysis of the horizontal jets on tine 7 indicates that much of the FA was below the nozzle, r_b being about 6.5 times greater than r_a when the estimated r_b value was 46 mm, and when using an estimated r_a value of 14 mm, r_b is still 2.9 times greater, being more than expected. Also the estimated r_b value of 50 mm, for tine 9 with the vertically downward jets, gives a larger than expected r_a value of 20 mm. This is questionable since it is greater than the r_a value estimated from the paint wear analysis on tine 8, which had shallower angled jets, so would be expected to have a greater r_a value. It is likely therefore that the r_b value determined in the paint

wear analysis was an underestimate. The paint wear analysis of tine 9 in Figure 2.17 shows that r_b was measured to the top of the paint wear zone, rather than the base of it, being assumed the jet lacked sufficient abrasiveness at that distance from its source and that it was the soil mass causing the wear. However, if it was the jet abrasion that caused the wear, then r_b measured to the base of the zone is 75 mm. Because of the limits to the FA, this reduces r_a to zero, so that that all the FA is below the nozzle. The reason for the positions of the simulated FAs for the backward raked tines being slightly different to that expected is therefore likely to be due to error in the estimation of the r_a or r_b value in the paint wear analysis.It is concluded therefore that the position and size of the simulated FAs are in general agreement to that expected from the discussion of the force results of the jet angle experiment in Section 2.6.2.

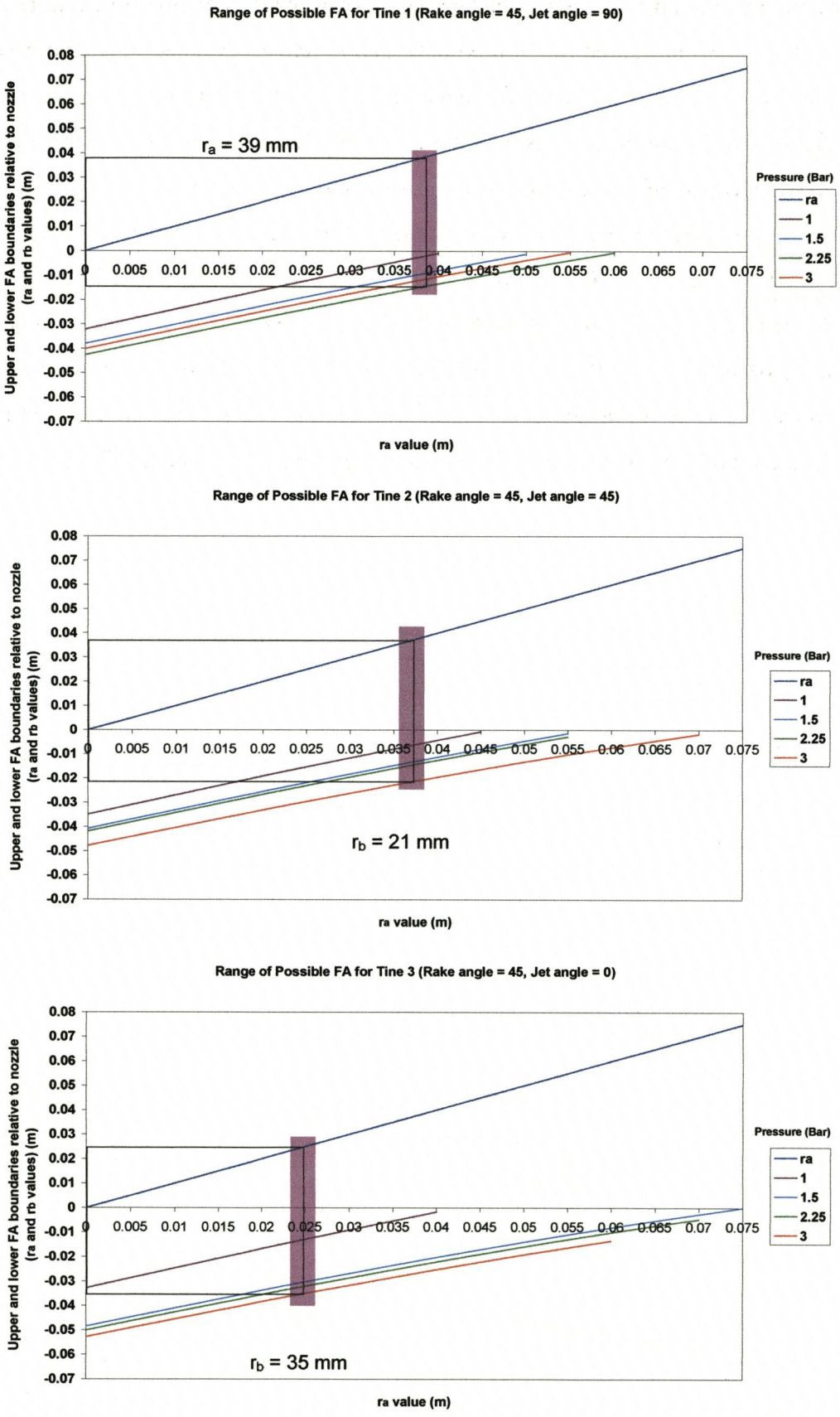

Figure 2.23 **Range of possible FA boundaries on the tests using forward raked tines**

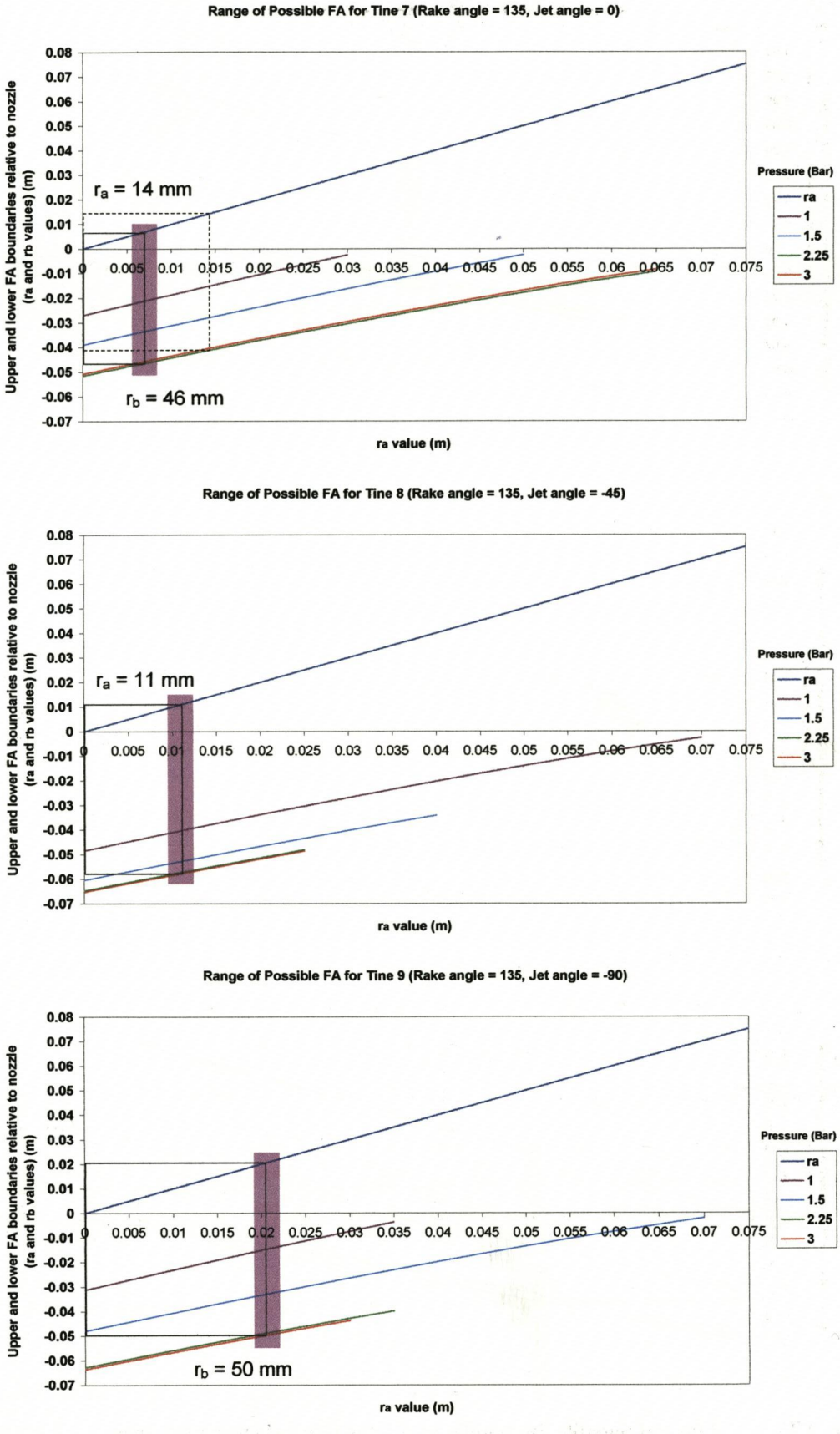

Figure 2.24 **Range of possible FA boundaries on the tests using backward raked tines**

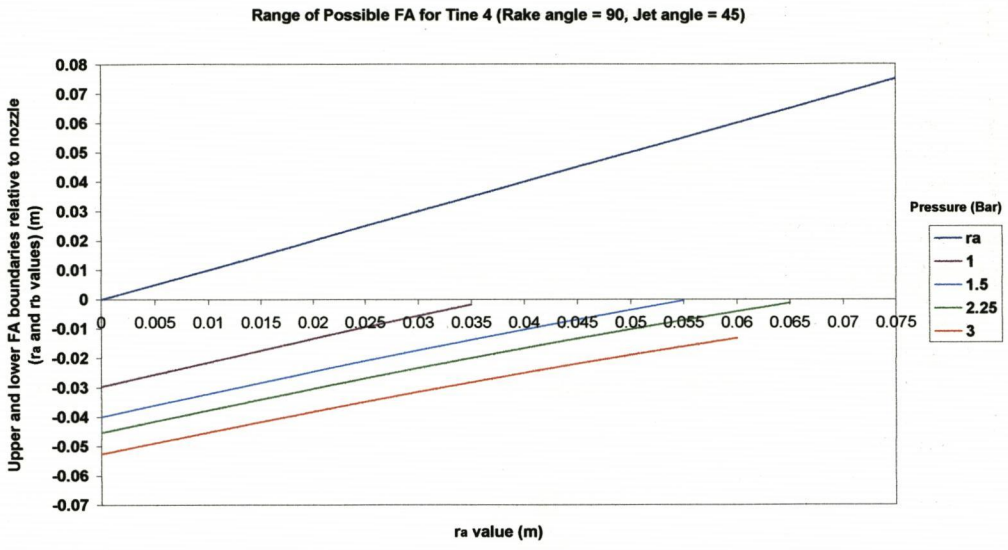

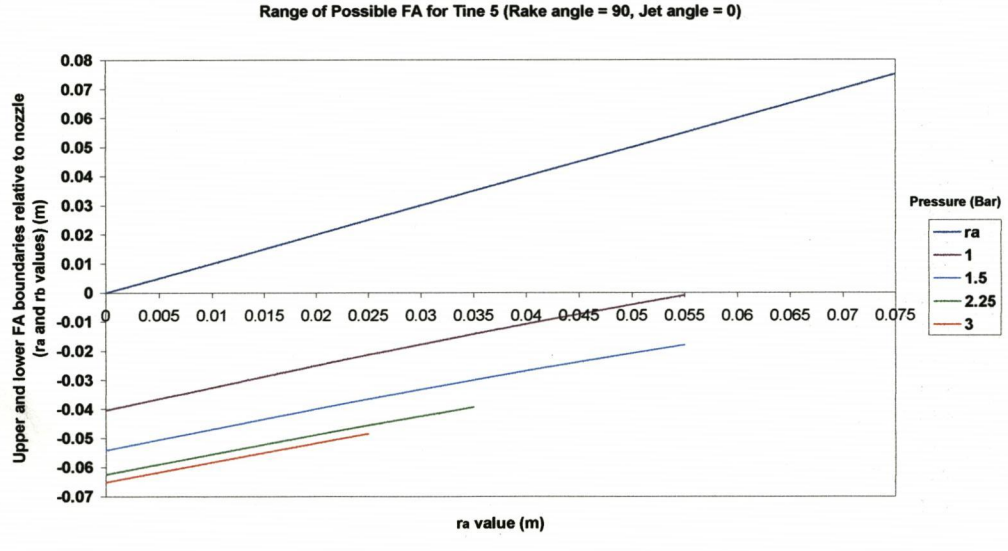

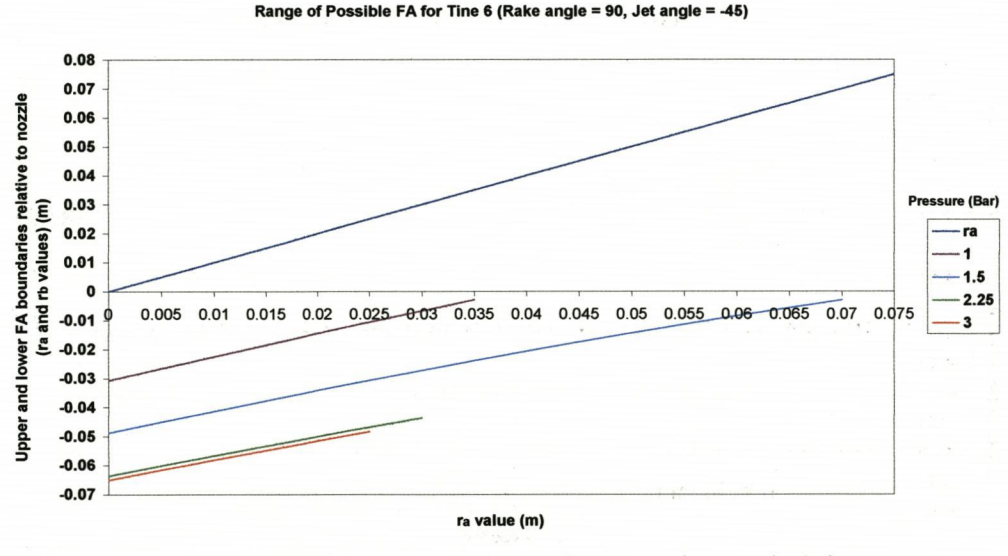

Figure 2.25 Range of possible FA boundaries on the tests using vertical tines

2.8 Conclusions

1. From the experiment investigating the effect of the nozzle area distribution on tine forces it was found that;
   a) The water jets eroded sand from in front of the tine, creating fluidised cavities. The areas of the tine face in contact with the cavities was termed the fluidised areas (FAs). Increasing the total FA on a tine face caused the horizontal force to decrease.
   b) Increasing the JMF caused the horizontal force to decrease, until a minimum force was reached, beyond which the JMF caused no further decrease in the force. This was because increasing the JMF caused the FA to increase, thus eliminating greater force from the tine face.
   c) The more evenly spaced the jet nozzles were across the tine face, the lower the force was, because it distributed the total JMF more evenly across the tine face. This increased the total tine FA, thus reducing the force.
   d) A threshold JMF was required for a jet to create a fluidised cavity in front of the tine. A JMF less than the threshold value resulted in the jet nozzle becoming blocked with sand.

2. From the experiment investigating the effect of jet and rake angle on tine forces it was found that;
   a) Increasing the total soil stress eliminated from the tine face by the FAs caused a reduction in tine force. This was achieved by either increasing the total FA, as stated in conclusion 1 b), or by shifting the FAs down the tine face so that they eliminated contact with soil that exerted a greater soil stress on the tine than soil further up the face, so increasing the total soil stress reuction. The interaction between jet and rake angle to achieve this was complex.
   b) Generally, the greater the downward component of a jet, the greater the soil force reduction. Downward angled jets create FAs that are positioned lower down the tine face than upward angled jets, and thus reduce larger stress values. However, increasing the downward component of the jets to the

vertical can also decrease the size of the FA, so that the net effect is to reduce the stress reduction from the tine face, resulting in higher forces. Therefore jets with a large downward component require a higher JMF to achieve the same force reduction.

c) Generally, greater rake angles (≥90°) resulted in lower horizontal forces. Increasing the rake angle shifts the FAs lower down the tine face, causing greater force reduction. However, this was not the case with horizontal jets, where the vertical tine had the lowest forces. The force was always greater with the forward raked tines than other rake angles tested.

d) Rake angle had no significant effect on soil forces for the passive tines. Therefore, according to the Godwin and Spoor (1977) narrow tine soil failure model, the soil fails laterally around the tine, with no significant crescent type failure.

3. A mathematical model was developed to simulate the force reduction generated by the water jets. Key elements of the model are;

a) The model was developed on the basis that the FAs eliminate soil stress from the tine face, causing a force reduction.

b) The force reduction over the FAs is given by;

$$F_{LOSS} = \frac{F_P}{z_m^2} \sum_{i=1}^{i=n} \left(z_{bi}^{\ 2} - z_{ai}^{\ 2} \right) \qquad [2.18]$$

where;

$$z_{ai} = z_{ni} - r_a$$

$$z_{bi} = z_{ni} + r_b \qquad [2.19\ (a,b)]$$

The net force on the tine is;

$$F_{NET} = F_P - F_{LOSS} \qquad [2.20]$$

c) For a non vertical tine it is assumed ra and rb are not equal, thus for forward raked tines at 45° below the horizontal;

$$x_a = \frac{-b_q + \sqrt{b_q^{\ 2} - 4.a_q.c_q}}{2.a_q} \qquad [2.22]$$

$$x_b = \frac{-b_q - \sqrt{b_q^{\,2} - 4.a_q.c_q}}{2.a_q} \qquad [2.23]$$

And for backward raked tines at 135° below the horizontal;

$$x_a = \frac{-b_q - \sqrt{b_q^{\,2} - 4.a_q.c_q}}{2.a_q} \qquad [2.24]$$

$$x_b = \frac{-b_q + \sqrt{b_q^{\,2} - 4.a_q.c_q}}{2.a_q} \qquad [2.25]$$

where;

$$a_q = 1 \qquad b_q = -l.\left(G^2 + 2\right) \qquad c_q = l^2 \qquad [2.26\ (a,b,c)]$$

Then;

$$r_a = G.\sqrt{l.x_a} \qquad [2.27]$$

$$r_b = G.\sqrt{l.x_b} \qquad [2.28]$$

d) For the tines tested, the range of possible FA positions was determined by;

$$r_b = \frac{-b_l \pm \sqrt{b_l^{\,2} - 4.a_l.c_l}}{2.a_l} \qquad [2.32]$$

where;

$$a_l = 3, \qquad b_l = 2.\sum_{i=1}^{i=3} z_{ni} \qquad c_l = 2.r_a.\sum_{i=1}^{i=3} z_{ni} - 3.r_a^{\,2} - \frac{F_L.z_m^{\,2}}{F_P}$$

[2.33(a,b,c)]

If the tine is vertical and the jets horizontal, so that $r_a = r_b$, then;

$$r_a = \frac{F_L.z_m^{\,2}}{4.F_P.\sum_{i=1}^{i=3} z_{ni}} \qquad [2.34]$$

e) The FAs simulated by the model and paint wear analysis are in general agreement with those expected in the discussion of the force results in Section 2.6.2. The model therefore provides a reasonable method to determine the force reduction generated by the jets, and thus the net force acting on a jet assisted tine.

f) The passive force is required in order to determine the force reduction and net force. It would be desirable to determine this theoretically rather than empirically.

3 Passive Plough Force Characteristics

3.1 Introduction

The purpose of this Chapter is to study the passive (non-jetted) plough force characteristics. This is necessary since the model developed in Chapter 2 for predicting the net force on a jet assisted implement requires the pressure profile and the total passive force on the face of the tool to be known. Therefore, the aim of this Chapter is to determine the pressure profile on the tool and the total passive force.

The Chapter consists of three elements, firstly, a review of literature on plough force, secondly, an investigation into the stress profile, and thirdly, an investigation into the passive plough force.

3.2 Review of Plough Force Prediction Models

Two categories of passive plough force models are considered. They are those concerned with saturated sands and then dry sands.

3.2.1 Force Models for Ploughs in Submerged Saturated Sands

Of the literature found, only a few papers related directly to the fundamental soil failure mechanics of seafloor ploughing, and these only considered saturated sands. The soil failure mechanics of implements in terrestrial soils are understood far better, of which a summary has been written by Smith (1989).

Despite the failure mechanics of implements in terrestrial soil being well understood, force models based on these mechanics are of limited use when applied to saturated sands, since the force generated in them can be orders of magnitude greater than in dry sands, (Coyne & Lewis, 1999), the difference being described as 'astonishing' by Reece and Grinstead (1986). The cause for the difference is due to the dilation properties of sands when sheared, which is described in a number of texts. (Lambe & Whitman, 1969, Terzaghi *et al.*, 1996). This phenomena is applied to submarine ploughs in a qualitative approach by Reece and Grinstead (1986), who's explanation for the difference is summarised as follows.

In the natural state granular particles of sand tend to rest interlocked with one another. The degree of interlocking depends on the density, with dense sands being very well interlocked. When dense sand is sheared, the only way the particles can accommodate the movement is to rise up over each other, which dilates the volume of the sand mass. The dilation draws water into the shearing zone, but the water flow through the small pores is impeded by its viscosity. If the dilation rate is high, the required water flow is large, and the impedance of this can cause a significant reduction in pore pressure. Since the effective stress acting on the soil is the difference between the total stress and pore pressure, a decrease in the pore pressure results in an increase in effective stress, and thus an increase in the shearing resistance of the sand. The greater the rate of shearing, the greater the dilation rate, thus the greater the pore pressure decrease, so resulting in an increased shear strength of the soil.

The amount by which force increases with speed depends on the extent of dilation of the sand volume, which in turn depends on the initial density and permeability of the sand. The shear strength of the sand is thus directly proportional to the dilation rate and shear speed, and inversely proportional to the permeability of the sand.

The magnitude of the pore pressure decrease is limited by one of two processes. Firstly, the pore pressure reduces to near absolute zero, at which cavitation occurs, limiting further increase in effective stress. Secondly, at greater sea depths the effective stress can increase to such an extent that it is greater than the sands compressive strength, causing grain crushing to occur, so limiting further increases in shear strength. These force speed characteristics are shown Figure 3.1

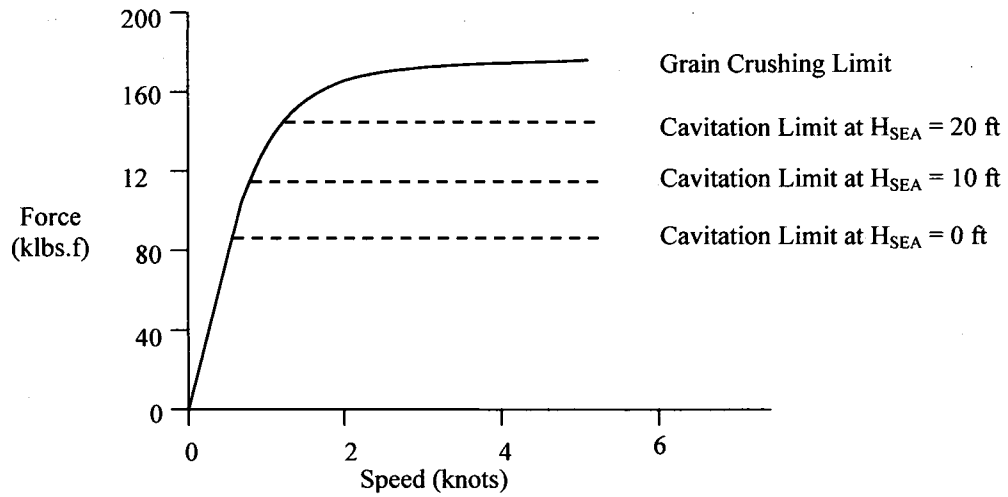

Figure 3.1 Plough force vs. Speed (Coyne & Lewis, 1999)

There are at least two models developed to predict passive plough force in seafloor sand. A summary of each is presented below.

I. Thin Blade Plough Force Prediction Model in Seafloor Sands

A model was developed by True and Girard (True, 1998) at the Naval Facilities Engineering Service Centre, Port Hueneme, CA. The method is based on data from various model plough tests that have been normalised to help develop empirically derived relationships, based on established soil mechanics relationships. It focuses on the critical confining stress as the key parameter controlling maximum ploughing force. The following summarises their analysis.

The model has four elements to reflect the characteristics of force created by a thin blade in sand.

- For near stationary ploughing speeds (quasi-static) the confining stress is predicted by the overburden stress (buoyant density * depth) multiplied by a static geometry factor. This force is expressed as:

$$F_{xo} = (z_m w)\, N_q \cdot (\gamma_s z_m)\, \alpha_o \cdot (z_m/w)^{po} A_R \qquad \textbf{3.1}$$

Where;

z_m = blade depth
w = blade width
N_q = strip footing frictional bearing capacity factor
γ_s = buoyant unit weight of soil
α_o = effective fraction of blade depth where overburden acts
p_o = exponent of depth/width ratio in static geometry factor
A_R = rake angle effect factor (greater than one for aft rake)

- At intermediate speeds (below critical speed) the over burden stress (above) is augmented by the hydraulic gradient created by the dilating shear zone giving the pre-critical, speed dependant plough force as:

$$F_{xv} = (z_m w) N_q \cdot (\gamma_w z_m)\, \alpha_v \cdot (z_m/w)^{pv}\, \varepsilon_v \cdot (U_n/k) A_R \qquad \textbf{3.2}$$

Where;

γ_w = unit weight of seawater
α_v = constant incorporating permeability-velocity-drainage effects
pv = exponent of depth/width ratio in drainage geometry factor
ε_v = volumetric strain = $(n_g - n_o)/(1 - n_g)$
U_n = plough speed
k = soil permeability
n_g = generated porosity = $n_m - R_\sigma * (n_m - n_o)$
n_m = maximum (ASTM standard) porosity at $\sigma = 0$
n_o = initial porosity before ploughing
R_σ = stress ratio (square root) = $(\sigma_g / \sigma_{cr})^{0.5}$
σ_g = generated confining stress = $F/[N_q h.b.(h/b)^{pv}]$

- The two pre-critical elements are combined by summing the two equations and dividing by the product of swept area, a strip footing frictional bearing capacity factor, seawater density and blade depth, resulting in:

$$F_x = A_R \cdot a_v \cdot e_v \cdot (U_n/k)$$

3.3

Based on many trials, values of $a_v = 0.8$, po = 0.33 and pv = 0.33 were found to give the best fit to a linear relationship.

- Above the critical speed where the critical confining pressure causes grain crushing, the bearing capacity stress is proportional to the strip footing cohesive bearing capacity factor N_c multiplied by the undrained shear strength S_u. The critical confining stress-limited ploughing force is expressed as:

$$F_c = (z_m \cdot w) \cdot N_c \cdot S_u$$

3.4

Where;

N_c = strip foot cohesive bearing capacity factor (~7)

S_u = effective undrained shear strength = $\sigma_{cr}/[(1/\sin(\varphi))-1]$

σ_{cr} = soil critical confining stress

φ = soil undrained friction angle

The maximum plough force is thus calculated from a large number of factors, exponents and constants accounting for the soil properties, implement geometry and plough velocity.

True states the relationships are useful for approximate predictions of ploughing force for a thin plough. The pre-critical ploughing force relationship has limits of agreement of +50% to –33% and the relationship predicting the force at critical confining pressure, the fourth element has a variability that depends on the measured or assumed critical soil conditions.

However, the model is of little use to this study since it requires the knowledge of some factors whose values or formulae are not defined in their paper.

II. Analysis of Ploughing Forces for a Finite-Width Blade in Dense Ocean Bottom Sand

An analysis, derived by Coyne and Lewis (1999), presents equations for the ploughing force as a function of plough speed, ocean depth, blade depth and width and various soil properties. The equations derived are based on Coulomb's theory of passive earth pressure, the force required to push a smooth vertical wall into a cohesionless soil. The predicted force is calculated by augmenting Coulomb's equation for passive earth pressure by one of 3 factors, accounting for either speed, cavitation or grain crushing effects, and by a factor accounting for end effects, due to the blade being narrow. Coulomb's equation of passive earth pressure is:

$$F_0 = \left(\frac{\rho_s \cdot w \cdot h_m^{\,2}}{2}\right) \cdot N_\varphi \qquad \textbf{3.5}$$

Where;

$$N_\phi = \tan\left(\frac{\pi}{4} + \frac{\phi}{2}\right)^2 \qquad \textbf{3.6}$$

The three factors are;

- N_{PORE} - Pore Water Effects

A factor accounting for the force element induced by the dilation effects in the soil is derived from the speed and dimensions of the blade and the volumetric strain of the soil. The derivation steps are as follows;

1. The swept volume per unit time is defined
2. The increase in pore volume is determined by multiplying the swept volume by the volumetric strain of the soil (assumed to be 0.05).
3. Pore water velocity is then determined by dividing the flow volume by the infiltration area on the soil surface (assumed to be two blade lengths by one blade width).
4. From Darcy's law, the necessary pore water pressure gradient is defined and integrated to give the pore water pressure profile

5. The constant of integration is evaluated from the condition that the total pressure at the sea bottom is the sum of the atmospheric and hydrostatic pressures. An equation for the absolute pressure profile is then defined.
6. The pore pressure increase has the effect of increasing the apparent weight density of the sand, defined as the sum of the original density and the average pressure gradient down the tine face. This effective weight density, when normalised to the original Coulomb equation for F_0, gives an N_{PORE} factor, given as,

$$N_{PORE} = 1 + \left(\frac{\rho_w}{\rho_s}\right)\cdot\left(\frac{U_n.\varepsilon_v}{4.k}\right) \qquad \textbf{3.7}$$

- N_{CAV} - Force at Cavitation Limit

A factor accounting for the cavitation limit is derived by analysis of the passive earth pressure on the face of the blade once the cavitation region has extended to the full blade depth. The cavitation factor, normalised to F_0 is:

$$N_{CAV} = 1 + 2\cdot\left(\frac{\rho_w}{\rho_s}\right)\cdot\left(\frac{H_{SEA} + H_{ATM}}{z_m}\right) \qquad \textbf{3.8}$$

- N_{GCR} - Grain Crushing Factor

A factor accounting for the force limit reached at the point of grain crushing is based on the analysis of confining stress in relation to volumetric strain and the apparent increase in the sand density. The factor, for large velocity (the grain crushing plateau in Figure 3.1) is given by:

$$N_{GCR} = 1 + \frac{\psi\cdot\sigma_{CRIT}}{z_m\cdot\rho} \qquad \textbf{3.9}$$

Where

$$\psi = \frac{4.5\cdot(N\varphi + 1)}{(2\cdot N_\varphi + 1)\cdot(N_\varphi + 2)} = \text{ratio of } \sigma_Y \text{ to } \sigma_{AVG} \qquad \textbf{3.10}$$

For lower velocity (the pre-critical ramp in Figure 3.1) the N_{GCR} factor is the same as N_{PORE}.

- Finite Width End Correction Factor

The finite width correction element is applied to account for the significant end effects of a narrow tine. Based on the analysis of forces on the three shear planes of a cohesionless soil wedge immediately ahead of the vertical tine face, the correction factor is given as:

$$\frac{F_x}{F_0} = \frac{\left(\frac{Sin(\alpha) + \mu \cdot cos(\alpha)}{N_\varphi}\right) \cdot \left(\frac{1}{tan(\alpha)} + tan\left(\frac{\varphi}{2} + \frac{\alpha}{2}\right)\right) \cdot \left[\frac{N_\varphi \cdot sin(\varphi)}{3} \cdot \left(\frac{h}{b}\right) + cos\left(\frac{\varphi}{2} - \frac{\alpha}{2}\right)\right]}{cos\left(\frac{\varphi}{2} + \frac{\alpha}{2}\right) - \mu \cdot sin\left(\frac{\varphi}{2} + \frac{\alpha}{2}\right)} \quad \textbf{3.11}$$

However, for a vertical blade the above reduces to:

$$\frac{F_x}{F_0} = 1 + \left(\frac{z_m}{w}\right) \cdot \left[\frac{N_\varphi \cdot sin(\varphi)}{3 \cdot cos\left(\frac{\varphi}{2} - \frac{}{4}\right)}\right] \quad \textbf{3.12}$$

The ploughing force is then $F_x \cdot N_{PORE}$ or $F_x \cdot N_{CAV}$ or $F_x \cdot N_{GCR}$ whichever is smaller.

True found the comparison of the results of the analysis with measured data difficult, since at the time of writing the paper, ocean ploughing data did not exist that gave all four key soil parameters needed for the analysis. However, in 1993 the Naval Facilities Engineering Service Centre (NFESC), Port Hueneme, CA, undertook a comprehensive program with a reduced scale laboratory test. True's analysis was compared to that data and was found to capture the main mechanisms involved. However, over the pre-critical range of speeds (where N_{PORE} is the limiting factor) the model underestimated the force by up to 50% for narrow tines. Thus, the equations give forces of the right order of magnitude rather than the exact solution which, according to Coyne and Lewis, cannot be expected, since as they say, 'ocean ploughing is extremely complicated'.

A discrepancy is found between the simple narrow wedge soil failure mechanism assumed by True and Girard and the experimental data of Chapter 2. The experimental data, unlike the narrow wedge model, shows no difference in the measured force between rake angles, suggesting a lateral failure type, as described by Godwin and Spoor (1977). Also, during the experiment it was observations that soil predominantly failed laterally around the tine rather than a in a narrow wedge ahead of it.

3.2.2 Soil Failure with Narrow Tines in Non-saturated Soils

Godwin's model (Godwin,1977) is reviewed in the light of applying the pore pressure mechanism developed by Coyne to build an N_{PORE} factor for lateral failure.

Godwin and Spoor found there to be two soil failure mechanisms, there being crescent failure above the critical depth and lateral failure below as shown in Figure 3.2. The crescent failure is characterised by soil moving forward, sideways and upwards. As the soil moisture content increases the critical depth reduces.

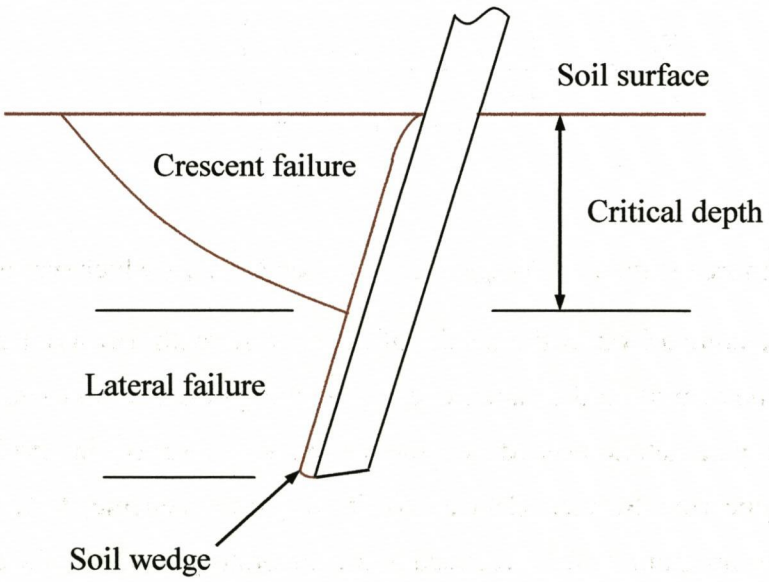

Figure 3.2 Soil failure pattern by a very narrow tine (Godwin & Spoor, 1977)

The lateral failure mechanism occurs in two dimensions regardless of the tine rake angle, where the soil has only forward, sideways and rearward movement. The failure is likened to that of a deep narrow footing oriented at 90 degrees to its normal

application. The logarithmic spiral analysis method, developed by Meyerhof, is used. A plan view diagram of the lateral failure mechanism is shown in Figure 3.3.

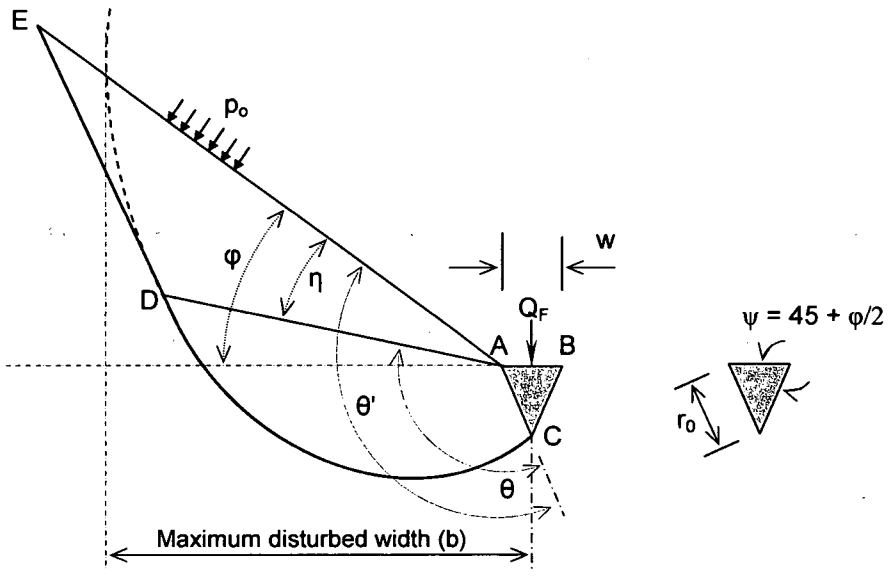

Figure 3.3 Lateral soil failure mechanism (Godwin & Spoor, 1977)

The horizontal force component of the lateral section is given by:

$$Q_F = w.c.N_c^{'}(z - z_c) + 0.5K_0\gamma.w.N_q^{'}(z^2 - z_c^{\ 2})$$

3.13

Where

K_0 = $(1-\sin\varphi)$

c = cohesion

z = tine depth

z_c = critical depth

w = tine width

N_c' = dimensionless cohesion number

N_q' = dimensionless gravitational number

γ = soil bulk density

The dimensionless factors are given by;

$$N_c' = \cot\phi\left[\frac{(1+\sin\phi)e^{2\theta\tan\phi}}{(1-\sin\phi\sin(2\eta+\phi))}-1\right] \quad \textbf{3.14}$$

$$N_q' = \frac{(1+\sin\phi)e^{2\theta\tan\phi}}{1-\sin\phi\sin(2\eta+\phi)} \quad \textbf{3.15}$$

There are no soil weight density terms in either of the dimensionless factors, the only soil property is the internal friction angle (φ). The soil weight density has a geostatic effect only on the rear face of the logarithmic spiral section AE ($p_o = K_0\gamma z$), since in the spiral section soil weight acts solely parallel to the vertical axis of the tine. Thus the effective weight density analysis of True can only be applied to the geostatic force p_o, and not to the shear force on the front section CD.

3.3 Objectives

The objectives of this Chapter are twofold.

1. To determine experimentally the spatial variation of soil pressure on a tine face, to fulfil the requirements of the force reduction model developed in Chapter 2.
2. To investigate the Coyne and Lewis (1999) force prediction model in seafloor sands by comparison to experimental data, and expand by application of their pore pressure analysis to Godwin's lateral failure model.

3.4 Methodology and Experimental Design

Three areas of experimental work were required to fulfil the objectives. They were;

1. An experiment to determine the soil pressure profile using a tine with five pressure sensors embedded in its face. The tine was pulled through the wet soil bin while the draught force and soil pressures were measured and recorded. The experiment was replicated seven times. The data from each sensor was plotted against depth to determine pressure variation with depth.

2. To examine the Coyne model some experimental data was needed. Passive force data from the jetted tines experiments related only to one speed (1 km/h) and was thus unable to provide force/speed characteristics. Therefore a short experiment was conducted to measure the draught force of a passive tine at a range of speeds in both saturated and damp conditions. Each condition was replicated twice.
3. Soil cohesion (c) and internal friction angle (φ) were measured to enable comparison of force models with experimental data. The properties were measured using the annular grouser plate (bevameter) method.

3.5 Equipment and Measurement Technique

3.5.1 Soil Stress Profile Measurement

I. Equipment

A. Tine Design

A tine designed for earlier work was adapted. It was constructed from mild steel and was instrumented with five circular ceramic pressure sensors embedded into the face. The sensors were equally spaced as shown in Figure 3.4. The tine had the same working depth as the jetted tines in the previous Chapter. The cables connecting the pressure sensors to the computer were routed through the centre of the tine and up to an outlet at the rear. The tine was used in the wet soil bin, details of which are in Chapter 2.

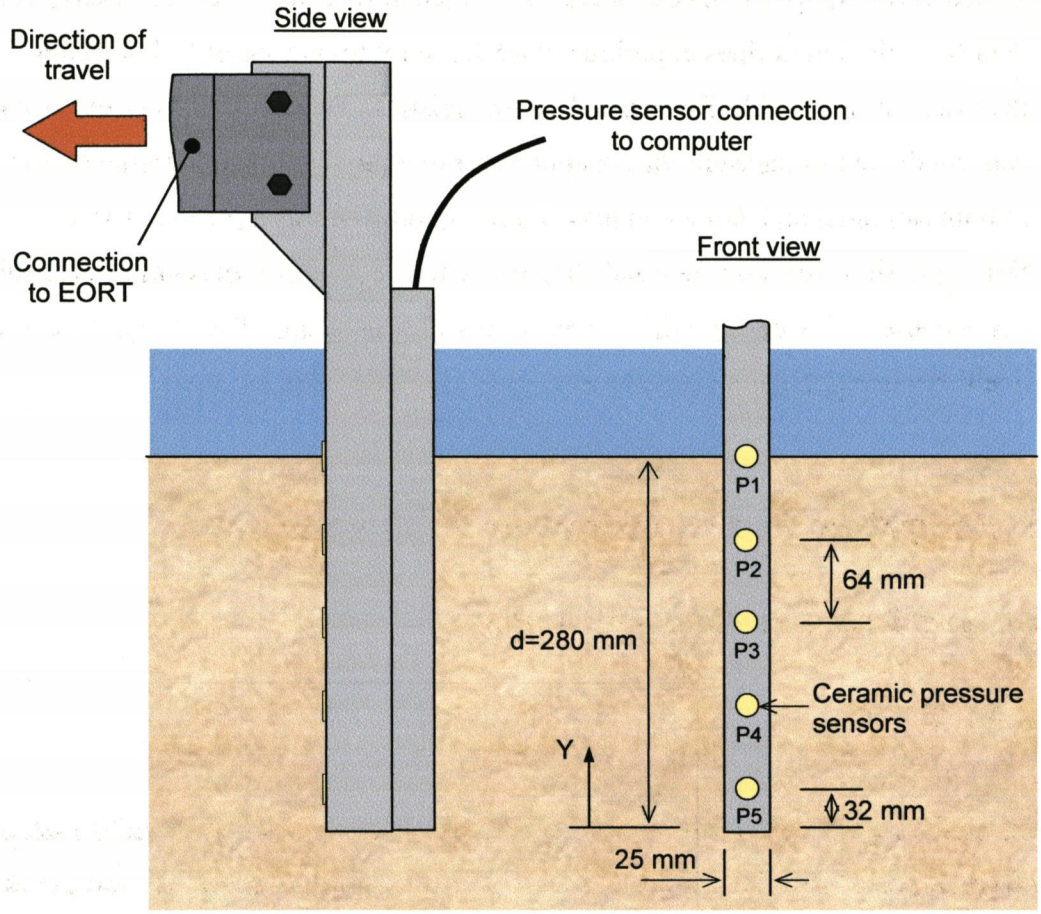

Figure 3.4 **Diagram of passive tine with embedded pressure transducers**

B. Tine Instrumentation

The draught force of the tine was measured in the same way as the jetted tines. The pressure sensor signals were connected to the computer via a separate data acquisition module (DataShuttle A/D converter). The hardware and software system connections are shown in Figure 3.5.

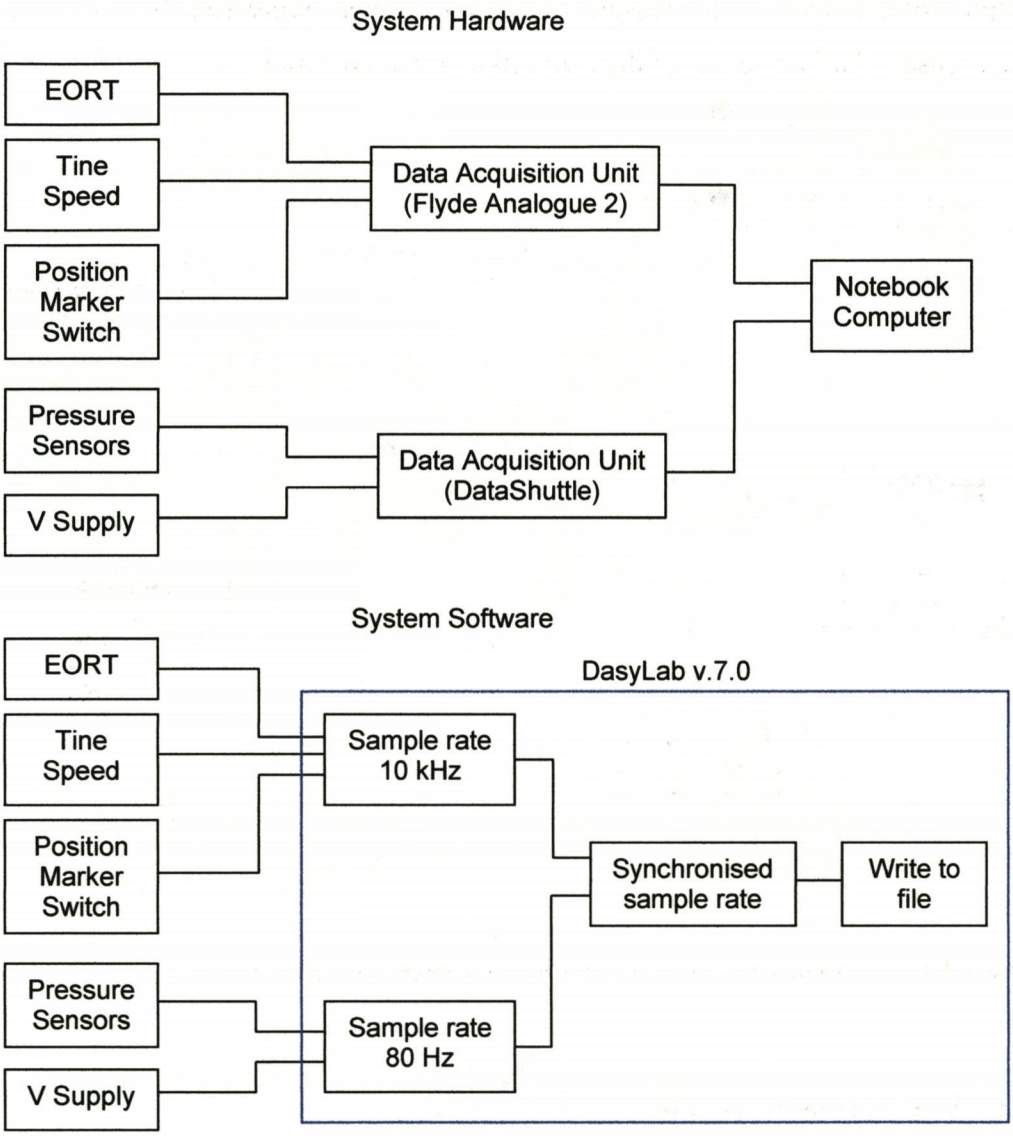

Figure 3.5 Details of passive tine instrumentation system

C. Calibration of Ceramic Pressure sensors

The pressure sensors were calibrated by applying air pressure onto the face of the sensor and recording the output voltage. Specialised equipment was used to apply the air pressure onto the sensor face, as shown in Figure 3.6. The applied air pressure was increased in steps from atmospheric pressure to 6.9 Bar (gauge) and reduced in equal steps. This was repeated three times for each sensor. The output voltage was divided by the supply voltage to give the signal voltage per unit of supply voltage. This method eliminated variation in the supply voltage affecting the calculation of pressure. The calibration equation for each sensor was determined by plotting sensor

output voltage against air pressure and fitting a linear regression line to the data of each sensor. Further details of the calibration are in Appendix 3.

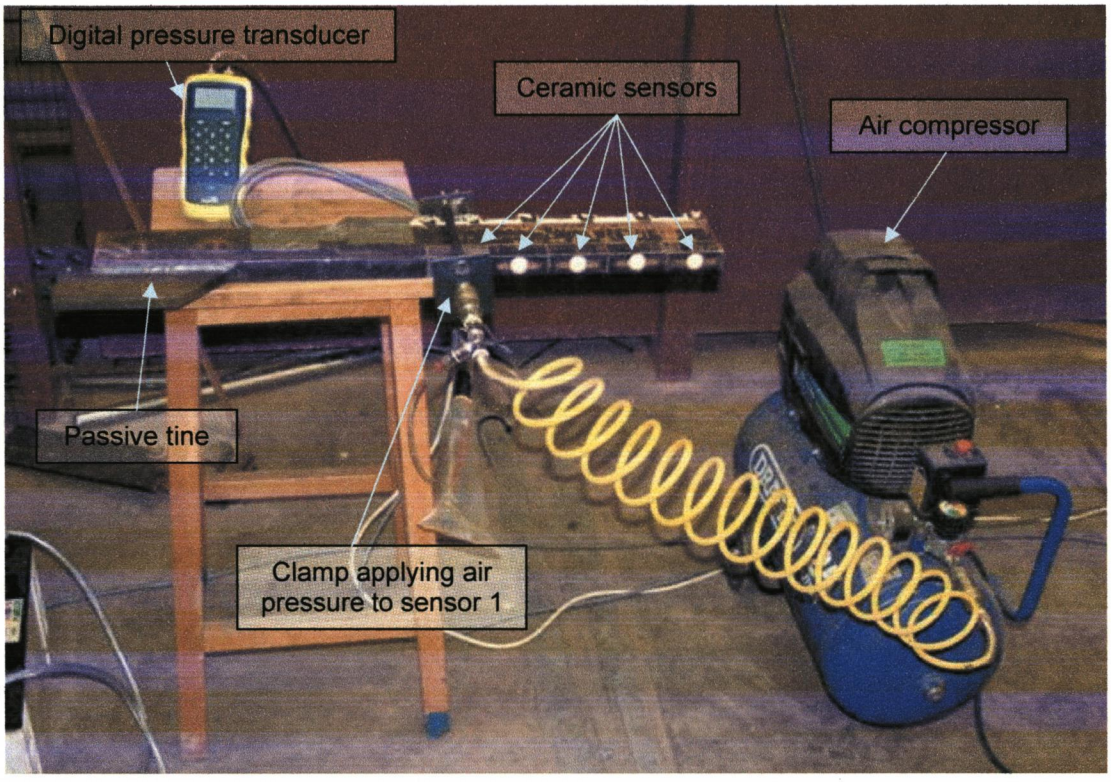

Figure 3.6 Calibration equipment for ceramic pressure sensors

II. Measurement Technique

The measurement technique was as follows.

1. The sand in the wet soil bin was prepared according to the standard technique detailed in Appendix 1.
2. The tine was put into the sand and geostatic soil pressure on the tine face was recorded for ten seconds with the tine stationary.
3. The tine was pulled through the sand by the wet soil bin carriage at 1 km/h.
4. On completion of the run the tine was extracted from the soil, after which the atmospheric pressure was recorded for a further ten seconds, to enable a reference pressure to be established for each sensor.

III. Method of Measurement Analysis

Force and speed data was analysed in the same manner as in the jetted tines experiments in Section 2.5.1. To analyse the soil stress data the difference between the measured gross dynamic soil stress and zero soil stress was taken as the net dynamic soil stress. The zero soil stress value (end reference section) was determined by removing the tine from the soil and measuring only atmospheric pressure. These sections of data are shown in Figure 3.7. The resulting soil stress values for each pressure sensor were plotted against the corresponding soil depth, for each of the tests, as shown in Figure 3.8.

However, pressure sensor 3 (P3) had technical problems and required a different method of analysis. The problem is seen in Figure 3.7. During the initial stationary period the stress reading is be higher than the other sensors, then at the point of initiation of movement the reading drops. Then, when the tine stopped, the pressure reading dropped significantly lower that the initial stationary reading at the start of the test. From thereon the pressure reading rose continually. The end reference value was therefore taken as the mean value of the 260 data immediately after the tine stopped moving, as shown in Figure 3.7.

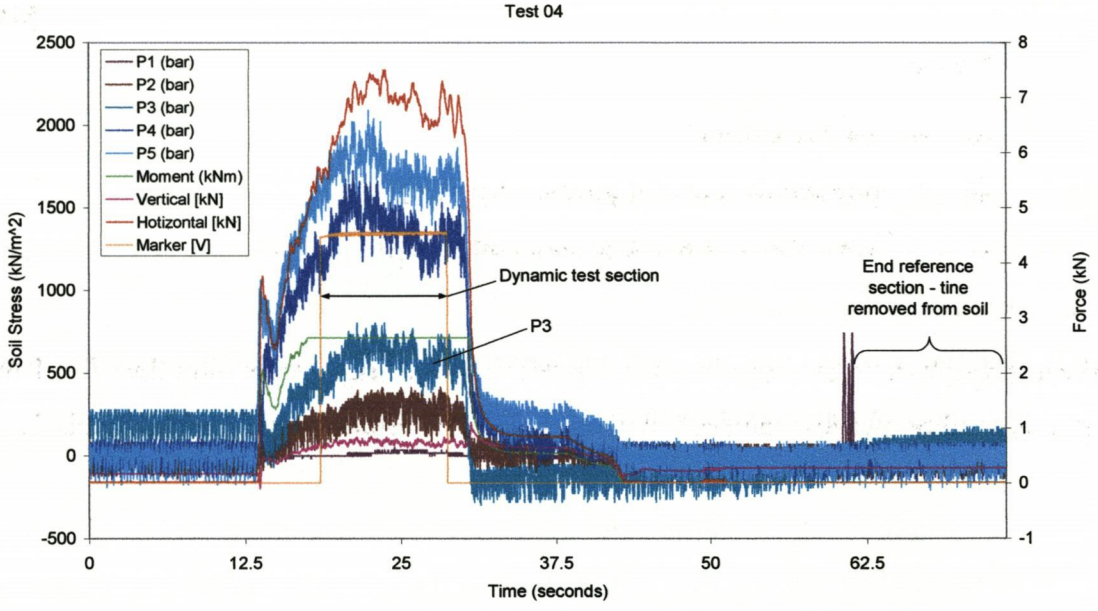

Figure 3.7 **Typical soil stress and tine force data from the stress profile experiment**

3.5.2 Passive Tine Force/Speed Measurement

A vertical tine from the jetted tine experiments was used. The instrumentation, the calibration of equipment, the measurement technique and method of analysis were the same as that used in the jetted tine experiments.

3.5.3 Measurement of Soil Properties

A standard annular grouser plate was used to measure the soil properties c (cohesion) and φ (soil internal friction angle). A standard technique was used, as advised by the Soils Research Laboratories at Cranfield University at Silsoe. The tests were conducted on the Cainhoe Quarry sand in saturated conditions in the wet soil bin, and in damp conditions in the same sand type in another small tank. Normal loads were applied up to 35 kN/m^2 in five even increments, at randomly allocated plots along the centreline of the wet soil bin. Each normal stress was replicated at two positions.

The torque required to shear the sand was measured and recorded. The shear stress (τ) was calculated from the equation;

$$\tau = \frac{3.M}{2\pi\left(R_0^{\ 3} - R_i^{\ 3}\right)} \qquad \textbf{3.16}$$

Where

M = Torque (N/m)

R_i = Internal diameter of grouser plate (m)

R_o = External diameter of grouser plate (m)

Shear stress was plotted against normal stress and a linear regression line fitted to establish soil properties c and φ. Full details of the measurements are in Appendix 2.

3.6 Results and Interpretation

3.6.1 Soil Stress Profile Experiment

Full results of the soil stress profile experiment are given in Appendix 4. The data from the fifth test has been ignored since the sensors gave erroneous readings just prior to the end of the run. The results therefore comprise of six replications of the test.

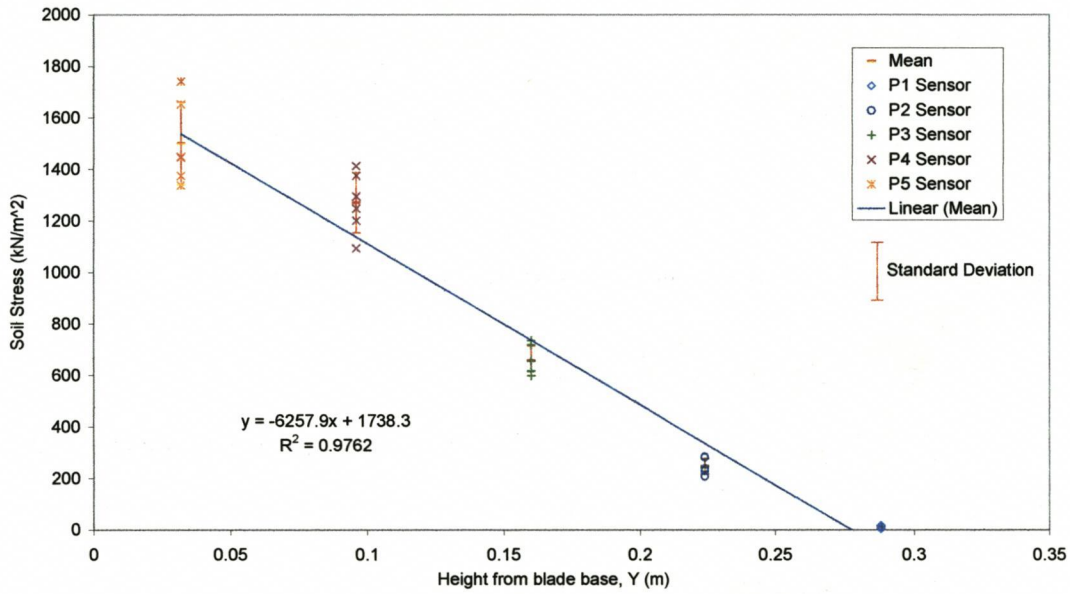

Figure 3.8 **Soil stress against height above blade base**

In Figure 3.8 the positions of the sensors are plotted relative to the blade base rather than the soil surface since the blade base is a fixed datum whereas the level of the soil surface could vary by ±15 mm. The standard deviation of the data of each sensor is also plotted, which show greater variation in stress readings for sensors closer to the blade base.

The results clearly show that soil pressure on the tine face reduces with height from the base, as was expected, and that for all practical purposes it is a linear relationship, having an R^2 (coefficient of determination) value of 0.9762. It is recognised that there is some variation of the data about the best fit line, but it is uncertain whether this is due to variation in the actual depth, technical difficulties with the pressure sensors or

an underlying non-linear pressure depth relationship. Nevertheless, since the R^2 value is high it is not unreasonable to conclude that pressure increases linearly with depth.

To determine whether the pressure sensors gave accurate or spurious values the force associated with the linear stress profile was determined and compared to the measured draught force.

The equation of the linear pressure line is;

$$\sigma = 1738.3 - 6257.9\ y \qquad \textbf{3.17}$$

Where

σ = soil stress

y = height from blade base

The height (y) where the stress equates to zero is given by;

$$y = \frac{-1738.3}{-6257.9} = 0.278m$$

The draught force (F) is calculated by integrating the area under the stress curve and multiplying by tine width, giving;

$$F = \int_0^{0.278} \sigma.w.dy$$

$$F = w.\left[\frac{-6257.9y^2}{2} + 1738.3y\right]_0^{0.278}$$

$F = 0.025$ m * 241.43 kN/m

$F = 6.036$ kN

The mean measured draught force was 5.72 kN. To determine whether there was a significant difference between the calculated and measured force a Students t test was conducted using the standard error as an estimate of the standard deviation, since the population mean and standard deviation are unknown. Students t test is given as;

$$\left(\bar{x} - t_{tab}\frac{s}{\sqrt{n}}\right) < \mu < \left(\bar{x} + t_{tab}\frac{s}{\sqrt{n}}\right) \qquad \textbf{3.18}$$

At 95% confidence interval with 6 degrees of freedom, $t_{tab} = 2.447$

With $\bar{x} = 5.72$ kN, s = 0.554 and n = 7 gives;

$$5.21\ kN < \mu < 6.23\ kN$$

Since the force calculated from the stress curve (6.04 kN) lies within this margin there is statistically no difference between the measured and the calculated draught forces. This indicates that the pressure sensors gave reliable readings, and gives weight to the judgement that stress increases linearly with depth.

It is also interesting to note that since the force on the tine face is effectively the same as the total draught force, the draught force is comprised of nearly entirely the force on the tine face, with little contribution from frictional forces on the sides, or suction from the rear of the tine.

In relating the stress profile results to the jetted tine data, it is interesting to note that the average soil stress on the tine face, 869 kN/m^2 (8.69 Bar) is 3.5 times greater than the maximum jet pressure used in the jetted tine work, while the maximum soil pressure at the base of the tine is 7 times greater. This fortifies the judgment in the jetted tine work that the nozzles at the base of the tine block first, due to the greater soil pressure. The fact that the jet pressure is much less than the soil stress suggests that sand is easily eroded by the jet, and thus does not make contact with the jet nozzle. However, the jetted tine data showed there was a critical jet pressure below which the nozzles blocked suddenly. This is because above the critical pressure the jet has an erosive capacity sufficient to create a cavity in front of the nozzle. However, once the pressure reduces below the critical value, the jet no longer has a sufficient erosive capacity to maintain a cavity, and non jetted sand contacts the nozzle. Since for most of the tine the soil stress is far greater than the jet pressure it leads to a rapid blocking of the nozzle. The fact that larger diameter nozzles had a lower critical pressure (in fact the larger nozzles in the power distribution experiment did not block) indicates that they have a greater erosive capacity than smaller diameter jets at a given pressure.

3.6.2 Passive Tine Force/Speed Experiment

The results of the force/speed experiment are displayed in Figure 3.9. In addition to the data from this experiment the data from the jet distribution and rake angle experiments and from previous work by Knight (2002) with jetted tines is also shown.

Straight lines give a good fit to both the data of saturated sands in this experiment and the previous work by Knight, thus agreeing with the work of Coyne and Lewis (1999), Reece and Grinstead (1986) and True and Girard (1998), which show that draught force increases linearly with tine speed. The intercept of the straight lines on the force axis is the quasi-static force on the tines. It seems reasonable therefore to assume that the quasi-static draught force may be augmented by a speed factor to determine the force at speed.

It is also interesting that the forces at 0.27 m/s from the jet nozzle distribution and rake angle experiments are approximately twice the magnitude of the forces from the present experiment. Since tine velocity and depth were the same in both experiments, soil density was likely to be the cause of the difference.

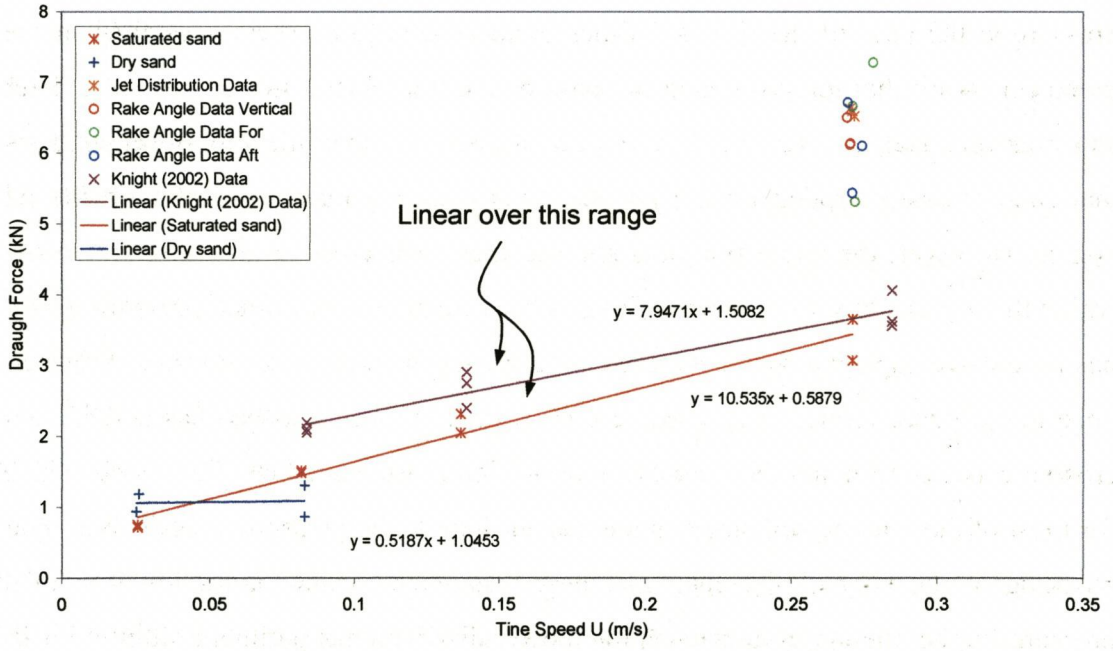

Figure 3.9 The effect of tine speed on the draught force together with data from previous experiments

The two speeds conducted in dry sand show that tine speed had very little effect on draught force. This agrees with the work of Wheeler and Godwin (1996) that speed has an insignificant effect for speeds up to 10 km/h for the size of tine used in this experiment.

The data in Figure 3.9 also highlights the difference in the force characteristics between dry and saturated sands. At speeds greater than 0.05 m/s the saturated forces were greater than the dry forces. However, for the quasi-static condition the data indicates the saturated force to be about half the dry force. This is due to the soils buoyant bulk density being less than the dry bulk density and thus the geostatic forces are less in the saturated case than when dry. According to Godwin's force equation (Eq. 3.13) this will result in a reduced shear force.

3.6.3 Soil Properties

The results of the annular grouser plate tests are displayed in Figure 3.10. They show the *in situ* shear strength of the saturated sand was significantly less than in the dry and damp conditions. The associated angle of internal friction (φ) was significantly lower in the saturated sand, though its lower density of 1516 kg/m^2, as opposed to 1600 kg/m^2 of the dry sand, may have contributed to this. The damp sand had a greater value of 'apparent' cohesion than the dry sand due to the effects of soil moisture content.

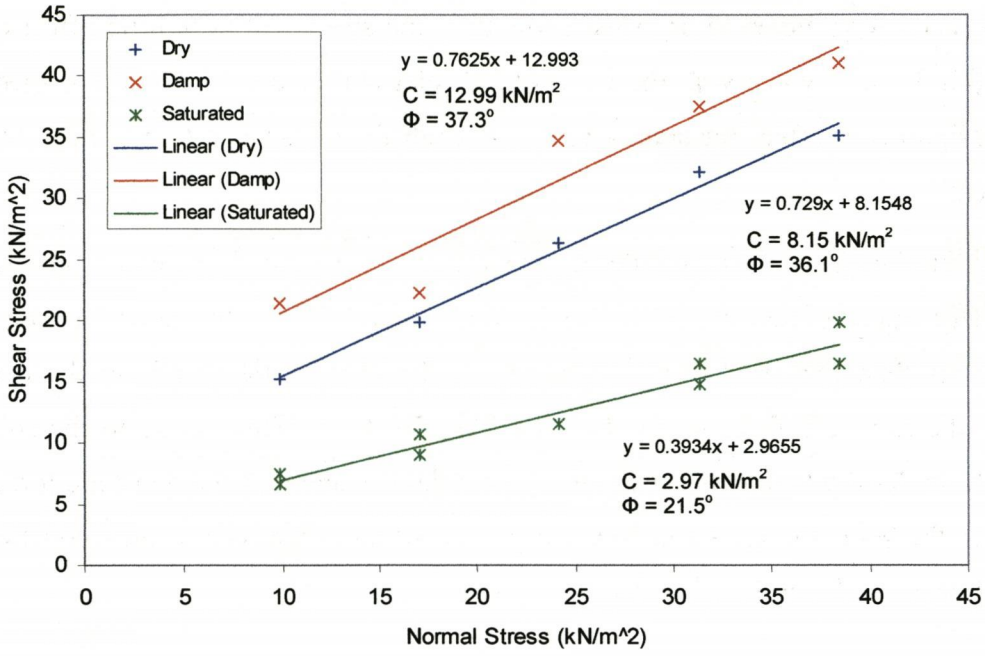

Figure 3.10 The relationship between normal and shear stress giving the Mohr-Coulomb soil properties in dry, damp and saturated conditions

To measure the shear torque the annular grouser plate was rotated at near quasi-static speed, to minimise speed effects on shear torque. Had the angular velocity been faster the shear strength would have likewise been higher, resulting in the measured dynamic properties of c and φ being greater, having been modified by the dilation properties of the sand.

3.7 Passive Tine Force Model Development

The purpose of this Section was to fulfil the second objective detailed in Section 3.3. There are therefore two parts, firstly a comparison of the Coyne and Lewis force prediction model with the tine force/speed data to determine how well it fits. Secondly, to gain a greater understanding of the pore pressure profile by application of their pore pressure analysis to the lateral soil failure model of Godwin and Spoor.

The properties used in the analysis are contained in Table 3-1.

Table 3-1 **Properties used in passive force modelling**

Soil Properties	Value
Water bulk weight (γw)	1.0 kN/m2
Sand bulk weight (γs)	1.6 kN/m2
Sand buoyant weight (γsb)	0.6 kN/m2
Soil permeability (k)	0.00027 m/s
Soil cohesion (c)	2.97 kN/m2
Internal friction angle (φ)	21.5°
Volumetric strain (εv)	0.05 (assumed)
Tine width (w)	0.03 m
Tine depth (zm)	0.28 m

3.7.1 Comparison of Coyne and True Force prediction Model to Experimental Data

The work in Chapter 2 highlighted the need for a means of predicting the passive draught force of an implement engaged in saturated sands. The force prediction model developed by Coyne and True (1999), described in Section 3.2.1, was unique in that all the variables and factors were either known or could be determined. It was therefore selected as the only viable force prediction model. To determine how well the model simulates reality it was compared to the force/speed experimental data. A predicted force speed relationship was calculated using the values in Table 3-1 and the following equations;

$$F_0 = \left(\frac{\rho_s . w . z_m^{\,2}}{2}\right) . N_\phi \qquad 3.5$$

$$N_\phi = \tan\left(\frac{\pi}{4} + \frac{\phi}{2}\right)^2 \qquad 3.6$$

$$N_{PORE} = 1 + \left(\frac{\rho_w}{\rho_s}\right) . \left(\frac{U_n . \varepsilon_v}{4.k}\right) \qquad 3.7$$

$$N_{WIDTH} = 1 + \left(\frac{z_m}{w}\right).\left(\frac{N_\phi.\sin\phi}{3.\cos\left(\frac{\phi}{2} - \frac{\pi}{4}\right)}\right) \qquad 3.12$$

$$F_x = F_0.N_{PORE}.N_{WIDTH} \qquad \textbf{3.19}$$

The results of the force/speed experiment and force values calculated using Coyne's model over the same speed range are plotted in Figure 3.11. It clearly shows that Coyne's model under predicted the measured force by a factor of about six, which is very significant. The only factor in the model whose value was estimated, and hence may be the cause of the discrepancy, is the volumetric strain (ε_v). Its value of 0.05 was also used in Coyne's paper when comparing the model to experimental data, and since the sand grain sizes in this study and in Coyne's are similar, it was thought reasonable to assume the same value. Increasing the value of ε_v increases the force values predicted by Coyne's model. Nevertheless, an ε_v value of 0.4 is required before the force discrepancy becomes small, which is a far greater dilation value than usually occurs in naturally packed sands.

The cause for the error of Coyne's model is thought to be largely due to the narrow soil wedge failure mechanism adopted for the analysis. As stated previously, that failure mechanism was not observed during the execution of the tine experiments, neither does the data from the rake angle experiment support it. Rather, both the observation of soil failure and the experimental data strongly indicate a lateral soil failure mechanism. The adopted soil failure mechanism in the Coyne analysis causes secondary problems when determining the N_{PORE} factor, in that it leads to an incorrect geometry when determining the flow area of pore water at the soil surface. The assumed flow area is a long narrow strip ($2.z_m$ * w) ahead of the tine, which if the soil is failing laterally is an incorrect assumption. The flow area consequently affects the pore pressure reduction, and thus the N_{PORE} factor. If the assumed flow area leads to a low pore water velocity, the resulting pore water pressure drop will consequently be low, resulting in a low N_{PORE} factor and thus low forces. This may be the case in Coyne's analysis.

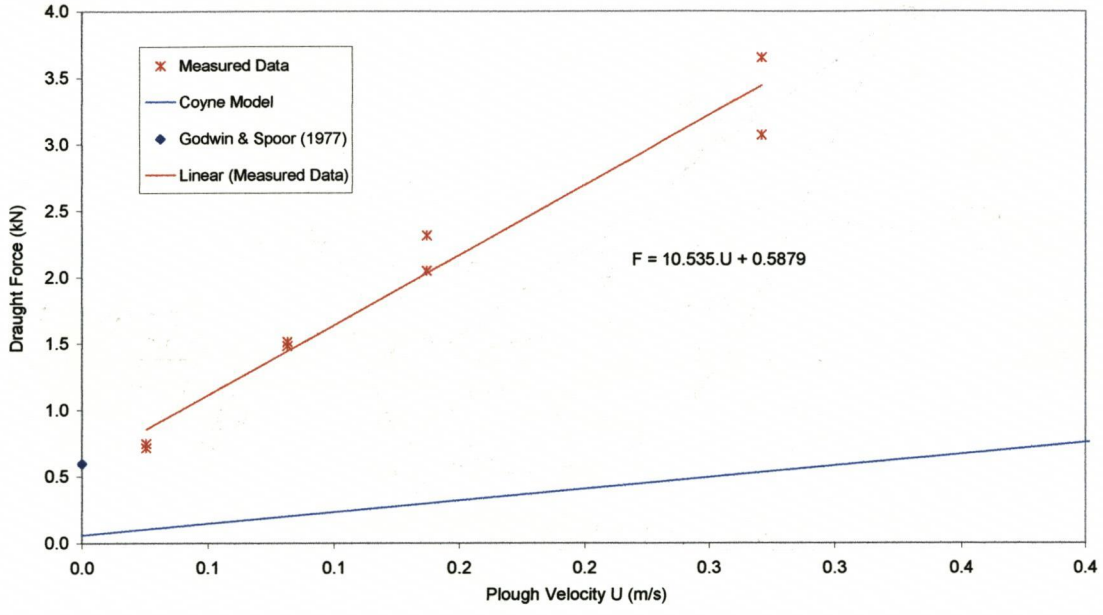

Figure 3.11 Comparison of measured and predicted draught force by Coyne & True (1999) model

3.7.2 Application of Coyne & True's Pore Pressure Analysis to Godwin & Spoor's Lateral Failure Model

Experimental data from the rake angle experiment shows soil fails laterally around the tine for most of the working depth. The lateral failure model of Godwin and Spoor (1977) predicts the quasi-static plough force exceptionally well, at 0.60 kN, compared with the extrapolated value of 0.59 kN from the measured data (Figure 3.11). Ideally therefore, an NPORE factor would be developed to augment Godwin's quasi-static force value to accommodate the speed element in saturated sands. This section goes part way in developing an NPORE factor by modelling the pore pressure profile developed by a lateral failure mechanism. Further research is required before the pressure profile analysis can be integrated into Godwin's lateral force equation. (Equation 3.13)

A pore pressure profile was established for the lateral soil failure mechanism by using the lateral failure model, detailed in Figure 3.3, and applying the approach of the pore pressure analysis of Coyne and Lewis (1999), discussed in Section 3.2.1.

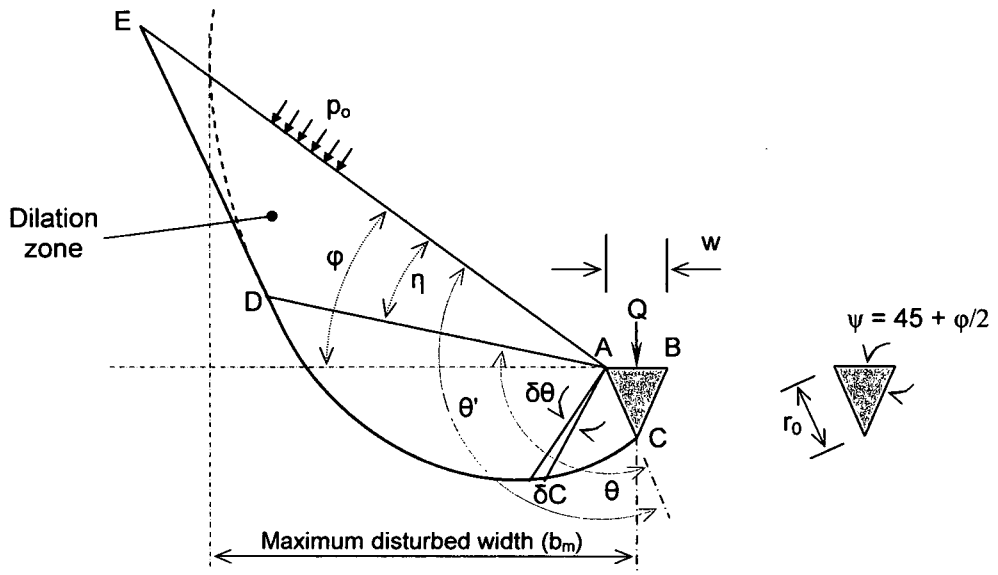

Figure 3.3 **Lateral soil failure mechanism (plan view) (Godwin & Spoor, 1977)**

$$r_0 = \frac{w}{2\cos\left(\frac{\pi}{4}+\frac{\phi}{2}\right)} \qquad \textbf{3.20}$$

$$\theta' = \frac{3\pi}{4}+\frac{\phi}{2} \qquad \textbf{3.21}$$

$$r = r_0.e^{\left(\frac{3\pi}{4}+\frac{\phi}{2}\right).\tan\phi} \qquad \textbf{3.22}$$

$$b_m = r.\cos\phi = \frac{w.\cos\phi.e^{\left(\frac{3\pi}{4}+\frac{\phi}{2}\right).\tan\phi}}{2.\cos\left(\frac{\pi}{4}+\frac{\phi}{2}\right)} \qquad \textbf{3.23}$$

The rate of soil disturbance is;

$$2.b_m.U_n.z_{max} \qquad \textbf{3.24}$$

Where;

b_m = disturbed width

U_n = speed of tine

z_{max} = maximum depth of tine

Assuming a uniformly distributed volumetric strain ε_v, void volume is created at the rate;

$$Q_m = 2.b_m.U_n.z_m.\varepsilon_v$$

3.25

Assuming water flows into the pore down from the surface only in the zone of the lateral failure disturbance, then pore water velocity is;

$$U_p = \frac{Q_m}{A_L}$$

3.26

Where A_L = surface area of disturbed logarithmic spiral section

To determine the surface area (A_L), taking a small element of the spiral section $\delta\theta$;

$$\delta A_L = \frac{\delta C.r}{2}$$

and since;

$$\delta C = r\delta\theta$$

then;

$$\delta A_L = \frac{r^2.\delta\theta}{2}$$

So;

$$A_L = \int_0^{\theta'} \frac{r^2}{2}.d\theta \quad \text{where} \quad \theta' = \frac{3\pi}{4} + \frac{\phi}{2}$$

Substituting Eq 3.22 as r gives;

$$A_L = \int_0^{\theta'} \frac{\left(r_0.e^{\theta.\tan\phi}\right)^2}{2}.d\theta$$

$$A_L = \int_0^{\theta'} \frac{r_0^{\,2}.e^{2\theta.\tan\phi}}{2}.d\theta$$

$$A_L = \left[\frac{r_0^{\,2}}{2} . \frac{e^{2\theta . \tan\phi}}{2 . \tan\phi} \right]_0^{\theta'}$$

$$A_L = \frac{r_0^{\,2} . e^{2\left(\frac{3\pi}{4}+\frac{\phi}{2}\right) . \tan\phi}}{4 . \tan\phi} - \frac{r_0^{\,2}}{4 . \tan\phi}$$

$$A_L = \frac{r_0^{\,2}}{4 . \tan\phi} \left(e^{\left(\frac{3\pi}{2}+\phi\right) . \tan\phi} - 1 \right)$$

3.27

However, there are two log spirals, therefore the total area is;

$$A_{L.Total} = \frac{r_0^{\,2}}{2 . \tan\phi} \left(e^{\left(\frac{3\pi}{2}+\phi\right) . \tan\phi} - 1 \right)$$

3.28

Substituting Equation 3.25 and3.28 into 3.26 gives the maximum pore water velocity at the surface;

$$U_m = \frac{4 . b_m . U_n . z_m . \varepsilon_v . \tan\phi}{r_0^{\,2} . \left(e^{\left(\frac{6\pi}{4}+\phi\right) . \tan\phi} - 1 \right)}$$

And the pore water velocity profile is;

$$U_p = \frac{4 . b_m . U_n . \varepsilon_v . \tan\phi}{r_0^{\,2} . \left(e^{\left(\frac{6\pi}{4}+\phi\right) . \tan\phi} - 1 \right)} . y \quad = S . y$$

3.29

where y is height above blade base

From Darcy's Law, the necessary vertical pore water pressure is;

Darcy's Law;

$$Q = kA \frac{\Delta h}{\Delta y}$$

Then pore water velocity is;

$$U_p = \frac{Q}{A} = k \frac{\Delta h}{\Delta l}$$

3.30

Now since;

$$\Delta P = \rho.g.\Delta h$$

Therefore $$\Delta h = \frac{\Delta P}{\rho.g} = \frac{\Delta P}{\gamma}$$

And substituting back into Eq.3.30 gives

$$U_p = \frac{k\Delta P}{\gamma.\Delta y} = S.y$$

Rearranging for pressure gradient;

$$\frac{\Delta P}{\Delta y} = \frac{\gamma.S.y}{k}$$

Then integrating for pore pressure gives;

$$P = \int \frac{\gamma.S}{k}.y.dy$$

$$P = \frac{\gamma.S}{k}.\frac{y^2}{2} + C \qquad \textbf{3.31}$$

To determine the constant C;

At $y = z_m$, then $P = P_{ATM} + P_{SEA}$

$$P_{ATM} + P_{SEA} = \frac{\gamma.S}{k}.\frac{z_m{}^2}{2} + C$$

Thus,

$$C = P_{ATM} + P_{SEA} - \frac{\gamma.S}{k}.\frac{z_m{}^2}{2}$$

Then substituting back into Eq. 3.31 gives the pore water pressure profile as;

$$P = P_{ATM} + P_{SEA} - \frac{\gamma.S}{2k}\left(z_m{}^2 - y^2\right) \qquad \textbf{3.32}$$

And substituting for S gives;

$$P = P_{ATM} + P_{SEA} - \frac{2.b_m.U_n.\varepsilon_v.\gamma.\tan\phi}{k.r_0{}^2\left(e^{\left(\frac{3\pi}{2}+\phi\right)\tan\phi} - 1\right)}\left(z_m{}^2 - y^2\right) \qquad \textbf{3.33}$$

Where b and r_o are defined in Equations 3.23 and 3.20 respectively. Equation 3.33 shows, in agreement with Coyne's model that pore pressure decreases linearly as speed (U) increases, and decreases quadratically with increasing depth z.

Equation 3.33 was used with the values in Table 3-1 and pore pressure profiles were generated for two speeds (0.5 and 1.0 km/h) and volumetric strain rates (0.05, 0.02), as shown in Figure 3.12. The depth of water (H_{SEA}) was the same as that used in the experiments, being 0.1m. The pore pressure profile according to Coyne and the hydrostatic pressure are also plotted for comparison.

The profiles show that the pressure reductions developed according to the lateral failure analysis are significant, and are in the order of nine times greater than those developed by Coyne's analysis. The difference is due to the pore volume in the lateral failure approach being significantly greater than in Coyne's, and the surface area of infiltration being relatively smaller, thus leading to a higher pore water velocity and a greater pressure differential required to drive it. The fact that Coyne's pressure reduction is significantly less reinforces the conclusion in Section 3.7.1, when discussing the agreement of Coyne's approach to experimental data, that their approach underestimates the pore water velocity, due to the inaccurate soil failure mechanism assumed.

However, the pore pressure reductions developed by the lateral failure analysis are greater than intuitively thought after conducting the experimental work, for if cavitation had occurred at these speeds, as the model indicates, the force/speed curve would not have been linear over the range of speeds tested. According to the lateral failure analysis, at the larger volumetric strain ($\varepsilon_v = 0.05$) cavitation occurs over the lower half of the blade at 0.5 km/h and increases to the lower three quarters at 1.0 km/h, Figure 3.12 (a & b). At the lower ε_v value (0.02) cavitation only occurs at the base of the faster blade. The assumed ε_v value of 0.05, which is the value Coyne assumed, may therefore be erroneous, since the value of 0.02 gives more realistic values. Nevertheless, based on the originally assumed value, the pressure reduction is too large.

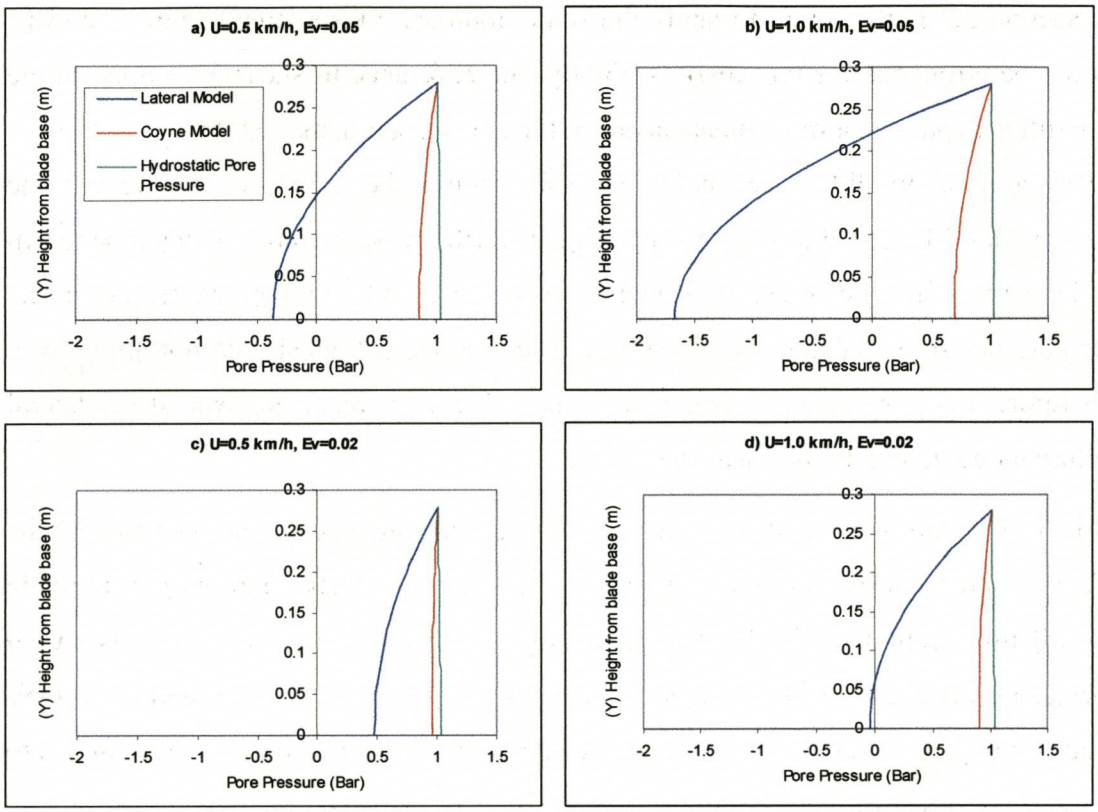

Figure 3.12 Pore pressure profiles according to the lateral failure analysis and Coyne's model

The reasons for the pore pressure reductions being too large in the lateral analysis are likely to be twofold. Firstly, the assumed surface area through which infiltration occurs, which is the area of the logarithmic spiral segment, is smaller than in reality. Water from the surrounding soil mass would also move in to fill the voids, creating a more complex three dimensional flow regime than for the assumed simple one dimensional approach. The three dimensional regime would require lower pore water velocities and pressure differentials. Secondly, as the soil dilates the permeability of the soil would increase due to the larger void diameters. As can be seen from Equation 3.33, the pressure reduction reduces as permeability (k) increases. Thus, the required pressure differential decreases as the sand dilates. This effect is not considered in the pore pressure analysis.

Coyne applies the pore pressure reduction by equating the average pressure gradient to an effective increase in apparent weight density. The apparent weight density is then normalised with respect to the plough force to define the N_{PORE} factor, described

in Section 3.2.1. However, to apply the same approach to the lateral failure analysis would be erroneous for two reasons. Firstly, the resistance to shear developed in the logarithmic spiral section is independent of the soil weight density (γ_s), for the reasons given in Section 3.2.2. Secondly, the soil behind the spiral section resists the movement of the spiral section by applying an earth pressure whose value depends on γ_s. However, since deformation of that zone is small, little dilation occurs and hence, the pore pressure analysis and increase in effective weight density do not apply to it. Therefore, the pore pressure reduction must influence another element of the lateral failure model to create the shear rate effect.

It is well established that a decrease in pore pressure causes an increase in the effective stress on the soil mass. However, there are no effective stress ($\gamma_s.z$) terms in the dilating section of the lateral failure model. Therefore an alternative means of increasing the shear resistance is to increase the apparent values of c and/or φ, their values being dependant on shear rate. Further fundamental research is required into the effect of shear rate on the apparent values of c and φ in saturated sands.

3.8 Conclusions

1. Soil stress profile
   a) The soil stress on the tine face was found to increase approximately linearly with depth.
   b) The linear approximation enables the soil stress to be calculated at any depth on the tine if the passive plough force is known.

2. Passive force prediction models
   a) The Coyne and Lewis (1999) analysis was found to underestimate the passive plough force by a factor of approximately six, when using the values of variables given in Table 3-1.
   b) A significant cause for the discrepancy is the inappropriate use of the narrow soil wedge failure mechanism.
   c) The Godwin and Spoor (1977) lateral failure model accurately predicts implement force at quasi-static speed in saturated sands.
   d) A pore pressure profile analysis has been developed for the Godwin and Spoor (1977) lateral failure mechanism, based on same approach as the analysis by Coyne and Lewis (1999). The assumed one dimensional flow regime results in the analysis over predicting pore pressure reduction.
   e) The pore pressure analysis provides the first stage of incorporating a speed element into the Godwin and Spoor lateral failure model for saturated sand.

4 Investigation into the Cavity Created by a Buried Static Horizontal Jet

4.1 Introduction

The study of the jetted tines in Chapter 2 showed the existence of a fluidised zone about each jet. The size of the fluidised zone is important in establishing the force reduction created by the jets. The need is therefore to predict the size of the fluidised zone given jet and soil parameters. This was conducted in two stages, the first being a study using a static nozzle to gain understanding of the mechanics of jet erosion of a jet internal to the soil, and secondly, the study of a dynamic (moving) nozzle to build on that understanding to enable the development of a mathematical model simulating the fluidised zone. The first stage is dealt with in this Chapter and the second in the next.

This Chapter presents a review of relevant literature for both stages. The objectives are then defined, followed by the main investigation using a static half nozzle. Another secondary experiment on the measurement of the uplift force of a metal plate is reported, the purpose being to aid the development of a mathematical model. Finally a mathematical model describing the cavity development created by a static buried jet is developed and discussed.

4.2 Objectives

The objectives of this Chapter are to;

1. Gain an understanding of cavity growth and jet scour characteristics of a horizontal jet issuing from a static nozzle internal to the soil.
2. Determine the effect of particle size and soil type on the above.
3. Develop a mathematical model to simulate the growth of a cavity with time.

4.3 Literature Review

4.3.1 Characteristics of a Submerged Jet

A study by Rajaratnam (1976) into circular turbulent jets emerging from a nozzle into a large stagnant mass of the same fluid found the size of the jet increased steadily as its distance from the nozzle increased. He found the velocity along the jet centreline remained constant with increasing distance from the nozzle up to the end of the potential core region, section 1-1 in Figure 4.1. After that point, the turbulence generated at the boundary of the jet penetrated to the axis, causing the velocity to decay with distance. Thus, within the potential core region, the jet velocity of the source (U_m) was maintained. Beyond this region, Rajaratnam found the velocity decay as;

$$\frac{U_m}{U_o} = \beta \frac{d_j}{x} \qquad 4.1$$

Where;

U_m = Velocity of centreline of jet at position 'x' from origin

U_o = Velocity of jet at source

β = Jet diffusion coefficient (typically 6.3)

d_j = Diameter of jet at source

x = Distance from jet origon

When the jet issued into opposing fluid, Rajaratnam found the jet diffusion coefficient (β) to reduce slightly, to the region of 5.7.

Rajarantam also found the axial jet velocity to decay with increasing radial distance from the jet centreline, creating a Gaussian velocity distribution. The relationship he developed for the radial decay of velocity was;

$$\frac{U}{U_m} = e^{-0.693\left(\frac{r_j}{b_2}\right)^2} \qquad 4.2$$

Where;

U = Jet velocity at radial distance r

b_2 = Radial distance where $u = u_m/2$

r_j = Radial distance from centreline

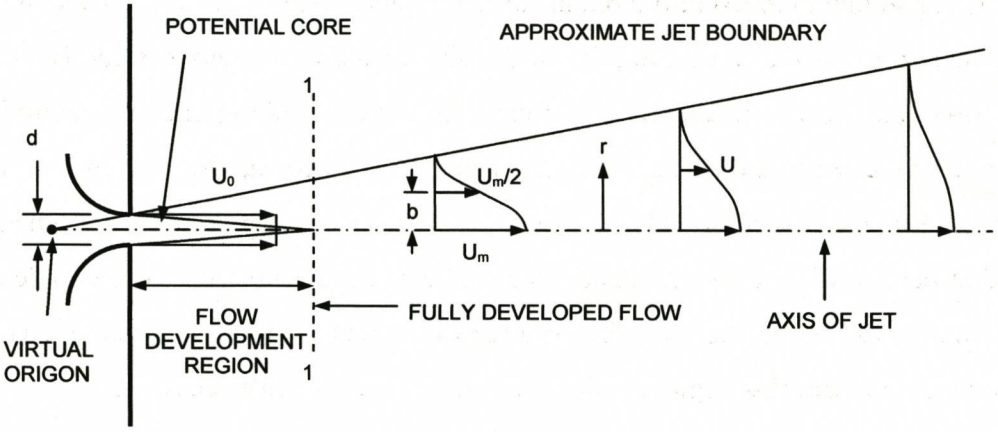

Figure 4.1 Definition sketch of circular turbulent jets. (Rajaratnam, 1976)

Rajaratnam also studied the impingement of a circular turbulent jet on a solid surface (Beltaos & Rajaratnam, 1974). They recognised three reasonably distinct regions of the jet, as shown in Figure 4.2. In the 'free jet region' the flow characteristics were the same as a free jet, described above. In the 'impingement region' the jet is strongly deflected and assumes a flow parallel to the wall in the 'wall region'. The shear stress was also measured on the wall surface and was found to be greatest at a radial distance of 0.15H, where H is the height of the nozzle above the wall surface.

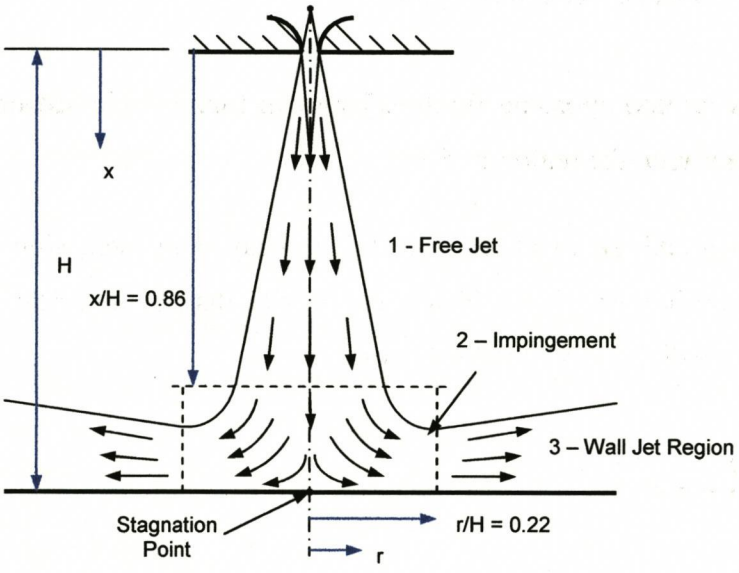

Figure 4.2 Definition sketch of impinging circular turbulent jets. (Beltaos & Rajaratnam, 1974)

The stagnation point is on the centreline of a vertical jet. However, according to Beltaos (1976) the stagnation point shifts as the jet angle becomes oblique, as shown in Figure 4.3. The jet velocities, shear stresses and resulting scour characteristics are describes in detail by Breusers and Raudkivi (1991)

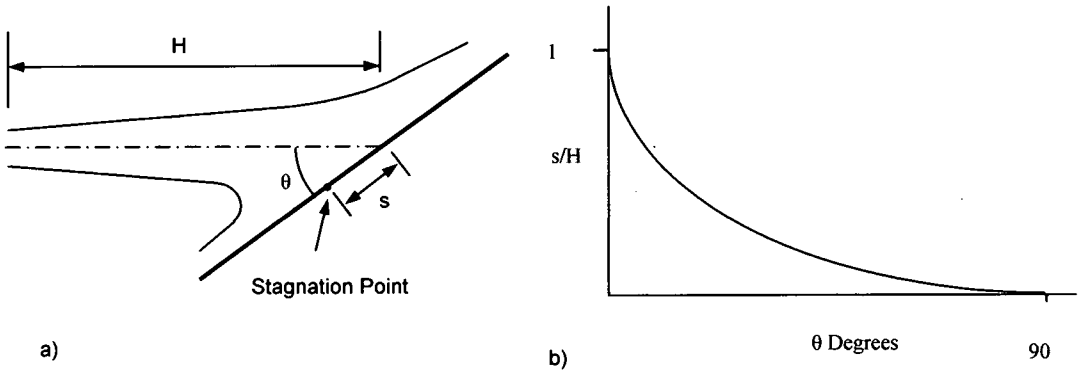

Figure 4.3 a) Definition sketch, b) Eccentricity of stagnation point with impingement angle

4.3.2 Mechanics of Scour

Most literature in the field of marine cable burial equipment concerning jetting concerns with the trial and development of new jetting tools rather than the fundamental mechanics of jet action. Most jet erosion literature concerned the scour around hydraulic structures, with a few exceptions. A review of the relevant and helpful aspects of this literature is presented.

A brief sketch of the mechanics of scour that are of interest to this work is presented. Scour is defined as the enlargement of a flow section by the removal of material composing the boundary through the action of the fluid in motion. (Laursen, 1952) The initiation of movement of a particle is defined as the instant when the applied forces due to fluid drag and lift causing the particle to move exceed the stabilising forces due to particle weight and interlocking. (Raudkivi, 1990) A number of theoretical approaches have been developed to attempt to model the initiation of scour, such as White (1940) and Leliavsky (1966), but according to Carson (1971) they suffer from inadequately modelling the physical processes and being limited to horizontal flow only. Empirical approaches by Bagnold (1953) and Shields (1936), together with the theoretical ones are limited in that they assume an average condition, whereas individual particles can deviate considerably from the average state due to the turbulent nature of the flow.

The shear stress from fluid flow acting on a unit area of soil surface is given in a number of texts and papers (Carson 1971, Breusers & Raudkivi 1991, Stein *et.al.* 1993) as;

$$\tau = C_f . \rho_w . U^2 \qquad 4.3$$

However, some omit the coefficient of friction. A threshold shear stress has to be overcome before scour occurs; therefore the rate of erosion is described by Stein *et.al.* (1993) as;

$$E = x_s . (\tau - \tau_c)^{\xi} \qquad 4.4$$

Where;

τ	=	Shear stress
τ_c	=	Critical shear velocity
C_f	=	Coefficient of friction
ρ_w	=	Density of fluid
E	=	Sediment detachment rate per unit area
x and ξ	=	Experimentally determined constants

The critical shear velocity was found, by Hjulstrom (1935) and Bagnold, to vary significantly between sands and clay, as shown in Figure 4.4. It shows that fine sands have the lowest critical shear velocity, whereas clay requires a very high velocity. This indicates that sands and clay have different jet erosion characteristics.

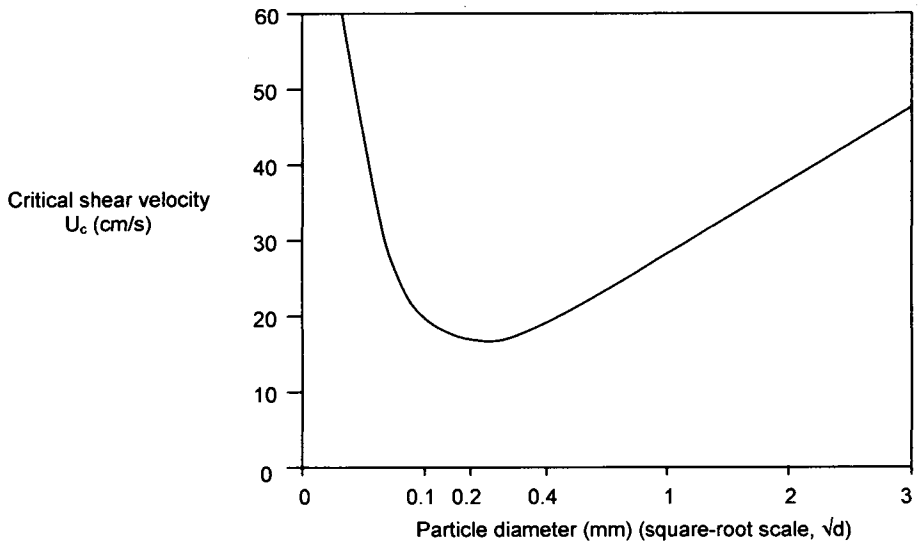

Figure 4.4 Variation of critical velocity with particle size for water (Hjulstrom 1935 & Bagnold 1953)

4.3.3 Models describing Scour Hole Development in Sand

The range of scour models and analysis that exist mainly concern the scour around hydraulic structures such as spillways, weirs and culverts. They are largely driven by safety considerations to prevent the structure being undercut by the scouring process. Consequently the vast majority of investigations relate to jets external to the soil, and very little were found concerning jet nozzles moving through the soil.

The investigations studied provide only guidance and not solutions. Breusers and Raudkivi (1991) highlight that the principles of analysis of scouring are not well established, and the results of various investigations often show differing trends. Their reason for this is that the turbulence, with its great complexity and randomness, and sediment transport, with its strong dependence on turbulent flow, are so complex that they preclude a complete understanding of the processes.

The complex nature of scouring has caused many researchers to adopt a dimensional analysis approach. A small number of researchers have taken an empirical/semi-theoretical approach, and a few have taken a largely theoretical analysis. Rouse (1939) was the pioneer investigator into the scour caused by a jet. The field flow and erosion

pattern of continuous and pulsating jets were studied experimentally by Kobus *et.al.* (1978). Karim and Ali (2000) compared the flow field, velocities and shear stress predicted by FLUENT CFD to those of experimental results and found close agreement.

The erosion caused by a single circular turbulent jet has been studied by Dabbagh *et.al.* (2002), Rajaratnam and Beltaos (1977), and for a submerged circular jet by Rajaratnam (1982). Rajaratnam found for large impingement heights (H >8.3d), the asymptotic dimensions of the scour hole were mainly functions of the erosion parameter $E_c = F_0/(H/d_j)$, whereas for small impingement heights (H <5.5d) the dimensions scaled with F_0, where F_0 is the densimetric Froude number $[U_0/\sqrt{g.D.(\Delta\rho/\rho)}$, where g = acceleration due to gravity, D = particle diameter, $\Delta\rho$ = difference between density of bed and fluid density ρ], H = impingement height and d_j = diameter of jet. They also found, in agreement with Rouse, that the maximum scour depth of erosion varied linearly with the logarithm of time, until some characteristic time value was reached, after which the length eventually approached an asymptotic state. Rajaratnam and Mazurek (2003) made further studies into the erosion of sands by circular impinging water jets with small tailwater, and developed similar dimensional arguments. They also found in another study that a similar dimensional argument applied to the erosion of a polystyrene bed by air jets (Rajaratnam and Mazurek, 2002). In another study Aderibigbe and Rajaratnam (1996) investigated the erosion of loose sand beds by a circular jet of low E_c values (<5). A semi-empirical method of combining equations of the modified Shields criterion, critical shear stress and the decay of jet centreline velocity was used to develop equations describing the asymptotic dimensions. However, the E_c values used in their work was significantly less than required for this study. Mih and Kabir (1983) studied the impingement of water jets on a non-uniform stream bed at oblique angles. They too found that the geometry of the scour hole varied with E_c, and developed empirical equations relating scour depth to the variable. Different equations were developed for small and large impingement heights, the given reason being that the centreline velocity remains constant in the core region of the jet, relating to the low impingement height, yet decreases with distance in the established flow region, relating to the larger impingement heights. They conducted tests using both a full nozzle in the centre of a tank and a half nozzle (semicircular jet nozzle) against the transparent side of

the tank. They found the contour lines of the scoured area by the half jet to be identical to those of the round jet under the same conditions. Chee and Yuen (1985) considered the erosion of unconsolidated gravel beds by oblique jets. Their interest was in the maximum depth of a scour hole, so they derived generalised relations to link the incipient motion condition at the deepest point of the scour hole with the scoured depth. Their approach was to combine dimensional analysis, bed velocity and threshold shear velocity to develop their equations. O'Donoghue *et.al.* (2001) experimented with vertical circular water jets in the context of pipeline burial. Consequently the jet velocities in their investigations were generally much greater than in the above studies. Their main interest was in the dynamic scour hole depth, with the jets in operation, rather than the static depth after the jets had stopped. They report that the maximum dynamic scour depth was found to be determined primarily by the jet momentum flux with a weak link to sediment size, while the scour hole diameter was determined by both jet momentum flux and sediment size. The empirically determined equations for scour hole dynamic depth were;

$$\frac{h_d}{D_s} = 2.18\left(\frac{J}{W_s}\right)^{0.34} = 2.18\left(1.5\left(F_0.\frac{d_j}{D_s}\right)^2\right)^{0.34}$$

Giving;

$$h_d = 2.18\left(\frac{1.5}{(s-1)g}\right)^{0.34}.(U_j.d_j)^{0.68} D_s^{-0.02} \qquad \textbf{4.5}$$

And in a similar manner, the maximum scour hole diameter was given as;

$$d_h = 1.62\left(\frac{1.5}{(s_r-1)g}\right)^{0.42}.(U_j.d_j)^{0848} D_s^{-0.26} \qquad \textbf{4.6}$$

Where;

h_d = Maximum dynamic scour hole depth

d_h = Maximum scour hole diameter

D_s = Representative size of sand particle

J = Jet momentum flux

W_s = Submerged weight of sediment

U_j = Jet velocity

s_r = Ratio of sand/water density

The scour caused by a submerged circular horizontal jet parallel to the bed material was studied by Chiew and Lim (1996). Their findings were similar to much of the work of Rajaratnam, that the densimetric Froude number (F_0) was still the main characteristic scouring parameter when correlated to the equilibrium scour depth. As the offset of the jet increased, the scour depth decreased.

The scour caused by a plane jet was analysed by Stein *et.al.* (1993), in the context of scour immediately downstream of a headcut. They considered the effect of jet diffusion on sediment detachment, and equations for equilibrium scour depth and the rate of scour hole development were developed analytically. However, their equations, like many others, contained coefficients that were determined empirically. They concluded that their measured and predicted rates of scour development showed that scour depth does not increase linearly with the logarithm of time, contrary to the findings of Rouse, Rajaratnam and others. Rather, their analysis showed that scour depth increased linearly with time within the potential core region of the jet, after which a linear increase with the log of time was an approximation, then scour rate decreased rapidly as the equilibrium scour depth was approached asymptotically. A theoretical investigation by Bormann and Julien (1991) into local scour from plane jets downstream of grade control structures was also analysed considering two dimensional jet diffusion and particle stability. Equilibrium scour depth was written as a function of jet velocity, flow depth and particle size. They found their theoretically derived equations were similar to regression equations from data of fifteen other papers.

Mason and Arumugam (1985) analysed thirty one earlier proposed formulas from literature for ultimate scour depth under jets issuing from dam overflows and flip buckets. They then increased the number of formulas by developing one of their own, which included an allowance for tailwater depth and found it gave an improved accuracy.

Niven and Khalili (1998 & 2002) were the only researchers found whose work concerned a single vertical jet internal to saturated sands. They conducted two series of

experiments, those with the jet in the centre of the sand tank, and those with the jet adjacent to the tank wall. The nozzle was progressively lowered into the sand and the steady state cavity dimensions were measured. They found that the nature of the cavity formation appeared identical in both tank centre and wall experiments. They observed four stages of cavity development as the nozzle depth increased. At shallow depths the fluidised profile remained an approximately constant shape as the jet was lowered into the soil, for any given soil, jet diameter and flow rate. The profiles could be fitted with the forms of either fourth order even functions or elliptical functions, although the former fit better. With increasing jet depth, the profile became asymmetric as the neck of the cavity at the soil surface closed in, forming a randomly migrating spout. At greater depths the successively greater 'pinching' of the spout lead to the formation of a submerged fluidised cavity, having no neck, with all jet water permeating through the soil. As the jet depth increased still further the cavity size diminished until a point where no cavity formed.

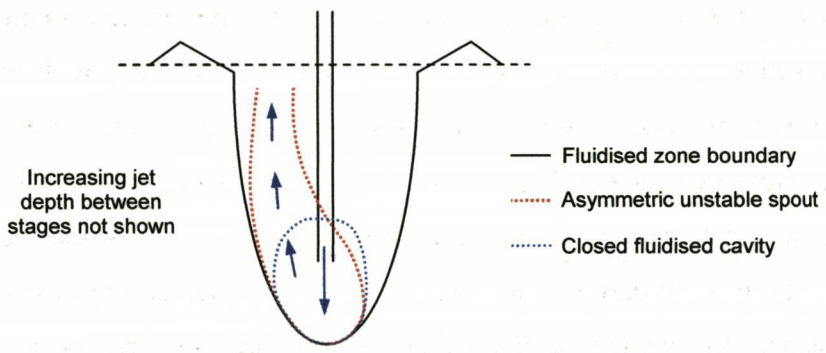

Figure 4.5 Schematic diagram of fluidised profiles created by a vertical internal jet (after Niven & Khalili, 1998)

4.3.4 Models Describing Scour Hole Development in Clay

The majority of literature describing scour hole development in clay concerns vertically impinging submerged jets. The erosion of clay by a water jet differs from that of sand (Mazurek *et al*, 2001) because of its cohesive properties, and due to its complexity is not well understood. Adamson and Kolle (1995), who studied jetting in both sand and clay soils, found the effective jetting techniques differed for each, due to the difference in erosion characteristics. Undermining and collapse techniques are effective in sands

but ineffective in cohesive soils, which require substantial energy to achieve full coverage over the trench cross-sectional area.

The scour of cohesive soil by submerged circular impinging jets was studied by Mazurek *et.al.* Their analysis, based on the mechanics of impinging jets, showed the equilibrium dimensions of a scour hole were a function of the momentum flux of the jet, the impingement height and the viscosity and density of the water. They observed three types of erosion, being 'flake erosion', where small circular flakes broke away, 'mass erosion' where large chunks of soil would break off, measuring up to 130mm by 40mm by 20mm, accounting for a large part of the erosion, and 'rapid surface erosion' where particles were assumed to be removed individually by the water. On some occasions it was considerable time before mass erosion overtook rapid erosion as the dominant mechanism. However, Mirtskhulava *et al.* (1967) observed large sized chunks being removed near the beginning of scour.

Trials by Rockwell *et al.* (1980) with a vertically impinging waterjet on very soft 1-2 psi clay found that it did not produce a smooth cut, but rather broke off chunks from pea gravel to basketball size. They found trench depth to vary directly with water pressure but inversely with traverse velocity. They observed the main gain in trench depth was up to a water pressure of about 75 psi. Fort *et al*, (1987) found that for effective waterjet cutting, the waterjet stagnation pressure should be 2 –3 times the target material compressive strength. In earlier work Rockwell (1976) observed the flow rate to have a greater influence on excavation depth than jet pressure, and that at constant power, increasing the flow rate produced a deeper trench than increasing the pressure. They found little correlation between jet nozzle diameter and the width of the trench created, and likewise for the standoff distance. They summarised the results with the empirical formula;

$$\frac{H_i}{D} = 4.64P^{0.33} - 1.05V^{1.25} \qquad \textbf{4.7}$$

However, other researchers (Moore and Masch, 1962 & Hollick, 1976) found the standoff distance does effect the shape of scour hole. Moore observed two types of scour hole generally formed, being either with impingement heights (H/d) of less than 7,

producing narrow and deep holes, or greater than 7, producing shallow and wide holes. Hollick observed some intermediate types and concluded hole shape depended on more than just the relative impingement height. Moore and Masch found there to be a linear relationship between scour depth and the logarithm of time, with an asymptotic approach to equilibrium scour. They used dimensional analysis to determine the key parameters describing the scour of clay by vertical submerged impinging jets and suggested the average depth of a scour hole was a function of jet velocity, nozzle diameter, impingement height, water density, viscosity, soil shear stress and exposure time.

Machin (2000) investigated the effects of stationary vertically impinging jets on stiff to very stiff clay soils (50 to 125 kPa). The key variables were nozzle diameter, water pressure, jet exposure time and soil shear strength. Initially a very rapid jet penetration occurred to a certain depth, followed by a slower propagation beyond it. He proposed the mechanism for the initial penetration was an almost instantaneous undrained shear failure in bearing of the soil by the impact or stagnation pressure from the jet, being supported by a bearing capacity analysis based on the jet stagnation pressure. Machin also observed lateral hydro fracturing of the soil in some cases when using high pressure jets. He notes a direct relationship between nozzle pressure and cavity depth, and for a given pressure there was a very strong trend of increasing depth with increasing nozzle diameter. However, there was a threshold pressure below which very little cavity was formed.

Hurlburt *et al.* (1978) investigated jetting onto submerged clay soils in which a series of 34 tests were conducted on saturated soft clay of 2-3 psi using a range of nozzle diameters, jet pressures and traverse velocities. They summarised the results with the empirical formula:

$$\frac{H_i}{D} = 0.13P\left(\frac{V}{1.67}\right)^{-0.3} \qquad \textbf{4.8}$$

The application to this study of the equations describing scour hole development in both sand and clay soils is of limited potential. The equations for cavity dimensions in sands and clay were predominantly empirically derived with coefficients being specific to the

investigations they were developed from. Also most analyses were for the steady state condition of the scour hole rather than the transient. All but one paper dealt with nozzles external to the soil, and the work of Niven and Khalili which concerned an internal jet was for a vertical nozzle and steady state conditions. No literature was found concerning a static or dynamic (moving) horizontal nozzle internal to the soil.

4.4 Methodology and Experiment Design

To fulfil the objectives three aspects of work were conducted. Firstly, examinations of cavity growth and jet scour characteristics using a half nozzle buried in a range of soil types. Secondly, an experiment to measure the uplift force exerted by an expanding cavity on the soil immediately above it, the purpose to determine the order of magnitude of the water pressure in the cavity. Thirdly, the findings of the two experiments were used to aid the development of a mathematical model simulating cavity development. The design of each experiment is detailed below.

4.4.1 Buried Static Half Nozzle in Sand and Clay

Tests were conducted in four soil types, being three sands and one clay. See Table 4-1 for details. The standard sand, from Cainhoe Quarry, was the same as that used in the experiments of preceding Chapters. The Oxford clay was from a Stewartby clay pit in Bedfordshire. Full details are in Appendix 2.

Table 4-1 Properties of soils used in half nozzle experiments

Soil Type	Particle Size (D_{50}, mm)	Hydraulic Conductivity (mm/s)
Standard Sand (SS)	0.2	0.27
Fine Sand (FS)	0.15	0.24
Coarse Sand (CS)	0.7	4.4
Oxford Clay		~ 0

The test program was designed where initially a full range of thirteen jet flow rates was examined in the standard sand (SS). The flow rates were designed to use the maximum range the equipment allowed. From these tests five critical flow rates were examined in the other soil types. See Table 4-2 for details on the designed flow rates. The reason was to establish the dominant characteristics using the SS, then to compare the other soils with these characteristics to determine similarities and differences.

Table 4-2 **Details of the flow rates tested in the half nozzle experiments**

Soil Type	Designed Flow Rates Tested (ml/s)
Standard Sand	25, 50, 75, 100, 125, 150, 175, 200, 250, 300, 350, 400, 450
Fine Sand	50, 100, 150, 250, 400
Coarse Sand	50, 100, 150, 250, 400
Oxford Clay	50, 100, 150, 250, 400

The purpose of the tests was to establish the mathematical relationship between factors, therefore a larger number of flow rates were chosen rather than replications. The test program conducted tests on soil types in the order shown in Table 4-2. For each soil the flow rates were tested in a random order.

4.4.2 Variation in Uplift Forces between Standard and Coarse Sands

An experiment was conducted in which the uplift forces for flat metal plates were measured. The plates were designed to resemble the profile of a cavity created by a buried jet. Two plate sizes were used, the larger being four times the area of the smaller, resembling the early and latter stages of cavity growth. Full details on the plate dimensions are in Appendix 2.

Tests were conducted on two soil types, being standard and coarse sand. These were chosen because of their large differences in hydraulic conductivity values, and thus their large difference in pore pressure reduction when sheared.

Tests were conducted in dry and saturated conditions for both soil types. This was to investigate the affect of pore pressure reduction on uplift force in both soils.

A matrix of the variables is shown in Table 4-3. The experiment program was design where initially tests were conducted on the dry sands, and afterwards on the saturated sands. For statistical purposes tests of each plate size were replicated three times in each condition. The order of tests was randomised in each condition.

Table 4-3 **Matrix of variables for the uplift force experiment**

	Standard Sand		Coarse Sand	
Dry Sand	Small	Large	Small	Large
Saturated Sand	Small	Large	Small	Large

4.5 Equipment and Measurement Technique

4.5.1 Buried Static Half Nozzle in Sands

A diagram of the equipment used for viewing the cavity is shown in Figure 4.6 to Figure 4.8. A diagram of the plumbing and fluid instrumentation systems are given in Figure 4.9.

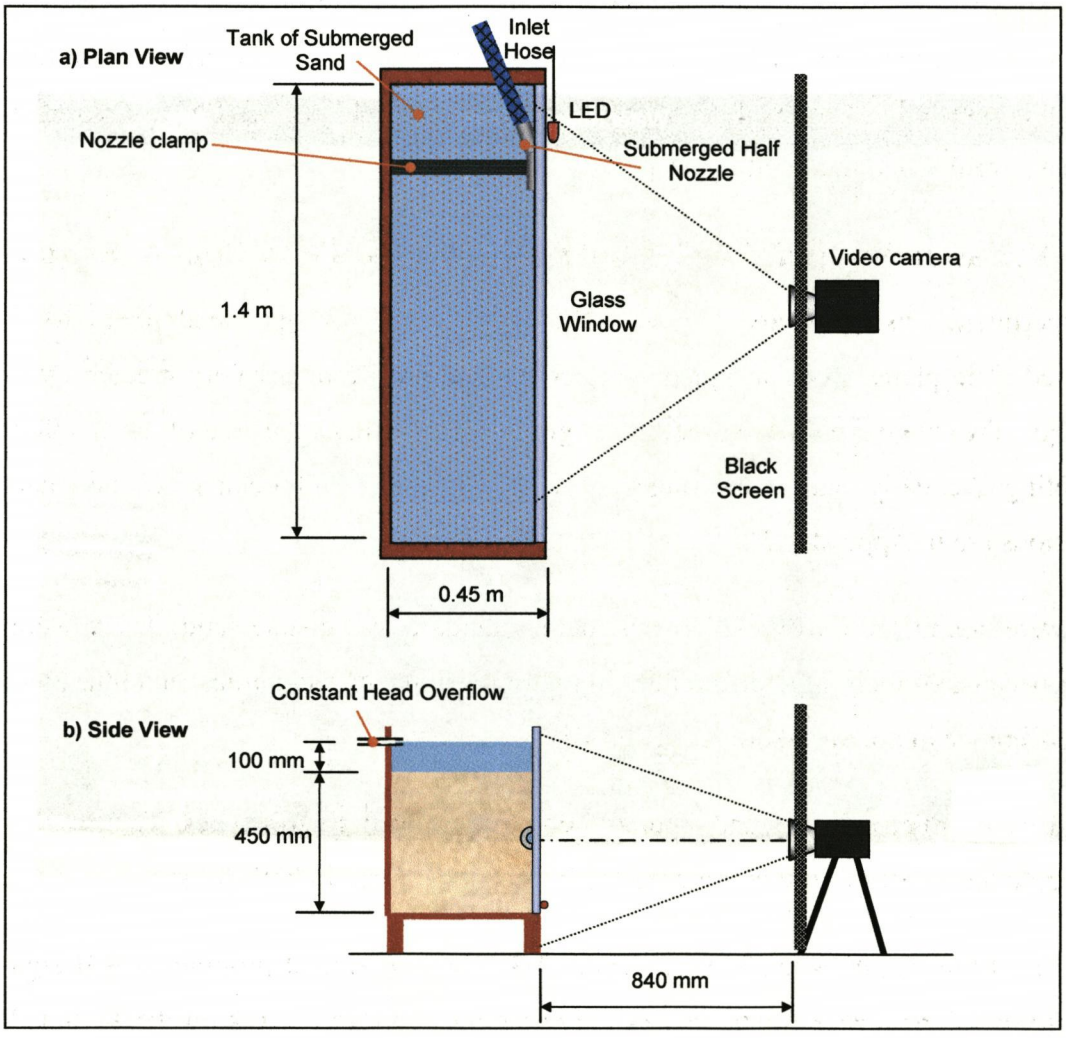

Figure 4.6 **Diagrams of the tank and video camera setup for half nozzle experiments**

The half nozzle was buried in the sand tank and held against the window by a clamp. It was sealed against the glass using a single layer of insulation tape. The video camera recorded the action of the jet in the sand through the glass window, as shown in Figure 4.6. An array of white crosses was marked onto the window to create a reference grid,

as shown in Figure 4.7. The grid was used in Erdas Imagine software to generate a coordinate reference system to enable measurement of the cavity created by the jets.

A purple dye (potassium permanganate) was injected into the flow stream to enable clear visualisation of the cavity development when analysing the video. Details of dye concentrations are given in Appendix 2. The dye flow rate was typically 0.4 ml/s, adding an insignificant volume to the mainstream flow between the flow sensor and the nozzle, so causing negligible error of flow measurement.

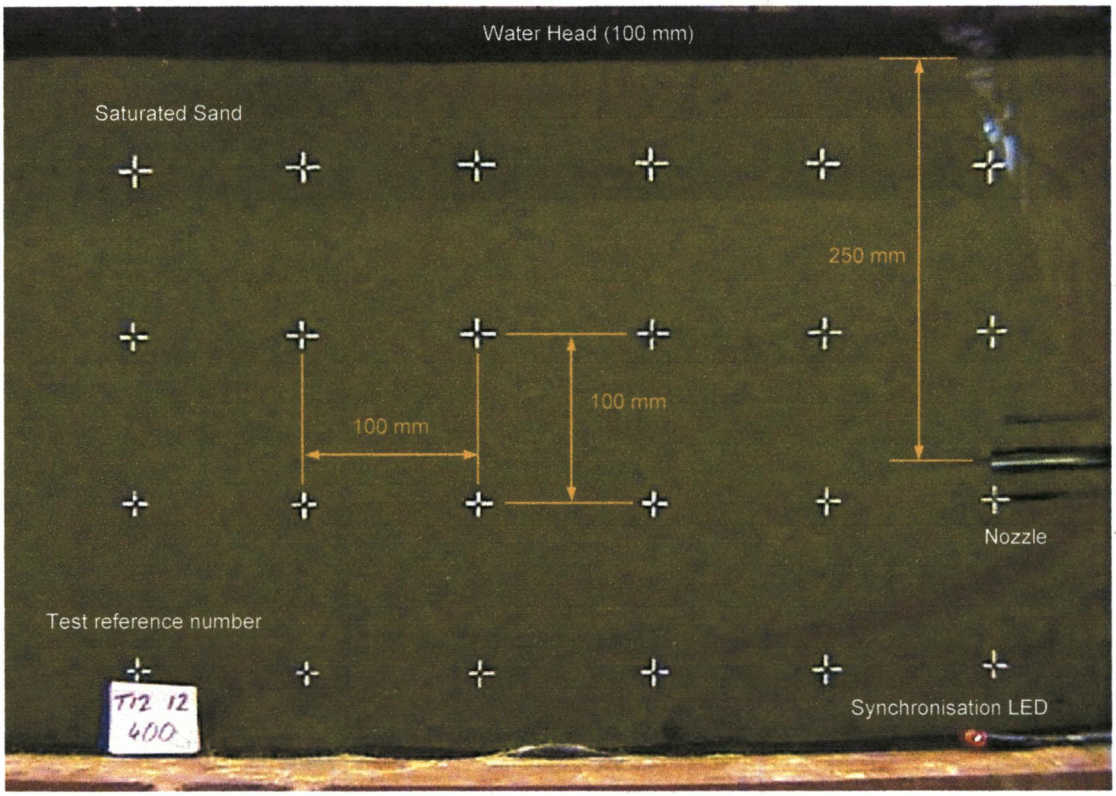

Figure 4.7 Reference grid on glass window for static half nozzle tests

The aluminium half nozzle had an internal diameter of 6 mm, being the same as the nozzle diameter used in the rake angle experiments of Chapter 2, as shown in Figure 4.8 with other nozzle dimensions. The bend was given the minimum possible angle to minimise turbulence and losses. After the bend the straight half section extended for 75 mm to reduce turbulence created by the bend and reduction in flow area.

The thickness of the glass window (25 mm) caused considerable refraction of light through it. The refractive index of the glass was determined by measuring the angles of

incidence and refraction of a laser beam shone at the window. Full details of this test are given in Appendix 3.

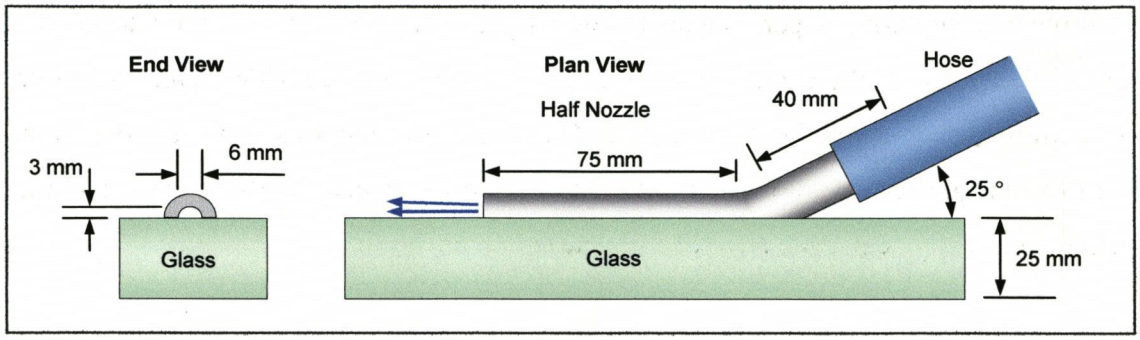

Figure 4.8 **Dimensions of half nozzle and glass window**

A Grundfos centrifuge pump supplied pressurised water to the jet nozzle from a large reservoir tank. The flow rate and the pressure of the water was measured downstream of the pump, as shown in Figure 4.9. Data from these sensors was recorded using a Flyde data acquisition module with a laptop computer using DasyLab software. The calibration details of the flow and pressure sensor are in Appendix 3.

The video and the flow data on the laptop were synchronised by creating a reference point on both during recording, using a manually operated switch that simultaneously turned on an LED, which was seen on the video, and sent a signal to the laptop.

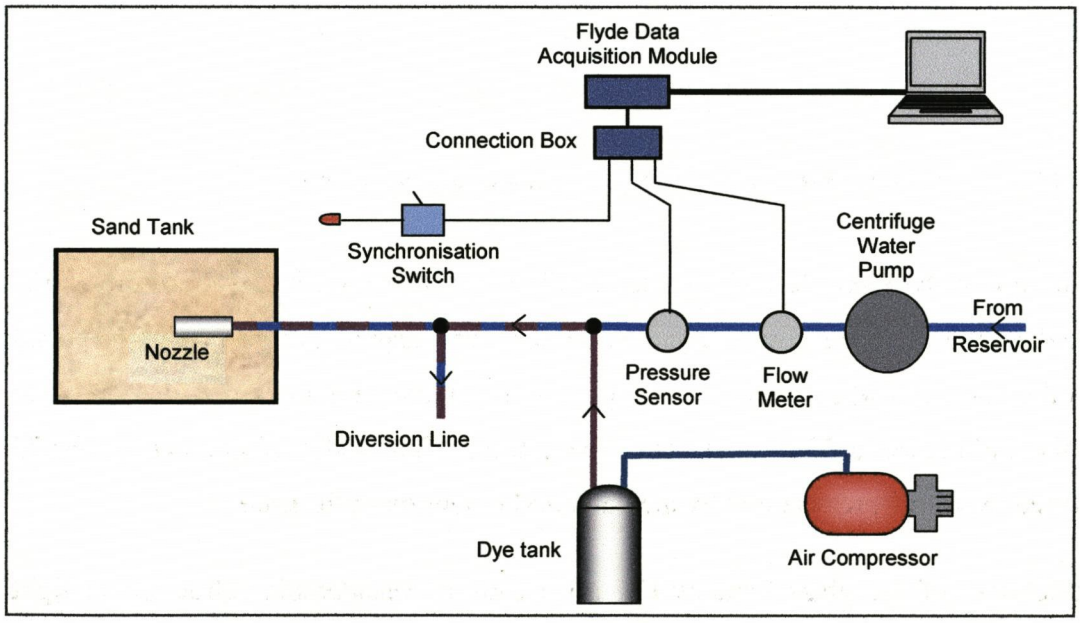

Figure 4.9 **Diagram of fluid and instrumentation systems for the half nozzle experiments**

The measurement technique was as follows.

1. Sand was prepared after a previous test by levelling the surface, then consolidating by shaking a 12 mm diameter steel rod while pushing it down through the soil to the base of the tank, then repeating this action at 100 mm intervals along the window side of the tank.
2. A density sample was taken using a density ring.
3. The jet was turned on and the test recorded on video and computer for approximately 1 minute.

The development of the cavity was determined from the video using the following steps.

1. The video was captured onto computer.
2. Individual frames were then extracted and saved in bitmap form. The cavity developed significantly in the first few seconds, therefore more frames were extracted from the early period than the latter stages of cavity growth. The cavity generally broke through to the soil surface within 20 seconds. Frames were therefore extracted at 0.24, 0.48, 1, 2, 4, 6, 8, 10, 12, 14, 16 & 20 seconds. Occasionally if the cavity had not broken the surface within 20 seconds frames were extracted at greater time periods.
3. A process to correct the image from optical distortion caused by the camera lens and the refraction through the glass was conducted using Erdas Imagine software. Coordinates were then assigned to the window reference grid in each image.
4. The cavity profile was digitised by drawing a polyline around its perimeter. The coordinates of the polyline where then exported into a Microsoft Excel spreadsheet.
5. The maximum length and depth of the cavity profile were calculated for each image. The results were then plotted against time for each flow rate.

The mean flow and pressure were calculated over each test run. Data of the initial two seconds after the initiation of the jet were not included in the calculations since both the flow and pressure values spiked as a result of the flow being redirected from the diversion line to the nozzle, as shown in Figure 4.10.

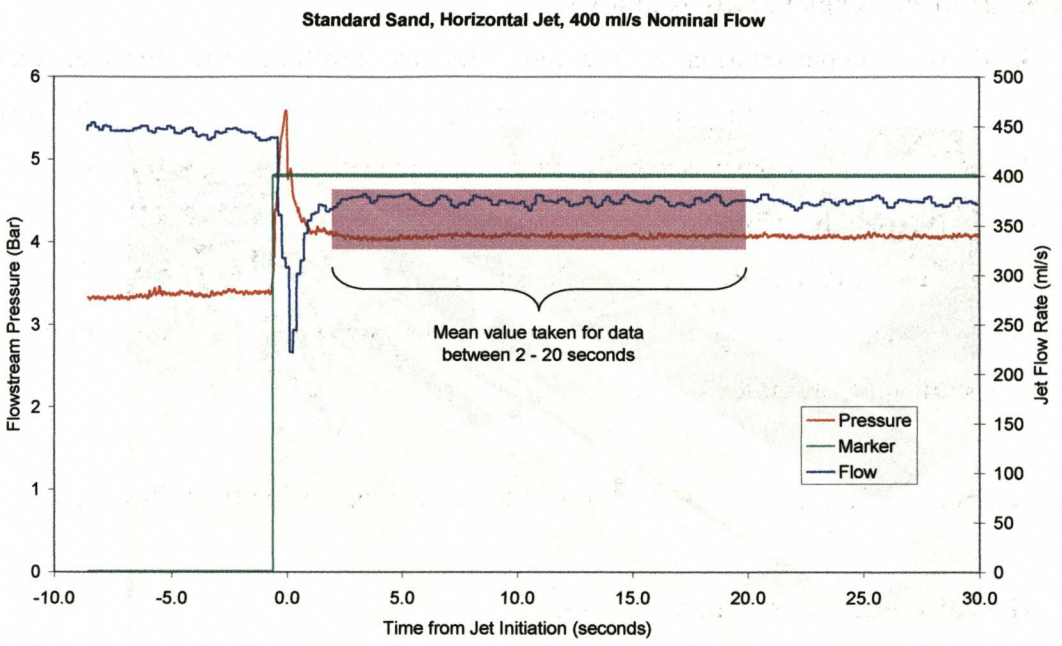

Figure 4.10 **Range of flow and pressure data over which mean values were calculated**

4.5.2 Buried Static Half Nozzle in Oxford Clay

The equipment and measurement technique used in the static half nozzle tests in clay was the same as that used in the sand tests. The only differences were the tank and the soil preparation method, both detailed below.

The static nozzle tests in clay were conducted in a separate tank to the tests in sand. It was expected the clay would be difficult to re-prepare after a test. Therefore each test was conducted in a different plot within the tank. The tank measured 3 m long by 0.4 m wide and deep. The tank had six windows, three on each side, one window for each of the five flow rates tested and the other for a trial run. The nozzles were glued onto the Perspex windows. Figure 4.11 shows a picture of the tank and windows along one side.

The clay was prepared by putting damp clay granules from Oxford clay pits into the tank. Water was added and the clay kneaded by walking back and forward through it. The tank was then left for six weeks to enable the clay to become saturated before tests were conducted.

The characteristics of the cavity development were significantly different to the sands and were analysed by observation of the video only.

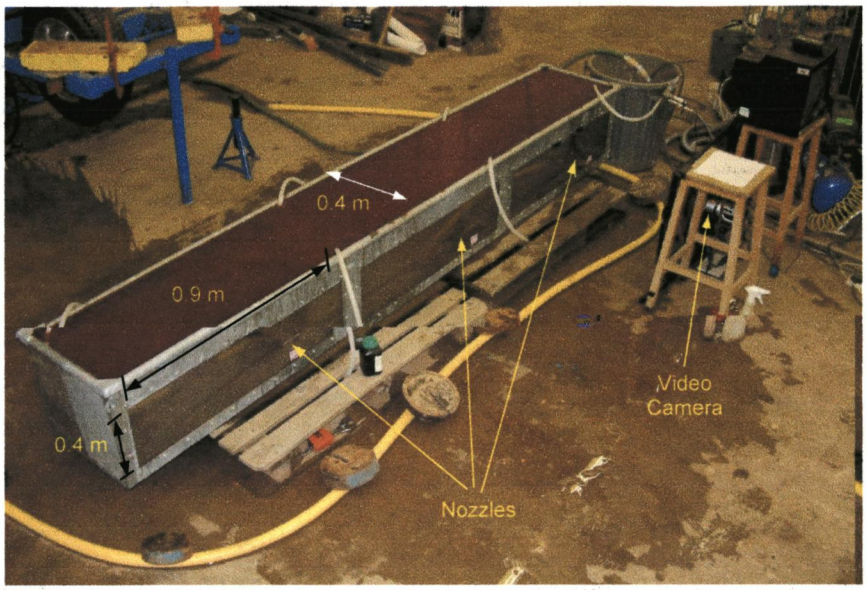

Figure 4.11 Photo of submerged clay tank

Figure 4.12 shows a photo of the setup of the video camera and one of the windows after a test.

Figure 4.12 Setup of video camera and tank with saturated clay

4.5.3 Uplift Forces Experiment

The equipment used to measure the uplift force of a buried plate is shown in Figure 4.13. The tests were conducted in a circular bin measuring 0.46 m diameter by 0.64 m deep. The tests were conducted after the half nozzle experiments had been analysed, so the typical shape of a cavity in these soils was known. The plates were designed to represent the shape and area of a cavity. Details of the plate design are in Figure 4.14.

The plates were pulled out of the soil using a hydraulic ram positioned above the bin. An EORT was used to measure the uplift force (refer to Section 2.5.1) and a string pot potentiometer was attached to the ram to measure its displacement. Both the signal from the EORT and the string pot potentiometer was connected to a Flyde data acquisition module and then recorded onto a laptop computer using DasyLab software. Details of the calibrations of the EORT and the string pot potentiometer are in Appendix 3.

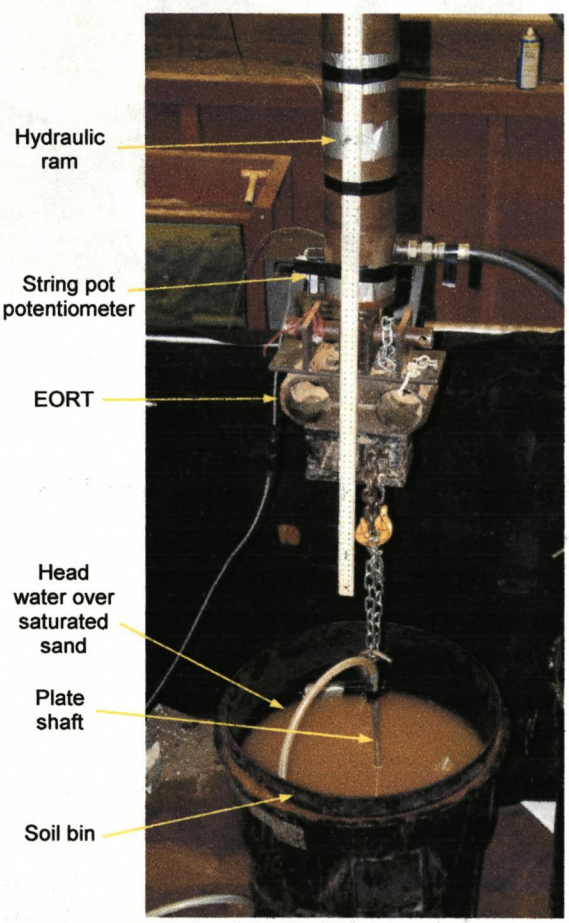

Figure 4.13 **Equipment setup for uplift force experiment**

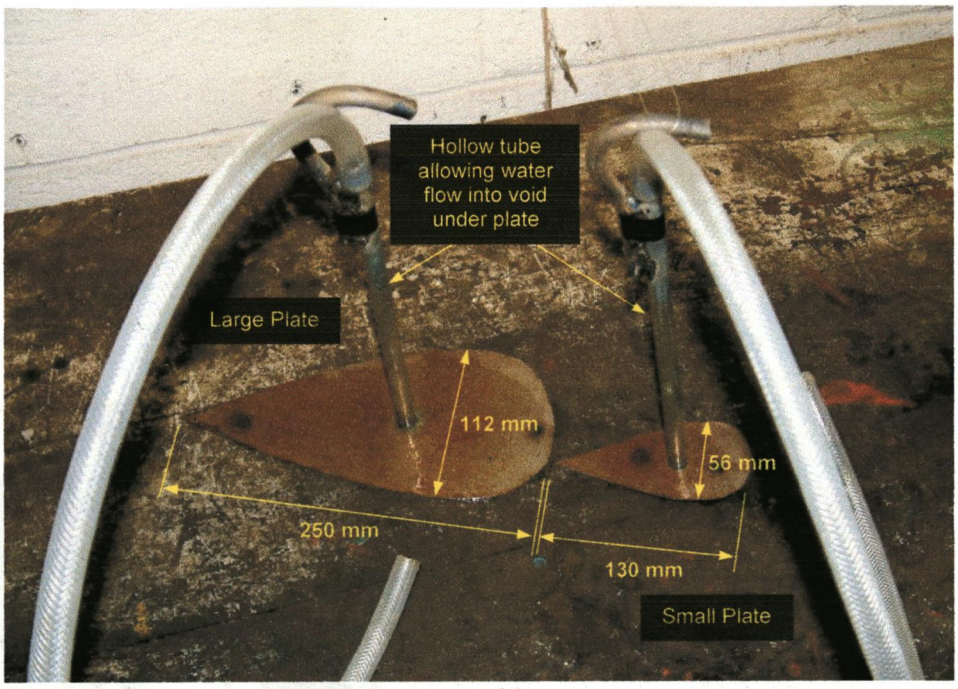

Figure 4.14 Design of uplift plates

The measurement technique was as follows.

1. The sand was prepared after a previous test by removing the top 200 mm of sand from the bin. The plate and connected hollow shaft were then buried to a depth of 40 mm in the remaining soil. The removed soil was then replaced into the bin, giving the plate a depth of 240 mm.
2. The bin was shaken from side to side ten times to consolidate the sand.
3. The plate shaft was connected to the EORT and then lifted by the hydraulic ram while the force and displacement readings were recorded onto the computer.

The recorded EORT data was analysed by determining the peak force for each test. Figure 4.15 shows typical force characteristics, with the peak force used as representative of the uplift force for a test.

The displacement data was used to determine the upward speed of the plate. The speed (displacement / time) was used to ensure all tests were conducted under similar conditions.

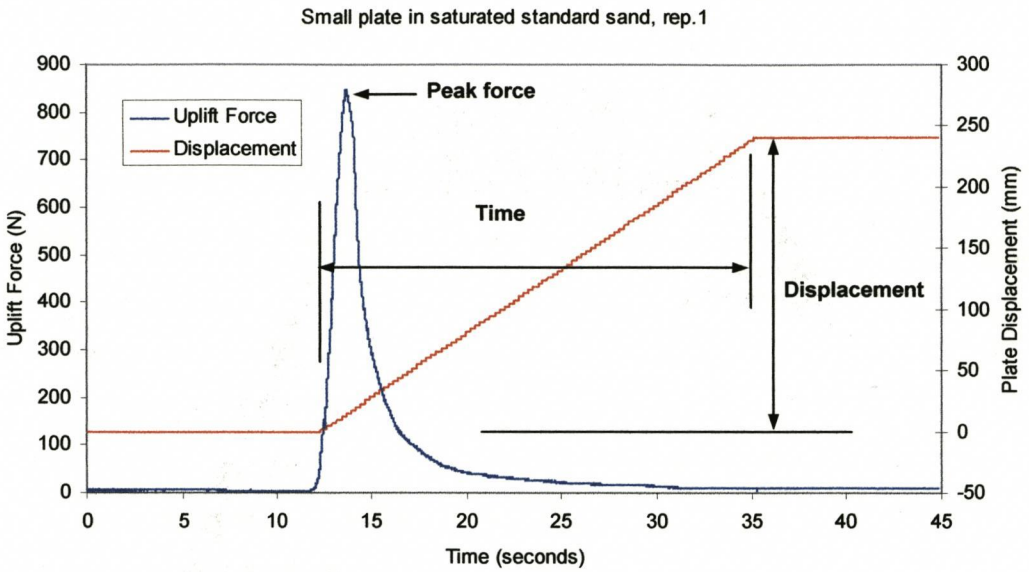

Figure 4.15 Analysis of uplift force and displacement

The maximum uplift force of each test was displayed graphically to determine differences between factors.

4.6 Results and Interpretation

Full results of the experiments are contained in the Appendix 4. Important aspects of the results are presented and discussed below.

4.6.1 Buried Static Half Nozzle Experiments

It has been shown that a half jet against a wall on its line of symmetry can be used to accurately represent a full jet. (Mih and Kabir, 1983 & Niven and Khalili, 1998 & 2002) On this basis it was assumed to be acceptable to use a half jet as representative of a full jet.

A. Stages of Cavity Growth

Studies of the video of the buried half nozzle tests show that the cavity growth characteristics differed between soil types. The characteristics of each are described below.

The standard sand (SS) and the fine sand (FS) behaved very similarly. The growth of the cavity in those soils may be divided into four stages, being;

1. Initially the jet created a symmetrical cavity about its longitudinal axis, creating a teardrop shape. The jet impinged onto the far wall of the cavity creating eddies around the edge of the impingement zone. These eddies eroded the sand from the sides of the cavity causing it to expand.
2. The inflow of water caused an expansion of the cavity which forced the surrounding soil to deform. The soil above the cavity gave the least resistance to deformation and therefore cavity expansion was greater at the top than the bottom of the cavity. This combined with the eddy erosion described above, resulted in the upper surface of the cavity rising and becoming more flat after about four seconds. This produced an asymmetric flow system within the cavity.
3. After about twelve seconds a shear plane formed up to the surface, usually from the rear of the cavity where shear deformation of the soil was greatest. This allowed the enclosed water to break through to the surface after about twenty seconds, forming a spout.
4. The flow of water through to the surface caused the water pressure within the cavity to reduce. As a result the sand above the cavity would then collapse down into the large water eddy undercutting it. The increase in cavity length was then abated.

Characteristics of the flow regime in a cavity after two seconds are shown in Figure 4.16. The profiles of the cavities in SS, shown in Figure 4.17, demonstrate the progression through the above stages. Larger plots of the SS cavities and plots of the FS cavities are contained in Appendix 4.

The growth rates of the cavities in development stages three and four were so slow that they have little relevance to the commercial application of this study. Therefore the analysis focuses on the first two growth stages where the growth rate is much greater.

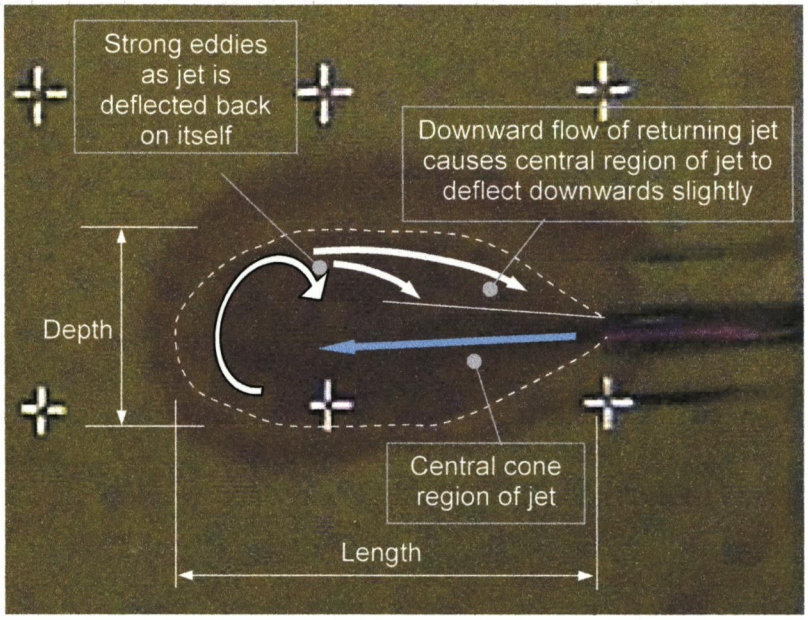

Figure 4.16 **Typical asymmetric flow patterns in standard and fine sand, after two seconds**

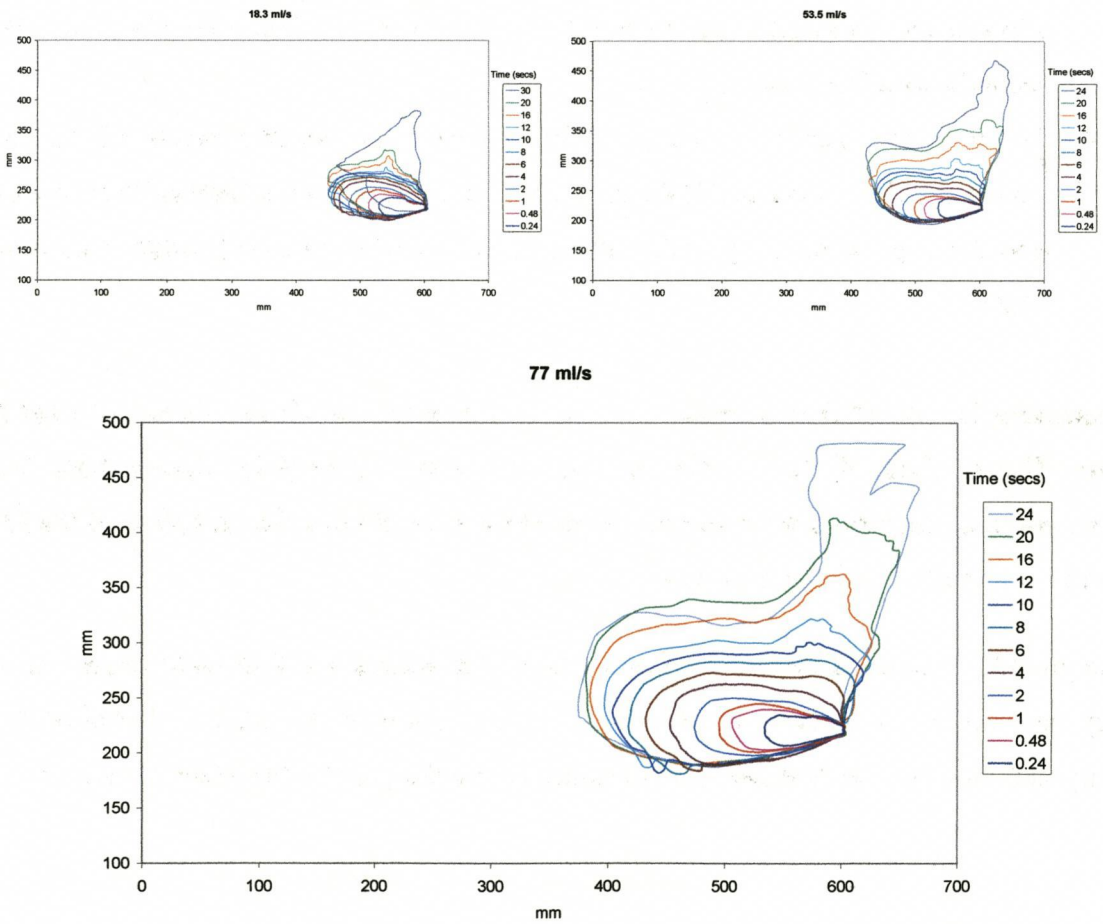

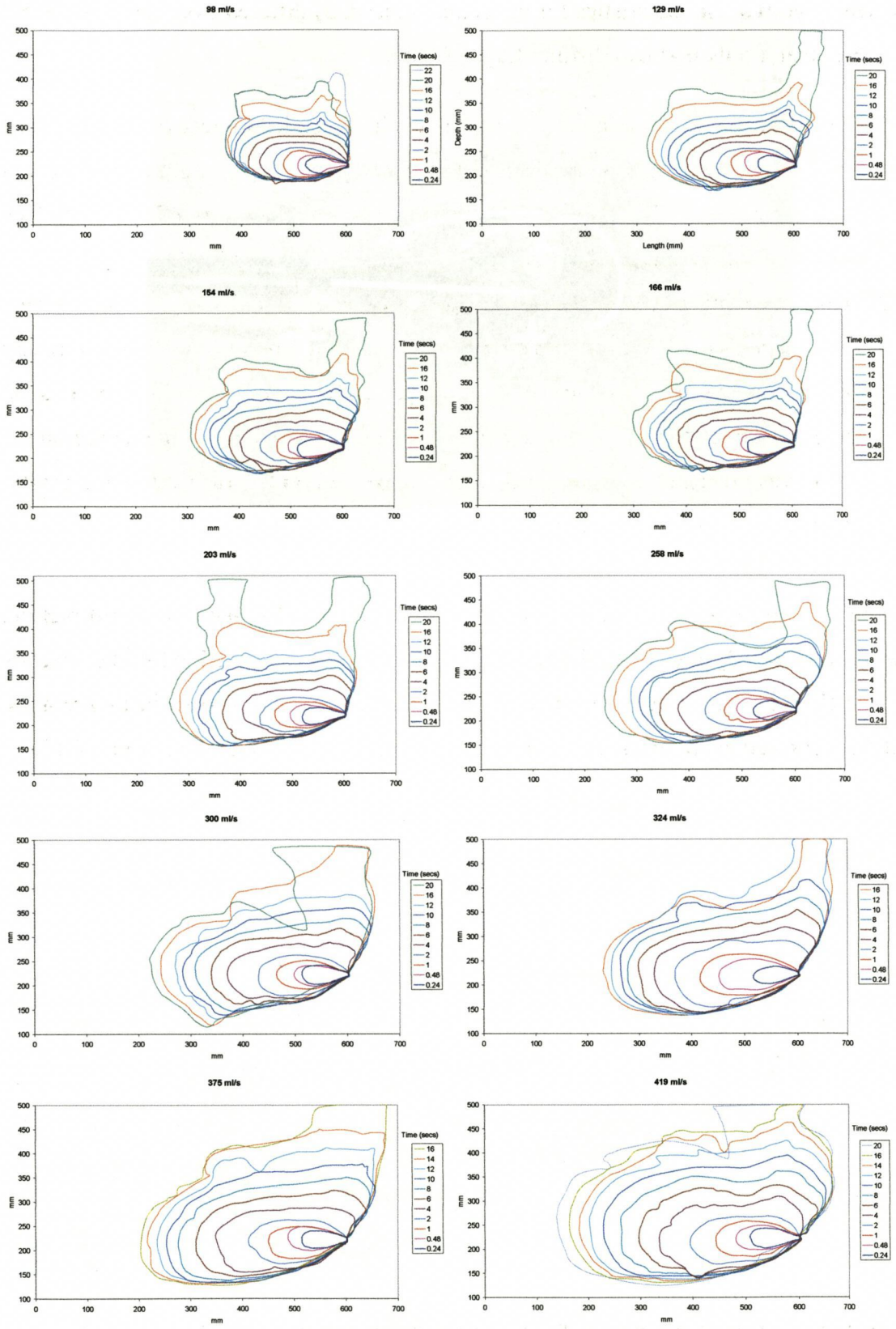

Figure 4.17 Cavity profile developments in standard sand for all flow rates examined. Also typical of fine sand cavity development

The cavity growth characteristics for the coarse sand (CS) differed from those of the SS and FS in that it only had two distinct stages, being;

1. When the jet was first initiated a conical cavity extended rapidly from the nozzle, with the jet pushing sand particles out of the way, causing a slight rise of the soil above the cavity. The angle of the jet cone was less than in the SS and FS. The rapid growth of the cavity continued for about 0.75 seconds.
2. Upon reaching a certain size the cavity ceased to expand, having reached a state of dynamic equilibrium, where the flow lost through permeation into the cavity walls equated the jet flow. Above the jet cone there was a region of sand migrating back to the jet source. Upon reaching the boundary of the jet region the sand was entrained into the jet flow and deposited on the far wall of the cavity, from where it was circulated back round to the jet source.

The circulating region of sand could only be detected on video and not in still picture. For this reason only the central jet region of the cavity could be defined in the analysis of the CS. The circulating flow characteristics of the cavity are shown in Figure 4.18, and the measured cavity profiles for each experiment in CS are shown in Figure 4.19.

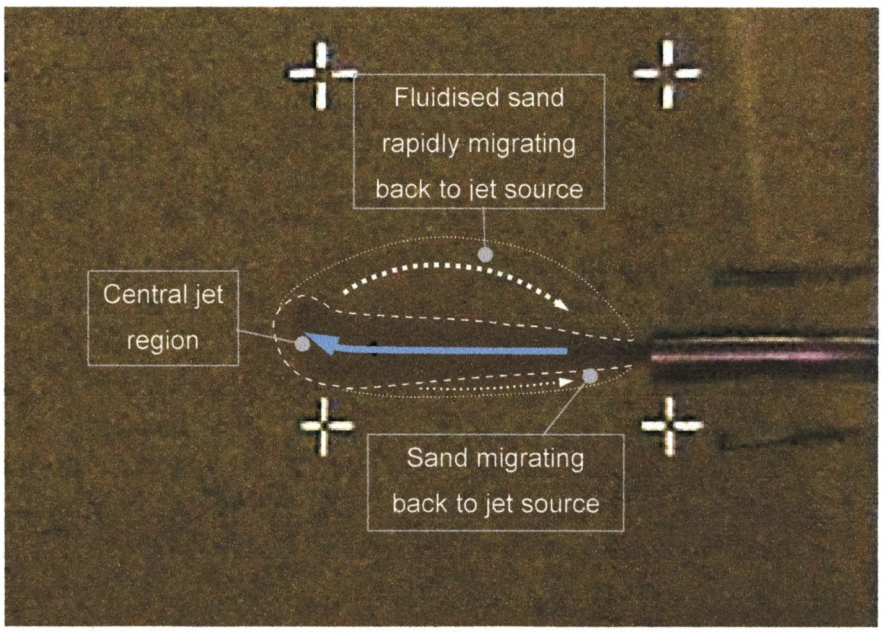

Figure 4.18 Typical dynamic equilibrium flow patterns in the coarse sand

There were two characteristics common to all the sands. Firstly, a ring of purple dye was seen to permeate through the soil from the cavity, as shown in Figure 4.20. The velocity of permeating water was faster in the CS than the SS and FS because of its higher hydraulic conductivity. The velocity appeared to remain constant over time in the CS whereas the velocity reduced to near zero in the SS and FS in the latter stages of the cavity development, as it expanded upwards. Secondly, soil above the cavity heaved upwards. The continued growth of the cavity in the SS and FS caused significant soil heave, whereas the much smaller cavity in the CS caused only slight movement.

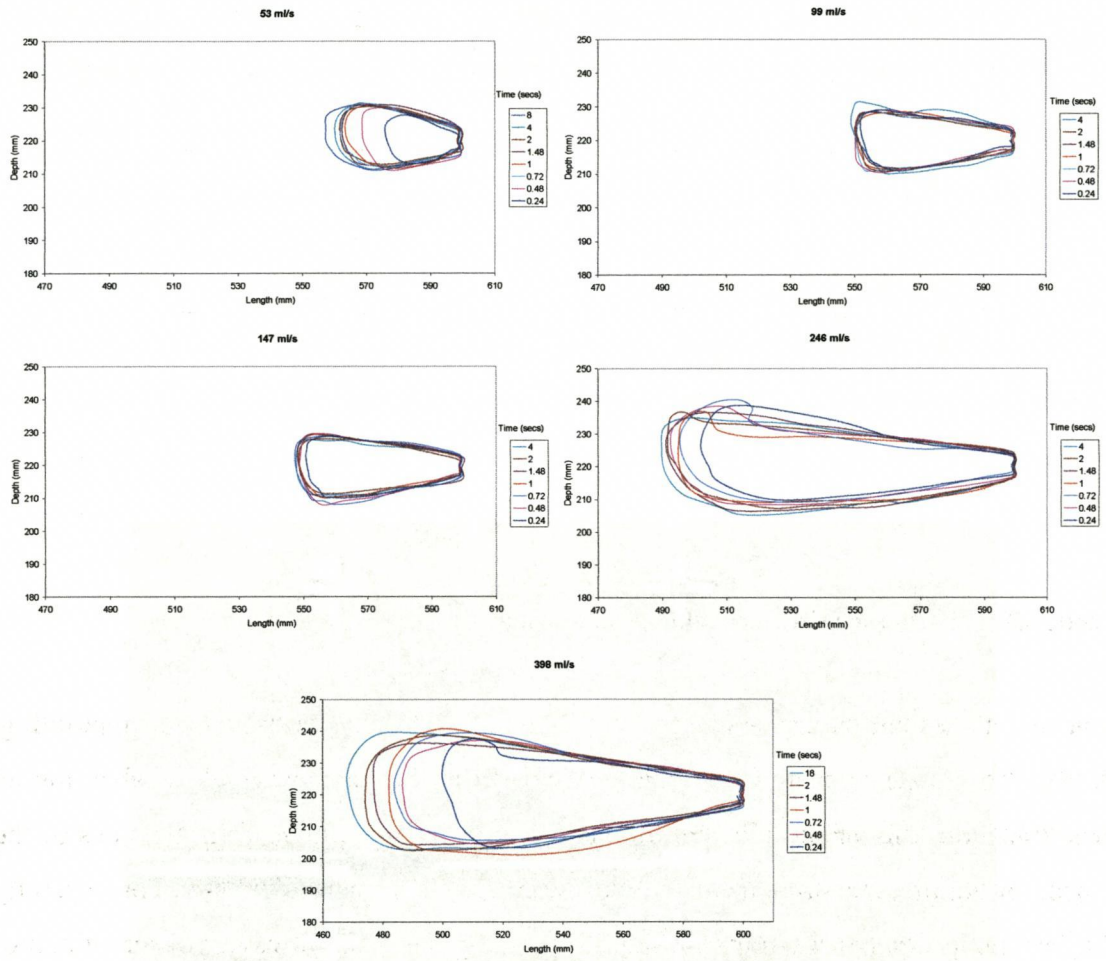

Figure 4.19 Example of typical cavity profile development in coarse sand

Both these characteristics are attributable to the hydraulic conductivity (k) of the sands. The sands with lower k values (SS & FS) created greater resistance to the permeating flow of water from the cavity, reflected by the slow advancement of the purple ring through the sand. As a result a large proportion of the jet water was contained within the

cavity, thus forcing the soil above the cavity upwards as the net flow into the cavity increased. However, the CS having a higher k value created little resistance to the permeation of water from the cavity, seen by the rapid advancement of the purple dye. Consequently only a small proportion of jet water remained in the cavity, resulting in very little soil heave.

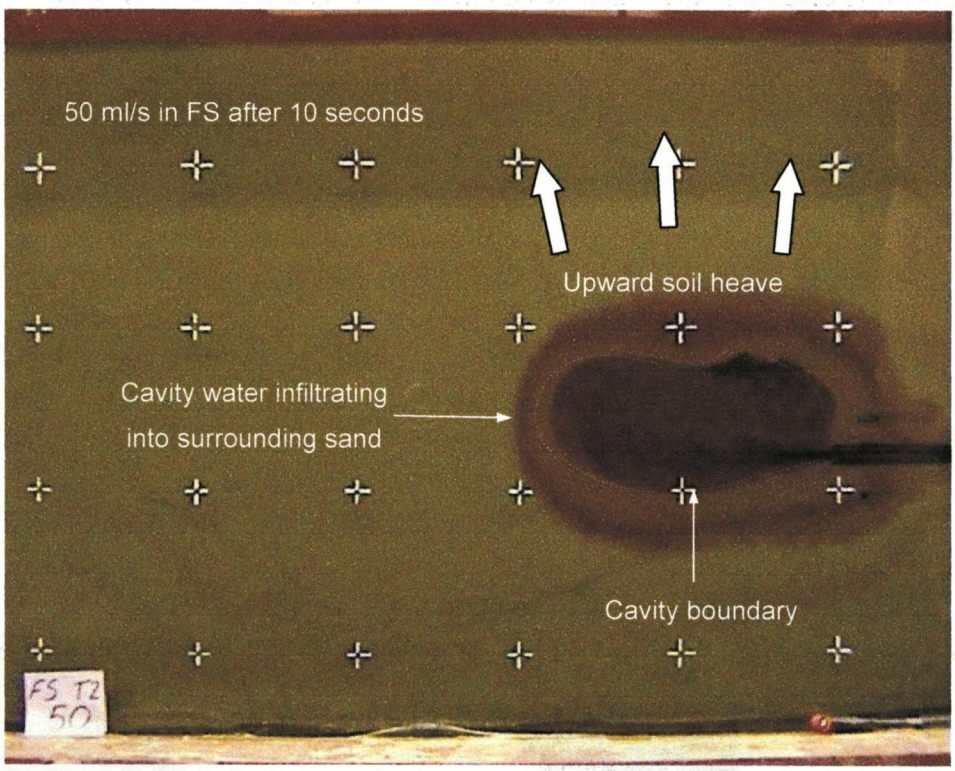

Figure 4.20 Characteristics common to all the sands

Two aspects of the experimental technique used in the clay tests were disappointing. Firstly, the nozzles appeared to partially detach from the Perspex window when the jet was turned on, this being indicated by purple water being emitted from the sides of the nozzle. Secondly, the strength of the clay was less than that anticipated, consequently the jet rapidly created fractures through to the clay surface. However, observations of the cavity development were still able to be made. The cavity growth characteristics in the saturated clay were very different to those in the sands in the following ways;

1. The initial action of the jet was to force a thin film of water between the clay and the Perspex window, detaching the two. The adhesion force of the clay to the window was thus less than its cohesion forces.

2. Within a few seconds of the initiation of the jet, fractures were formed up to the soil surface. The fractures grew slowly with time, and generally once a fracture ruptured the surface its width ceased to expand. This therefore demonstrates that the pressure of the jet forces the clay apart creating fractures through lines of inherent weakness. Upon creation of a fracture the pressure in the cavity can dissipate, reducing the separation force, thus the fracture width increases no further. Therefore, after fracture occurs, the further separation of clods becomes dominated by the flow rate.
3. Two types of erosion were noted. There was the scour of individual particles, seen in that the jet water became opaque, and the more dominate erosion of larger aggregates, seen by clods breaking off into the water flow.
4. Each test resulted in a different steady state profile being generated. The most common feature between tests was that often a wedge shaped section of clay above the nozzle was lifted upwards as the fractures formed, as shown in Figure 4.21, rather like a standard passive failure at 45 - φ/2 to soil surface, where φ is very small and the failure angle is about 40°.

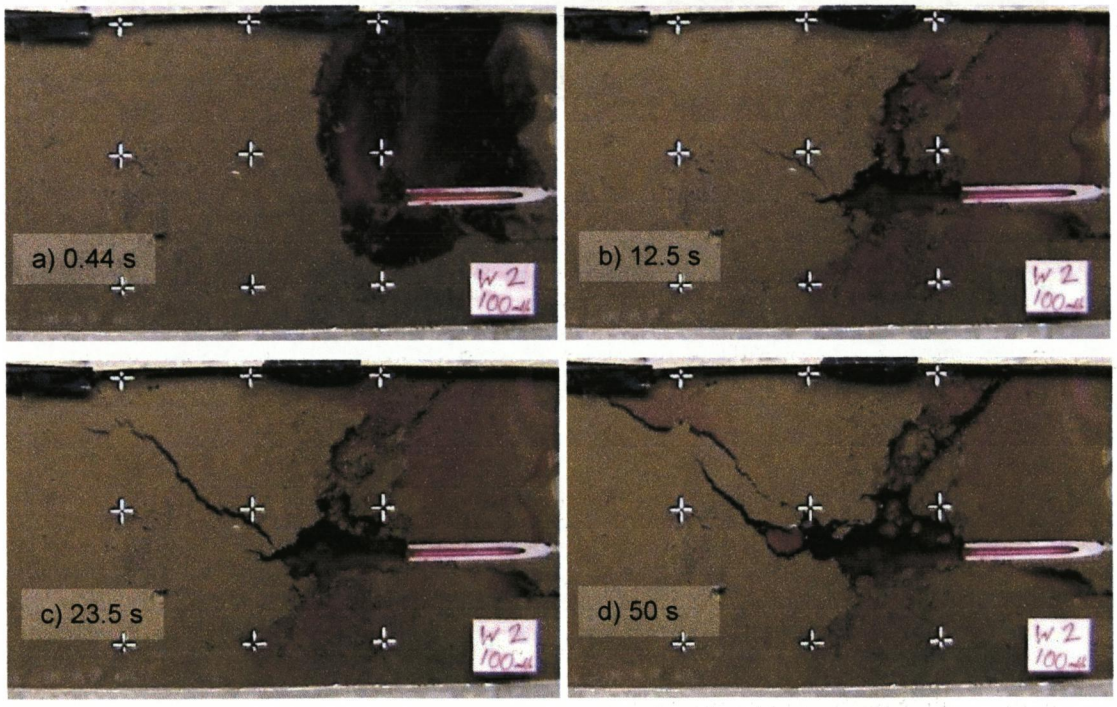

Figure 4.21 Progression of cavity development in clay (100 ml/s jet flow rate)

B. Length Characteristics

Plots of the cavity length against time for each of the jet flow rates are shown in Figure 4.22 and Figure 4.23 for the SS and FS respectively. Both data sets are similar and show the following features;

1. The growth of the cavity over the first half second was very rapid, the length reaching 30 – 50% of its final recorded length.
2. At any time, greater flow rates created longer cavities.
3. Each data set takes the form of a power curve with the equation $l = C.t^A$ where l = cavity length, t = time after the initiation of the jet, and C and A are constants depending on the flow rate.

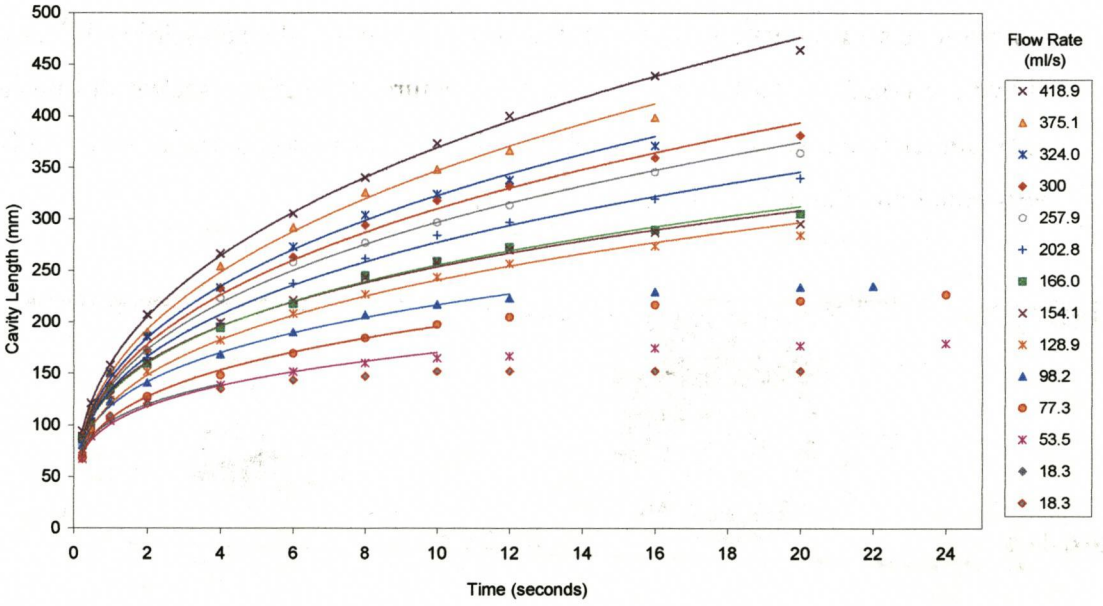

Figure 4.22 Plot of cavity length against time for each flow rates in standard sand, showing power curves fitted to the data.

A plot of cavity length against time for each flow rate in CS is displayed in Figure 4.24, which shows the following features;

1. The cavity length increased rapidly for the first 0.24 seconds, the growth rate being higher with greater flow rates.
2. After approximately 0.75 seconds the length increases very little, having reached equilibrium.

3. Higher flow rates created greater lengths, although the equilibrium lengths were not proportional to flow rates.

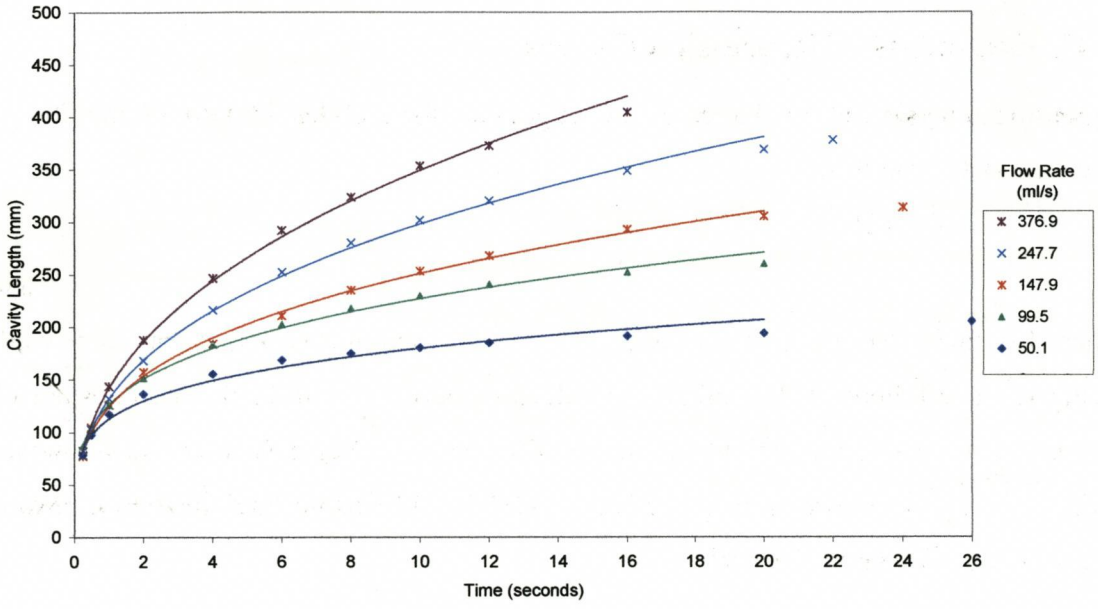

Figure 4.23 **Plot of cavity length against time for each flow rates in fine sand**

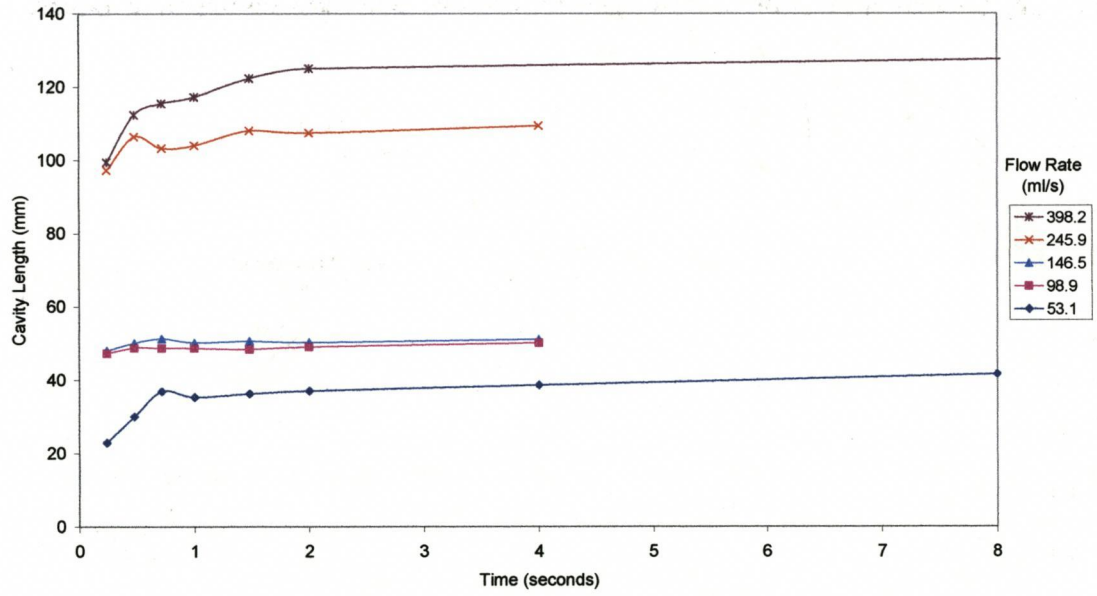

Figure 4.24 **Plot of cavity length against time for each of the flow rates in coarse sand**

When conducting tests to determine the hydraulic conductivity of the sands it was found that soil density had a significant effect on hydraulic conductivity. Any variation in soil density between tests could therefore cause the non proportionality between the length and flow rate in the CS. The 150 ml/s cavity had a similar equilibrium length to the 100

ml/s most likely because the soil density was less, with a correspondingly greater hydraulic conductivity, and consequently, a smaller equilibrium cavity.

C. Exponents of Regression Curves

Regression analysis was conducted on the length data for each test in both SS and FS. Power curves of the form

$$l = C.t^A \qquad \textbf{4.9}$$

(where l = cavity length, C = constant, t = time, A = exponent) fit the data very well having R^2 (coefficient of determination) values of between 0.98-0.99. The constant *C* and exponent *A* value for each test in SS and FS was plotted against flow rate as shown in Figure 4.25 and Figure 4.26 respectively. Data for CS was not included since power curves did not fit well to their data.

Straight lines fit well through the plots of the constant *C* values for both SS and FS data, illustrating they are a function of flow rate. Both sets of data show comparable values.

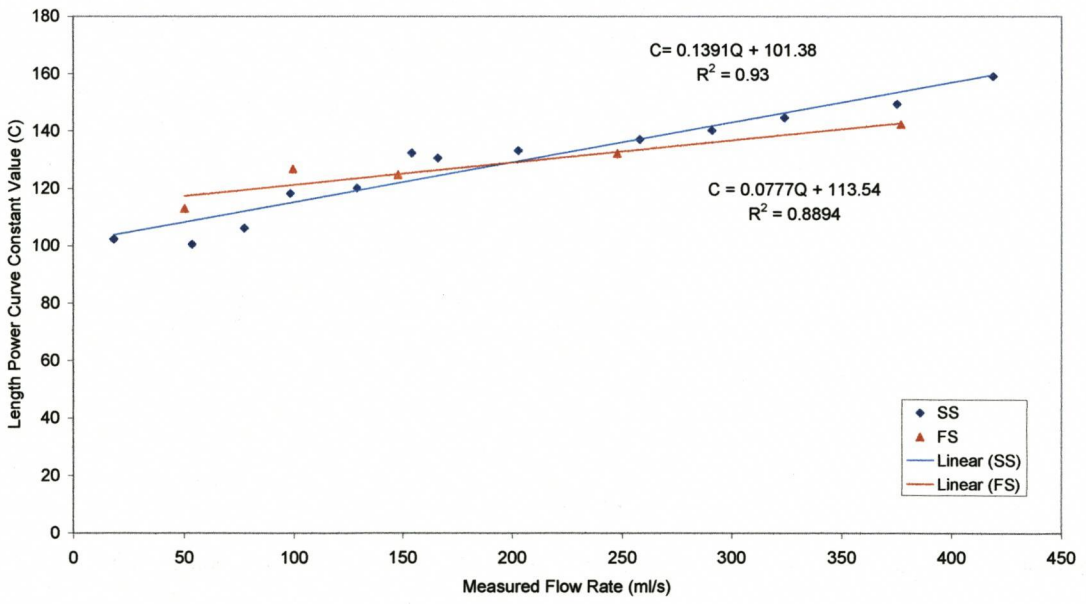

Figure 4.25 Length regression equation constant *C* values against flow rate for standard sand & fine sand

Power curves fit well through the plots of the exponent *A* values for both SS and FS data. Exponent values for flow rates in the range of 150 - 400 ml/s were between 0.3

and 0.4. This indicates that length is a function of the cavity volume, and thus jet flow rate, because if;

$$l^3 \propto V \text{ and since } V = Q.t$$

$$l^3 \propto Q.t$$

$$l^3 = \frac{Q}{B}.t \qquad \text{where } B = \text{some constant}$$

$$l = \sqrt[3]{\frac{Q}{B}.t}$$

Then,

$$l = C.t^{1/3} \qquad \textbf{4.10}$$

$$\text{where } C = \sqrt[3]{\frac{Q}{B}}$$

For the very low flow rates of 50 ml/s and below the exponent values are lower. The likely cause is that the low flow rates created cavities that initially grew until the cavity began to break upwards, at which point the velocity of the jet was insufficient to remove the excess sand entering its flow, so the cavity length then decreased.

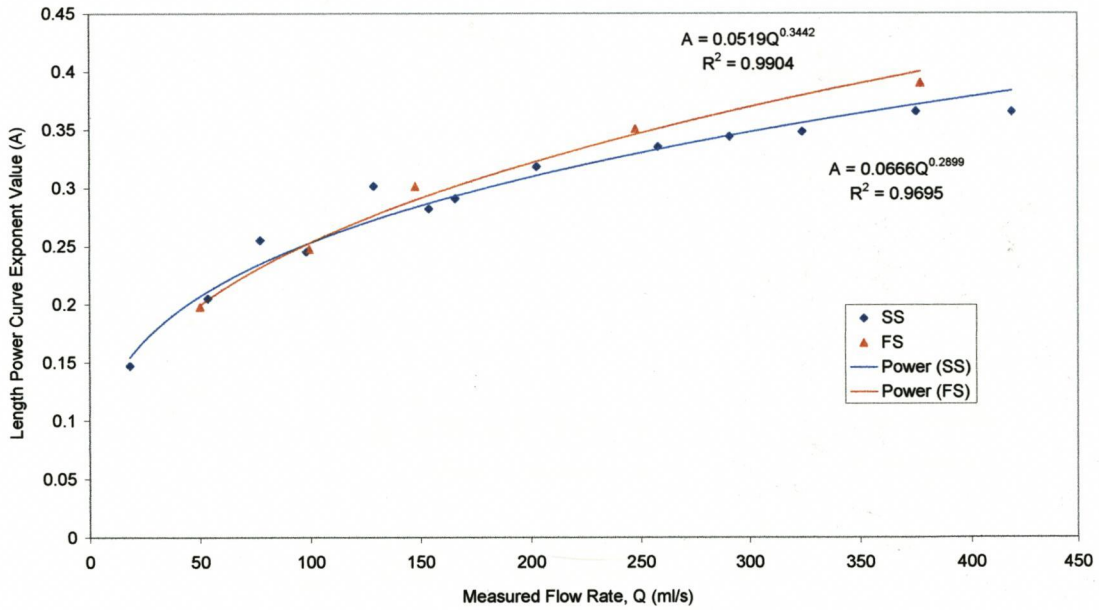

Figure 4.26 Length regression equation exponent *A* values against flow rate for standard sand & fine sand

D. Length to Depth Ratio

To examine the shape of the cavities for all three sands, the cavity depth was plotted against the length for each profile, as shown in Figure 4.27. Only profiles of the first two stages of cavity development were considered, because in growth stage three the cavity began to break up to the surface causing the depth/length ratio to change significantly. The depth/length ratio is termed *G*.

The plots of depth against length show a number of interesting characteristics about the growth and shape of the cavities. They are;

1. For all the sands the *G* ratio remained approximately constant as the length increased.
2. The data of all three sands are grouped very closely giving very similar *G* ratios.
3. A linear regression line with a gradient of 0.45 fits well through the data over the length range of 50 – 250 mm (i.e. $G = 0.45$), although not quite so good for SS above a length of 200 mm. However, at lengths exceeding 200mm the cavities had usually entered the third stage of development, giving non-representative *G* ratios. At lengths greater than 250 mm the growth rate was so slow it is of little commercial application, as mentioned previously.

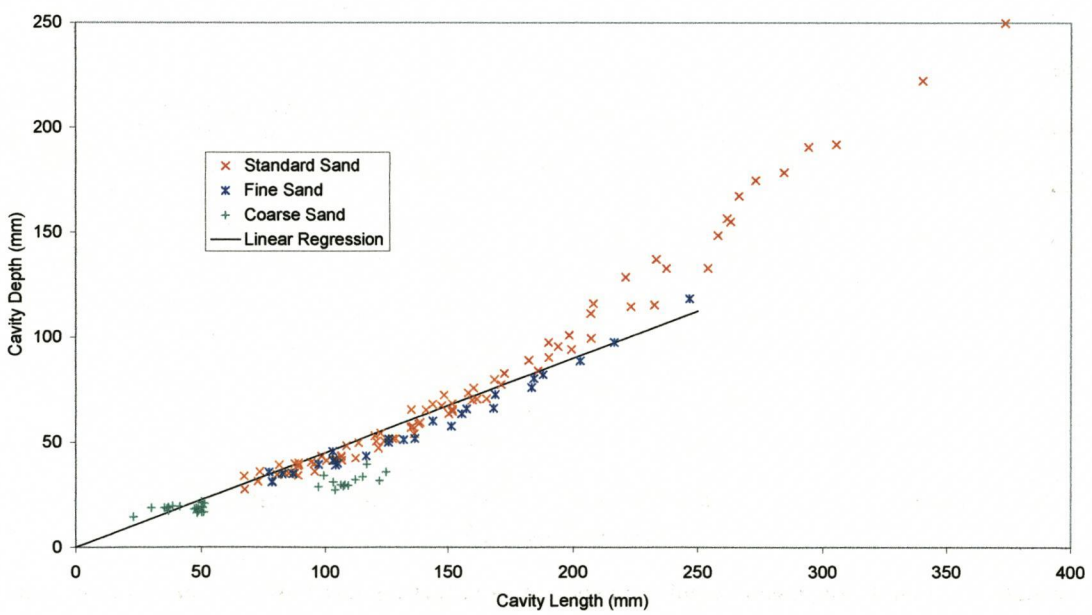

Figure 4.27 Plot of cavity depth against length for all three sands

E. Cavity Shape

The shape of the cavity was defined to enable the prediction of cavity length and depth for a given sized cavity. It was found that a composite function of a parabolic curve and straight line produced a curve that fit the cavity profiles remarkably well. The result was the following general equation;

$$y = 2\sqrt{ax} - bx \tag{4.11}$$

Where

$$a = \frac{d^2}{l} \tag{4.12}$$

$$b = \frac{2d}{l} \tag{4.13}$$

Now since

$$G = \frac{d}{l} \tag{4.14}$$

then,

$$a = G^2 l \tag{4.15}$$

And,

$$b = 2G \tag{4.16}$$

hence,

$$y = 2G\sqrt{lx} - 2Gx \tag{4.17}$$

The form of curve generated by Equation 4.17 is shown in Figure 4.28, the values of the coefficients of a and b in the Figure are not significant in this case, other than they give the correct depth/length ratio of 0.45. The cavity profile is created as the curve is rotated around the x axis.

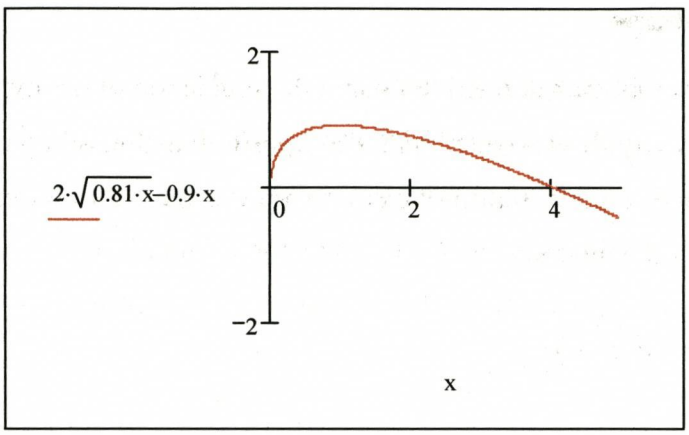

Figure 4.28 **Form of curve generated by cavity profile equation**

Figure 4.29 shows the calculated curves fit the measured curves very well for the first three seconds of the cavity development for the example profiles in SS. At four seconds the upper surface of the cavity becomes more horizontal and the shape deviates from the calculated curve. However, this is not a significant problem since only the initial stages of growth are of interest in this study.

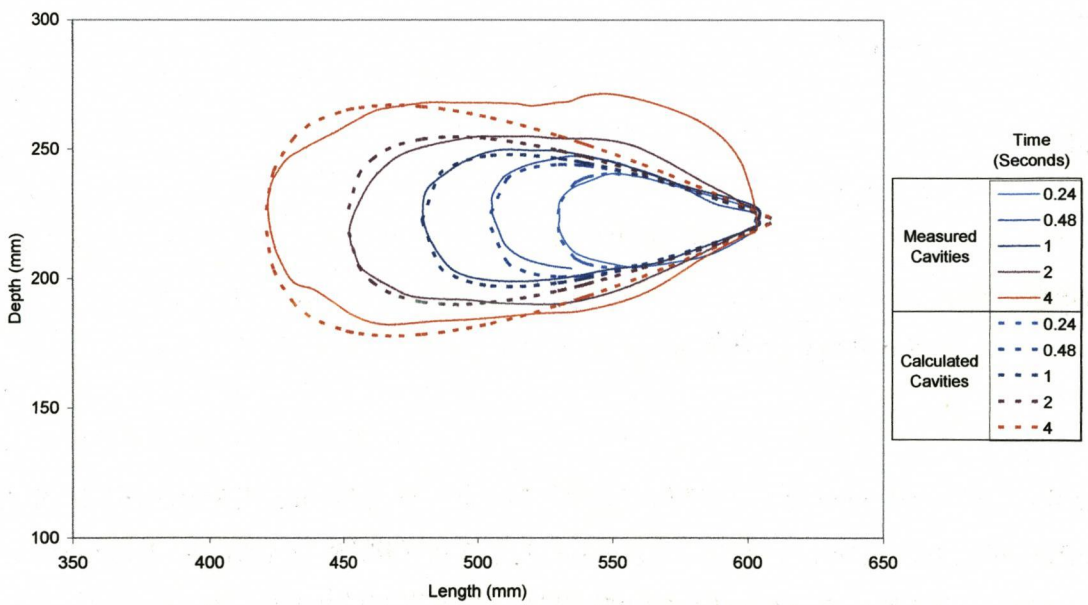

Figure 4.29 **Example comparison of calculated cavity shapes and measured cavities**

4.6.2 Uplift Forces

Full results of the uplift force experiment are in Appendix 4. Typical uplift force characteristics are shown in Figure 4.15 and Figure 4.30 for saturated and dry sands respectively. Note the force scale covers a smaller range in the dry sand graph. The general characteristics for all tests are that the force initially rose rapidly as the plate was displaced and then gradually reduced as the plate neared the soil surface.

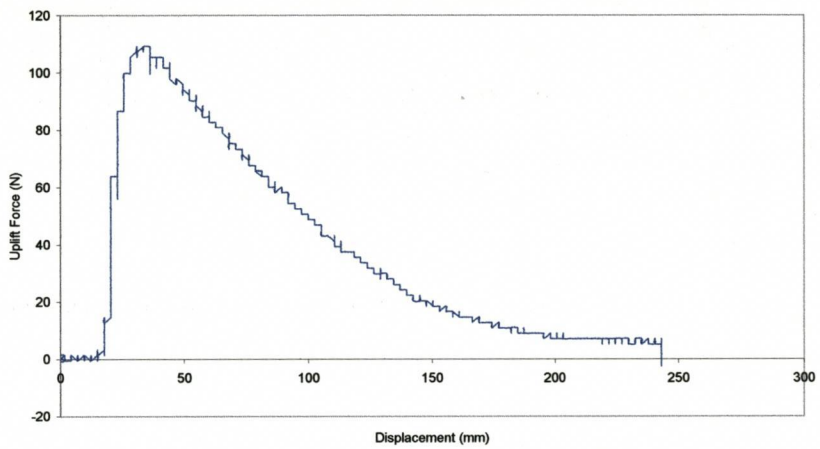

Figure 4.30 Example of uplift force characteristics in dry standard sand (test was small plate in dry sand, rep.1)

The mean force values of the three replications of each condition are plotted in Figure 4.31. The standard deviations, which are all small give confidence in the results, and are plotted with each mean. The results show that the difference between the uplift forces in dry SS and CS are small, whereas in the saturated condition the difference is large. The saturated force in the SS was in the order of six times greater than the dry force, whereas for the CS it was only marginally greater, in the order of 1.2 times.

The reason for the results found is as follows. The relatively low hydraulic conductivity of the SS created large impedance to the flow of pore water upon the dilation of the sand during shear. This caused a decrease in pore water pressure and thus an increase in effective stress and consequently a high shear strength and hence a larger uplift force. For the CS, its high hydraulic conductivity caused little impedance to the flow of pore water, causing little decrease in pore water pressure and thus a marginal increase in effective stress, with therefore little increase in shear force and uplift force for the plate.

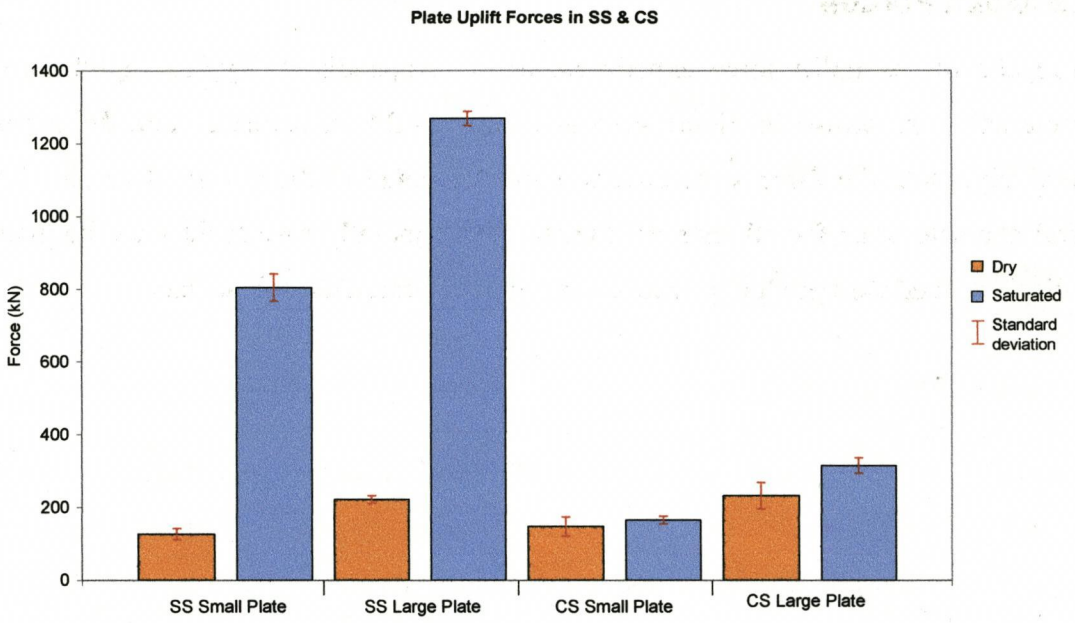

Figure 4.31 Mean uplift forces of small and large plates in dry and saturated standard sand (SS) & coarse sand (CS)

It is also worth noting that for the SS there was a large reduction in the magnitude of the uplift force between minimum and maximum displacement (being the start of shear and the plate reaching the soil surface), from 800 N to nearly zero for the small plate. However, for the CS the force difference was less. Therefore, if water pressure in a cavity beneath the soil pushed the soil upwards (instead of a plate lifting it as in the experiments),it is expected that in SS an initially high but decreasing water pressure would be required as the deformation increased. However, in CS the initial pressure would be about one quarter of t hat in the SS (shown in Figure 4.31 by the uplift force in saturated CS being about one quarter of the force in SS), and thus the reduction of water pressure with increasing deformation would be much less than in the SS. This has relevance to the modelling of cavity water pressure, in Section 4.7.

4.7 Development of Cavity Size Prediction Model

4.7.1 Concept and Development of Model

A mathematical model was developed to simulate the growth of a cavity created by a single buried water jet in saturated sand. The model, developed from an understanding gained from the above results, is based on the continuity of flow. This Section first considers the basis upon which the model is built, and then details the mathematical embodiment of it.

The model was based on the concept that the flow of water from the jet is either contained within the cavity or lost into the surrounding sand through permeation through the cavity walls. Therefore, the rate of volume increase of the cavity is equal to the net flow rate into it. The net flow rate (Q_{NET}) is the difference between the flow in (Q_{IN}) and the flow lost through the cavity walls (Q_{LOSS}). If the relationship between Q_{NET} and time is known, then the net volume of the cavity can be determined. Since the shape of the cavity has already been defined, the dimensions of a cavity can be calculated for a given volume. Therefore to determine the relationship between cavity size and time, Q_{IN} and the relationship between Q_{LOSS} and time must be known.

Considering the case where there is no permeation of jet water through the cavity walls, so Q_{LOSS} equals zero, then the following is true;

$$Q_{NET} = Q_{IN} \tag{4.18}$$

$$V_{NET} = V_{IN} = \int_0^t Q_{IN}.dt \tag{4.19}$$

$$V_{NET} = Q_{IN}.t \tag{4.20}$$

In this case the volume can easily be calculated since Q_{IN} is known and constant.

Now considering the case where jet water permeates through the cavity walls, such as in soils with larger hydraulic conductivity, the Q_{LOSS} is governed by the factors in Darcy's law of one dimensional flow. They are;

1. Q_{LOSS} is directly proportional to the surface area of the cavity (A). Since the surface area increases with time, Q_{LOSS} also increases with time.
2. Q_{LOSS} is directly proportional to the head difference (Δh) between the water in the cavity and the water at the soil surface (sea floor).
3. Q_{LOSS} is inversely proportional to the length of the flow path (L) between the cavity and the soil surface. Therefore the deeper the jet is buried under the soil surface, the less Q_{LOSS} will be.
4. Q_{LOSS} is directly proportional to the hydraulic conductivity (k) of the soil.

These are represented by Darcy's equation;

$$Q_{LOSS} = kA\frac{\Delta h}{L} \tag{4.21}$$

It is therefore true that;

$$Q_{NET} = Q_{IN} - Q_{LOSS} \tag{4.22}$$

$$V_{NET} = V_{IN} - V_{LOSS} \tag{4.23}$$

and thus;

$$V_{NET} = Q_{IN}.t - \int_0^t k.A.\frac{\Delta h}{L}.dt \tag{4.24}$$

To determine the size of the cavity when V_{NET} is known, the relationships between cavity volume and cavity length and depth must be known. However, to calculate V_{NET} the surface area of the cavity must be known. These relationships are now derived.

A. Volume of a Cavity

The volume generated by a curve is;

$$V = \int_{x_1}^{x_2} \pi.y^2.dx \tag{4.25}$$

Substituting Eq. 4.17 as y into Eq. 4.25 gives;

$$V = \int_{x_1}^{x_2} \pi\left(2G\sqrt{lx} - 2Gx\right)^2.dx \tag{4.26}$$

And solved over the cavity boundaries of $x_1 = 0$ and $x_2 = l$ gives the volume of the cavity as;

$$V = \frac{2}{15}\pi.G^2 l^3 \qquad \textbf{4.27}$$

B. Volume Length and Depth

The length of a cavity can be determined if the volume is known by rearranging Eq. 4.27 for l, giving;

$$l = \left(\frac{15V}{2\pi.G^2}\right)^{1/3} \qquad \textbf{4.28}$$

Since the volume is a function of time, Eq. 4.28 could be abbreviated to $l = Ct^{1/3}$ where C is a constant incorporating $\left(\frac{15}{2\pi.G^2}\right)^{1/3}$. This is in agreement with the power form of regression curves fit to the results of length/time data from the static nozzle, in Section 4.6.1.

The depth of the cavity can be calculated by rearranging Eq. 4.14, giving $d = Gl$, then substituting Eq. 4.28 as l, giving;

$$d = \left(\frac{15.G.V}{2\pi}\right)^{1/3} \qquad \textbf{4.29}$$

C. Surface area of cavity

It is assumed that jet water flows through the entire surface area of the cavity walls. According to Darcy's law (Eq. 4.21) the cross sectional area of flow is required to determine the value of Q_{LOSS}. The cross sectional area is assumed to be equal to the surface area of the cavity.

The equation of the cavity profile was found to be $y = 2G\sqrt{lx} - 2Gx$ (Eq. 4.17). The surface area generated by rotating this profile around the x axis is given by;

$$A = \int_{x_1}^{x_2} 2\pi . y \sqrt{1 + \left(\frac{dy}{dx}\right)^2} .dx$$

4.30

Substituting Eq 4.17 as y then gives;

$$A = \int_{x_1}^{x_2} 2\pi . \left(2G\sqrt{lx} - 2Gx\right) \sqrt{1 + \frac{G^2 l}{x} - \frac{4G^2\sqrt{l}}{\sqrt{x}} + 4G^2} .dx$$

4.31

This integral proved difficult to solve algebraically, so a numerical solution was found using a scientific calculator. The integral was then solved numerically for sixteen cavity lengths ranging from 10 mm to 310 mm, in 10 mm intervals, all having a G ratio of 0.45. A power regression curve was then fit to the results of surface area against cavity length. The regression curve was $A=1.0369.l^2$ with an R^2 value of 1. This can be closely approximated by;

$$A = l^2$$

4.32

This approximation underestimates the true theoretical surface area by 3.56%, which is insignificant since the profile equation is also an approximation of reality.

If Eq. 4.28 is substituted as l in Eq. 4.32, then the surface area is;

$$A = \left(\frac{15V}{2\pi . G^2}\right)^{2/3}$$

4.33

Further details concerning the numerical solution of the surface area are contained in Appendix 4.

D. Relationship between Volume and Time

The relationship between cavity volume and time can then be found by replacing Eq. 4.33 as A in Eq. 4.24,

$$V_{NET} = Q_{IN}.t - \int_0 k.A.\frac{\Delta h}{L}.dt \qquad (4.24)$$

giving;

$$V_{NET} = Q_{IN}.t - \int_0 \frac{k.\Delta h}{L_s}.\left(\frac{15.V_{NET}}{2\pi.G^2}\right)^{2/3}.dt$$

4.34

The variable V_{NET} is on both sides of the above equation, giving difficulty in solving it algebraically, nevertheless, a numerical solution was found. This solution was different for sands with constant Δh (CS) and variable Δh (SS & FS), although the approach is the same. Since the solution to the constant Δh case is simpler, it is dealt with first.

4.7.2 Sands with Constant Pressure Head

The experiment measuring uplift forces demonstrated that for CS the water head difference Δh would remain nearly constant during the growth of the cavity. Therefore V_{NET} remained the only time dependant variable in Eq. 4.34. The equation was then solved numerically by a process of iteration.

The solution utilised a numerical process substituting the calculated value of V_{NET} from the precedent time as the input V_{NET} on the right side of Eq. 4.34. Starting at time $t_0 = 0$ the volume is known to be zero. Then at time $t_1 = t_0 + \delta t$, V_{NET} is approximately the same as at t_0, and can be substituted as the V_{NET} required to calculate V_{NET} at time t_1. If δt is very small, then the error is small. This process is shown in the following table.

Table 4-4 **Numerical solution to V_{NET}**

	Time	V_{NET} precedent	V_{NET} dependent
t_0	0	0	V_0
t_1	δ_t	V_0	V_1
t_2	$2.\delta_t$	V_1	V_2
⋮	⋮	⋮	⋮
t_n	$n.\delta_t$	V_{n-1}	V_n

The process was executed in Microsoft Excel. An example of the first seven iterations is shown in Table 4-5 for a half jet flow rate of 100 ml/s in CS. The time increments (δt) were 0.001 seconds. The cavity length was calculated using an adjustment of Eq. 4.28 using the previous iterations V_{NET} value, being;

$$l = \left(\frac{15 V_{NET(n-1)}}{2\pi . G^2} \right)^{1/3} \qquad \textbf{4.35}$$

The cavity depth was then calculated by multiplying Eq. 4.35 by G, since $d = Gl$ (from Eq. 4.14). The blue (central) section of the Table deals with the flow rates in the cavity. To calculate Q_{LOSS} the cavity surface area is required, which was found using Eq. 4.32,

$$A = l_n^{\,2}$$

The Q_{LOSS} was then determined using Eq. 4.21,

$$Q_{LOSS} = kA_n \frac{\Delta h}{L}$$

The lavender (right hand) section of the table calculates the resulting volumes. The V_{IN} is,

$$V_{IN(n)} = Q_{IN} . t_{(n)} \qquad \textbf{4.36}$$

And V_{LOSS} is,

$$V_{LOSS(n)} = V_{LOSS(n-1)} + Q_{LOSS(n)} . \delta . t \qquad \textbf{4.37}$$

The V_{NET} for that time period is then calculated using Eq. 4.23,

$$V_{NET(n)} = V_{IN(n)} - V_{LOSS(n)}$$

This process was used to calculate the first six seconds of cavity development.

Table 4-5 Example of numerical solution to cavity development model for coarse sand

G	0.45	k	4.4 mm/s	QIN/2	100 ml/s
Time (s)	2	dh	4000 mm	QIN	200 ml/s
L (mm)	9.9	Ls	250 mm		200000 mm^3/s

Time (s)	Length (mm)	Depth (mm)	Surface area (mm^2)	Qloss (mm^3/s)	Qnet (mm^3/s)	Vin (mm^3)	Vloss (mm^3)	Vnet (mm^3)
0	0	0	0	0	200000	0	0	0
0.001	0	0	0	0	200000	200	0	200
0.002	13.3	6.0	177.2	12471.4	187529	400	12.47	387.53
0.003	16.6	7.5	275.3	19383.5	180616	600	31.85	568.15
0.004	18.9	8.5	355.3	25015.1	174985	800	56.87	743.13
0.005	20.6	9.3	425.0	29918.5	170081	1000	86.79	913.21
0.006	22.1	9.9	487.6	34325.0	165675	1200	121.11	1078.89

The values of the variables at the top of the Table were all measured except Δh. This value was not measured during the experimental work and attempts to solve it theoretically were not successful. This creates a limitation in that the model only calculates the growth characteristics with the use of empirically determined Δh values.

A curve of simulated length was plotted for each of the flow rates and suitable Δh values chosen to give best fit to the measured data. These curves are shown in Figure 4.32. The measured data of the test with 150 ml/s flow rate was not included because its length was very similar to that of the 100 ml/s test. The chosen Δh values ranged from between 2400 to 4500 mm of water head. Figure 4.32 shows that the form of the simulated lengths closely represents those of the measured data. The magnitudes are similar due to the chosen Δh values. The model therefore portrays the correct characteristics but its use is limited since the Δh values are empirically determined.

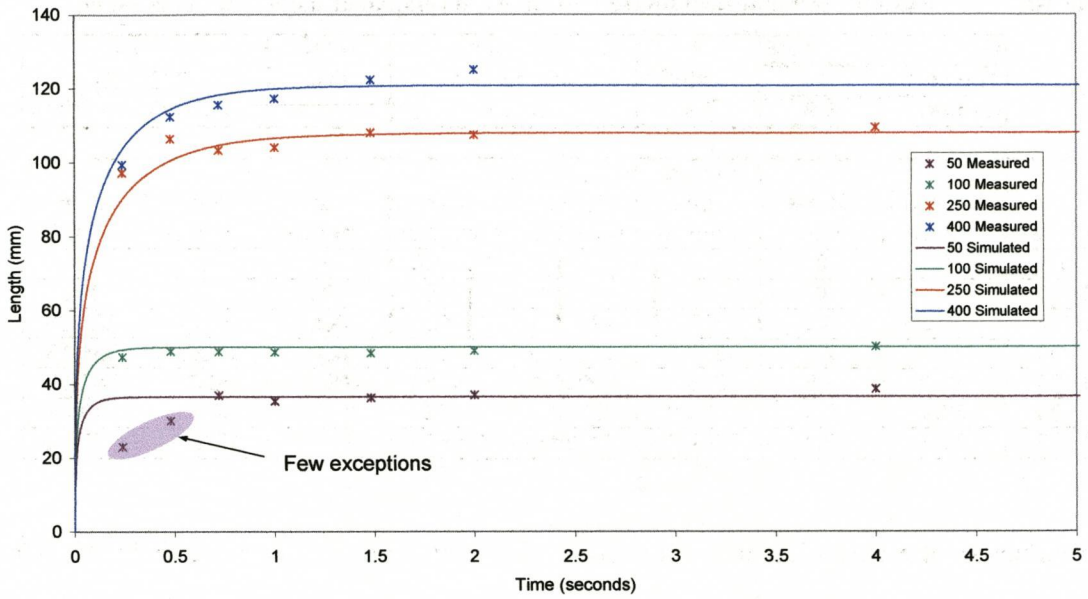

Figure 4.32 Comparison of measured and simulated cavity lengths for CS with constant Δh

4.7.3 Sands with Varying Pressure Head

The experiment measuring uplift forces demonstrated that for SS and FS the water head difference Δh would reduce during the growth of the cavity. Therefore Δh as well as V_{NET} were time dependant variables in Eq. 4.34. To solve the equation the relationship between Δh and time had to be established, as well as V_{NET} and time as in the constant Δh case. These problems were solved numerically using the same approach as the constant Δh case with an additional element included to account for the variation of Δh.

The variation in Δh was modelled by analysing the two elements that comprise Δh, being the dynamic and static head. The dynamic head is caused by the jet impinging on the rear wall of the cavity creating a stagnation pressure. The static head is generated by the weight of soil above the cavity acting on the water in the cavity. These two components of Δh, shown in Figure 4.33, are developed below.

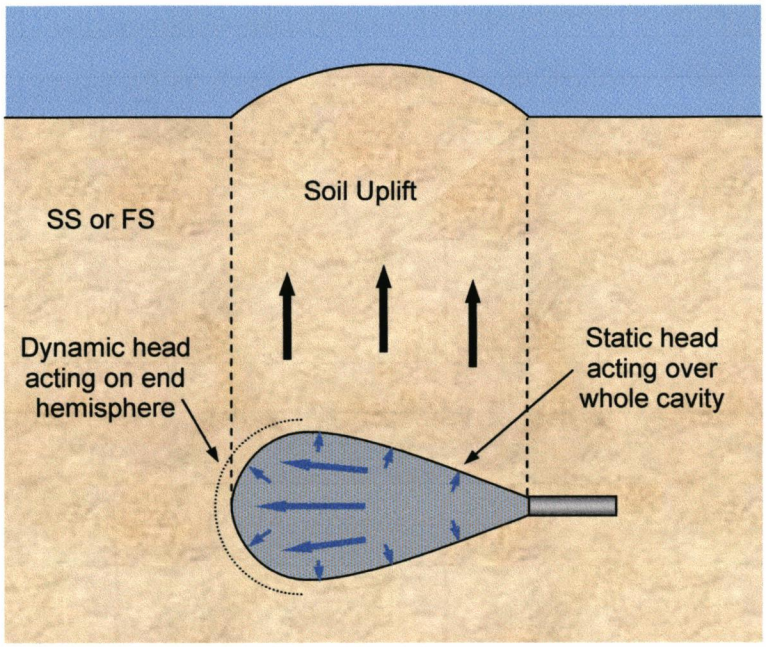

Figure 4.33 **Elements constituting the head driving water loss from the cavity**

1. Dynamic Head

The water jet impinging on the far wall of the cavity creates a dynamic velocity head as water is forced to change momentum. It is assumed that the impingement of the jet acts on the fall wall, which is approximated as a hemisphere. The pressure of the jet impinging on the far wall is;

$$P_J = \frac{F_J}{A} = \frac{Q_{IN} \cdot \rho_w . U_J}{A} \qquad \textbf{4.38}$$

The flow loss, according to Darcy's law is;

$$Q_{LOSS.DYN} = \frac{kA.\delta P_J}{L.\rho_w . g} \qquad \textbf{4.39}$$

And substituting Eq. 4.38 as P_J gives;

$$Q_{LOSS.DYN} = \frac{kA.Q_{IN} \cdot \rho_w . U_J}{L.A.\rho_w . g}$$

Thus;

$$Q_{LOSS.DYN} = \frac{k.Q_{IN} . U_J}{g.L} \qquad \textbf{4.40}$$

2. Static Head

The water in the cavity pushed the soil above it upwards as the cavity expanded. This required a certain water pressure in the cavity to overcome the shearing forces of the soil. The soil was assumed to shear vertically around the perimeter of the cavity, as shown in Figure 4.33. From the work in Chapter 3 it is known that in saturated sands as the shear rate increases so does the shear force. Therefore the higher the cavity expansion rate, the higher the shear force per unit area of shear surface. The expansion rate of the cavity is equivalent to Q_{NET}. To model this system, a similar approach was taken to that of Coyne and Lewis (1999) in their analysis of pore pressure effects on shear resistance. A detailed description of their approach is presented in Section 3.2.1. The analysis of this system is then as follows.

The weight of soil above the cavity is;

$$P_s = \gamma_s . L$$

4.41

The weight density is increased to an apparent weight density by the pore pressure effects as the soil shears. The pore pressure gradient was analysed in the following way.

The plan area of the cavity is given as;

$$A = \int_0^l 2G\sqrt{lx} - 2G.x.dx$$

$$A = \left[\frac{4}{3}G.l^{0.5}x^{1.5} - G.x^2\right]_0^l$$

$$A = \frac{4}{3}G.l^2 - G.l^2$$

$$A = \frac{1}{3}G.l^2$$

4.42

Assuming a uniformly distributed volumetric strain ε_v, void volume is generated at the rate;

$$Q_m = Q_{NET} . \varepsilon_v$$

4.43

Therefore the pore water velocity is;

$$U_m = \frac{Q_m}{A} = \frac{3.Q_{NET}.\varepsilon_v}{G.l^2}$$

4.44

A profile of the velocity with depth is therefore;

$$U_p = \frac{3.Q_{NET}.\varepsilon_v}{G.l^3}.\left(\frac{y}{L}\right)$$

4.45

Now from Darcy's law;

$$U_m = k.\frac{dh}{dy}$$

4.46

And since $dh = \frac{dP}{\gamma_w}$, then;

$$U_m = \frac{k}{\gamma_w}.\frac{dP}{dy}$$

4.47

Therefore the pressure gradient is;

$$\frac{dP}{dy} = \frac{U_m.\gamma_w}{k} = \frac{3.Q_{NET}.\varepsilon_v.\gamma_w}{k.G.l^2}.\left(\frac{y}{L}\right)$$

4.48

So the average pressure gradient is;

$$\left(\frac{dP}{dy}\right)_{AVG} = \frac{3.Q_{NET}.\varepsilon_v.\gamma_w}{k.G.l^2}.\left(\frac{L/2}{L}\right)$$

$$\left(\frac{dP}{dy}\right)_{AVG} = \frac{3.Q_{NET}.\varepsilon_v.\gamma_w}{2.k.G.l^2}$$

4.49

The pore pressure gradient increases the apparent weight density of the soil to;

$$(\gamma_s)_{EFF} = \gamma_s + \left(\frac{dP}{dy}\right)_{AVG}$$

$$(\gamma_s)_{EFF} = \gamma_s + \frac{3.Q_{NET}.\varepsilon_v.\gamma_w}{2.k.G.l^2}$$

$$(\gamma)_{EFF} = \gamma_s.\left[1+\frac{\gamma_w}{\gamma_s}.\frac{3.Q_{NET}.\varepsilon_v}{2.k.G.l^2}\right]$$

4.50

$$(\gamma)_{EFF} = \gamma_s.N_{PORE}$$

4.51

Then substituting Eq. 4.50 as γ_s into Eq. 4.41, the soil pressure then becomes;

$$P_s = \gamma_s.L.\left[1+\frac{\gamma_w}{\gamma_s}.\frac{3.Q_{NET}.\varepsilon_v}{2.k.G.l^2}\right]$$

4.52

$$P_s = \gamma_s.L.N_{PORE}$$

4.53

The flow loss, from Darcy's law, through the cavity wall driven by the static head is therefore;

$$Q_{LOSS.STAT} = \frac{kA.dP}{L.\gamma_w}$$

And substituting Eq. 4.53 as P gives;

$$Q_{LOSS.STAT} = k.A.\left(\frac{\gamma_{sb}}{\gamma_w}\right).N_{PORE}$$

4.54

The total flow loss from the cavity is then;

$$Q_{LOSS} = Q_{LOSS.DYN} + Q_{LOSS.STAT}$$

4.55

The numerical solution to determine the cavity length and depth was found using the same process as that used for sands with constant head, detailed in Section 4.7.2. Equations 4.35 to 4.37 were used, with Eq. 4.55 being substituted for Q_{LOSS} in Eq. 4.37. An example of the first seven iterations is given in Table 4-6, showing the calculations of length and depth for a half jet flow of 375 ml/s in SS.

The variables at the top of the table were measured or calculated values, with the exception of ε_v whose value was estimated as 0.2. Greater values caused the N_{PORE} factor to oscillate significantly between large positive and small negative numbers.

Table 4-6 Example of numerical solution to cavity development model for standard & fine sand with variable h

	Time (s)	0.003	k	0.27 mm/s		Qin/2	375.0 ml/s		V1	26525.8238 mm/s	
	L (mm)	11.9	rho s	1.60E-06 kg/mm^3		Qin	750 ml/s		Ls	250 mm	
	G	0.45	rho w	1.00E-06 kg/mm^3		Qin	750000 mm^3/s		Ev	0.2	
Time (s)	Length (mm)	Depth (mm)	Surface area (mm^2)	Q.loss.dyn	Npore	Q.loss.stat	Qloss	Qnet (mm^3/s)	Vin (mm^3)	Vloss (mm^3)	Vnet (mm^3)
0	0	0	0	2190.2	1.00	0.0	2190.2	747809.8	0	0.0	0.0
0.001	20.66	9.30	426.76	2190.2	2705.15	498724.2	500914.4	249085.6	750	2.19	747.81
0.002	22.74	10.23	516.92	2190.2	744.62	166280.4	168470.6	581529.4	1500	503.10	996.90
0.003	26.50	11.92	702.22	2190.2	1278.98	387989.7	390179.9	359820.1	2250	671.58	1578.42
0.004	28.38	12.77	805.25	2190.2	690.57	240228.0	242418.2	507581.8	3000	1061.76	1938.24
0.005	30.66	13.80	940.32	2190.2	834.02	338794.1	340984.3	409015.7	3750	1304.17	2445.83
0.006	32.29	14.53	1042.43	2190.2	606.51	273127.5	275317.7	474682.3	4500	1645.16	2854.84

A comparison of measured and simulated lengths is shown in Figure 4.34 for five of the flow rates in the SS, and Figure 4.35 for the FS.

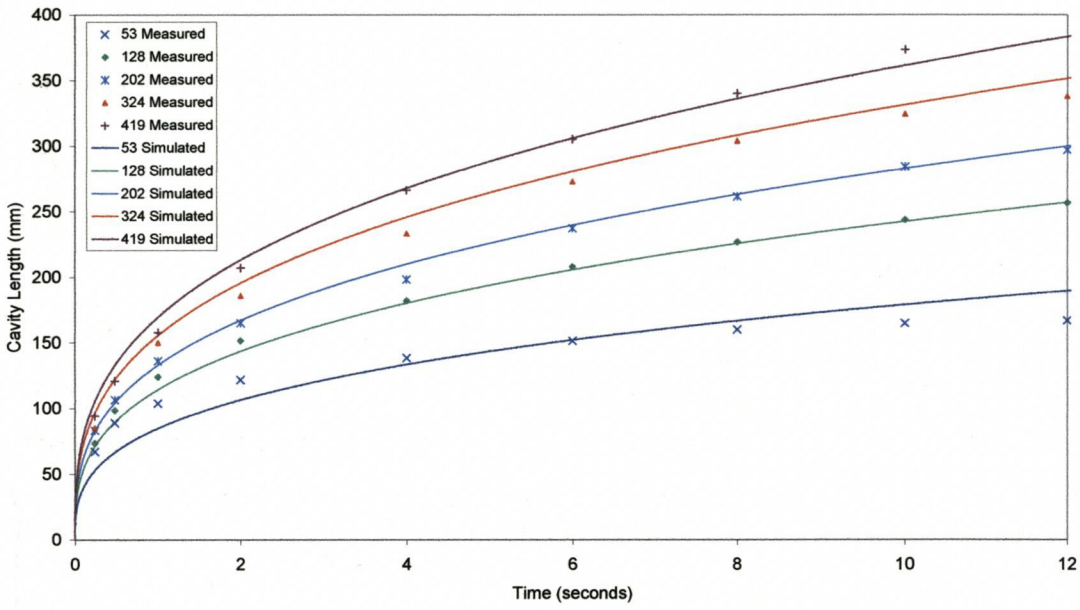

Figure 4.34 Comparison of measured and simulated cavity lengths for standard sand with variable Δh

The simulated curves fit very well to the measured data for the SS, and slightly less well for the FS over the time range displayed. The lowest flow rate in the SS fits least well to the data, especially over the first two seconds. For the FS the simulated curves of the high and low flow rates over or underestimate, respectively, the measured lengths for the first four seconds

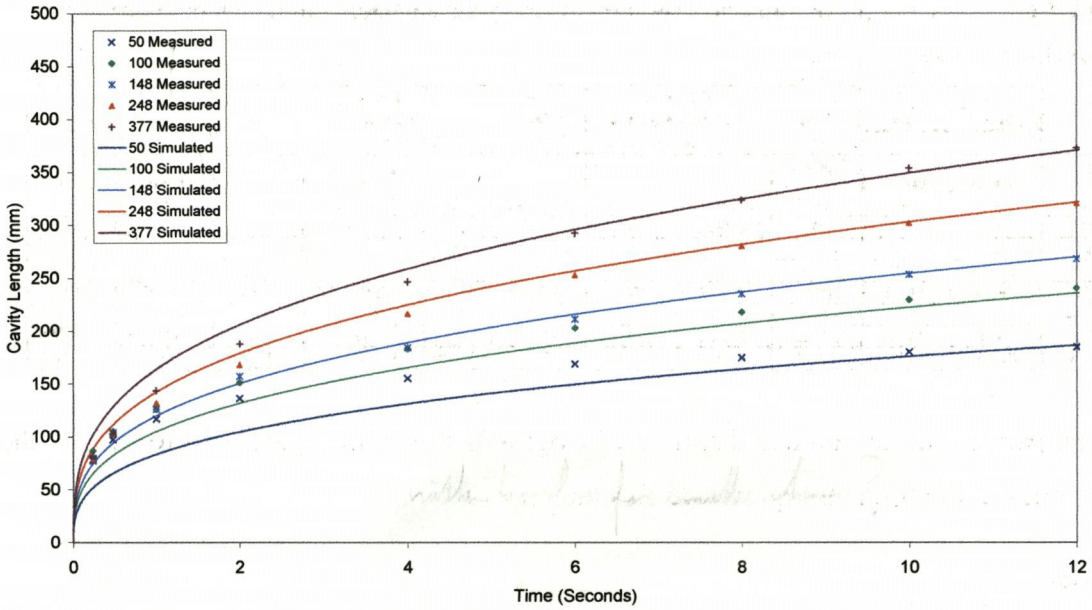

Figure 4.35 Comparison of measured and simulated cavity lengths for fine sand with variable Δh

4.7.4 Limitations of the Model

It was encouraging that the developed model correlated well with the static results for all three sand types, as long as an appropriate ε_v value was used for the standard sand and fine sand, and an h value used in the coarse sand. However, the approach of the flow conservation model and the degree to which it simulates the sands gives rise to the following comments.

1. The model does not consider the strength of the soil. A weak soil would behave differently to a strong soil even if the hydraulic conductivity were the same.
2. The model is based on the cavity shape being symmetrical. However, after about 4 seconds the cavity becomes asymmetric. This affects the relationship between cavity volume and length. Nevertheless, it appears that this does not have a major effect on the model, since there is no sudden step in the curves of measured length against time at the point where the cavity becomes asymmetric. This gives rise to the question as to why the flow continuity model fits the length curves even though it assumes a constant and symmetrical cavity shape.
3. The length/depth ratio (G) of the cavity in the coarse sand was slightly less than in the finer sands, i.e. the divergence angle of the jet was less in the coarse sand.

This was no doubt due to the particle weight of individual grains being greater for the coarse sand, and thus a higher jet velocity was required to detach them. However, the model assumes a uniform cavity shape regardless of the sand size. This highlights the fact that the model does not account for the mechanism by which the soil is eroded from the cavity walls, but assumes the erosion mechanism causes a fixed cavity shape. This is not the case in reality and the problem remains as to how to simulate the erosion mechanism within the cavity, having turbulent and complex dynamics.

4. The model has limitations for the design engineer because it uses empirically determined values of ε_v for the standard and fine sands, and h values for the coarse sand.
5. The principle of continuity of flow does not apply so readily to the case of a dynamic nozzle. In the static case the cavity is closed and water can only escape through the cavity walls. In the dynamic case this does not apply, since water can also be lost through the open rear neck of the cavity. This affects the hydrostatic pressure of the water in the cavity as well as the flow regime and volume calculations.
6. It is of interest that other researchers have not used a flow continuity approach in similar fields and the question arises as to whether the continuity of mass is the correct hypothesis to use. Other researchers who have looked at the effects of an external (non-buried) impinging jet on sands have taken a dimensional analysis approach or a semi-theoretical approach in considering some of the properties of jet velocity decay with distance from jet source, velocity required for particle scour, ratio of soil to water densities and the Froude number (as discussed in Section 4.2). A difficulty with this work is that the highly turbulent and complex flow within the cavity is very complicated to model. To consider jet velocities at the cavity boundary would be complex. It is considered therefore that a different approach, based on momentum, would be more suitable to the modelling of the cavity created by a dynamic nozzle and this is developed in the next Chapter.

4.8 Conclusions

1. The effect of soil type (sand or clay) on the cavity development was that;
   a) A significant difference existed between the development characteristics of a cavity created by a static half nozzle in sands and clay. In sands the development was characterised by erosion and continuity of flow, whereas in clay it was characterised by soil fracturing created by the jet pressure.

2. The cavity development in the sands was characterised by the following;
   a) Four distinct growth stages were recognised in the development of cavities in standard and fine sands. The coarse sand differed in that it was characterised by only two distinct stages. Understanding of the mechanics of each stage was gained.

   b) Cavities in the larger particle sand (coarse sand) were smaller than those in the smaller particle sands (standard and fine sands).

   c) Water permeated into the soil from the cavity, the permeation rate being dependant on the hydraulic conductivity (k) of the soil, which is influenced by the sand particles size. The head of water driving the flow loss varied with cavity size in the standard and fine sands but remained nearly constant with cavity size in the coarse sand.

   d) The profile of the cavity was approximated by the curve;

$$y = 2G\sqrt{lx} - 2Gx \qquad 4.17$$

   Where;

   G = Depth / Length ratio of cavity

   l = Cavity length

   x = Distance from nozzle

3. A mathematical model was developed to simulate the growth of a cavity created by a static jet nozzle in sands.
   a) The following equations summarise the model.

      Cavity length (l) is given as;

$$l = \left(\frac{15 V_{NET}}{2\pi . G^2} \right)^{1/3} \qquad 4.28$$

Cavity depth as;

$$d = G.l \qquad 4.14$$

Where;

$$V_{NET} = Q_{IN} . t - \int_0^t \frac{k.\Delta h}{L_s} . \left(\frac{15 . V_{NET}}{2\pi . G^2} \right)^{2/3} . dt \qquad 4.34$$

b) Numerical solutions were found for the above equations. For the standard sand and fine sand a variable head (h) value was incorporated, and for the coarse sand a constant head. The model fitted the data well when using appropriate values of ε_v for the standard and fine sands and of h for the coarse sand.

c) The model has limitations in that true values of ε_v and h are unknown. The flow continuity approach upon which the model is based does not transfer to the case of a buried dynamic nozzle.

5 Investigation into the Cavity Created by a Buried Dynamic Horizontal Jet

5.1 Introduction

The two investigations using jetted tines described in Chapter 2 made it clear that the role of the jets in reducing soil forces was to fluidise a section of soil which effectively eliminated the soil stress on the corresponding section of the tine face. In order to predict the jet induced force reduction, the section of soil fluidised by a buried jet moving through the soil must be determined, so the associated passive soil stress of the section may be calculated.

The purpose of this Chapter is to develop a method of determining the extent of the fluidised section created by a buried dynamic jet. This was accomplished in three stages, outlined in the objectives below.

A review of relevant literature is given in Section 4.3 of the previous Chapter.

5.2 Objectives

The objectives of this Chapter are;

1. To conduct an experiment to enable the examination of the extent of the fluidised soil generated by a single dynamic jet buried in saturated sand, in order to gain an understanding of the jet scour characteristics and the size of the fluidised cavity when in dynamic equilibrium.
2. To combine knowledge gained from both the dynamic and static nozzle experiments to develop a mathematical model simulating the extent of the fluidised cavity.
3. To evaluate the model by comparison of measured and simulated values.

5.3 Methodology and Experimental Design

To fulfil the first objective, an experiment using a dynamic nozzle was designed. Experiments were conducted in the standard sand (SS), as used in all the preceding experiments. The experimental program was designed in which ten nozzle velocities (U_n) were examined. The range of velocities was designed to cover a broad range of the jet centreline velocity of the cavity boundaries (U_b) calculated from the cavity length/time data from the static nozzle experiments, in Section 4.6.1. The designed velocities were from 10mm/s to 100 mm/s increasing in steps of 10 mm/s.

A constant jet flow rate, designed to be 200 ml/s, was maintained throughout the tests. This value was chosen for two reasons. Firstly it was the mid range of the flow rates tested in the Static Nozzle Experiment. Secondly, the range of U_b velocities generated by that flow rate in the Static Nozzle Experiment matched the range of U_n velocities achievable with the experimental equipment (shown in Figure 5.7).

Since the purpose of the experiment was to establish the mathematical relationship between cavity size and nozzle velocity, the available tests were deployed to maximise the number of U_n values used rather than replicating a fewer number of velocities. The ten velocities were tested in a random order, with only one replication of each velocity. The cavity profile was analysed at thirteen nozzle positions for each test.

5.4 Equipment and Measurement Technique

5.4.1 Equipment

A half nozzle of 3 mm radius, positioned against a glass window, was connected to a hydraulic ram that drove the nozzle forward through the soil. A diagram showing details of the nozzle unit is given in Figure 5.1. The hydraulic ram was mounted on a frame connected to the tank. A steel shaft, mounted through a brass bush in the side of the tank, connected the nozzle to the ram. The hydraulic ram was driven by an electrically powered hydraulic motor unit. The sand tank was the same one used in the Static Nozzle Experiment. It had been modified to receive the steel shaft, and an extra 20 mm thick glass sheet was added to the inside of the glass window to act as a spacer

between the original window and the nozzle. The refractive index of the thickened window was determined by measurement of the angles of incidence and refraction of a laser beam shone through the window, full details being given in Appendix 3. A video camera was positioned in front of the tank window to record the action of the jet. A diagram of the equipment setup is given in Figure 5.2.

The plumbing system and equipment were also the same as that used in the Static Nozzle Experiment, with the exception that the attachment of the hose to the nozzle was more robust. The water flow rate and pressure were measured in an identical manner to that of the Static Nozzle Experiment.

The same instrumentation system was used as in the Static Nozzle Experiment (see Section 4.4.1), with the addition of a string pot potentiometer to measure the displacement of the hydraulic ram.

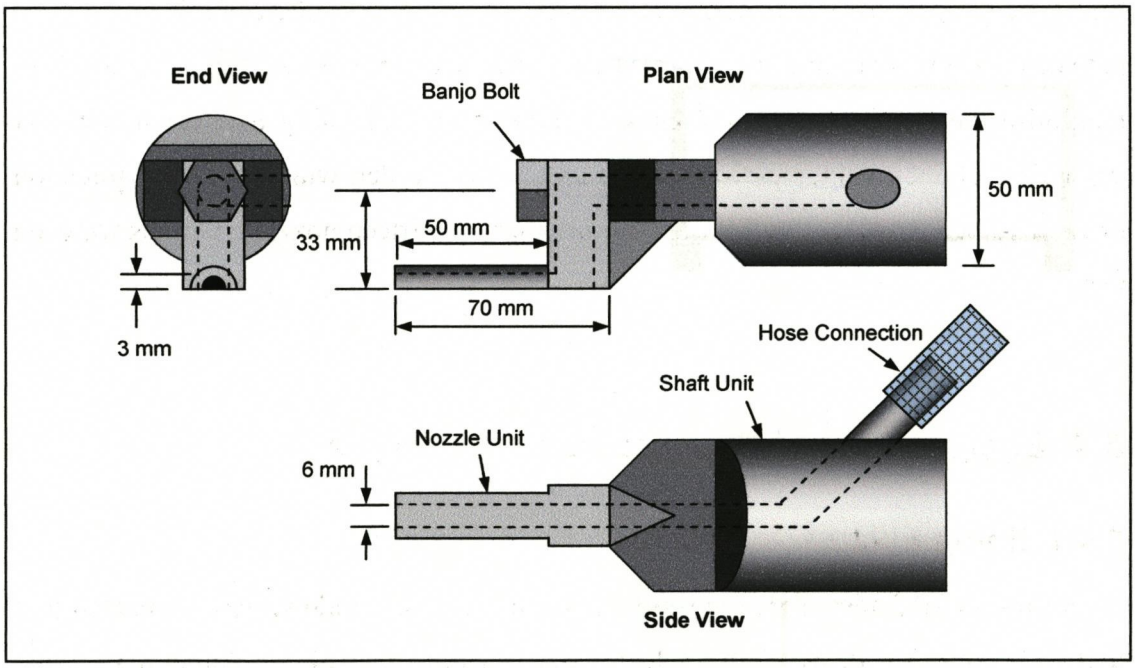

Figure 5.1 Details of the dynamic nozzle, the end of the connection shaft and their plumbing system

5.4.2 Measurement Technique

The measurement technique was very similar to that of the Static Nozzle Experiment, and was as follows.

1. The sand was prepared by the same technique as in the previous experiment.
2. The water pump, hydraulic pump and dye were started and the laptop computer and video were set to record.
3. After a few seconds the LED and nozzle flow were turned on simultaneously.
4. When the jet was flowing freely, the test was conducted, the nozzle being pushed forward through the soil by the hydraulic ram at the required velocity.
5. After the end of the test, the nozzle velocity was set to that required for the next test, before the soil was prepared again.

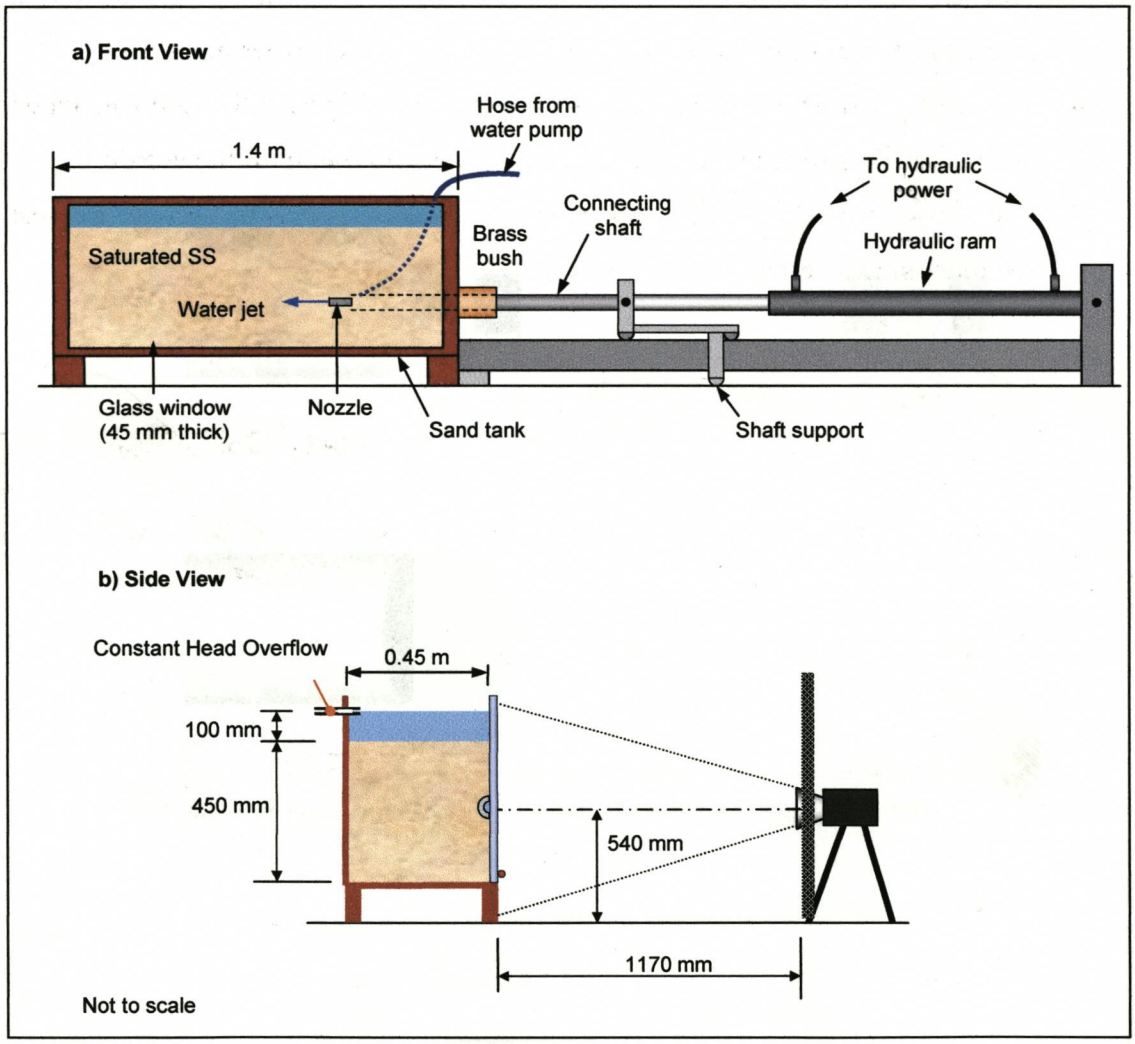

Figure 5.2 **Diagrams of the equipment setup for the dynamic nozzle experiment**

5.4.3 Measurement Analysis

The video of each test was analysed in a manner similar to that for the Static Nozzle Experiment. The processes are described below, with more detail on the processes specific to this experiment.

1. The video was captured onto a computer.
2. The video was viewed on VirtualDub software on the computer. Frames were then extracted from the video at 50 mm intervals along the experimental length at the positions shown in Figure 5.3, giving thirteen frames per test section. The frames were saved in Bitmap format.
3. The process of assigning a coordinate reference system, performing an optical correction, digitizing each profile by drawing a polyline around each cavity profile in Erdas Imagine software, then exporting the profile coordinates into a Microsoft Excel spreadsheet was the same as the earlier experiment.
4. The length and depth of each cavity (as defined in Figure 5.6) were calculated and the profiles for each test were plotted relative to the tip of the nozzle.
5. The mean of the flow rate (Q_{IN}), pressure (P) and U_n was taken over the test section, using Microsoft Excel software.

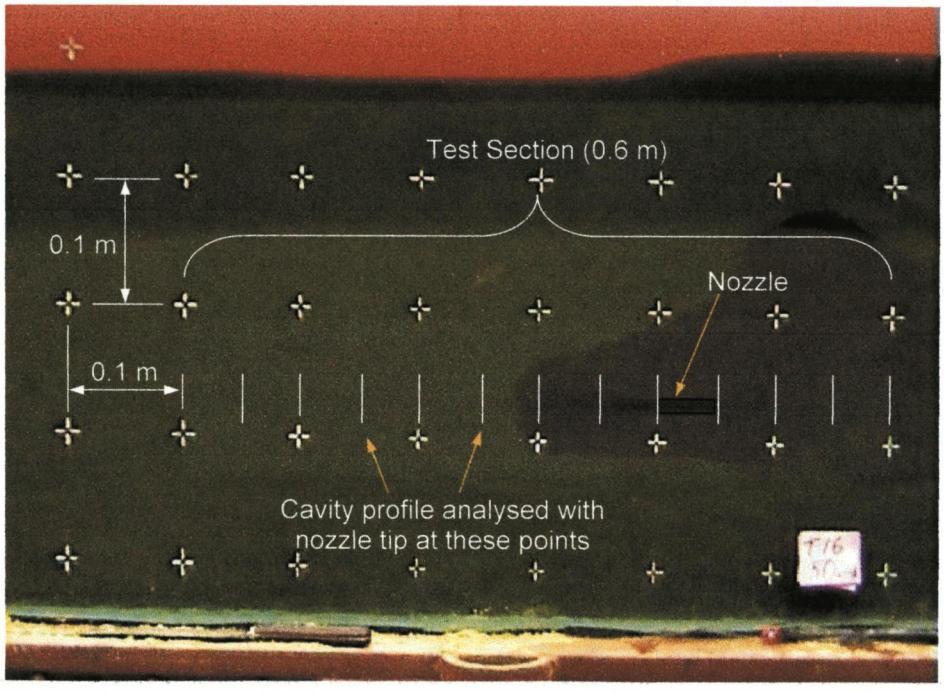

Figure 5.3 Test section in sand tank for dynamic nozzle tests

5.5 Results and Interpretation

The results of nine of the ten tests are presented and discussed below. One of the experiments was not analysed because the flow rate was incorrect. Full results of the experiments are contained in the Appendix 4.

5.5.1 Cavity Profile Shape

The development of the cavities created by the jets progressed through three or four stages, depending on the nozzle velocity. Examples of the typical stages are shown in Figure 5.4 and are described below;

1. The stage of static imbalance, prior to the start of the test, where the nozzle remained stationary yet the cavity grew. At the start of the test the nozzle was stationary until the jet flow was steady, resulting in the formation of a cavity within the soil.
2. The stage of dynamic imbalance, where the nozzle velocity was greater than the cavity boundary velocity ($U_n > U_b$), because the cavity size created during the first stage was greater than that sustainable with a dynamic nozzle. Therefore the dimensions of the cavity boundary reduced.
3. The stage of dynamic equilibrium, where the nozzle velocity equated to the boundary velocity ($U_n = U_b$), so the cavity dimensions remained constant. For the higher velocity nozzles the neck of the cavity adjacent to the nozzle, reduced in size considerably as the displacement of the nozzle, and thus the flow path of the water, increased. This caused a high velocity flow of water through the neck.
4. The cavity of the highest velocity nozzle (100 mm/s) entered into a fourth stage, where the cavity neck closed completely and the cavity size reduced, becoming smaller than its dynamic equilibrium size. This only occurred as the nozzle neared the end of its run.

The reason for the reduction of the cavity neck with increasing nozzle displacement for the faster nozzles was likely to be due to two effects either singly or in combination. Firstly, as the nozzle displacement increased, so too did the flow path length for water from the jet back to the ruptured soil surface above the initial starting

point of the cavity. The increased flow path length resulted in an increased volume of sediment transported at any moment in time, thus requiring a greater energy input. There is, therefore, a stage where the rate of eroded sediment entering the flow path is greater than can be transported by the energy of the jet, causing the neck of the cavity to close. This occurred first with the highest velocity nozzle since it required the greatest rate of sediment transport. It could also be argued that the shaft immediately behind the nozzle obstructed the flow, causing energy losses and redirecting the flow path around it. The results may arise from the combined effect of both of the above effects. However, the reduction of the cavity neck with increasing nozzle displacement is not a concern of this study, since in commercial situations the nozzles are fixed to an implement that remains stationary relative to the nozzle, thus the flow path remains of near constant length.

The analysis was only concerned with the third stage, that of dynamic equilibrium. Therefore, of the thirteen cavity profiles digitized from each test, only between seven and eleven profiles were analysed from each experiment.

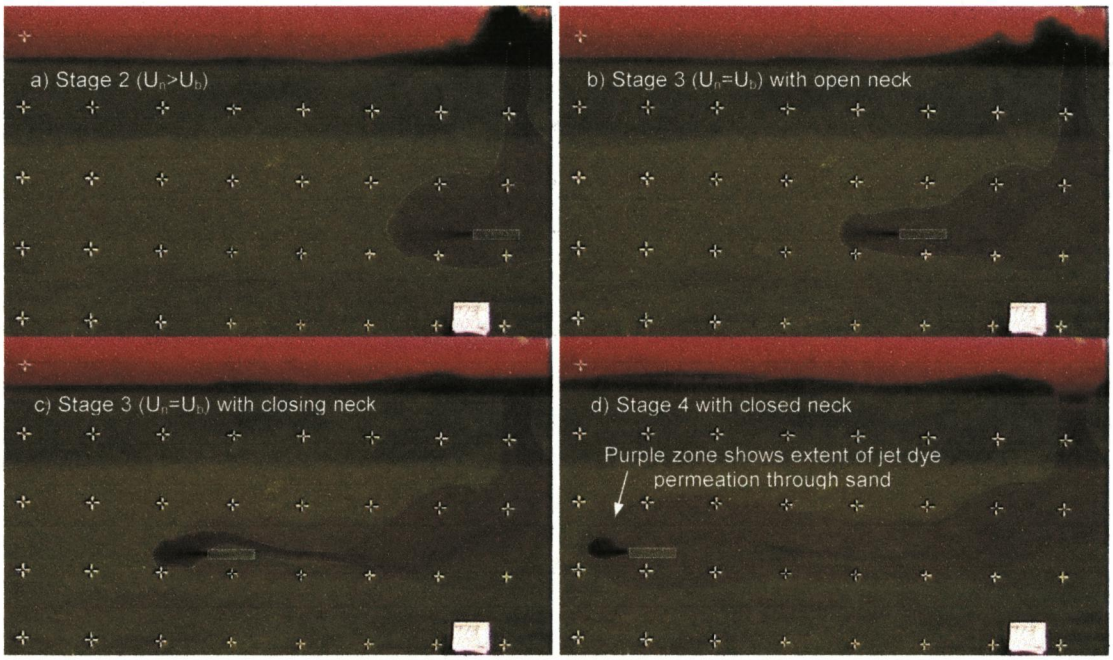

Figure 5.4 Progression of cavity profile through stages 2 to 4, for 100 mm/s test

Typical flow characteristics of the jet in the cavity are shown in Figure 5.5. The jet issuing from the nozzle formed a diverging cone which impinged on the far wall of the cavity. Upon impingement the jet was strongly deflected through at least 90° to

follow the profile of the cavity, eroding and transporting sand in the process. Upon leaving the impingement zone the return flow opposed the jet flow creating shear stresses, and thus energy losses, on the jet cone boundary.

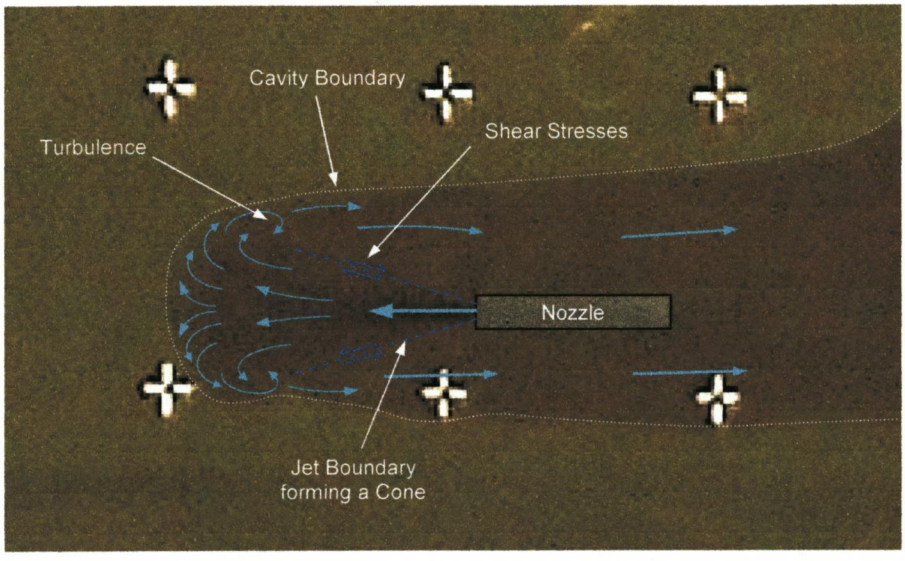

Figure 5.5 Typical flow patterns from a dynamic jet nozzle (60 mm/s) in the third stage of cavity development

The profiles of the cavity boundaries from the third stage of development are plotted in Figure 5.6, relative to the end of the nozzle, for each of the experiments analysed. Note that the measured rather than the designed nozzle velocities are used, and that the scale on the slowest test (7.5 mm/s) is smaller than that of the other plots. A larger version of each plot is given in Appendix 4. The plots show that during dynamic equilibrium (development stage 3) there was little variation in the size of the cavity boundary in front of the nozzle. The results also make it clear that the cavity size reduced as the nozzle velocity increased. The plots also show the upper and lower boundaries of the cavity becoming more horizontal as the nozzle velocity increased, until the cavity neck diameter began to reduce in size, as seen in the velocities of 82.5 mm/s and above. In the plot of the 48.5 mm/s experiment the shape of a simulated static cavity having the same length as the mean of the dynamic cavities of that test is also shown. It demonstrates that the cavities are of very similar shape over the impinging jet region (left side of the cavity).

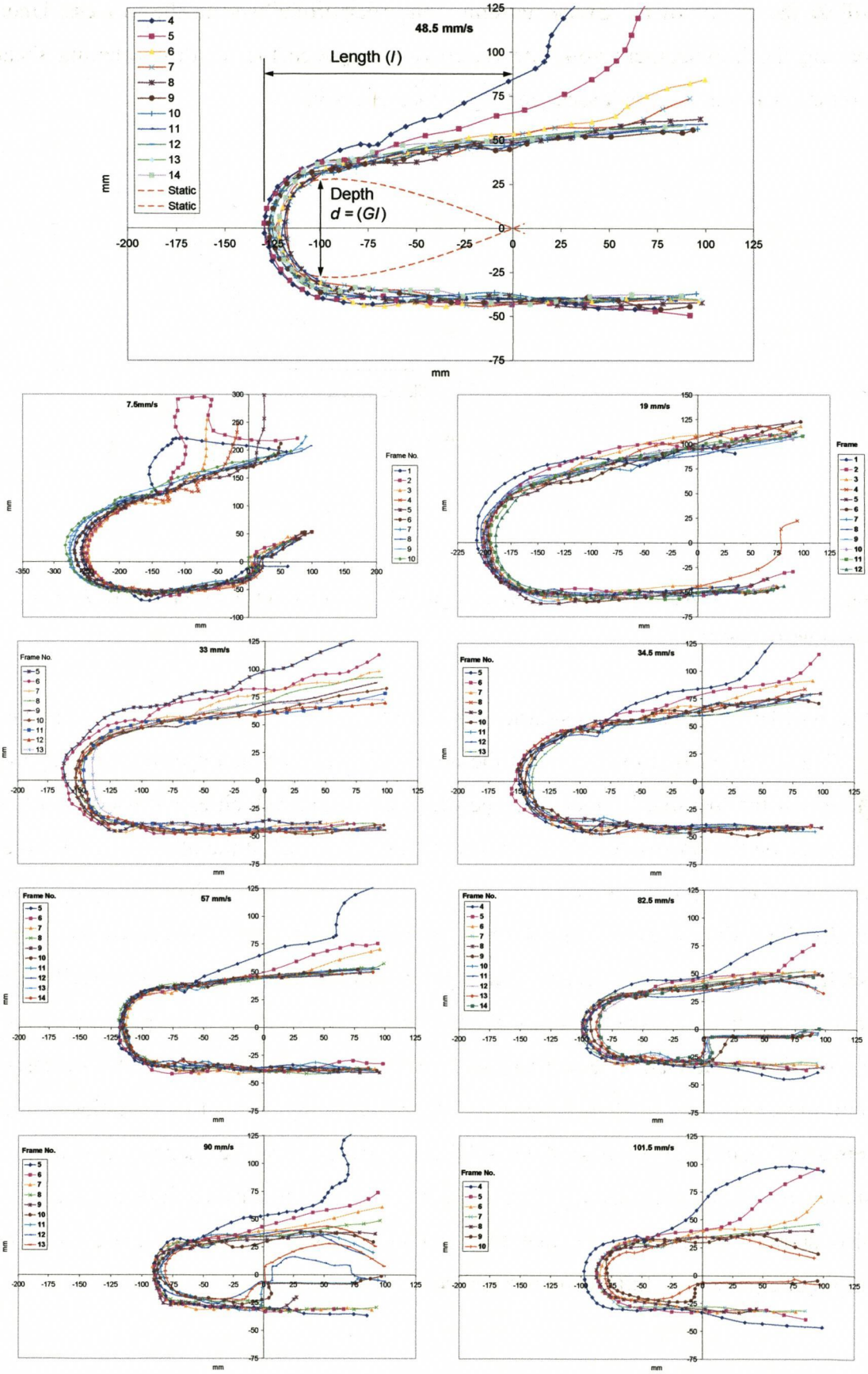

Figure 5.6 **Plots of cavity profiles from the Dynamic Nozzle Experiment**

5.5.2 Relationship between Nozzle Velocity (U_n) and Cavity Length

The mean cavity length of each test is plotted against nozzle velocity (U_n) in Figure 5.7. A regression curve of a power form fits the data well, having an R^2 value of 0.973. It is true that in the third stage of cavity development, that of dynamic equilibrium, the nozzle velocity is the same as the cavity boundary velocity ($U_n = U_b$), and they are thus interchangeable. Therefore it was also possible to plot U_b from the Static Nozzle Experiment against length on the same pair of axis as the dynamic results. The U_b curve from the static nozzle test with the equivalent flow rate (200 ml/s) was thus plotted in Figure 5.7, enabling a comparison of the two sets of data. The static curve was generated from Eq. 5.5 which was derived from the regression curve through the 200 ml/s data of cavity length against time, as shown below;

Regression equation through the 200 ml/s static nozzle data;

$$l = 133.26t^{0.3184} \tag{5.1}$$

Rearranged for t (time);

$$t = \left(\frac{l}{133.26}\right)^{3.1407} \tag{5.2}$$

Derivative of the length equation (Eq.5.1), giving U_b in terms of t;

$$U_b = \frac{dl}{dt} = 42.43t^{-0.6816} \tag{5.3}$$

Rearranging U_b in terms of l, by replacing t with Eq. 5.2, and simplifying gives;

$$U_b = \frac{dl}{dt} = 42.43.\left(\frac{l}{133.26}\right)^{-2.1407} \tag{5.4}$$

And rearranging for l in terms of U_b gives;

$$l = 767.44.U_b^{-0.4671} \tag{5.5}$$

The regression curve fit through the dynamic nozzle data had the equation;

$$l = 706.17.U_n^{-0.4513} \tag{5.6}$$

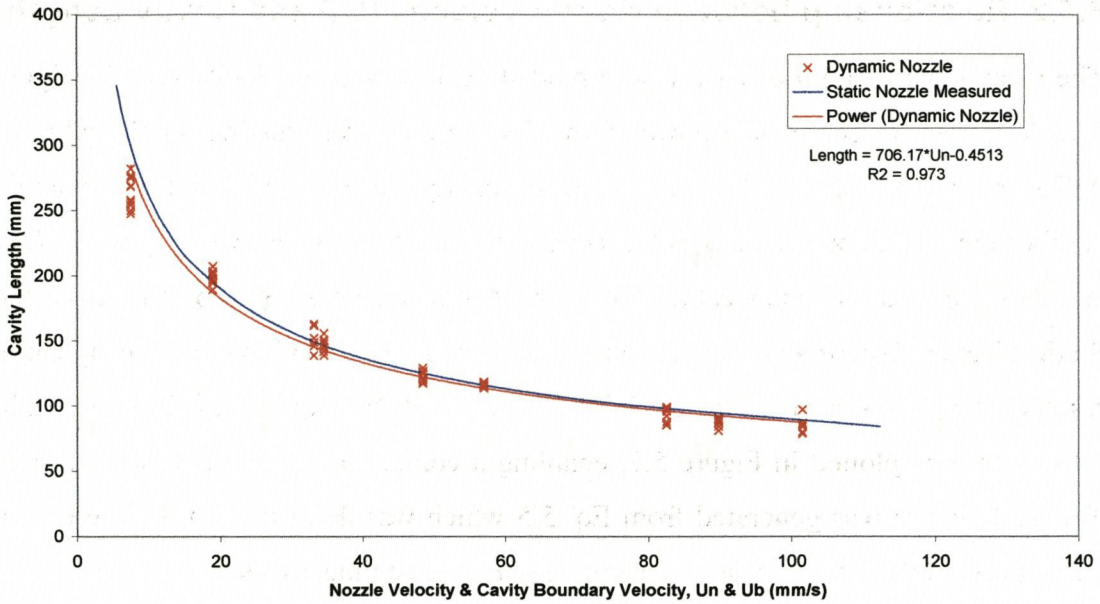

Figure 5.7 **Results of cavity length against nozzle velocity (U_n)**

Figure 5.7 shows there was no significant difference between the curve through the dynamic nozzle data and the static regression curve, since the two curves are virtually identical. This consequently shows that U_b is a function of the distance from the jet source, l, since the value of U_b was the same at a given length regardless of the U_n value. Thus, the rate of erosion from the cavity wall is a function of its distance from the jet source. It is also true that the cavity length is an inverse power function of the nozzle velocity, as the regression equation (Eq. 5.6) demonstrates.

5.5.3 Relationship between Nozzle Velocity (U_n) and Cavity Depth

The cavity depth dimensions r_a and r_b, defined in Figure 5.6, are plotted against U_n in Figure 5.8. They show the overall depth of the cavity was smaller at greater nozzle velocities, and that most of this was due to the reduction in the value of r_a, with the magnitude of r_b almost independent of velocity.

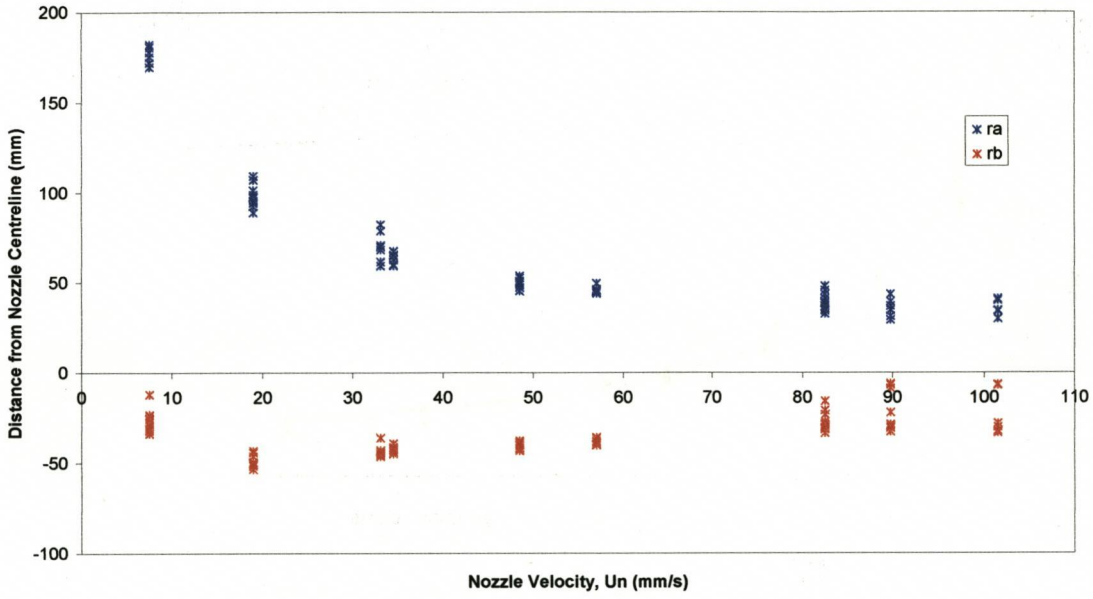

Figure 5.8 **Results of cavity depth, r_a & r_b, against nozzle velocity (U_n)**

The ratios of the dimensions r_a and r_b to the cavity depth ($G.l$) are plotted against U_n in Figure 5.9, together with linear best fit lines through both sets of data. The data from the slowest velocity test, 7.5 mm/s, had significantly greater values than the rest of the data, so it was thought justifiable to omit this data in the analysis because its U_n value was very small and thus exhibited abnormal characteristics.

Since the intercept of the line through the r_a data has a value of almost one and its gradient is nearly zero, it is reasonable to approximate the ratio $r_a/(G.l)$ to unity over the range of velocities displayed, although it is recognised there is some scatter of data about the best fit line. Likewise, the best fit line through the $r_b/(G.l)$ data has zero gradient and an intercept of -0.64, which can be closely approximated to -2/3.

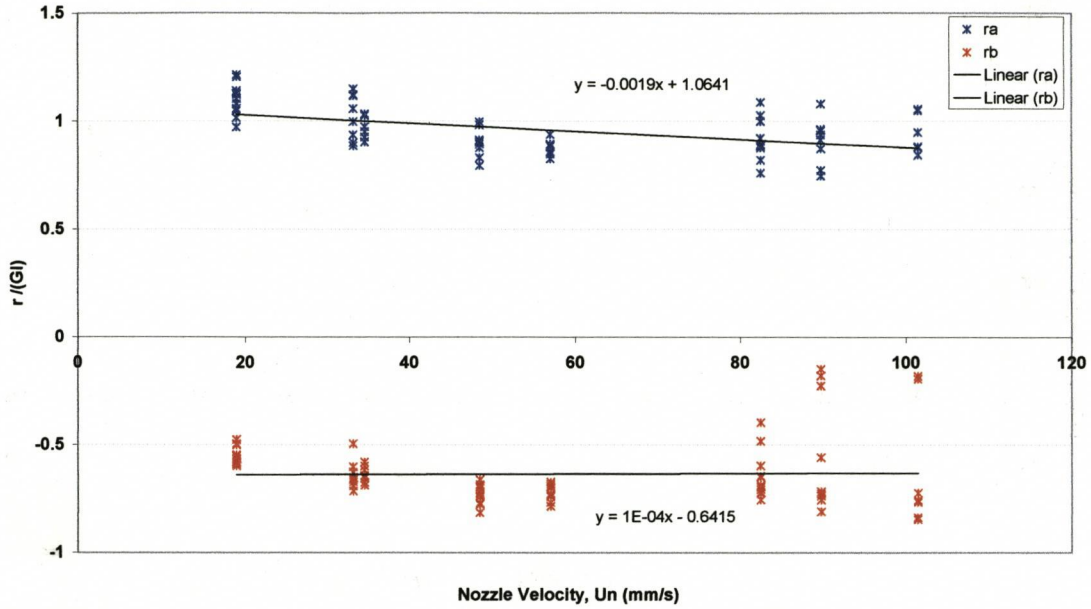

Figure 5.9 **Ratio of depth dimensions r/(G.l) against nozzle velocity (Un)**

5.6 Development of Mathematical Model Simulating the Extent of the Fluidised Cavity

5.6.1 Fluidised Cavity Geometry

A definition of the geometry of the cavity and jet flow paths was made after detailed study of the cavities from the videos of the experiments. A diagram of the geometry is shown in Figure 5.10.

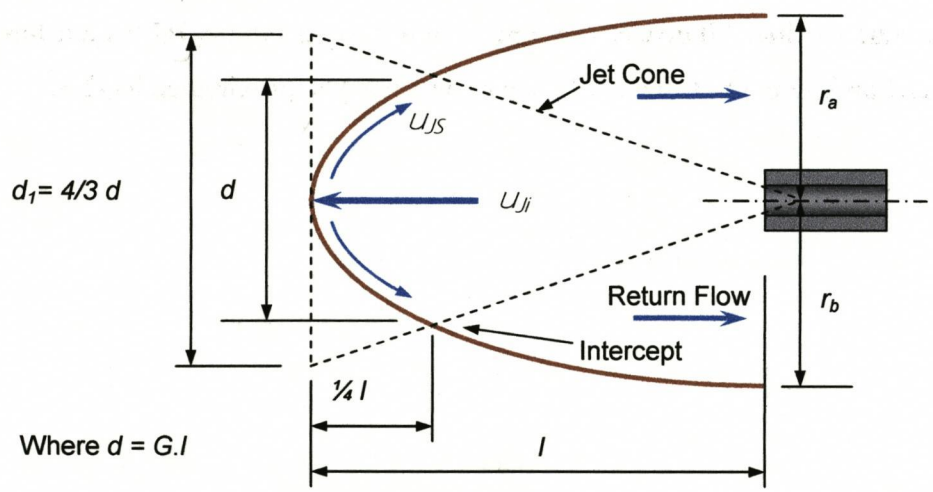

Figure 5.10 **Schematic of the geometry of a dynamic cavity and the flow paths of the jet**

5.6.2 Jet Velocities

Definitions of the cavity geometry used in the model are;

l = Length of cavity

d = Depth of cavity at the point the jet boundary intercepts the soil boundary. It was found, as shown in Figure 5.6, that the intersection was approximately at the deepest point of the static cavity of the same length, and therefore from Eq. 4.14.

$$d = G.l \tag{5.7}$$

Where $G = 0.45$.

The jet diverges with increasing distance from the nozzle, forming a cone. The geometry of the cone is calculated on the basis that the depth d occurs at *(3/4)* l, and therefore d_1 = *(4/3)* d at length l, as shown in Figure 5.10.

If the assumption is made that the impingement velocity (U_{ji}) of the jet on the cavity boundary is equivalent to the average velocity at the boundary cross section of the jet cone, then the impingement velocity is derived by;

$$U_{ji} = \frac{Q_{IN}}{C.S.A \quad at \quad d_1} \tag{5.8}$$

$$C.S.A \quad at \quad d_1 = \frac{\pi.d_1^2}{4} = \frac{1}{4}.\pi\left(\frac{4}{3}G.l\right)^2$$

Therefore,

$$C.S.A = \frac{4}{9}\pi.G^2.l^2 \tag{5.9}$$

Then substituting Eq. 5.9 into Eq. 5.8 gives the impingement velocity as;

$$U_{ji} = \frac{9.Q_{IN}}{4.\pi.G^2.l^2} \tag{5.10}$$

However, the shear stresses at the boundary between the jet cone and the returning flow cause energy loss from the jet cone, reducing its momentum and thus flow rate and velocity. Thus an energy loss factor (η) is added to account for the losses, giving;

$$U_{ji} = \eta . \frac{9.Q_{IN}}{4.\pi.G^2.l^2}$$

5.11

Upon impinging on the cavity wall, some of the flow is forced to permeate into the sand mass. The remaining flow is deflected and caused to follow the profile of the cavity, creating a shear stress on the adjacent sand boundary as it does so. The velocity of the shear flow is termed shear velocity (U_{js}). It is reasonable to assume that the impingement velocity is maintained as the flow is deflected, except it is slightly reduced by some flow being lost through permeation into the sand mass. The shear velocity is then determined by;

$$U_{js} = \frac{Q_{NET}}{C.S.A \quad at \quad d_1} = \frac{\eta.Q_{IN} - Q_{LOSS}}{C.S.A. \quad at \quad d_1}$$

5.12

According to Darcy's Law, the flow lost through permeation into the soil is;

$$Q_{LOSS} = \frac{k.A.\Delta h}{L}$$

5.13

Where A is the surface area of the impingement zone, for which a half sphere is a good approximation, thus;

$$A = 2.\pi.r^2 \quad = \quad 2.\pi.\left(\frac{d}{2}\right)^2$$

Then substituting d with Eq. 5.7 gives;

$$A = \frac{\pi.G^2.l^2}{2}$$

5.14

Also, h is the velocity head of the impinging jet, being;

$$h = \frac{U_{ji}^{\ 2}}{2.g}$$

5.15

Then replacing A and h in Eq. 5.13 with Eq. 5.14 and Eq.5.15 gives the flow loss as;

$$Q_{LOSS} = \frac{\pi.G^2.l^2.k.U_{ji}^{\ 2}}{4.g.L}$$

5.16

The shear velocity is then determined by substituting Eq. 5.9 and Eq. 5.16 into Eq. 5.12, giving;

$$U_{js} = \frac{\eta.Q_{IN} - \frac{\pi.G^2.l^2.k.U_{ji}^{\ 2}}{4.g.L}}{\frac{4}{9}\pi.G^2.l^2}$$

$$U_{js} = \left(\eta.Q_{IN} - \frac{\pi.G^2.l^2.k.U_{ji}^{\ 2}}{4.g.L}\right).\left(\frac{9}{4.\pi.G^2.l^2}\right)$$

$$U_{js} = \eta.\frac{9.Q_{IN}}{4.\pi.G^2.l^2} - \frac{9.k}{16.g.L}.U_{ji}^{\ 2}$$

Now since from Eq. 5.11,

$$U_{ji} = \eta.\frac{9.Q_{IN}}{4.\pi.G^2.l^2} \qquad 5.11$$

Then,

$$U_{js} = U_{ji} - \frac{9.k}{16.g.L}.U_{ji}^{\ 2} \qquad 5.17$$

5.6.3 Determination of the Loss factor (η)

Shear stress develops at the boundary of the jet cone and the returning flow, causing momentum loss from the jet flow. The momentum loss eventually penetrates to the centreline of the jet, causing its velocity to reduce. Prior to that point, closer to the jet source, the jet flow remains constant. These two zones, being the potential core region (PCR), where velocity is undiminished, and the established flow region (EFR), where velocity diminishes with increasing distance from the jet source, are shown in Figure 4.1.

According to Rajaratnam (1976) the jet core region extends a distance of $\beta.d_j$ from the jet source, where β is equal to 5.8. However, Rajaratnam and Beltaos (1977) define the potential core region as $<5.5.d_j$ and the established flow region as $>8.3.d_j$, while Mih and Kabir (1983) define the start of the established flow region at $6.2.d_j$. It is therefore reasonable to deduce that β is in the region of 6 to 7.

Since the losses are caused at the jet boundary, the losses at any cross section through the jet cone are proportional to the ratio of the perimeter to the area of the cross

section. Therefore the losses at any section through the jet decrease as the distance from the jet source increases, since the perimeter/area ratio decreases with increasing section diameter. The geometry of the jet cone and two sections through it, one at the end of the PCR and the other in the EFR, are displayed in Figure 5.11. On the basis that the losses are proportional to the perimeter/area ratio, the dimensionless loss factor (η) of the jet cone section can be determined, as shown below.

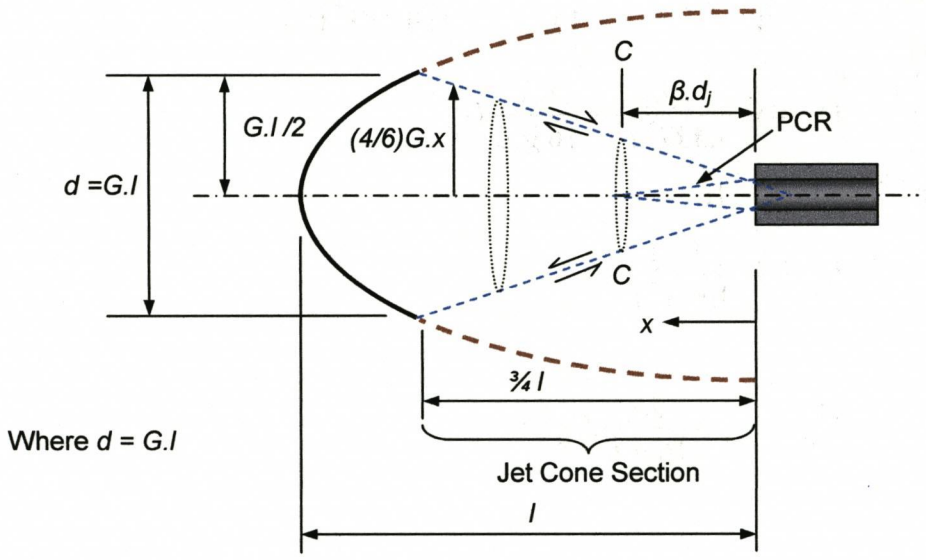

Figure 5.11 Geometry of Jet Cone Section over which the η factor was determined

Perimeter of a cross section;

$$p = 2.\pi.r$$

Since,

$$d = G.l \qquad \text{at} \qquad x = \left(\tfrac{3}{4}\right)l$$

Then rearranging gives,

$$l = \left(\tfrac{4}{3}\right)x \qquad \text{and} \qquad d = \left(\tfrac{4}{3}\right)G.x$$

Thus,

$$r = \left(\tfrac{2}{3}\right)G.x \qquad \textbf{5.18}$$

Therefore

$$p = \left(\tfrac{4}{3}\right)\pi.G.x \qquad \textbf{5.19}$$

The cross sectional area of a section is;

$$c.s.a = \pi.r^2 = \pi\left(\frac{2.G.x}{3}\right)^2$$

$$c.s.a = \frac{4.\pi.G^2.x^2}{9}$$

5.20

So the perimeter/area ratio at any cross section is therefore;

$$Loss_x = \frac{p}{c.s.a} = \frac{\left(4/3\right)\pi.G.x}{\left(4/9\right)\pi.G^2.x^2}$$

$$Loss_x = \frac{p}{c.s.a} = \frac{3}{G.x}$$

5.21

The total loss over the jet cone is therefore the sum of the losses over the length of the cone, thus;

$$Loss_{total} = \int_0^{3.l/4} \frac{p}{c.s.a}.dx$$

$$Loss_{total} = \int_0^{3.l/4} \frac{3}{G.x}.dx = \left[\frac{3.Ln(x)}{G}\right]_0^{3.l/4}$$

$$Loss_{total} = \frac{3.Ln\left(3.l/4\right)}{G}$$

5.22

However, as was discussed previously, there are no losses on the jet centreline in the PCR, the losses only effect the centreline velocity in the EFR. Therefore the losses in the PCR may be neglected, and it is only at the start of the EFR that the losses take effect. The loss values were therefore normalised with respect to the loss value at the start of the EFR, which is section C in Figure 5.11.

Normalised dimensionless loss;

$$Loss_{normalised} = \frac{Loss_{total,x}}{Loss_{total,C}}$$

5.23

However, the η factor must give the fraction remaining, not the fraction lost, therefore;

$$\eta = \frac{1}{Loss_{normalised}}$$

$$\eta = \frac{Loss_{total,C}}{Loss_{total,x}}$$

5.24

$Loss_{total,c}$ occurs at the end of the PCR, where $x = \beta.d_j$, therefore;

$$Loss_{total,C} = \frac{3.Ln(\beta.d_j)}{G}$$

5.25

The total loss for any other length is;

$$Loss_{total,X} = \frac{3.Ln(3.l/4)}{G}$$

5.26

Therefore, substituting Eq. 5.25 and Eq. 5.26 into Eq. 5.24 and simplifying gives the loss factor η as;

$$\eta = \frac{Ln(\beta.dj)}{Ln(3.l/4)}$$

5.27

The relationship between η and cavity length is shown in Figure 5.12. The upper and lower boundaries of the possible η values are represented by the green and red curves, based on the range of β values of 5.5 to 8.3 used by other researchers. The η curve for the β value used by Mir and Kabir (1983) of 6.2 is plotted as the dashed line. The η value is displayed over the equivalent range of cavity lengths measured in the Dynamic Nozzle Experiment. Cavity lengths less than 50 mm correspond to nozzle velocities in excess of 350 mm/s, and lengths greater than 250 mm to velocities less than 10 mm/s.

The η value required to make the simulated lengths from this model fit the measured data exactly is also displayed in Figure 5.12, as the blue curve. The curve was generated by combining the regression equation through the Dynamic Nozzle Data (Eq. 5.6) and the nozzle velocity equation (Eq. 5.37, developed later in this model) and rearranging for η, giving;

$$\eta = \frac{-b_\eta - \sqrt{b_\eta{}^2 - 4.a_\eta.c_\eta}}{2.a_\eta}$$

5.28

Where;

$$a_\eta = \frac{9.k.T^2}{16.g.L}, \quad b_\eta = -T, \quad c_\eta = U_b.\left(\frac{\rho_s}{\rho_w}\right), \quad T = \frac{9.Q_{IN}}{4.\pi.G^2.l^2}$$

5.29 (a,b,c,d)

The curve of the required η values lies within the range of theoretical η values and is almost the same as the theoretical η curve for $\beta = 6.2$. Between cavity lengths of 50 – 250 mm the η value ranges from 1 to 0.65. A η value of 0.8 gives lengths values within ± 5% of the measured length value, and is thus a good approximation of η over the range of length values measured in the experiment.

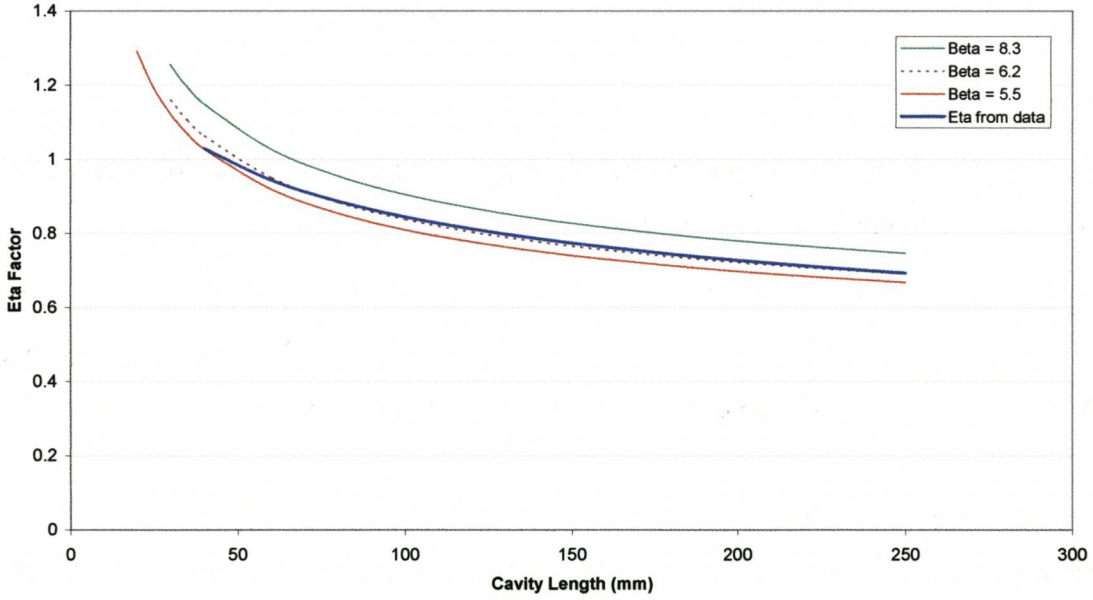

Figure 5.12 Theoretical and measured relationships between η and cavity length

5.6.4 Derivation of the Rate of Erosion and Boundary Velocity (U_b)

The shear stress generated at the boundary of a moving fluid is given as;

$$\tau_0 = \rho_w.U_{js}{}^2$$

5.30

(Carson, 1971)

Shear stress is also defined as;

$$\tau_0 = \frac{Force}{Area} = \frac{dMomentum/dt}{Area}$$

5.31

If considering a unit area of boundary surface, the momentum required to accelerate a unit volume of sand from the boundary wall, assuming the detachment force is insignificant, is;

$$Momentum = Mass \times Velocity$$

$$Mom = \rho_s . U_{js}$$

5.32

The total momentum absorbed per unit time, per unit area of boundary surface is then;

$$dMom/dt = V.\rho_s.U_{js}/dt$$

5.33

Where V = volume of sand eroded

Thus, substituting Eq.5.33 into Eq.5.31 gives the shear stress required to erode this volume of sand per unit time, per unit area, being;

$$\tau_0 = V.\rho_s.U_{js}$$

5.34

And rearranging for volume eroded per unit area, per unit time;

$$V = \frac{\tau_0}{\rho_s.U_{js}}$$

Then replacing τ_o with Eq. 5.30 gives the eroded volume as;

$$V = \frac{\rho_w.U_{js}^{\ 2}}{\rho_s.U_{js}}$$

$$V = \frac{\rho_w}{\rho_s}.U_{js}$$

5.35

And since this is per unit area, the velocity of the boundary is equivalent to the volume, thus the boundary velocity is;

$$U_b = \frac{\rho_w}{\rho_s}.U_{js}$$

5.36

or,

$$U_b = \frac{\rho_w}{\rho_s}.\left(U_{ji} - \frac{9k}{16.g.L}.U_{ji}^{\,2}\right)$$

5.37

where,

$$U_{ji} = \eta.\frac{9.Q_{IN}}{4.\pi.G^2.l^2}$$

5.11

This defines the relationship between boundary velocity on the jet centreline, U_b, and the cavity length, l.

5.6.5 Derivation of the Relationship between Cavity Length and Nozzle Velocity

When in the dynamic equilibrium condition, $U_b = U_n$, then Eq. 5.37 can be solved to give the length of a cavity in terms of nozzle velocity, as shown below;

Now if;

$$U_{ji} = \eta.\frac{9.Q_{IN}}{4.\pi.G^2.l^2} = \frac{E}{l^2}$$

5.38

Where;

$$E = \eta.\frac{9.Q_{IN}}{4.\pi.G^2}$$

5.39

Then substituting Eq. 5.38 into Eq. 5.37 gives;

$$U_b = \frac{\rho_w}{\rho_s}.\left(\frac{E}{l^2} - \frac{9k}{16.g.L}.\left(\frac{E}{l^2}\right)^2\right)$$

5.40

And thus;

$$U_b.\frac{\rho_s}{\rho_w} = \frac{E}{l^2} - \frac{9.k}{16.g.L}.\frac{E^2}{l^4}$$

So,

$$\frac{9.k.E^2}{16.g.L}.\frac{1}{l^4} - E.\frac{1}{l^2} + U_b.\frac{\rho_s}{\rho_w} = 0$$

5.41

This is of a quadratic form, therefore;

$$\frac{1}{l^2} = \frac{-b_l \pm \sqrt{b_l^2 - 4.a_l.c_l}}{2.a_l}$$

$$l = \sqrt{\frac{2.a_l}{-b_l - \sqrt{b_l^2 - 4.a_l.c_l}}}$$

5.42

Where;

$$a_l = \frac{9.k.E^2}{16.g.L}, \qquad b_l = -E, \qquad c_l = U_b.\frac{\rho_s}{\rho_w}$$

5.43 (a,b,c)

These equations (Eq. 5.42 & Eq. 5.43) enable the determination of equilibrium cavity length at a given nozzle velocity, for a horizontal jet in easily eroded sand.

5.6.6 Definition of Cavity Boundary

The typical geometry of a dynamic cavity profile is shown in Figure 5.13. It is asymmetric, with the lower boundary tending to the horizontal in the return flow section, as discussed in Section 5.5.3. The experimental results showed that $r_a = G.l$ and $r_b = 2/3\ G.l$ were both acceptable approximations. This can be supported theoretically on the basis that the upper boundary is of parabolic form, as shown below;

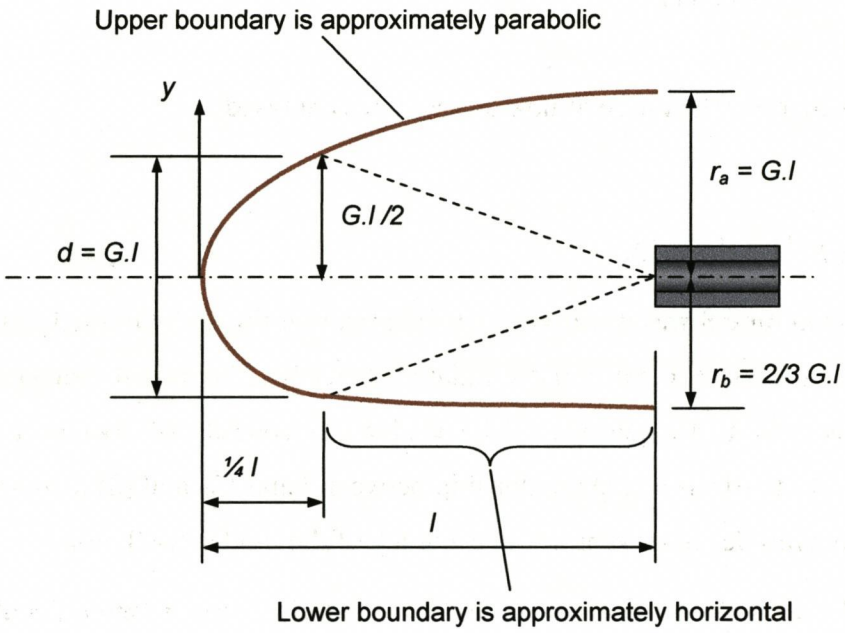

Figure 5.13 Typical geometry of dynamic cavity boundary

The form of a parabolic curve is;

$$y^2 = 4.a.x \qquad \text{thus} \qquad y = 2.\sqrt{a.x} \tag{5.44}$$

and;

$$a = \frac{y^2}{4.x}$$

The limiting conditions, shown in Figure 5.13, are that $x = \frac{l}{4}$ at $y = \frac{G.l}{2}$, therefore;

$$a = \frac{\left(G.l/2\right)^2}{4.\left(l/4\right)} = \frac{G^2.l}{4} \tag{5.45}$$

So the height of the profile at the nozzle (r_a), where $x = l$, is;

$$r_a = 2.\sqrt{\frac{G^2.l}{4}.l}$$

$$r_a = G.l \tag{5.46}$$

This is in agreement with the experimental results. The depth of r_b was somewhat less than $G.l$ and can be defined as;

$$r_b = D_z.G.l \qquad 5.47$$

Where D_z = 2/3 over the range of nozzle velocities analysed.

5.7 Model Evaluation

The momentum model was evaluated by comparison of the measured lengths from the Dynamic Nozzle Experiment to the simulated cavity lengths over the range of nozzle velocities used in the experiment. The evaluation consists of two aspects, (1) a comparison of the forms of the relationship between l and U_n, and (2) a comparison of the length magnitudes to determine the accuracy of the model prediction.

Figure 5.14 shows the simulated and measured relationships between l and U_n. The two simulated curves were generated with η values of 1 and 0.8, simulating the condition of no losses and average losses detailed in Section 5.6.3, respectively. It was shown in Section 5.6.3 that η varies slightly with l and thus U_n, but to incorporate the variation into the model requires an iterative process to determine both l and η numerically. For this reason a constant value of 0.8 was used as a close approximation of η. The simulated lengths were generated using Eq. 5.42.

Figure 5.14 shows very close agreement between the simulated and measured cavity lengths over the range of U_n tested. The form of curve generated by the model is very similar to that of the measured data. However, because a constant η value was used, the model overestimates l very slightly at low U_n values, but nonetheless, it simulates the data very well even with a constant η value.

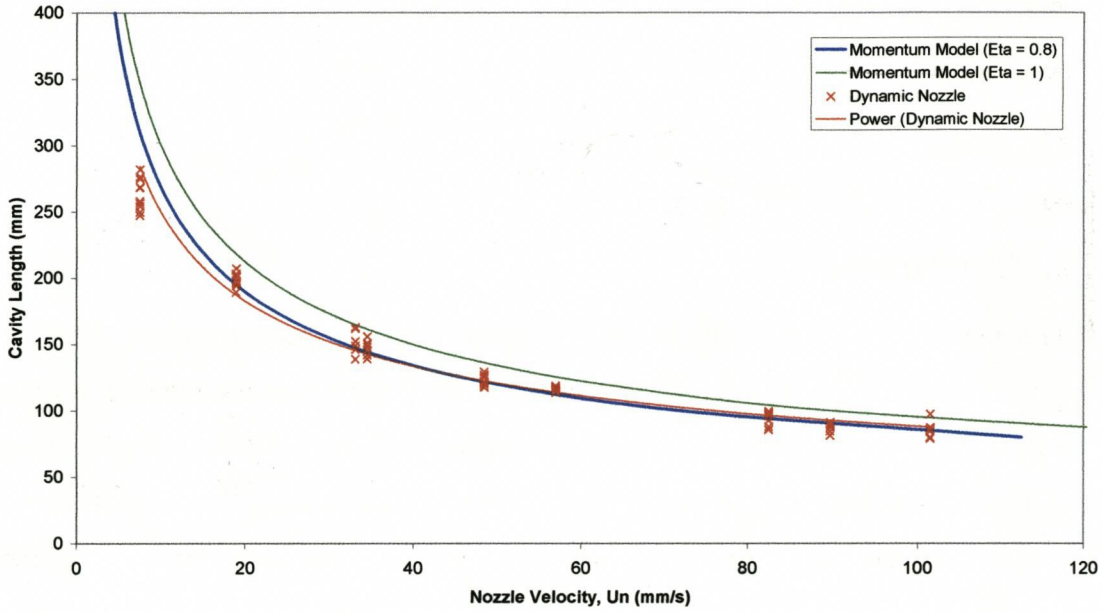

Figure 5.14 Simulated length: nozzle velocity relationship and comparison to measured data

The magnitudes of the measured and simulated lengths are plotted against each other in Figure 5.15. It shows the error in the magnitude of the simulated length is small between the measured lengths of 75 – 200 mm. At the largest measured length of 250 mm the simulated lengths overestimate by approximately 20%. However, the U_n values associated with the very large lengths are very low (7.5 mm/s), and are thus of little practical importance. If the data of the 250 mm cavity is ignored, the best fit line through the remaining data has a gradient of 1.0, showing the average error between the measured and simulated lengths is nil. However, the gradient increases to 1.07 if the large cavity data is included, giving an average error of +7% over the range of U_b tested.

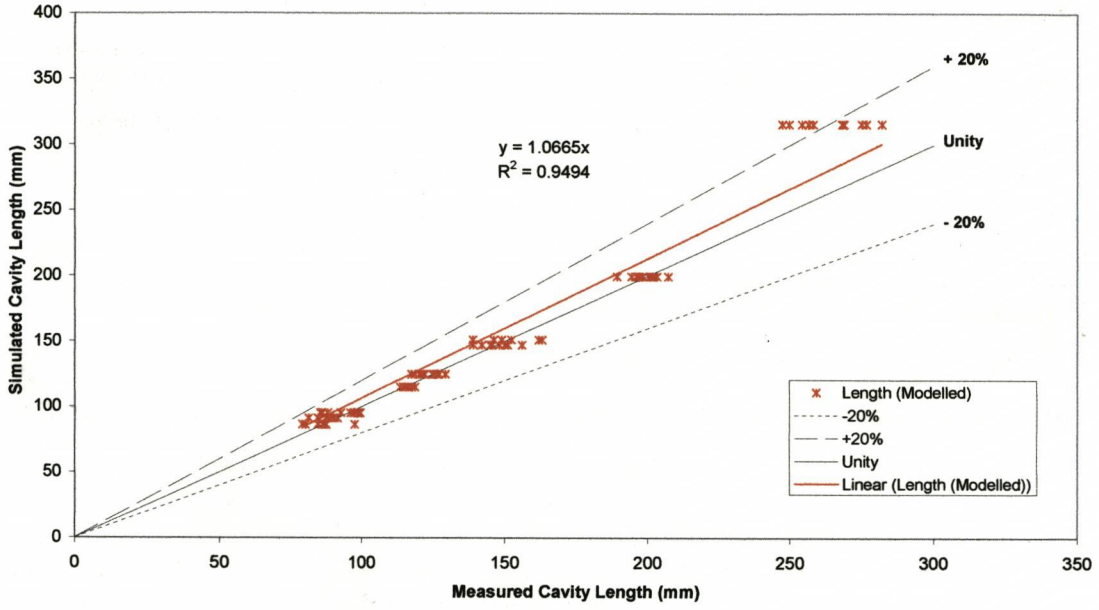

Figure 5.15 Comparison of measured and simulated cavity lengths

The model applies to an easily eroded non cohesive soil where detachment forces are assumed to be minimal, so the jet shear force has only to mobilise soil particle acceleration. The model will therefore become less accurate when simulating soils with significant detachment forces. The jet shear force has to then overcome particle detachment forces, leaving only the excess shear to accelerate particles from the boundary surface. The excess shear is thus;

$$\tau_e = \tau - \tau_c \qquad \textbf{5.48}$$

Where;

τ_e = excess shear

τ_c = critical shear, required for particle detachment

τ = jet shear

The model is consequently not appropriate for cohesive soils.

The model was evaluated against data from tests in one soil type (standard sand) using one flow rate (200 ml/s). Data from the Static Nozzle Experiment indicated the value of the G ratio may differ somewhat between soils, its value being slightly lower than 0.45 in coarse sand. The model could be improved by the development of a means of determining the value of G theoretically rather than empirically.

5.8 Conclusions

1. A fluidised cavity created by a dynamic buried nozzle in saturated sand had the following characteristics;
   a) The cavity profile was approximately of parabolic form.
   b) The relationship between cavity boundary velocity, U_b, and cavity length, l, from the static nozzle experiment was the same as that between nozzle velocity, U_n, and cavity length, l, in the dynamic nozzle experiment.
   c) The velocity of the cavity boundary U_b is a function of the cavity length l. This is true for both dynamic and static nozzle cases.
   d) The cavity length l is an inverse power function of the nozzle velocity U_n when the cavity is in dynamic equilibrium.

2. The mathematical model developed to simulate the extent of the fluidised cavity generated by a dynamic nozzle, based on the conservation of momentum, defined the following;
   a) The axial impingement velocity of the jet on the cavity boundary was;

$$U_{ji} = \eta . \frac{9.Q_{IN}}{4.\pi.G^2.l^2} \qquad 5.11$$

   b) The shear velocity on the cavity boundary was defined as;

$$U_{js} = U_{ji} - \frac{9.k}{16.g.L}.U_{ji}^{\,2} \qquad 5.17$$

   c) The dimensionless loss factor;

$$\eta = \frac{Ln(\beta.dj)}{Ln(3.l/4)} \qquad 5.27$$

   d) The cavity boundary velocity;

$$U_b = \frac{\rho_w}{\rho_s}.U_{js} \qquad 5.36$$

   e) The resulting cavity length as;

$$l = \sqrt{\frac{2.a_l}{-b_l - \sqrt{b_l^{\,2} - 4.a_l.c_l}}} \qquad 5.42$$

   Where;

$$a_l = \frac{9.k.E^2}{16.g.L}, \quad b_l = -E, \quad c_l = U_b.\frac{\rho_s}{\rho_w} \qquad 5.43\ (a,b,c)$$

And,

$$E = \eta.\frac{9.Q_{IN}}{4.\pi.G^2} \qquad 5.39$$

f) The cavity height and depth at the nozzle tip as;

$$z_a = G.l \qquad 5.46$$

$$z_b = D_z.G.l \qquad 5.47$$

Where D_z was found to be 2/3.

3. Evaluation of the model showed;
   a) There was a very good fit between the measured and simulated cavity length, the simulated overestimating by an average of 7% over the range of nozzle velocities tested (7.5 to 100 mm/s), when using a loss factor η of 0.8.
   b) The simulated cavity lengths overestimated the measured lengths by an average of 7% when including the slowest U_n data (7.5 mm/s). This error reduced to zero when the slowest U_n data was excluded.
   c) The application of the model is limited to easily eroded non cohesive sands.
   d) The model could be developed further by deriving a means of accounting for soil particle detachment forces.
   e) The model would be improved if G could be determined theoretically rather than empirically.

6 Final Evaluation

Mathematical models have been developed to predict the two key elements of jetting tool force reduction. The first element is a model predicting the size of the fluidised area created on the tool face by a single horizontal jet, and was developed in Chapter 5. This requires knowledge of the jet flow rate, nozzle diameter, tool speed, soil hydraulic conductivity and depth of nozzle below the soil surface. The second element is the model predicting tool force reduction created by the fluidised areas, and was developed in Chapter 2. This requires knowledge of the number and position of fluidised areas and the passive tool force. The purpose of this Chapter is to evaluate the combined models by comparison of the predicted to the measured values from the nozzle distribution and the rake angle experiments which had horizontal jets.

6.1 Method of Calculating Predicted Values

To calculate the first element, being the size of the fluidised areas, predicted values of the cavity length (l) were generated using Equations 5.38, 5.41 and 5.42(a,b,c). The resulting depth of the FA was then calculated using Equations 5.45 for z_a and 5.46 for z_b. Depth faction (D_z) values of 2/3 (from analysis of the dynamic nozzle experiments) and 1 were used, creating two sets of predicted values. A loss factor (η) of 0.8 was used throughout.

To calculate the second element, being the force reduction created by the fluidised areas, the predicted values were generated using Equations 2.19(a,b) for z_a and z_b values, 2.18 for force loss and 2.20 for the net force. In the case of the non vertical tines in the rake angle experiments, Equations 2.27 and 2.28 were used to calculate the r_a and r_b values respectively. These also required the use of Equations 2.22, 2.23 and 2.26(a,b,c) for the forward raked tines and Equations 2.24, 2.25 and 2.26(a,b,c) for the backward raked tines. All predicted values were generated using Microsoft Excel.

6.2 Measured verses Predicted Forces

Measured verses the predicted values for the nozzle distribution experiments are shown in Figure 6.1, and for the forward and backward raked tines with horizontal jets in the rake angle experiments, in Figure 6.2.

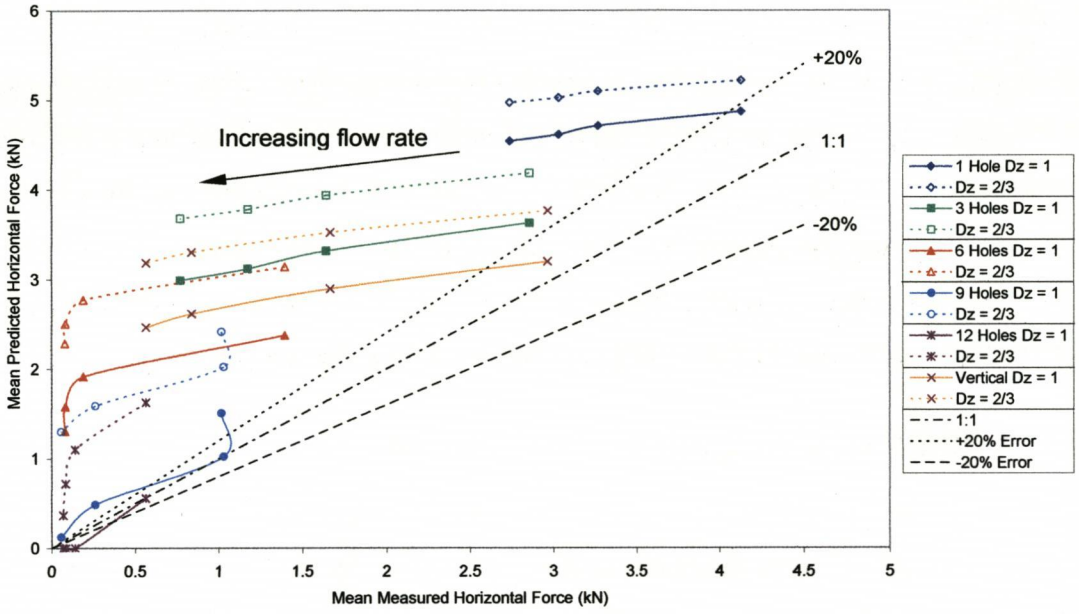

Figure 6.1 Comparison of measured to predicted forces for the nozzle distribution experiments and the horizontal jets on the vertical tine in the rake angle experiments

The data for the vertical tines in Figure 6.1 shows three distinct characteristics, being;

1. The predicted values over estimate the tool force, with the error tending to increase as the flow rate increased, and were proportionally greater for experiments with lower measured forces. All the predicted values calculated using a D_z value of 2/3 over estimated the force by more than 20%.
2. Predicted values calculated using a D_z value of 1 gave lower forces and smaller errors than those calculated using a D_z value of 2/3, since the larger D_z value generated a larger FA, and thus a greater force reduction.
3. The gradient of each data set is too low, indicating the predicted force is insufficiently responsive to changes in the flow rate. The gradients of the data for the tines with one or three nozzles varied between 0.2 and 0.3, being less than the desired value of unity.

The data for the forward and backward raked tines in Figure 6.2 shows similar characteristics, being;

1. The error in the predicted force was less than with the vertical tines, with the predicted values of the lower flow rates being within ± 20% of the measured value.
2. The D_z value has a greater effect on the backward raked than the forward raked tine. This is due to the profile of the base of the cavity of the backward rake angle intercepting the tine at a greater distance from the front of the cavity than with the forward rake angle. The r_b value therefore has a greater influence on the force with the backward rake angle, hence the greater sensitivity to D_z.
3. Generally the gradient of each data set is too low, although the data at the higher flow rates of the forward raked tines assumes a gradient closer to unity.

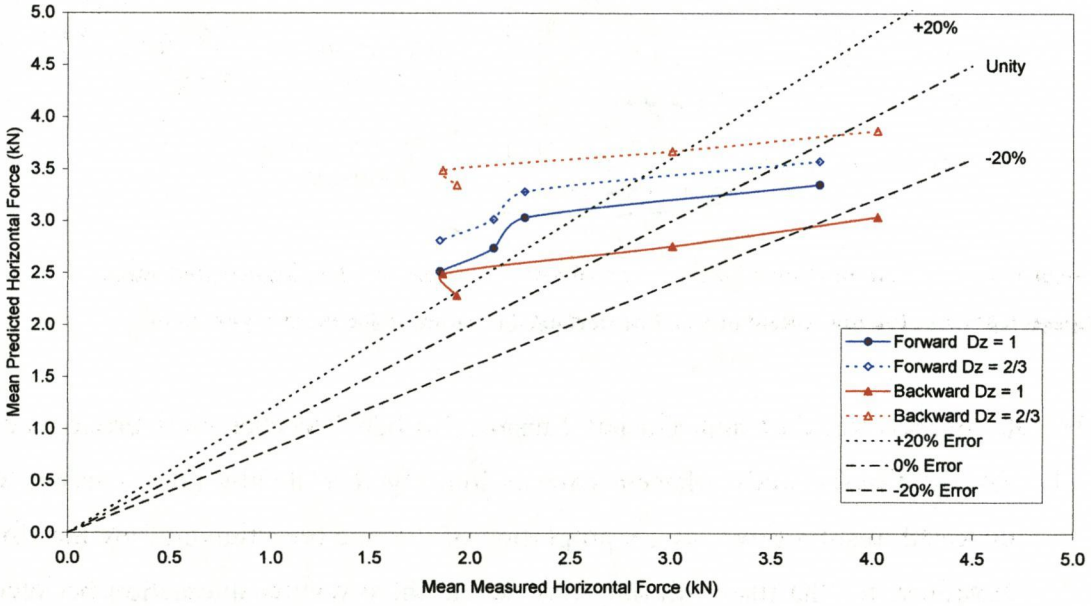

Figure 6.2 Comparison of measured to predicted forces for the forward and backward raked tines with horizontal jets

6.3 Causes for the Discrepancies

There are considered to be two aspects of the discrepancy between the measured and predicted forces, being that causing the model to over predict the force, creating the vertical offset, and that causing the predicted force to be insufficiently responsive to

changes in the flow rate, creating the gradient error. Causes for these two aspects are discussed below.

6.3.1 Causes for the Force Offset

1. The tine interferes with the jet flow path causing its deflection at the interface with the tine. This may cause the flow to be deflected vertically on the tine face, as shown in Figure 6.3, creating a larger FA and thus a lower force. Also the tine reduces the cross section area of the cavity, causing the velocity of the flow in the remaining area around the sides of the tine to increase. Consequently it has a greater ability to transport sediment from the cavity, so increasing the r_b and possibly r_a values.

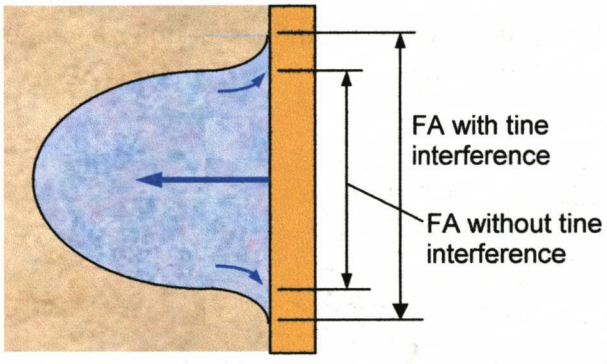

Figure 6.3 Possible effect of tine interference on depth of FA

2. Interaction between adjacent jets causing soil between cavities to erode more readily. Consequently adjacent cavities join together at flow rates lower than expected, resulting in a larger proportion of the tine being covered by the FA. However, for the tine with only one nozzle there was no interaction between jets, yet the predicted forces were still significantly greater than the measured, indicating that interaction between jets was not the principal cause.
3. The jetted cavities enable the surrounding soil to fail more easily, so that the soil pressure exerted on the tine by the soil surrounding the cavities is reduced, being less than that predicted by the force model of Chapter 2. The force model assumes the soil stress is only reduced in the FA's, as shown by the soil stress diagram in Figure 2.21. The undisturbed soil is assumed to retain it original 'passive' pressure. However, in reality this is unlikely since the soil adjoining

the cavity is able to fail vertically, moving into the cavity volume, rather than just laterally around the sides of the tine. It is reasonable to assume that the extent to which the cavity effects soil failure is a function of the length of the cavity as illustrated in Figure 6.4(a,b). However, there is no experimental data showing the variation of soil pressure on the tine face about a fluidised cavity, hence the pressure profile in Figure 6.4 remains speculative. The pressure value is assumed to increase linearly between the cavity boundary, point A, and the original 'passive' stress profile, point B. However, in reality this is likely to be the form of a more complex curve. The extent of the region where the cavity causes a reduction in soil stress is also unknown.

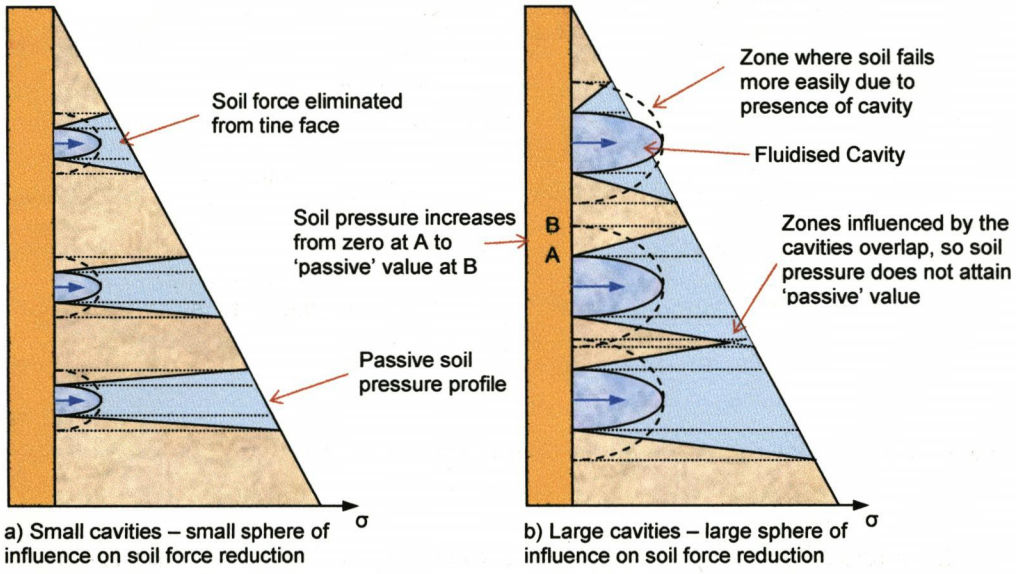

Figure 6.4 Possible soil pressure reductions caused by fluidised cavities

To examine this argument, the force model of Chapter 2 was modified by assuming a soil stress reduction in the regions about the cavities. The force characteristics in the previous paragraph were considered too ambiguous to put values to. Consequently the model is modified by the simple assumption that the cavity depth values r_a and r_b are extended by a certain percentage. This simulates the zone over which the cavity has the effect of reducing soil pressure by increasing the size of the FA in the model. Consequently the predicted force values are reduced, as shown in Figure 6.5.

To give as much validity to this modification as possible, the value of the percentage increase was engineered to give minimal error for the predicted force of the nozzle

distribution experiments having the most similar parameters to the dynamic nozzle experiments, being a nozzle diameter of 6 mm and a flow rate of 200 ml/s respectively. The reason being that the cavities in those tests are likely to bear closest resemblance to those of the cavities in the dynamic nozzle experiments, from which part of this model was developed. The tests with the closest resemblance were those of the tine having three 6 mm diameter nozzles with a flow rate of 320 ml/s, being highlighted in Figure 6.5. A percentage increase of 30% was required to achieve approximate unity between the measured and predicted force values when using a Dz value of one for both r_a and r_b.

The modified force model was applied to the data of the nozzle distribution experiments, and modified predicted force values generated, as shown in Figure 6.5. They show that a slight modification to the proposed soil stress profile can have a significant effect on the predicted force, since the predicted force values show closer agreement to the measured values than those of the original force model. It is therefore reasonable to conclude that the soil stress profile about a cavity is more complex than that assumed in the original force model, and is the likely cause of the vertical offset of the predicted to measured force values, shown in Figure 6.1 and Figure 6.2.

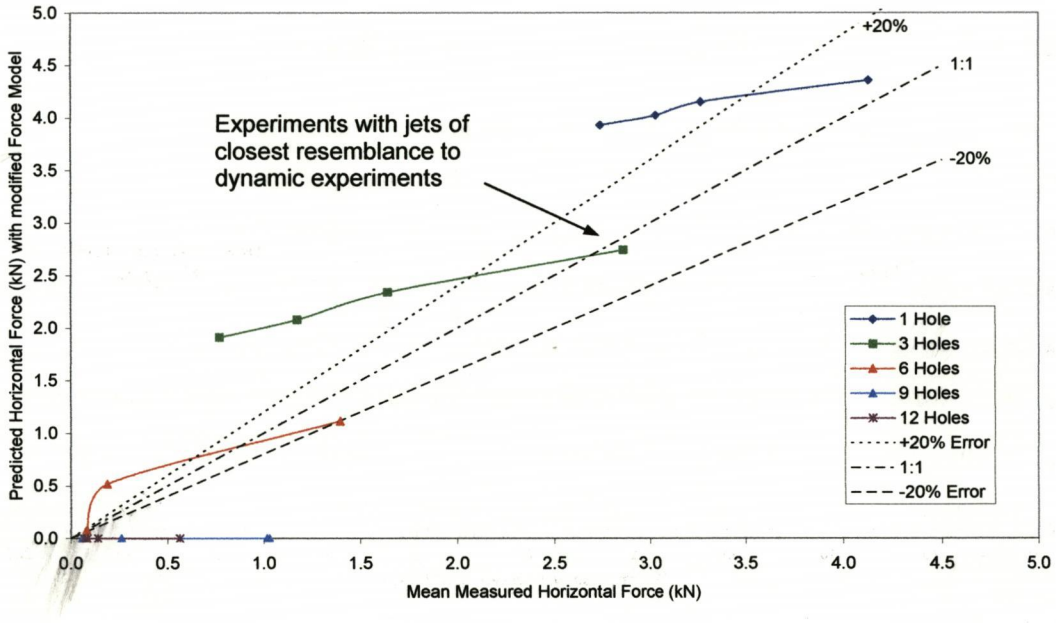

Figure 6.5 Result of modifying the force model by increasing the r_a and r_b values by 30%

6.3.2 Cause for the Gradient Error

The likely cause for the gradient error is the model assuming a constant cavity depth fraction value (D_z) regardless of the jet flow rate and energy. However, the dynamic nozzle experiments showed that the depth of the cavity at the nozzle reduced when sand was deposited from the flow. Larger quantities of sand were deposited when the flow had insufficient energy to transport it from the cavity at the required rate. It therefore follows that the rate of transportation of sand from the cavity is a function of the energy of the flow. This is in agreement with Raudikivi (1990, p477) who stated, regarding the transportation of sediment in pipelines, 'the maximum amount of solids is transported per unit energy input'. Thus, the hypothesis is generated that the depth of the cavity, and thus the value of D_z, are a function of the energy of the flow.

To test this hypothesis, the D_z value required to equalise the predicted to the measured force was determined for each of the nozzle distribution experiments. The resulting D_z values were plotted against the corresponding energy value of the jet at its source (the energy value at the interface with the tine is unknown, thus the energy of the source was used), which is shown in Figure 6.6. The data shows a clear relationship between the energy of the jet and the D_z value, with a logarithmic regression curve fit to the data having a goodness of fit coefficient value (R^2) of 0.7319.

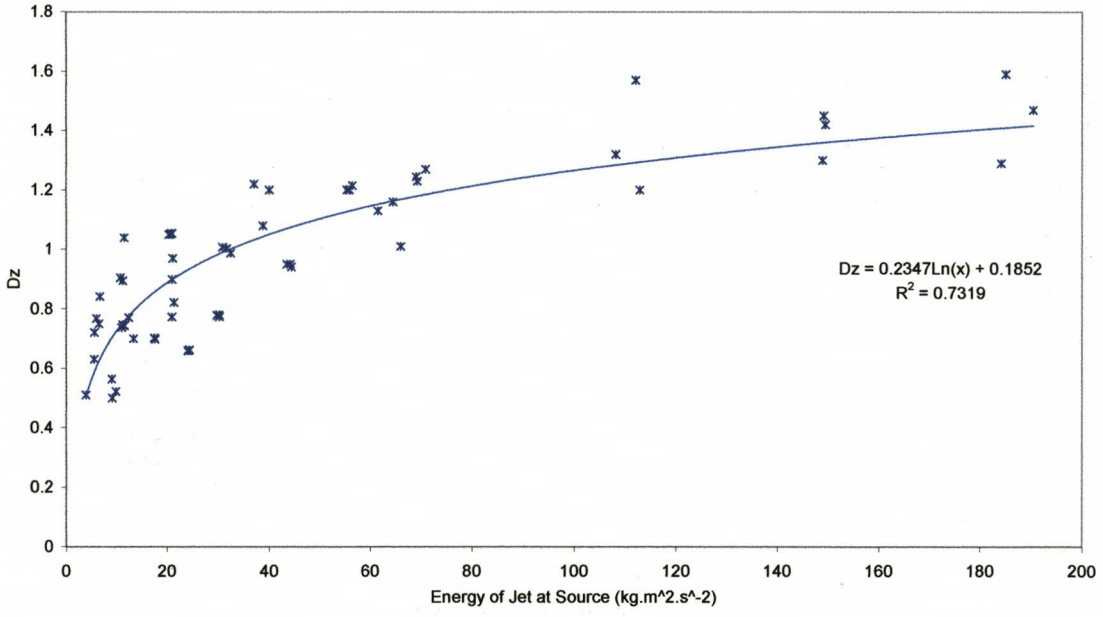

Figure 6.6 Modified cavity depth fraction against the energy of the jet at its source for the nozzle distribution experiments

Therefore the above indicates that the value of D_z increases with increasing flow rate, and since the size of the fluidised area increases with increasing D_z, the resulting force reduces with increasing D_z. Incorporating the function between D_z and flow rate in the model would increase the sensitivity between flow rate and tool force, and thus increase the gradient in Figure 6.1.

6.4 Conclusion

It is concluded that the force model developed in Chapter 2 embraces the appropriate mechanisms of force reduction on jet assisted tools acting in saturated sands, yet the soil stress profile about a cavity is more complex than that assumed by the model. Also, the cavity depth model developed in Chapter 5 incorporates appropriate mechanisms to simulate cavity development, yet does not account for the relationship between the jet energy level and D_z.

7 Conclusions and Recommendations

7.1 Conclusions

This Chapter contains the macro conclusions to the project. Detailed conclusions relating to each aspect of the study are contained at the end of each Chapter. This research project has significantly extended the knowledge and understanding of the mechanics of jet assisted ploughs in the subsea burial of cables in the following areas;

1) Investigations into the cavity created by a single horizontal jet internal to the soil found;
   a) The velocity of the cavity boundary to be a function of the cavity length.
   b) The cavity length is an inverse power function of the nozzle velocity when in dynamic equilibrium.
   c) A mathematical model was developed simulating the extent of the fluidised cavity created by a dynamic water jet in easily eroded saturated sands. Based on the conservation of jet momentum the cavity length and depth are determined from the tool velocity, soil hydraulic conductivity, soil and water densities and depth of nozzle below soil surface. The model gave very good fit to measured data, the average predicted length being 7% greater over the range of flow rates tested.

2) Investigations into the forces acting on jet assisted tines lead to the development of a mathematical model simulating tool force reduction generated by jetting, and the resulting draught force. Force reduction is determined from the size and position of the fluidised areas created by the jets, and the resulting draught force is determined by subtracting this from the passive (non-jetted) draught force.

3) Combining the above two models resulted in the predicted forces tending to be greater than the measured by more than twenty percent. The reasons are the soil pressure profile around a cavity is more complex than that adopted in the force reduction model, and the cavity depth fraction (D_z) being a function of the jet energy, which is not accounted for in the cavity model.

4) Study of force reduction on jet assisted tines found;

a) Water jets reduced soil force on the tool by creating fluidised areas in which the soil pressure was reduced.

b) The total soil pressure on the tool was reduced by;

   i) Increasing the fluidised area by increasing the jet momentum flux. Tool force reduced to negligible when the fluidised area fully covered the tool face.

   ii) Arrangement of the fluidised areas giving maximum tool face coverage, optimising their benefit.

   iii) Targeting the position of the fluidised areas on the tool face to the areas where the soil pressure is larger, by positioning the jets at greater depths on the tine face or by having downward angled jets. However, jet angles approaching vertical downward had a reduced fluidised area, due to the increased cross flow component of the soil on the jet flow path.

c) The combined effect of jet angle, rake angle and momentum flux on force reduction was complex, however, forward raked tines tended to generate greater forces than the vertical and backward raked tines.

d) Rake angle had no significant effect on soil forces for passive tools.

5) Studies of the soil pressure profile on the tool face found:

   a) Soil pressure acting on the tool face was found to increase approximately linearly with depth.

   b) To develop a passive tool force prediction model for saturated sands the approach of the pore pressure analysis of Coyne and Lewis was applied to the Godwin and Spoor narrow tine lateral soil failure model to incorporate a speed element. Further study is required to relate pore pressure changes to 'apparent' soil cohesion and internal friction angle to fully develop the model.

6) Study of the cavity created by a single static horizontal jet internal to the soil found:

   a) The cavity development differed considerably between sand and clay soils, being characterised by shear erosion in sands and pressure fracturing in clay.

   b) Larger cavities developed in fine sands with low hydraulic conductivity than in coarse sands. Mathematical models, based on the continuity of flow, were developed to simulate cavity development for coarse and fine sands.

7.2 Recommendations

This research program has made significant steps forward in the understanding of the mechanics of jet assisted cable burial tools. However, a longer term research program is required to gain a complete understanding of these mechanics. Three areas of further research coming out of this study are highlighted below.

1) Study of the soil stress profile on the tool.
   a) To develop a model predicting soil forces on tools in saturated sands by building on the analysis in Chapter 3 to establish the effect of pore pressure on the soil properties of apparent cohesion and internal friction angle.
   b) To determine the effect of a jetted cavity on the surrounding soil pressure profile, and to modify the force model of Chapter 2 accordingly.

2) Study of the erosion of a cavity by a jet internal to the soil.
   a) Incorporation of soil particle detachment forces into the cavity model, to accommodate soils with some particle cohesion.
   b) Relate the divergence angle of the jet to soil properties, in order to determine the depth to length ratio (G) theoretically.
   c) Determination of the effect of jet energy on cavity depth at the tool interface by examination of the cavities created by a single dynamic jet at a range of flow rates.
   d) Investigation into the effect of jet angle on cavity shape is required to understand the effect of jet angle on tool forces.

3) Study of a jet assisted tool
   a) Investigation of the interference of the tool on the jet flow path and the resulting effect on the cavity depth at the tool.
   b) Investigation of the interaction occurring between adjacent cavities, with particular attention on the soil section separating cavities and the force it exerts on the tool.

Many of the investigations in points 2 and 3 could be examined using a glass sided tank, as in the experiments of Chapters 4 and 5.

References

Adamson, J.E., Kolle, J.J. (1995). Development of a Waterjetting Cable Burial System for a Broad Range of Soils up to 2500 meters of Seawater. *Conf., Proc. of Underwater Intervention '95.* 1995.

Aderibigbe, O.O., Rajaratnam, N. (1996). Erosion of Loose Beds by Submerged Circular Impinging Vertical Turbulent Jets. *J. Hydraulic Res.* 34(1), 19-33.

Amirtharajah, A. (1978). Optimum Backwashing of Sand Filters. *J. Environmental Eng. Div. ASCE*, 104, 917-931.

Bagnold, R.A. (1953). *The Physics of Blown Sand and Desert Dunes*, Methuen, London.

Beltaos, S., Rajaratnam, N. (1974). Impinging Circular Turbulent Jets. *J. Hydraulics Division,* 1313-1328.

Beltaos, S. (1974). Oblique Impingement of Plane Turbulent Jets. *J. Hydraulics Division,* 1177-1192.

Breusers, H.N.C., Raudkivi, A.J. (1991). *Scouring, Hydraulic Design Considerations, Hydraulic Structures Design Manual. 2.* IAHR. ISBN 90 6191 983 5

Bormann, N.E., Julien, P.Y. (1991). Scour Downstream of Grade-Control Structures. *J.Hydraulic Eng.* ASCE, 117(5), 579-594.

Carson, M.A. (1971). *The Mechanics of Erosion*, p.29. Pion Limited, London. SBN 85086 029 6.

Chee, S.P., Yuen, E.M. (1985). Erosion of Unconsolidated Gravel Beds. *Can. J. Civ. Eng.* 12, 559-566.

Chiew, Y.M., Lim, S.Y. (1994). Local Scour by a Deeply Submerged Horizontal Circular Jet. *J. Hydraulic Eng.,* ASCE. 122(9), 529-532.

Coyne, J.C., Lewis, G.W. (1999). Analysis of Plowing Forces for a Finite-Width Blade in Dense, Ocean Bottom Sand. *Oceans 99 Conf., MTS / IEEE,* Seattle, Sept.13-16.

Dabbagh, A.A., Gonzalez, A.S., Pena, A.S. (2002). Soil Erosion by a Continuous Water Jet. *Soils and Foundations, Japanese Geotechnical Society*, 42(5), 1-13.

Davidson, J.F., Harrison, D., eds., (1971). *Fluidisation,* Academic Press, Inc. New York, N.Y.

Fort, J.A.,Hashish, M., Echert, D.C., Reichman, J.M. (1987). Feasibility of waterjet trenching in seafloor soils. Flow Proposal no. TD237068, Rev. 1Flow Research Company, Tech. Div., Washington.

Godwin, R.J. (1975) An Extended Octagonal Ring Transducer for use in Tilliage Studies. *J. Agric.Engng Res.* 20, 347-352.

Godwin, R.J., Spoor, G. (1977). Soil Failure with Narrow Tines. *J. Agric.Engng Res.* 22, 213-228.

Hill, J.A., Elliott, R., Messina, F.D. (1999). Development of an Improved Cable Trenching Plowshare. *Oceans Conference, MTS / IEEE*, Seattle, Sept. 13-16, 1999.

Hjulstrom, F. (1935). Studies of the Morphological Activity of Rivers as Illustrated by the River Fyris. *Bull. Geol. Inst. Univ. Uppsala,* 25, 221-527.

Hollick, M. (1976). Towards a routine assessment of the critical tractive forces of cohesive soils. *Trans., ASAE,* St. Joseph, Mich., 19, 1076-1081.

Hulburt, G.H., Cheung, J.B., Reichman, J.M., Marvin, M.H. (1978). Waterjet trenching of a simulated seafloor soil. *Flow Technology Report No. 115,* Prepaired for Civ. Engrg. Lab., Naval Construction Battalion Center, Port Hueneme, CA, by Flow Industries, Inc. Washington 98031.

Karim, O.A., Ali, K.H.M. (2000). Prediction of Flow Patterns in Local Scour Holes caused by Turbulent Water Jets. *J. Hydraulic Res.* 38(4), 279-287.

Knight, C.S. (2002). An Investigation into the Factors Influencing the Performance of Jet Assisted Submarine Cable Ploughs. Unpublished MSc by Research Thesis, Cranfield University at Silsoe.

Kober, J.H., Messina, F.D., Dean, D. (2000). New Advances in Jet-Assisted Plowing for the Undersea Cable Construction Industry. *Proc. Oceans 2000 Conf.– Where Marine Science and Technology Meet, MTS / IEEE,* Providence, RI, USA, Sept. 11-14.

Kobus, H., Leister, P., Westrich, B. (1978). Flow Field and Scouring Effects of Steady and Pulsating Jets Impinging on a Movable Bed. *J. Hydraulic Res.* 17(3), 175-192.

Lambe, T.W., Whitman, R.V. (1969). *Soil Mechanics,* p.439-454. John Wiley & Sons, Inc. SBN 471 51192 7.

Laursen, E. (1952). Observations on the Nature of Scour. *ASCE, Proc, 5th Hydr. Conf.,* No. 426, 179-197, June 1952.

Leifer, N., Fihn, E., Messina, F.D. (1999). New-Generation Undersea Cable Burial Plow. *MTS-IEEE Proc.* September. 1999.

Leliavsky, S. (1966). *An Introduction to Fluvial Hydraulics*, Dover Publications, New York.

Letterman, R.D. (1999). Water Quality and Treatment, A Handbook of Community Water Supplies. *American Water Works Association.* 5 Ed. McGraw-Hill. p8.12-8.71

Lewis, B. (2002). The Role of Jetting in Installation of Submarine Cables. Unpublished BEng. Dissertation, Writtle College, University of Essex.

Lewis, G.W., Messina, F.D. (1998). Development of a High Performance Jetter for Ocean Cable Burial. *Proc. Oceans '98 Conf., MTS / IEEE,* Baltimore, USA, Nov. 16-19.

Machin, J. (2000). Recent research on cable jet burial. *Marine Tech. Soc. J.,* 34(3), 5-10.

Mason, P.J., Arumugam, K. (1985). Free Jet Scour Below Dams and Flip Buckets. *J. Hydraulic Eng.* ASCE. 111(2), 220-235.

Mazurek, K.A., Rajaratnam, N., Sego, D.C. (2001). Scour of Cohesive Soil by Submerged Circular Turbulent Impinging Jets. *J. Hydraulic Eng.* ASCE. 127(7), 598-606.

Messina, F.D. (2000). Advances in Undersea Cable Burial Technology for the Twenty-First Century. *Underwater Intervention Conference, MTS*, Houston, TX (USA), Jan. 24-26.

Messina, F.D., Fihn, E., Hill, J.A. (2001). Enhanced Cable Burial Protection using Jet-Assisted Plowing. *Sea Technology*, Arlington, July 2001.

Mih, W.C., Kabir, J. (1983). Impingement of Water Jets in Nonuniform Streambed. *J. Hydraulic Eng.* ASCE. 109(4), 536-548

Mirtskhulava, Ts.E., Dolidze, I.V., Magomedova, A.V. (1967). Mechanisms and computation of local and general scour in non-cohesive, cohesive soils, and rock beds. *Proc., 12th Congr. Og IAHR,* Delft, The Netherlands, 3, 169-176.

Moore, W.L., Masch, F.D. Jr. (1962). Experiments on the scour resistance of cohesive sediments. *J. Geophys. Res.*, 67(4), 1437-1449.

Niven, R.K., Khalili, N. (1998). In Situ Fluidisation by a Single Internal Vertical Jet. *J. Hydraulic Res.* 36(2), 199-228.

Niven, R.K., Khalili, N. (2002). In Situ Fluidisation for Peat Bed Rupture, and Preliminary Economic Analysis. *J. Contaminant Hydrology.* 59(1-2), 67-85.

O'Donoghue, T.O., Trajkorvic, B., Piggins, J. (2001). Sand Bed Response to Submerged Water Jet. *Proc. Eleventh International Offshore and Polar Eng. Conf.* Stavanger, Norway, June 17-22, 2001. p.66-72.

Rajaratnam, N. (1976). *Turbulent Jets*, Developments in Water Science, p27. Elsevier Scientific Publishing Company.

Rajaratnam, N. (1982). Erosion by Submerged Circular Jets. *J. Hydraulics Div.* ASCE, 108(HY2), 262-267.

Rajaratnam, N., Beltaos, S. (1977). Erosion by Impinging Circular Turbulent Jets. *J. Hydraulics Div.* ASCE. 103(HY10), 1191-1205.

Rajaratnam, N., Mazurek, K.A. (2002). Erosion of a Polystyrene Bed by Obliquely Impinging Circular Turbulent Air Jets.. *J. Hydraulic Res.* 40(6), 709-716.

Rajaratnam, N., Mazurek, K.A. (2003). Erosion of Sand by Circular Impinging Water Jets with Small Tailwater. *J. Hydraulic Eng.* ASCE, 129(3), 225-229.

Raudkivi, A.J. (1990). *Loose Boundary Hydraulics,* 3rd Ed. p28. Pergamon Press. Oxford. ISBN 0-08-034073-3

Reece, A.R., Grinstead, T.W. (1986). Soil Mechanics of Submarine Ploughs. *Proc. 18th Offshore Technology Conf.* Houston, Tex., May 5-8, 1986, 453-459.

Rockwell, P.K. (1976). Deep ocean cable burial concept development. TN-1453, Civil Engineering Laboratory, Naval Construction Battalion center, Port Hueneme, CA, 93043.

Rockwell, P.K., Engel, J.H., Piercy, W.B. (1980). Field tests of a deep ocean cable burial concept. *Proc., 12th Offshore Technology Conf.* Houston, Tex., May 5-8, 1980.

Rouse, H. (1939). Criteria for Similarity in the Transportation of Sediment. *Proc. Hyd. Conf. Studies Eng. Bull.* Univ. of Iowa, 33-49.

Sanks, R.L. (1978). Water Treatment Plant Design for the Practicing Engineer. Ann Ardor Science.

Shields, A. (1936). Anwendung der Ahnlichkeitsmechanik und der Turbulenzforschung auf die Geschiebebewegung, *Mitt. Preuss. Vers Anst. Wasserb. Schiffbau,* 26.

Smith, D.L.O., Godwin, R.J., Spoor, G. (1989). Modelling Soil Disturbance due to Tillage and Traffic. *Mechanics and Related Processes in Saturated Agricultural Soils.* 121-136. Kluwer Academic Publishers.

Stein, O.R., Julien, P.Y., Alonso, C.V. (1993). Mechanics of Jet Scour Downstream of a Headcut. *J. Hydraulic Res.* 31(6), 723-738.

Terzaghi, K., Peck, R.B., Mesri, G. (1996). *Soil Mechanics in Engineering Practice*, 3rd Ed. p.134-145. John Wiley & Sons, Ins.

True, D., Girard, J. (1998). Thin-Blade Plow Behavior in Seafloor Sand. *Proc. Oceans '98. Conf., MTS / IEEE,* Baltimore, USA, Nov. 16-19.

Wheeler, P.N., Godwin, R.J. (1996). Soil Dynamics of Single and Multiple Tines at Speeds up to 20 km/h. *J. agric. Engng Res.* 63, 243-250.

White, C.M., 1940, Equilibrium of Grains in the Bed of a Stream, *Proc. Roy. Soc.* (London), Ser.A, 174, 322-334.

Bibliography

Annandale, G.W. (1995). Erodibility. *J. Hydraulic Res.* 33(4), 471- 494.

Atmatzidis, D.K., Ferrin, F.R. Laboratory Investigation of Soil Cutting with a Water Jet. (Source not known).

D'Agostino, V., Ferro, V. (2004). Scour on Alluvial Bed Downstream of Grade-Control Structures. *J. Hydraulic Eng.* ASCE. 130(1), 24-37.

Hogg, A.J., Huppert, H.E., Dade, W.B. (1997). Erosion by planar turbulent wall jets. *J.Fluid Mech.* 338, 317-340.

Nearing, M.A., Foster, G.R., Lane, L.J., Finkner, S.C. (1989). A Process-Based Soil Erosion Model for USDA-Water Erosion Prediction Project Technology. *Soil & Water Div. Asae.* 32(5), 1587-1593.

Appendices

Appendix 1

The Development of an Improved Soil Preparation Method for the Wet Soil Bin

Contents

A1 The Development of an Improved Soil Preparation Method for the Wet Soil Bin

A1.1 Introduction

Knight (2002) had in previous work conducted similar experiments, at Cranfield University at Silsoe, in which tines were pulled through sand in the wet soil bin. He adopted a method similar to one that had previously been used at the University, after his initial trials with another method had failed to reproduce consistent soil conditions. Details of those methods are summarised below.

A1.1.1 Concrete Vibrator Probe Method

The initial preparation method consisted of pushing a concrete vibrator probe into the saturated soil to a depth of about 0.4m and held there for about 20 seconds. This was repeated at 0.3m intervals along the length of the soil bin. It was hoped that the vibrations would consolidate the low density soil, in the trench created by the tine, producing a uniform soil density and strength for the whole bin.

This method was found to be effective in creating a uniform soil level across the whole of the soil bin. However, it was found that each repetition of the method consolidated the soil further, so much so that after ten repetitions the soil was so dense a tine was bent when being pulled through it. A form of soil loosening was evidently required. The method consequently proved to be inadequate and was not employed.

A1.1.2 Rodding Method

The alternative method developed worked on the basis of mixing the low density soil in the trench with the adjacent denser soil. It consisted of manually pushing a rod, of 20 mm diameter, to a depth of 0.35 – 0.4 m into the soil alongside the trench. The rod was then forced forwards, then to the right and left in a figure of eight shape. This was repeated at 0.3 m intervals along each side of the trench. A levelling tool was then pulled along the length of the tank to ensure a consistent soil depth between tests.

Tests were conducted to determine the ability of the method to produce consistent soil conditions between tests. The force exerted on a passive tine pulled through the soil was used to give an indication of the soil strength. Analysis of the results showed no trend of an increase in the soil strength with subsequent repetitions.

However, despite the method showing continuity between tests, if failed to produce a uniform soil strength along the length of the tank. Figure 3.1 shows an oscillatory form to the force exerted on the tine. The amplitude of the oscillations was greater in tests with higher forces. It was noticed that the typical number of oscillations in a test was approximately 10, the wavelength being similar for all tests, about 0.3 m. It was suspected therefore that the variation in force was caused by the rodding in the preparation method. This was confirmed by a couple of tests, the first having only two prods with the rod and the second having about 25. After pulling a passive tine through the soil in each case, the first test showed a steady force except for two force peaks where the rod had been inserted, and the second test showed many peaks. This confirmed that the insertion of the rod caused a localised compacting of the soil. Still, Knight used the preparation method since he considered the variation to be consistent throughout his experiments.

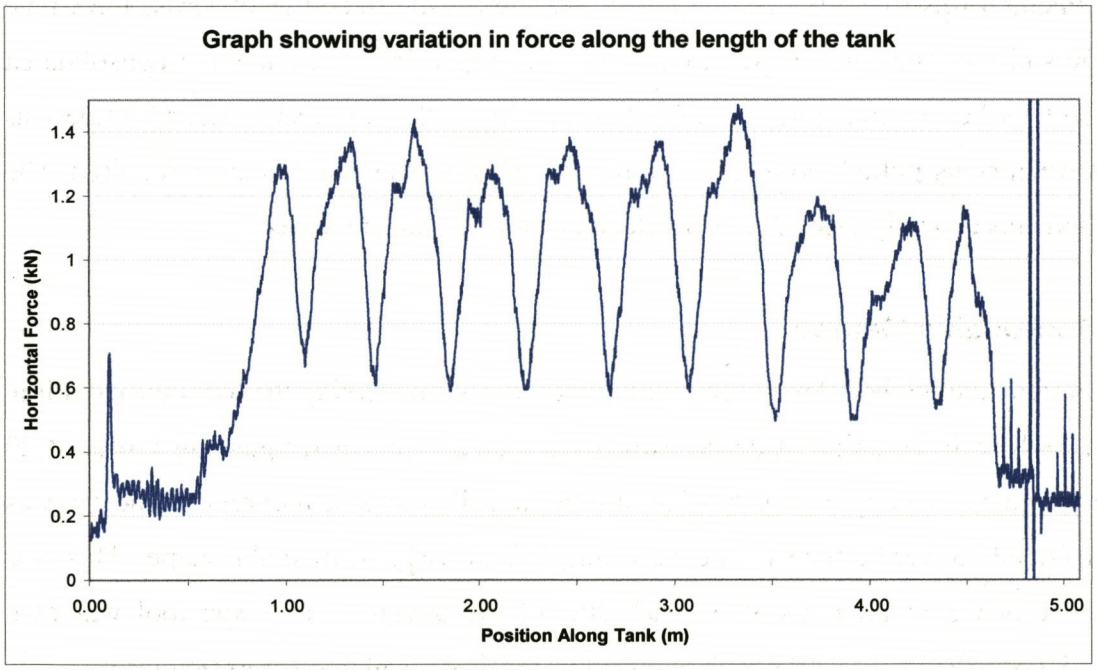

Figure A1.1 Example of variation in draught force in the wet soil bin using the Knight (2002) soil preparation method.

The example in the above Figure has a mean force value of 0.89 kN, a standard deviation of 0.25 kN giving a coefficient of variation of 28.3 %, which in some tests was up to 125 %. It was therefore thought desirable at the outset of this study to develop a preparation method that created consistent soil conditions within and between tests.

A1.1.3 Objectives of soil Preparation Method

The objectives of a new soil preparation method are;

1. To create repeatable and consistent soil conditions.
2. To create a uniform soil condition throughout the tank.
3. To consolidate soil fluidised by the previous jetting tine, while loosening dense and compacted soil.
4. To produce a soil strength similar to that used in the previous work of Knight (2002).
5. To prepare the soil down to a depth of at least 0.4 m.
6. Minimum time endurance for preparation completion.

A1.2 Review of Design Techniques

A variety of potential solutions were considered, but generally consisted of two types. Firstly there was the type that used implements to mechanically move the soil, while the second used water to prepare the soil. Some of the concepts were developed somewhat and tested, and are discussed in section 3.5 – 3.8, but the remainder are presented below.

Three types of potential solutions are considered, some were developed and tested to evaluate their performance. The three types are;

a) Mechanical Techniques
b) Jetting Techniques
c) Fluidisation

A1.2.1 Mechanical Techniques

a) Rotating Tines

A horizontal shaft with curved tines attached would be dragged over the surface of the soil, the soil force on the tines causing the shaft to rotate, mixing the soil as it did so.

However, to penetrate to the required depth the implement would need a diameter of nearly 0.9 m (2 x 0.45 m) and would thus prove impractical.

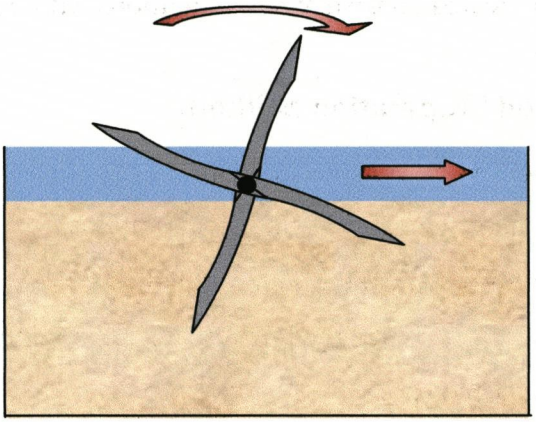

Figure A1.2 Diagram of rotating tines concept

b) Rotating Harrows

Two pairs of counter-rotating vertical harrows mix soil laterally as they move through the soil. The harrows would be rotated mechanically or driven by their movement through the soil. However, the power to drive them and the horizontal force would be considerable.

c) Rotating Drum

A horizontal drum, rotating about its longitudinal axis, shifting soil either over or under it as it travels the length of the tank. However, the required diameter of the drum would be large in order to reach the required working depth, making it cumbersome. A diagram of the concept is shown in Figure A1.3.

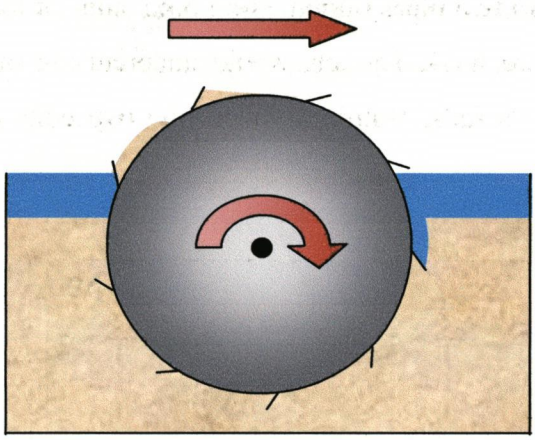

Figure A1.3 Diagram of rotating drum concept

d) Horizontal Subsurface Blade

A horizontal blade inclined at a shallow angle would be pulled through the soil just below the working depth of the tines. The idea was to lift the soil, the movement causing sand particles to consolidate in the fluidised region, while loosening particles in compacted zones.

e) Vibrating Tine

A vibrating tine, able to prepare the soil through two mechanisms. Firstly, by creating a zone of soil disturbance as it passes through the soil, loosening compacted regions, as in agricultural practices. Secondly, the vibration element is to consolidate the soil, increasing the density of fluidised areas. The additional purpose of the tine was to transmit the vibration to depth within the soil. The combined action of the two elements was aimed to create a homogeneous soil condition.

A1.2.2Jetting Techniques

Previous work by Knight (2002) in the wet soil bin had observed the effects of water jet assisted tines on the sandy soil. He noted that at high jet pressure (6 bar), or slow tine velocity, the jets created a large fluidised cavity. This jetting action could be used to fluidise the whole tank, creating a uniform soil condition throughout. A vibrating tine could then be used to consolidate the soil.

Two methods of fluidising the soil were considered and are outlined below.

a) Jetting from Buried Pipes

Water jets originating from two pipes buried along both sides of the tank would fluidise the soil as shown in Figure A1.4. The jets would undercut the sand forming a cavity, into which the above sands falls. Within a short time two eddy currents would form creating soil mixing.

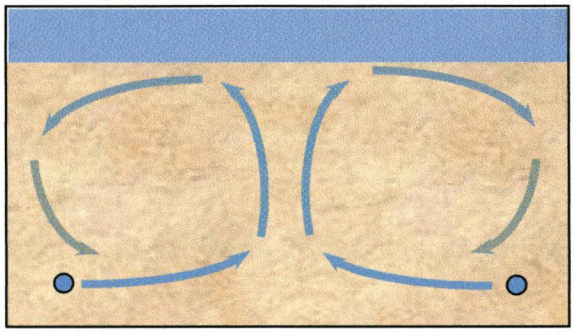

Figure A1.4 Diagram showing cross section through soil bin with two jetting pipes

b) Jetted Tines

Two jetted tines passing along either side of the tank, each with forward facing jets to create a passage for the tine to pass through, and inward facing jets to mix the sand between the tines. The tines require a greater working depth than that of the implements. It was anticipated this method would guarantee a uniform soil treatment along the whole length of the tank, whereas te buried pipes method may have experienced differences due to pressure loss along the pipe lengths. For this reason the jetted tines method was chosen to develop further. Figure A1.5 shows a diagram of the jetted tines.

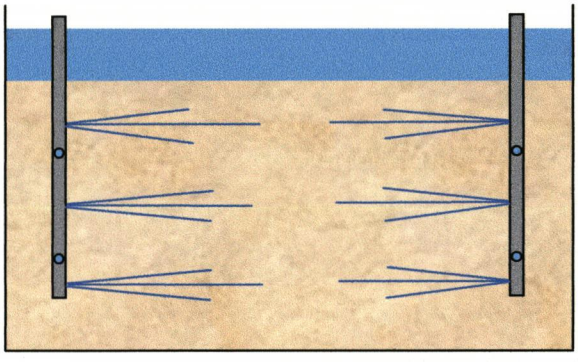

Figure A1.5 Cross section through tank showing two jetting tines

The jetting method would also require two further stages, being;

i. Levelling the sand surface, using a blade, to create a constant working depth.
ii. Reconsolidating of the soil using a vibrating tine.

A1.2.3 Fluidisation

Sand filters in the water treatment industry are purified by an upwashing of water through the sand pores, fluidising the bed. This process is developed to form a preparation method.

According to Davidson & Harrison (1971), Letterman (1999) and Amirtharajah (1978) fluidisation describes the upward flow of fluid through a granular bed at a sufficient velocity to suspend the grains in the fluid. If a fluid flows up through a bed of solid particles the pressure drop of the fluid will initially rise linearly as the velocity increases, the relationship being described by the Carman-Kozeny equation, for fine particles. As the fluid velocity is increased further a stage is reached where the pressure drop equalises the buoyant weight of the solid particles, and is the maximum pressure drop achievable across the bed. The particles will then begin to separate and go into suspension, which is the point of incipient fluidisation. Increasing the fluid velocity further will cause the particles separation to increase further creating a volume expansion of the bed, although the pressure loss will remain relatively constant. The fluid velocity at the point of incipient fluidisation is termed the 'fluidisation velocity' and can be calculated by the equation derived by Wen and Yu (1966) as:

$$V_{mf} = \frac{\mu}{\rho d_{eq}}(33.7^2 + 0.0408\,Ga)^{0.5} - \frac{33.7\mu}{\rho d_{eq}}$$

A1.1

where Ga is the dimensionless Galileo number:

$$Ga = d_{eq}^3 \frac{\rho(\rho_s - \rho)g}{\mu^2}$$

A1.2

The theoretical fluidising velocity for the soil in the wet soil bin was calculated as 0.000321 m/s (1.154 m/h) giving a total flow rate of 1.92 l/s (or 2.5 l/s with an extra 30% margin as recommended).

Figure A1.6 shows an ideal pressure drop – velocity curve, and the fluidisation velocity marked as the point where the fixed bed region intercepts the fluidised region.

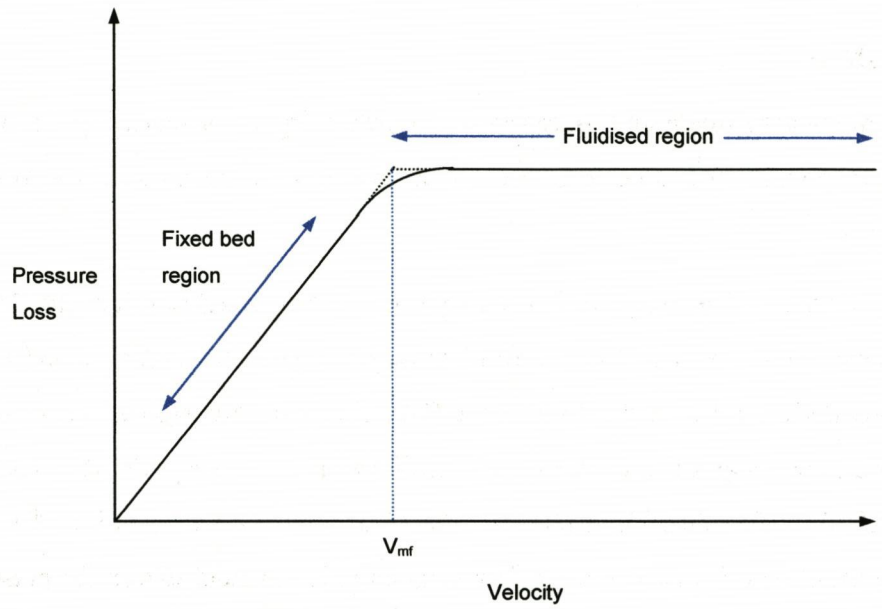

Figure A1.6 Pressure drop – velocity curve for a fluidised bed. (Davidson & Harrison, 1971)

The fluidisation velocity is partly dependent on the particle size, the smaller particles becoming fluidised at a lower velocity than larger particles. In the case of a bed containing a range of particle sizes, there is a gradual change from the fixed bed to the fluidised stage, shown by the curve between the two regions in Figure A1.6. Therefore when calculating the fluidisation velocity the larger particle size must be used, usually the D_{90} value, to ensure complete fluidisation (Letterman 1999).

Fluidising can stratify the particles by size, smaller particles with lower bulk density and fluidising velocity shift to the top, while the larger denser particles with a higher fluidising velocity settle to the bottom. However, this process is often partially compensated by nonuniform upflow of the fluid creating localised regions of above average velocity, termed sand boils or gulf streaming. This creates eddy currents in which larger particles are transported readily to the surface while in adjacent regions the downward movement forces finer particles towards the base. Higher upwashing velocities often create the more turbulent flow patterns, so stratification occurs more readily at velocities barely exceeding the fluidisation velocity. However, if the velocity in the sand boil regions becomes excessive they form channels in the bed, with a large

proportion of upflow fluid passing through them, resulting in the remainder of the bed being unfluidised. Once a channel has formed, it will increase in size as the flow rate through it increases, and are therefore undesirable features in a fluidised bed.

The upflow fluid is usually delivered to the base of the bed through a series of nozzles or porous medium. To avoid the formation of channels, the fluid should be turned on gradually over a period of 30 seconds, to allow the particles to fluidised gradually. If the fluid is turned on suddenly it begins to lift the whole bed until a weakness allows the formation of a channel.

The fluid distributor at the base of the bed can also have a significant effect on the formation of channels. To prevent channel formation the distributor should be a porous structure with fine texture to allow an even distribution of the fluid. A coarse distributor gives high injection rates at specific points increasing the likelihood of channel formation. With large beds a porous structure may have poor mechanical strength, and therefore a coarser distributor is often necessary, yet may create channelling problems.

The water treatment industry uses sand as the bed medium and has water distributors (underdrains) at the base of the bed. A range of types of underdrains are used, the simplest and most appropriate to the wet soil bin being the manifold-lateral system, in which perforated laterals are positioned regularly along the base of the bed. Perforations in the laterals are 6 – 13 mm in diameter and located at 80 – 300 mm spacing. Other types are more complex, using false floors with nozzles protruding through at between 130 – 300 mm spacing, with openings of about 6 m diameter or in some cases very fine openings that retain the filter medium.

The approach adopted to develop a fluidising preparation method consisted of three stages, being;

1. Pilot tests to establish the feasibility of the upwashing concept for a preparation method, and to determine a realistic design for the lateral system. These are detailed in Section A1.3.3.
2. The second consisted of four investigations into the effects of upwash flow rate combined with mechanical aids, with the purpose of optimising soil uniformity,

3. Uniformity tests were conducted on the developed preparation method to examine its fulfilment of the objectives

The second and third stages are detailed in Section A1.4.3.

A1.3 Equipment Design

A1.3.1Mechanical Techniques

a) Horizontal Subsurface Blade

A trial blade was fabricated and a number of tests conducted to investigate the idea. Details of the design are shown in Figure A1.7.

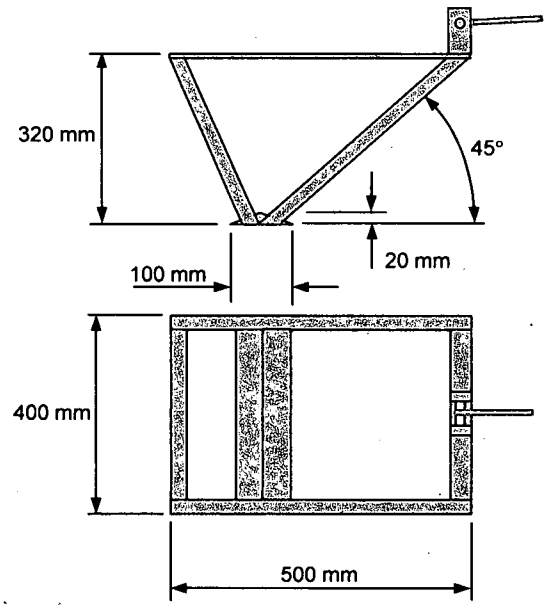

Figure A1.7 Design of horizontal subsurface blade equipment

b) Vibrating Tine

A trial tine was fabricated and a number of trials were conducted. Details of the design are shown in Figure A1.8.

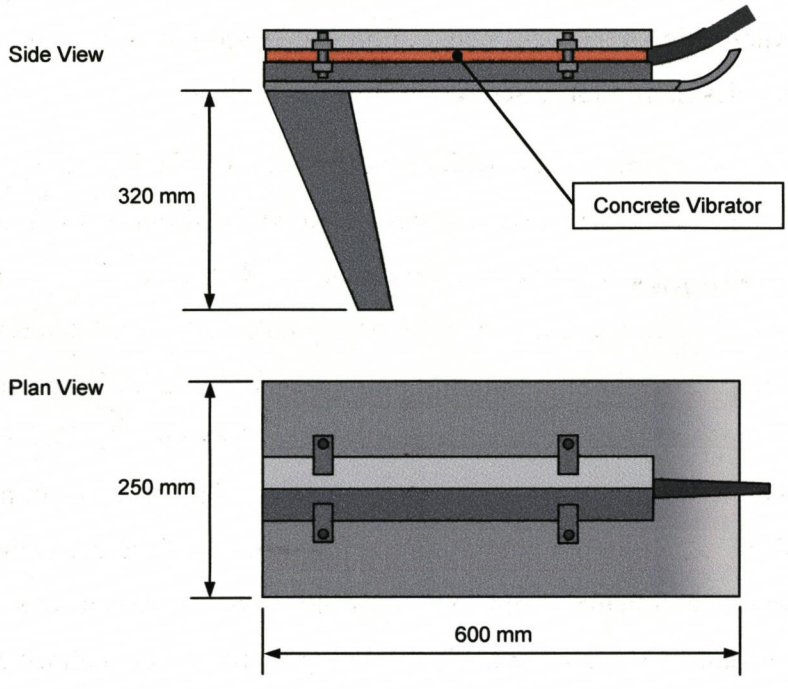

Figure A1.8 Design of vibrating tine apparatus

A1.3.2Jetting Techniques

Pilot trials were conducted to prove the concept and optimise the design, particularly the nozzle positions and diameter of the nozzles. Initial trials used four inward and two forward facing jets. The diameters of the all the jet nozzles were 4 mm. Initially the penetration of the inward facing jets were insufficient to reach the centre of the tank, thus to compensate the tines were positioned closer to the centreline. Two jets were added on the outward side of each tine. However, the increased number of jets reduced the performance of the inward facing jets, in due to the reduced pressure drop across the nozzles and decreased jet penetration. A solution without outward facing jets was thus desirable.

Therefore to increase the penetration of the inward facing jets the nozzle diameters were increased to 7 mm and the forward velocity of the tines was halved. At the maximum possible jet pressure (6 bar) the jets fluidised the full width of the tank except the central 200 mm section. However, shortly after the tines passed, the flow of water eroded some of that section, and it was thought that the action of the vibrating tine would disintegrate the remainder of it.

Two passes of the vibrating tine produced a moderate soil density, creating 450 kPa penetration resistance when using a standard penetration cone. Equipment for full trials was built according to the design in Figure A1.10.

The equipment comprised of a trolley onto which two tines and levelling blade were mounted. The tines and the blade were hinged so they could be lifted out of work when not required. The trolley was mounted onto the top of the soil bin tank. The vibrating tine (vibroskid) consisted of a separate unit having two very narrow forward raked tines mounted onto the base of a sheet of metal spanning nearly the full width of the tank. A concrete vibrator probe was mounted onto the upper surface of the sheet. The sheet had two spurs spanning from the concrete vibrator to the positions of the tines to transmit vibration to the tines. The tines were positioned 200 mm either side of the centreline of the tank, not where the experimental implements would pass. A winch was also mounted on the end of the tank, to which the trolley or vibrating tines were connected.

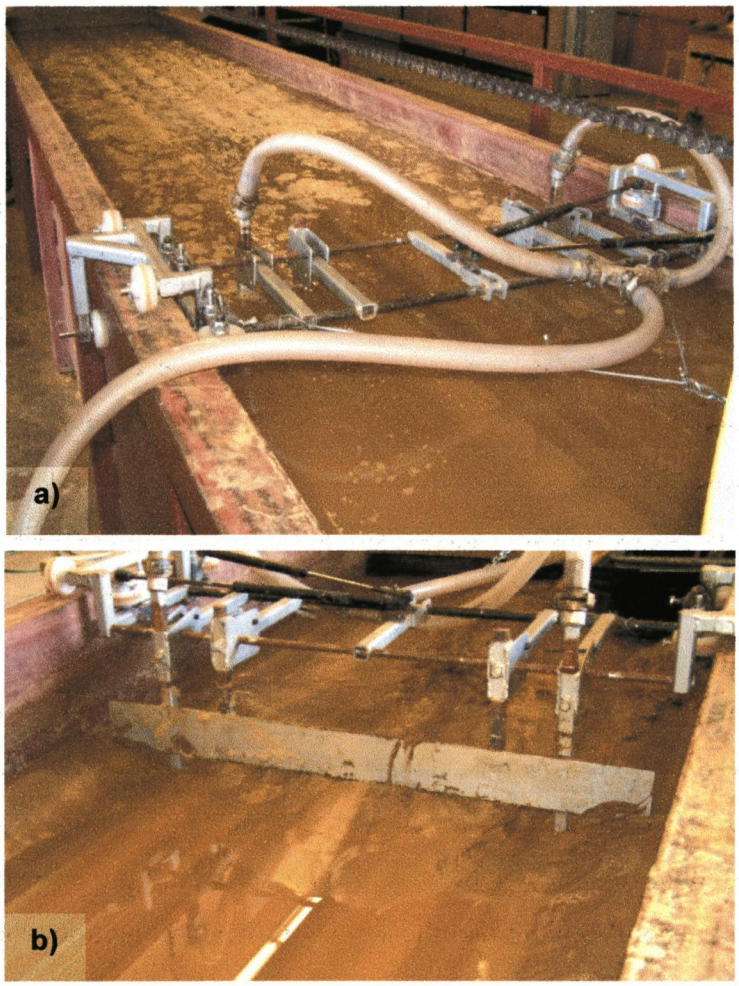

Figure A1.9 Jetted trolley a) during operation, b) after jetting

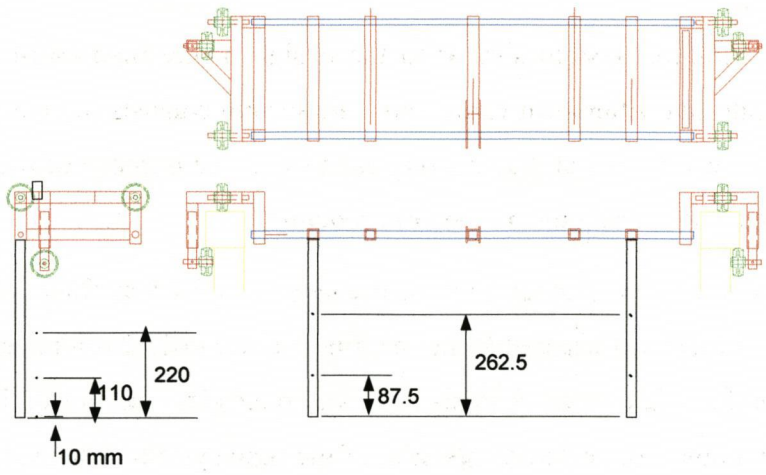

Figure A1.10 Design of jetting trolley

A1.3.3Fluidisation

Pilot tests were conducted to determine a suitable design for the upwashing system by developing the method initially on a small-scale to ensure its suitability before building a full-scale system for the tank. Pilot tests were conducted on a number of distributor types and the results used to develop a satisfactory system.

1. Pilot test No. 1

An initial test was conducted to establish suitability of the upwashing concept. It consisted of an irrigation hose buried at a depth of 0.4 m below the surface of the soil in the wet soil bin. Water was supplied to the hose at pressures up to 2.5 bar, creating fine jets emerging from small perforations along the length of the hose. The jets created small vertical channels of fluidised sand rising to the surface, producing a shallow cone shape at the surface where the sand was deposited. The jets, and hence channels, were originally at approximately 150 mm intervals, leaving areas of harder soil between the channels. To reduce the spacing, perforations were put in the hose at 30 mm intervals, creating almost overlapping channels. The whole mass of soil in the vicinity above the hose was either fluidised, as in the channels, or semi fluidised, between the channels. It was then found that gentle vibration of the soil after the water jets were turned off created a more homogeneous soil condition, demonstrating the potential suitability of the upwashing technique as a preparation method.

2. Pilot test No. 2

An upwasher distribution system similar to the design of the manifold-lateral system used in commercial sand filters was examined. The system consists of an array of lateral pipes, each with a series of small holes along each side. The purpose of the tests was to determine suitable lateral spacing and the hole spacing.

The tests were conducted in a small tank measuring 0.9 x 0.65 m filled with sand to a depth of 0.4 m. Water was drained from the tank via a vertical drainage pipe in one corner. A distribution system was built from waste water pipe and placed in the bottom of the tank, with a hose connected to the inlet of the pipe system. The system consisted of three laterals, 0.6 m long, initially with a spacing of 0.3 m, but later reduced to 0.2 m. All laterals had holes along each side, at a spacing of 0.04 m on alternate sides. The diameter of the holes was minimised to restrict the flow of soil into them when there was no jet pressure, yet to prevent them from blocking were larger than the largest sand particles, having a diameter of 1 mm. Figure A1.11 shows a diagram of the apparatus.

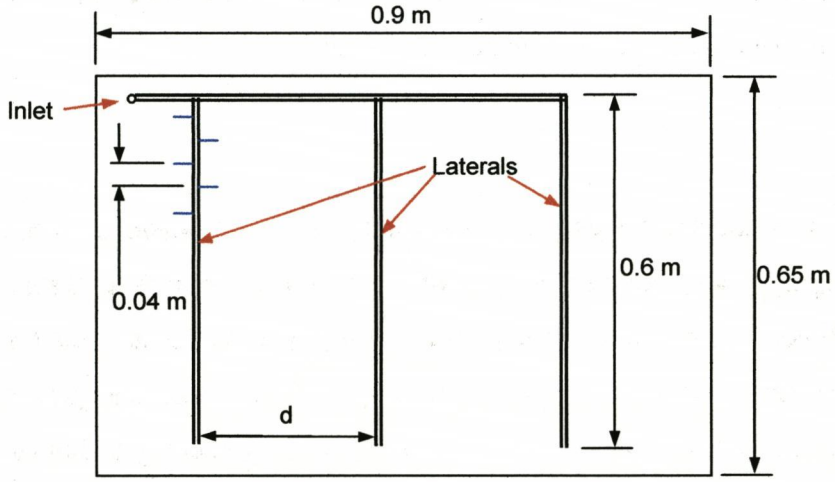

Figure A1.11 Plan view of pilot test apparatus

Methodology of pilot tests

Initially tests were conducted with a larger lateral spacing (0.3 m), then were reduced to 0.2 m to compare the performance. The spacing was based on that of commercial systems.

The individual pilot tests were conducted using the following methodology.

i. The surface of the sand in the pilot tank was levelled with the aim of creating a uniform soil condition.

ii. The water pump was initiated and the water pressure to the laterals was slowly increased to the desired setting over a period of about 15 seconds. The upwashing was timed from the moment the control valve was opened.

iii. During the upwashing process the behaviour of the sand and water movement was observed.

iv. On completion the surface water was drained and the 'sand boils' patterns studied.

v. Soil penetration readings were taken on two of the tests, using a standard soil penetrometer to give an indication of the uniformity of the soil condition.

For each lateral spacing, tests were conducted at a number of upwasher flow rates and duration times to study the ability of the technique to uniformly fluidise the sand and its condition at the end of the process.

3. Results and Discussion of Pilot Tests

Figure A1.12 to Figure A1.14 show the progressive stages of the upwashing process. Figure A1.12 shows the compact and uniform sand surface before upwashing. Figure A1.13 shows the first sand boil rupturing the surface after one minute operating at 0.8 bar (<0.2 l/s). Previously water seeped up through the sand surface creating a little movement of sand particles. After the initial 'sand boil' formed, numerous others formed, with their flow paths tending to shift with time. Figure A1.14 shows the drained sand surface after 4.5 minutes of upwashing at 1 bar (0.22 l/s). The three horizontal darker sand patches reflect the positions of the three laterals, with boil points in the interlaying areas. The water jets exited the laterals horizontally, thus explaining this pattern. Similar patterns were created by all the flow rates, only the greater flow rates produced larger and generally more even sand boils.

The smaller lateral spacing of 0.2 m resulted in reduced areas between sand boils. Despite the presence of sand boils there was little variation in the strength of the sand when the operator pulled their hand through it. At the end of each test the whole sand mass was in a semi fluidised state, requiring mechanical input to consolidate it.

Figure A1.12 Pilot tank before upwashing

Figure A1.13 First 'sand boil' appearing after one minute

Figure A1.14 Soil surface after upwashing at 0.22 l/s

Thus, the pilot test showed;

vi. The lateral pipe upwashing system was capable of partially fluidising the sand.

vii. Sand boils were easily created, but at the end of the process there was little spatial variation in sand strength.

viii. Lateral spacing of 0.3 m was adequate, but 0.2 m was had an improved performance.

After conducting the pilot tests, the design shown in **Error! Reference source not found.** was developed for the full scale upwashing lateral system. A detailed drawing is in Figure A1.15. Key design features of the system were;

i. Laterals were spaced at 0.25 m, being mid way between the two values in the pilot tests. The 0.2 m spaced laterals performed very well, the 0.3 m spaced laterals had performed adequately and required less of them, thus the 0.25 m was chosen for the full scale design.

ii. Water nozzles were spaced at 0.08 m intervals along both sides of the laterals. The nozzles on each side of a lateral were offset by 0.04 m to the other side, creating an even distribution of upwash water.

iii. Nozzle diameter was 1 mm, the same as in the pilot tests.

iv. Water was introduced midway down the lateral supply pipes, to minimise the maximum pressure difference between laterals.

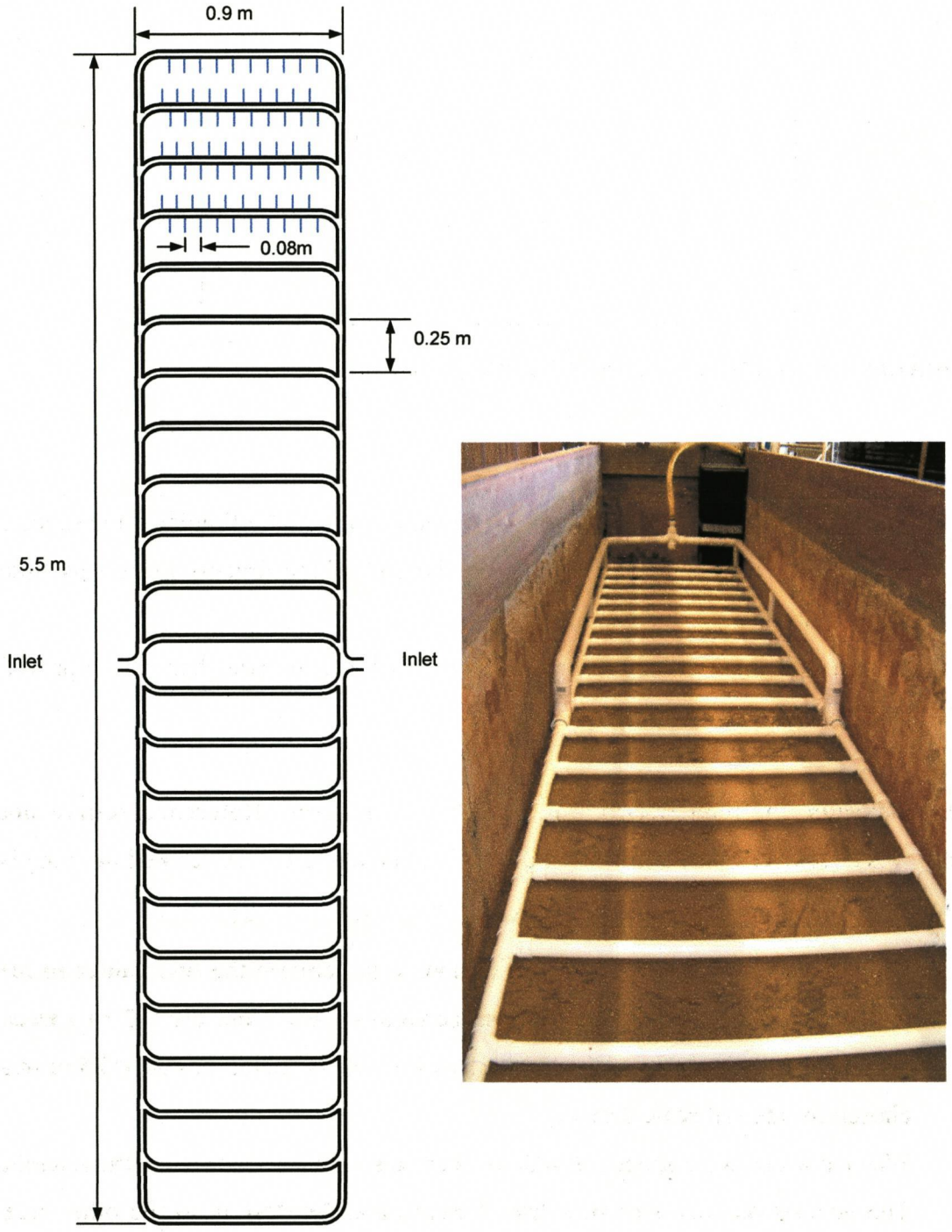

Figure A1.15 Design of upwash lateral system

A1.4 Experimentation

A1.4.1 Mechanical Techniques

a) Horizontal Subsurface Blade

To test the equipment a winch was attached to the hitch point and then pulled the blade along the length of the soil bin. In initial tests the blade was allowed to penetrate under its own weight, in secondary tests a mass of 40 kg was added to the frame.

b) Vibrating Tine

The tine unit was attached to a winch and pulled the length of the wet soil bin. Tests were conducted with and without tine vibration.

A1.4.2 Jetting Techniques

Uniformity tests were conducted to examine whether the jetted tines preparation method satisfied its objectives. The draught force of a passive time (measuring 280 mm deep by 30 mm wide) was used as an indicator of soil strength. the jetted tines preparation method was used between each test. The following methodology was used;

i. The levelling blade and jetting tines were put into their working positions with the trolley at the far end of the tank. Two narrow holes were dug in the sand to enable the tines to be rotated to their vertical working position.
ii. The jets were operated at 6 bar, with initially 10 mm of headwater on the sand surface.
iii. The winch pulled the trolley along the length of the tank at 40 mm/s.
iv. Upon the trolley reaching the end of the tank the water pump was switched off and the surplus water drained from the tank
v. The vibrating tine skid was pulled the length of the tank by the winch, and while vibrating.
vi. The passive tine was connected to the EORT force transducer and pulled through the soil at 500 m/h. The force was converted using a Flyde data acquisition module and recorded onto computer using DasyLab v7.0.
vii. The passive tine was then removed from the soil.
viii. Steps i. to vii. were then repeated a total of seven times.

The acquired data was then analysed on Microsoft Excel.

A1.4.3Fluidisation

Investigation into the Effect of Upwasher Flow Rate – Total Flow being Constant

A key factor in operating the upwashing system is the upwash flow rate. As stated in Section A1.2.3 the theoretical upwashing flow rate for the wet soil bin was 2.5 l/s with the recommended 30% extra margin. Part of the requirements of the upwashing system were to use minimal time and water. However the relationship for the system between flow rate, total flow and time were unknown. Therefore the objective of this investigation was to determine the effect of differing upwash flow rate on soil condition, given a constant total flow.

To conduct experiments using three flow rates and a constant total cumulative flow. Each flow rate was replicated three times in a block design. The draught force on a passive tine pulled through the soil was to give indication of the condition of the sand after the upwash process.

Details of the flow rates and upwash endurance times are shown in Table A1-1 Preliminary tests were used to determine appropriate flow rates.

Table A1-1 Flow rates and upwash endurance times

Flow Rate (l/s)	Duration Time (minutes)	Cumulative Flow (l)
1	4	240
1.3	3	≈ 240
1.5	2.5	≈ 240

The experimental procedure was as follows.

i. The upwash was operated for the time duration corresponding to the flow rate for each test.

ii. After two minutes of upwashing, the concrete vibrator probe was pulled through the sand along the length of the tank, taking approximately thirty seconds. This consolidated the sand.

iii. After the completion of the upwashing process the concrete vibrator probe was again pulled through the sand along the length of the tank.

iv. The draught force on a passive tine were measured and recorded in the same manner as described in Section 2.5.1 of Chapter 2.

v. The tine was removed from the soil bin.

vi. Steps i.– v. were repeated for each test.

Investigation into the Effect of Vibration

The aim of this investigation was to gain an understanding of the effect of the speed of the concrete vibration probe on the soil condition.

The objectives were;

i. To determine the effect of the vibrating probe on the soil strength profile.

ii. To determine the effect of vibrating probe speed on the soil strength.

The methodology was to conduct four simple tests, each having a different vibrating probe forward speed. The horizontal force exerted on a passive tine pulled through the soil gave an indication of the soil condition.

The four vibration probe treatments were;

i. No vibration except at one point midway along the length of the tank.

ii. Slow vibration probe forward speed, 0.05 m/s.

iii. Fast vibration probe speed, 0.167 m/s.

iv. Alternating between the slow and fast forward speeds in 0.5 m intervals.

The experimental procedure was the same as used in the investigation into the effect of upflow flow rate, above, except the vibration was not done during the upwashing period as described in step (ii.) of the procedure, and the vibration in step (iii.) was tailored for each test, as detailed above.

The passive tine forces were measured and used as an indicator of soil strength.

Investigating Alternative Vibration Methods

The results of the previous two investigations considerable variation in soil condition within the bin. The previous investigation showed the vibrating probe was not the cause of the variation and neither had the ability to reduce it. Sand boils and spatial differences in the upflow rate were thought to cause the variation. Therefore for the upwash system to be suitable an alternative method of vibrating or moving the sand mass was required, and it was the aim of this investigation to find one.

The objective of the investigation was to conduct tests using a range of differing methods to reduce the sand strength variation, and to compare the results in order to select the most effective method to develop further.

This was achieved by conducting a number of tests, each utilizing a different method to move and consolidate the semi fluidized sand. Details of each method are contained in Table A1-2. Details of the upwash method are not mentioned in the table unless it differs from being operated at 1.5 l/s for 3 minutes. The vibration probe was not used unless stated.

Table A1-2 Details of methodology used in the alternative vibration investigation

Test Number	Description of Method
1 + 2	The operator pushed the palms of their hands, at shoulder width, up and down on the surface of the sand along the centreline of the tank.
3	A flat sheet of wood (0.4 m x 0.15 m) pushed on the surface of the sand along the length of the soil bin, in a similar way to the palms of the hands in tests 1. The greater surface area of the wood prevented sinkage into the soil.
4	A 12 mm diameter steel rod pushed into the soil to a depth of 0.4 m at numerous random positions in the soil bin.
5	A steel rod pushed into the soil to a depth of 0.4 m, then and pushed from side to side in a figure of eight shape, about 0.3 m wide, in the same pattern as was used by Knight. (Knight, 2002)
6	A steel rod pushed into the soil to a depth of 0.4 m and stirred around. Repeated in random positions in the soil bin.

7	A steel rod pushed into the soil to a depth of 0.4 m and pulled along the centreline of the tank, pushing it back and forth towards the sides of the tank.
8	Upwash operated at 2.85 l/s (3 bar) for three minutes. No mechanical vibration or mixing was used. The purpose was to eliminate any mechanical vibration to determine if higher upflow rates created more uniform soil conditions.
9	Upwash operated at 2.4 l/s (2.5 bar) for three minutes. No mechanical vibration or mixing was used. The purpose for this was the same as that of test 8.

Data was measured and recorded in the same manner as the previous investigations.

Effect of Low Upwash Flow Rate Combined with the Rodding Technique

The conclusions from the previous investigation showed that a reduced upwash flow rate was required and that a rodding technique for vibrating the soil created more uniform conditions than the previously used concrete vibration probe. The aim of this investigation was to determine the effect of lower upwash flow rates combined with rodding the soil on the strength characteristics created.

Previous studies Knight (2002) used a preparation method which included inserting a steel rod to a depth of 0.4 m then skewing it in a figure of eight shape. He repeated this at 0.3 m intervals along the length of the tank. It resulted in a sinusoidal force fluctuation along the soil bin, the wavelength being about 0.3 m. Thus the force variations were caused by the rodding technique.

The combined effect of the two elements of upwashing and rodding were to create a uniform soil in the following way. The upwashing was to create a partially fluidized state allowing mobilization of the soil. The rodding utilized the semi-mobilized state of the soil to create soil mixing and movement, producing reduced strength variation than the method previously used by Knight (2002) in which the upwashing element was absent.

The objectives were;

i. To determine the optimum flow rate by conducting a series of tests using a range of low upwash flow rates combined with a rodding technique.

ii. To refine the rodding method by conducting a series of tests using a range of rodding techniques combined with low upwash flow rates.

Table A1-3 describes the tests conducted detailing the methodology used.

Table A1-3 Details of methodology used in the low upwash/rodding investigation.

Test No.	Detail of Test Methodology
1	Upwash flow rate – 0.5 l/s. Rodding – same as Knight (2002). 0.02 m diameter steel rod used. Inserted to depth of 0.4 m, then skewed in figure of eight shape, repeated every 0.3 m along tank. The purpose of using the same rodding technique as Knight's previous work was to create a reference enabling a comparison of the soil condition to Knight's previous work.
2,3,4,5	Upwash flow rate – 0.5 l/s. Rodding – 0.012 m diameter rod inserted to 0.4 m depth, at 0.075 m the operator's side of the soil bin centreline, then pushed toward the centreline, then towards the bin side. Repeated every 0.15 m (30 repetitions per length) on both sides of the tank.
6,7,8	Upwash flow rate – 0.5 l/s. Rodding – same as test 2 except all the rodding was from just one side of the soil bin for practical simplicity.
9,10,11,12	Upwash flow rate – 0.75 l/s. Increased upwash flow rate was to indicate whether it produced a lower soil strength. Roding – same as Test 6.
13	Upwash flow rate – 1.0 l/s. Increased upwash flow rate was to indicate whether it produced a lower soil strength. Rodding – same as Test 6.

Data was recorded and analyzed by the same method as in the previous investigation.

Initial Uniformity Tests

The aim of the uniformity tests was to ensure the repeatability of soil conditions produced by the method of soil preparation selected by the previous investigation.

The objective was to conduct a series of tests to determine;

i. The uniformity of the soil condition created within a preparation, using the coefficient of variation of the horizontal force acting on a passive tine as an indication of uniformity.
ii. The repeatability of the soil condition created, using the mean horizontal force on a passive tine as an indication of the soil condition.

A series of fourteen replications were conducted in the following manner.

i. The tine from the previous replication was removed from the soil while the upwash system was operating with a flow rate of 0.75 l/s. The tine was then gently pushed into the soil at the other end of the bin and connected to the carriage.
ii. Standing against the side of the soil bin tank, and starting at the far end, the operator pushed the steel rod into the sand, to a depth of 0.4 m, at 0.075 m on the operator's side of the tank centreline, going into the denser sand at the edge of the trench from the previous test. The rod was then pushed and rotated forward to the vertical, then pulled and rotated back to about forty five degrees and removed from the soil. This was repeated thirty times along the length of the tank. (0.15 m intervals) Upon reaching the end of the tank the operator worked back to the opposite end of the tank, repeating the same procedure, except entering the rod into the far side of the previously created trench. On completion the upwash system was stopped.
iii. The duration of the upwashing period was timed and kept to approximately 2 minutes 50 seconds. (1 min. for tine, 1 min. 50 seconds for rodding.)
iv. The draught force of the tine pulled through the soil was recorded using the instrumentation system described in Section 2.5.1 of Chapter 2. The head water during at the start of a test was 0.1 m.
v. Stages (i.)-(viii.) were repeated for each test.

Final Uniformity Tests

A soil levelling process was added to the soil preparation method after the results from the initial uniformity tests highlighted its need. In addition, rodding was started at alternate ends of the tank for consecutive preparations, since starting the rodding process from the same end may have caused differing soil treatments at each end of the bin. The aim of these uniformity tests is to ensure the uniformity and repeatability of soil conditions produced by the refined method of preparation. The objectives were the same as in the initial uniformity tests.

Twelve tests were conducted using the same soil preparation method as that in the initial uniformity tests, with two alterations. Firstly, after stage (iii.) the soil surface was levelled by pulling a fixed depth blade along the length of the tank levelling the surface. Secondly, the rodding process between was started at alternating ends of the soil bin.

A1.5 Results

A1.5.1Mechanical Techniques

Horizontal Subsurface Blade

In initial trails the blade was placed on the surface and allowed to penetrate under its own action as it passed over the soil. The leading edge of the frame under the hitch point penetrated into the soil, resulting in a high rake angle of the blade and very poor penetration. To reduce this, a skid shaped sheet of metal was added onto the front third of the frame. This kept the frame from digging into the soil, but blade penetration was still poor. Lowering the hitch point to reduce the moment causing the blade to rise showed little improvement in penetration. The addition of a 40 kg mass onto the rear of the frame increased the penetration to 200 mm, but was still less than the desired 320 mm. A concrete vibrator was then attached to the frame, but caused little increase in penetration.

Nevertheless, the blade caused a slight lifting of the soil and the formation of cracks as it arched over the blade but caused very little lateral mixing of the soil. The blade also generated a high draught force.

Vibrating Tine

Without vibration the tine penetrated poorly, but with vibration penetration met the objectives and the draught force was very low. It was very effective at consolidating fluidised sand, but ineffective at loosening dense areas, since the vibration tended to compact them further.

A1.5.2Jetting Techniques

Figure A1.16 shows an example of the force results obtained from the uniformity tests on the jetted tines preparation method. The mean and standard deviation of the force values were calculated. The complete length of the run was 4.5 m but the mean force was calculated over a length of 3 m (1800 data). The first 1 m (600 data) and last 0.5 m (300 data) of run were excluded from the calculation due to large end effects. Results of the mean force and standard deviation are shown in Figure A1.17.

Originally a series of 15 tests were to be conducted, giving an expected power level of 90% to the uniformity experiment. However, after the seventh test it was apparent that there was considerable variation in horizontal force, thus the remainder of the experiment was aborted.

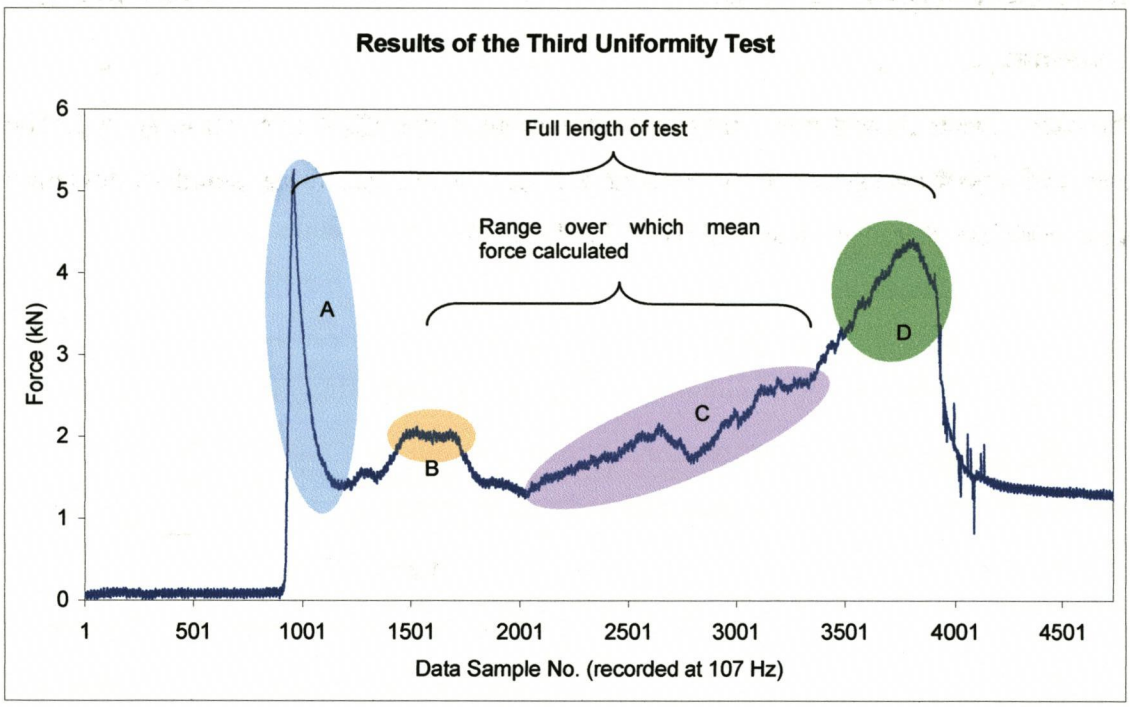

Figure A1.16 An example of the force exerted on the passive tine in one of the uniformity tests

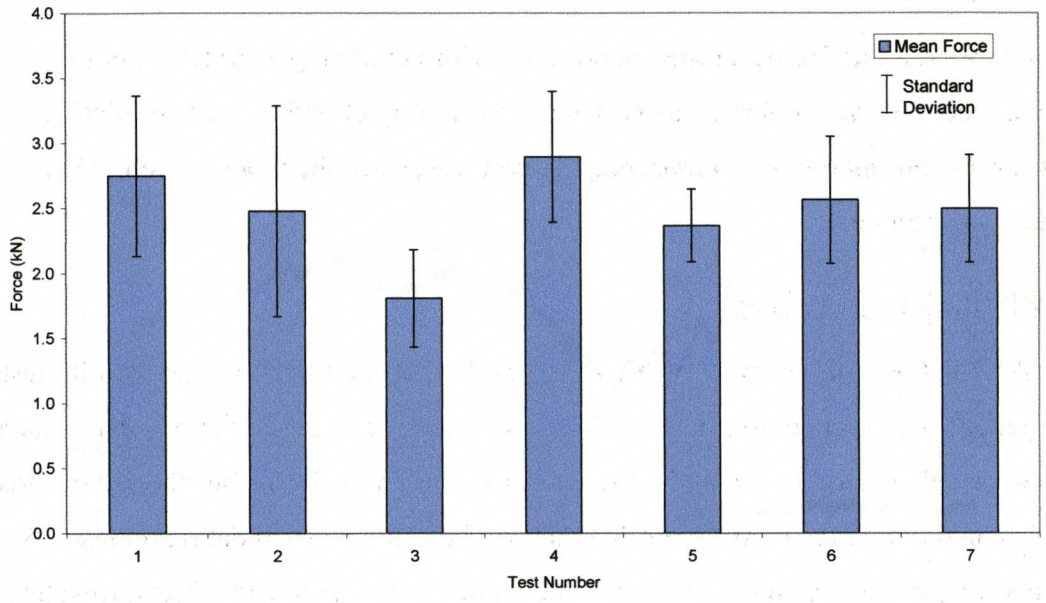

Figure A1.17 A plot of the mean force and standard deviation values for each of the uniformity tests

A1.5.3 Fluidisation

Investigation into the Effect of Upwash Flow Rate – Total Flow being Constant

The data from each test was analysed by the method described in Section A1.5.2. The results of a typical test are shown in Figure A1.18. The mean force, standard deviation and coefficient of variation are shown in Table A1-4.

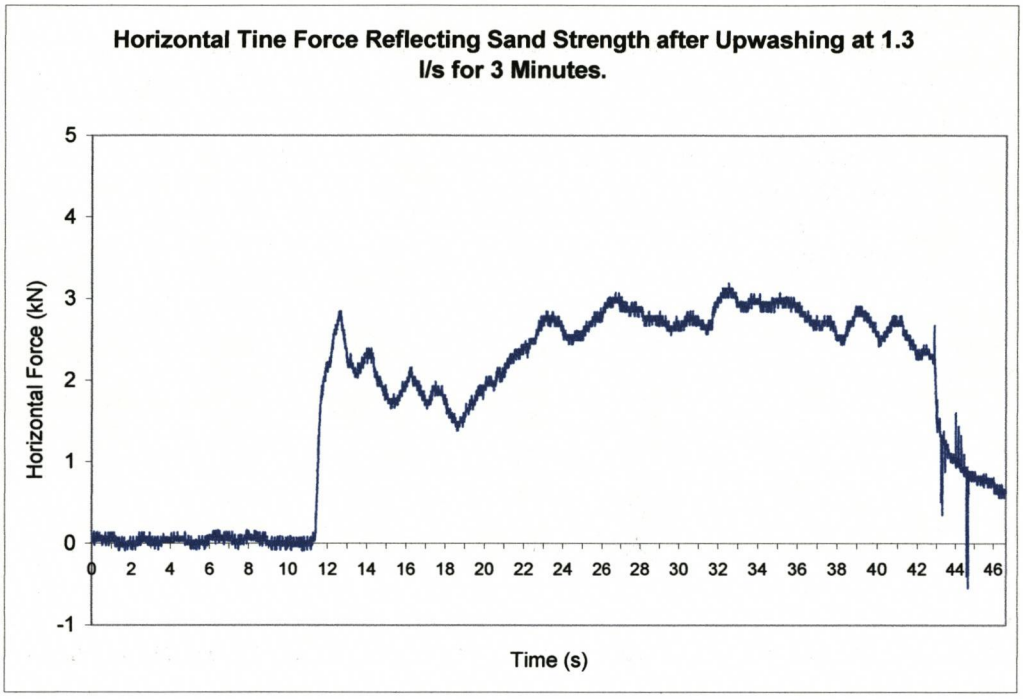

Figure A1.18 **Typical result from the variable flow rate, constant total flow investigation**

Table A1-4 **Results from the variable flow rate, constant total flow investigation**

	Horizontal Force (kN)			
Treatment	B1	B2	B3	Mean
1l/s, 4min	3.04	3.54	3.18	3.25
1.3 l/s, 3mins	2.62	3.24	2.97	2.94
1.5 l/s, 2.5mins	2.43	2.82	2.74	2.66
	Standard Deviation (kN)			
1l/s, 4min	0.38	0.63	0.53	0.51
1.3 l/s, 3mins	0.34	0.49	0.77	0.53
1.5 l/s, 2.5mins	0.30	0.48	0.66	0.48
	Coefficient of Variation (%)			
1l/s, 4min	12.46	17.80	16.51	15.59
1.3 l/s, 3mins	12.83	15.15	25.79	17.92
1.5 l/s, 2.5mins	12.47	17.06	23.97	17.83

Investigation into the Effect of Vibration

The data for each test is displayed graphically Figure A1.19. The mean force values were calculated using the data of the full length of the tank (the section denoted by the orange line in Figure A1.19). These values are shown in Table A1-5 together with the standard deviation and coefficient of variation of each test.

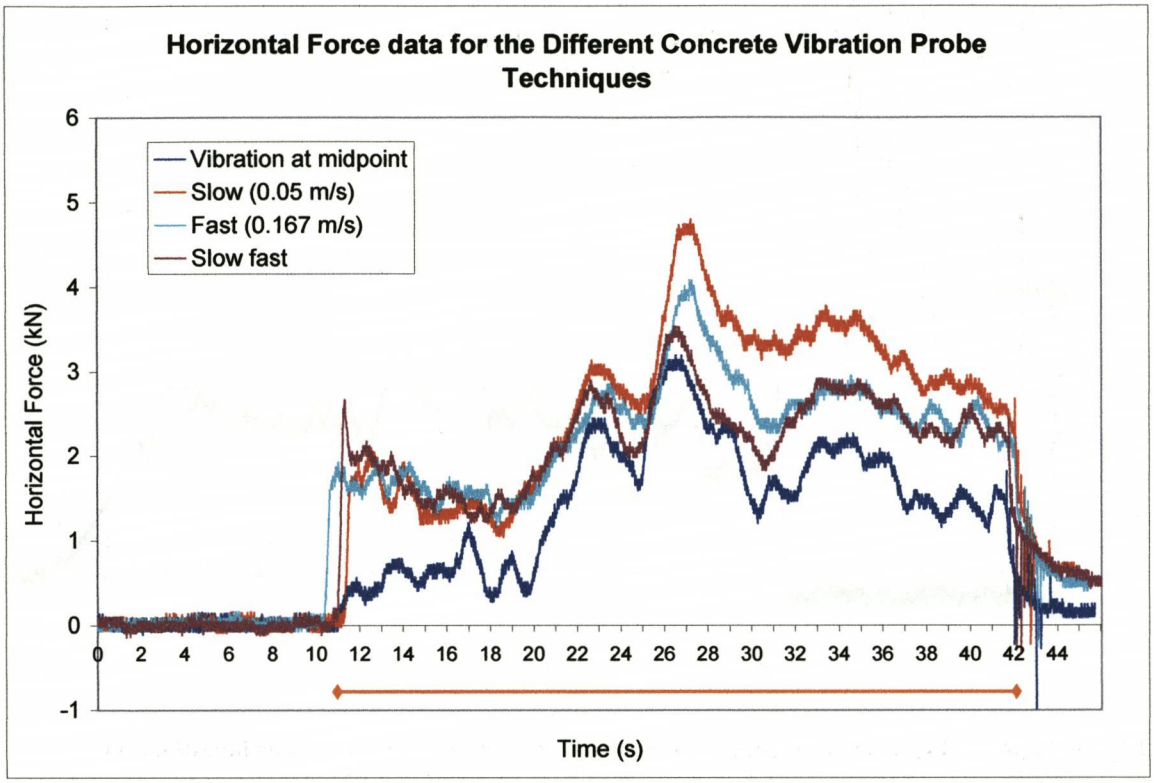

Figure A1.19 Force profiles of tests in the vibration investigation

Table A1-5 Results from the vibration probe speed tests.

	Horizontal Force (kN)	Standard Deviation (kN)	% C.V.
Vibration at Midpoint	1.49	0.74	49.5
Slow Speed (0.05 m/s)	2.66	0.93	34.8
Fast Speed (0.167 m/s)	2.28	0.62	27.1
Slow/Fast Alternating	2.24	0.51	23.0

Investigating Alternative Vibration Methods

Typical results are shown in Figure A1.20, which also shows areas of high and low draught force common to all the tests. Results of the mean force and standard deviation for each of the nine tests are shown graphically in Figure A1.21.

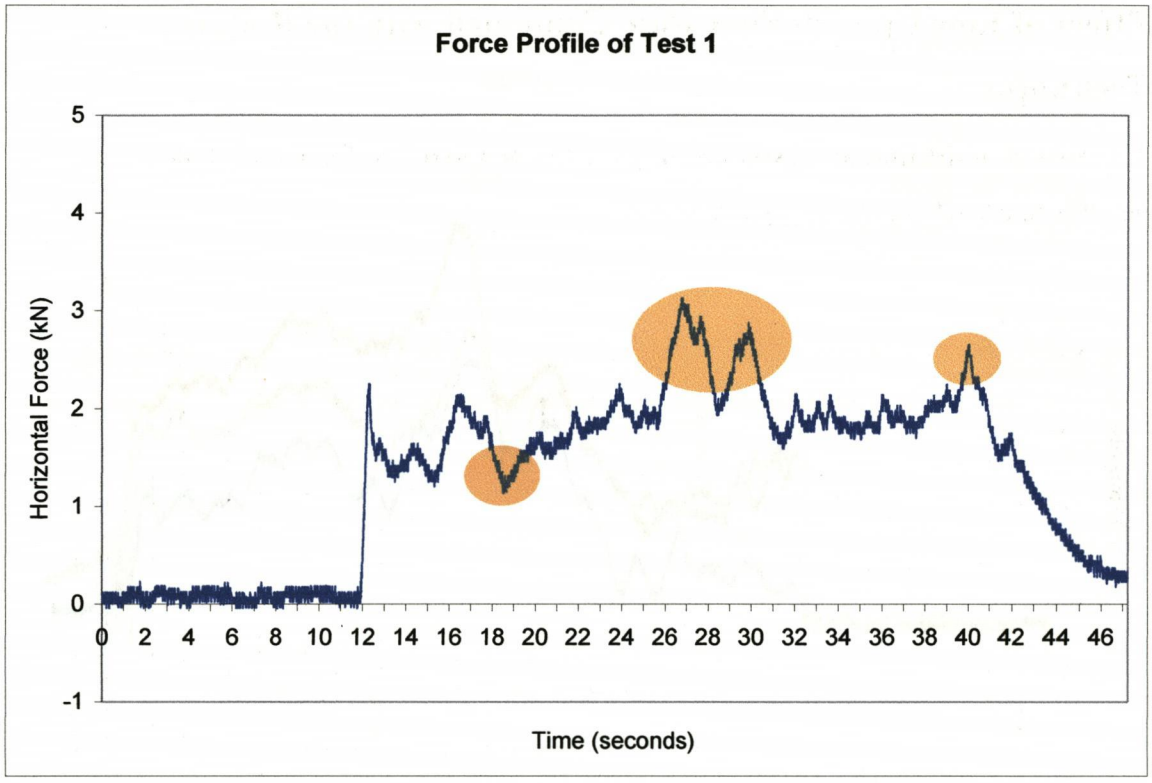

Figure A1.20 The force profile of Test 1 - Pushing with hands (coloured areas strong and weak areas common to all tests)

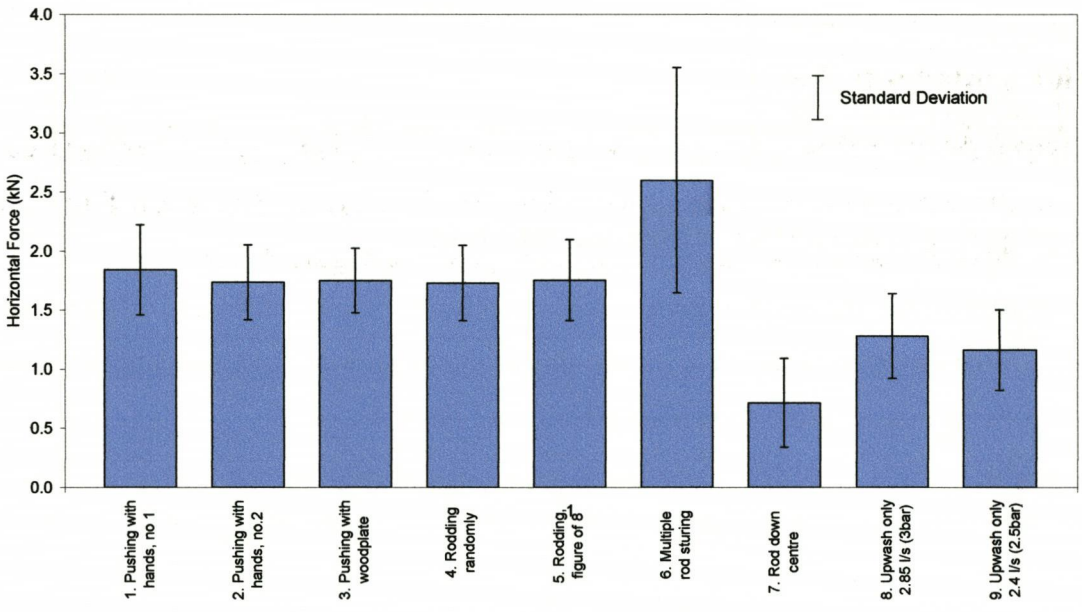

Figure A1.21 Results of the alternative vibration methods investigation

Effect of Low Upwash Flow Rate Combined with the Rodding Technique

The results of the thirteen tests, showing the mean horizontal force and standard deviation, are presented in Figure A1.22.

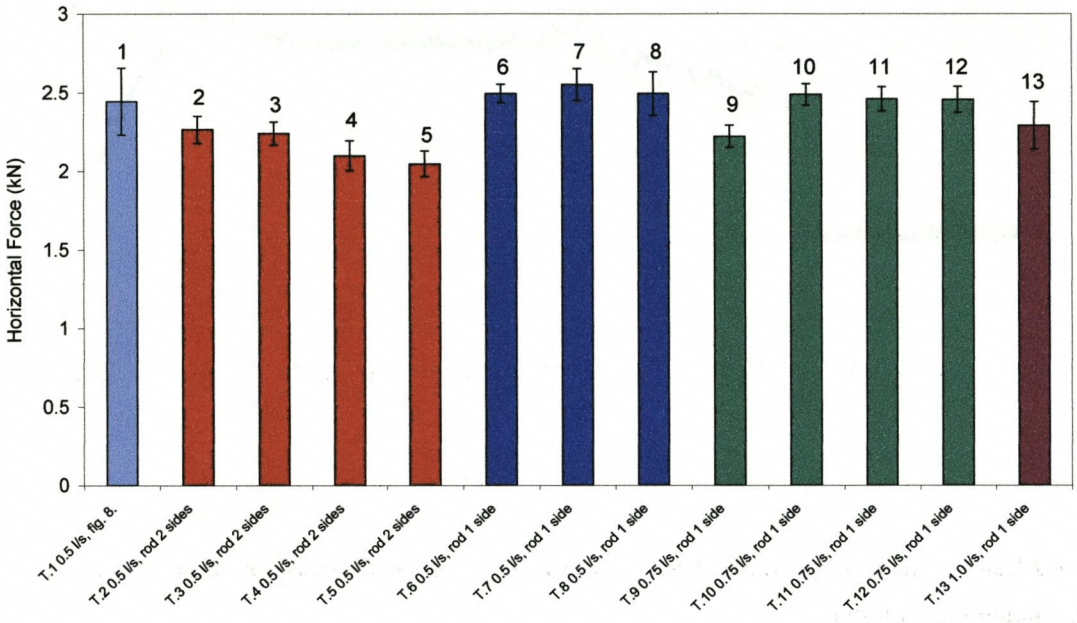

Figure A1.22 Results of the low upwash/rodding investigation

Initial Uniformity Tests

The results were analysed according to that shown in Figure A1.23 to exclude end effects. The mean force was calculated using data in Zone B. The mean force and standard deviation data for each replication is displayed in Figure A1.24.

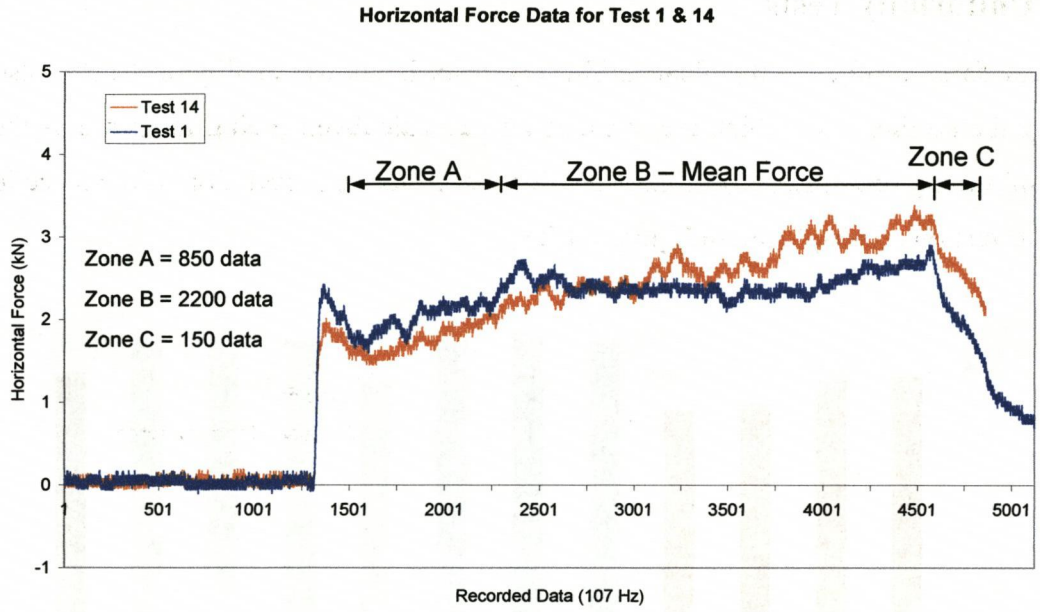

Figure A1.23 Section of data used to calculate mean force in uniformity tests

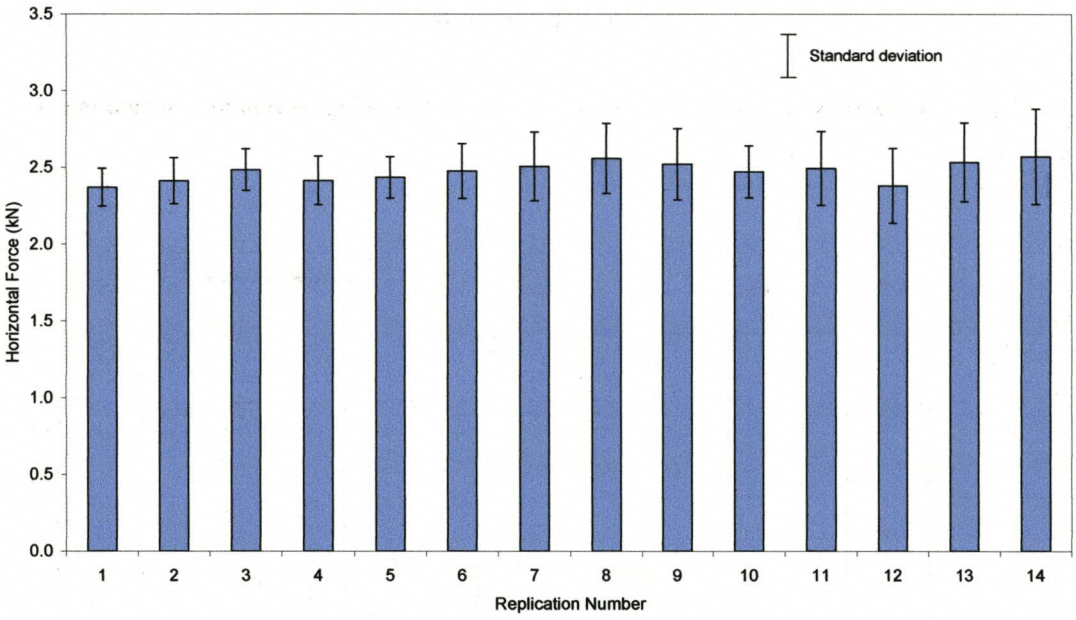

Figure A1.24 Force and Standard Deviation Results for the Initial Uniformity Tests.

Final Uniformity Tests

A typical force profile of the final uniformity tests is shown in Figure A1.25, also showing the section over which the mean force was calculated (being the same as the initial uniformity tests). Results of the mean force and standard deviation of the force in the mean section are displayed in Figure A1.26.

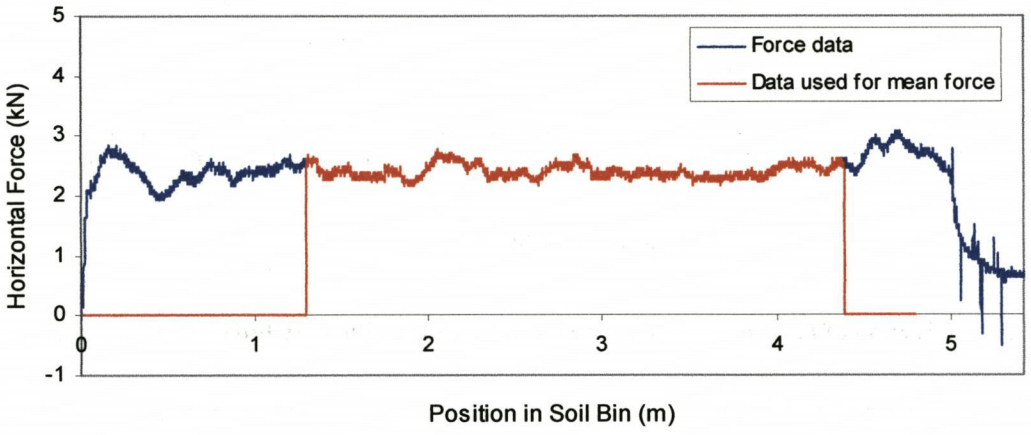

Figure A1.25 Typical force profile of final uniformity tests showing section over which mean value was taken

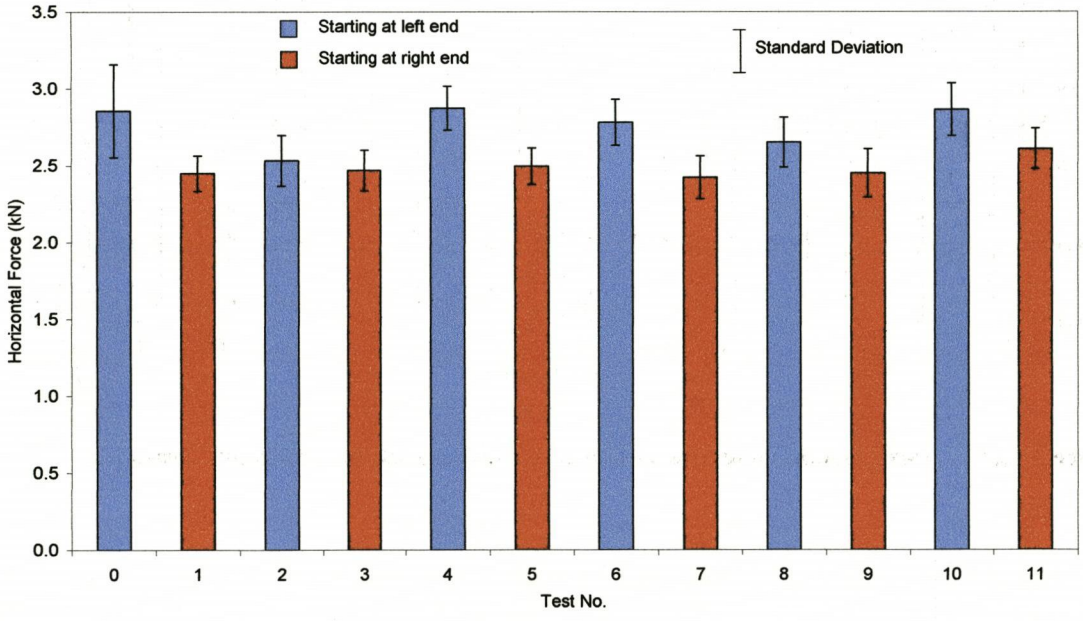

Figure A1.26 Force and Standard Deviation Data for the Final Uniformity Tests

A1.6 Discussion

A1.6.1 Mechanical Techniques

a) Horizontal Subsurface Blade

The problem of poor penetration could have been improved by modifying the frame and blade design. However, it was not worthwhile to pursue the option given the difficulties already encountered.

b) Vibrating Tine

The vibrating tine by itself was not sufficient to prepare the soil adequately, but requires additional loosening of the soil before its use.

A1.6.2 Jetting Techniques

The uniformity tests showed two distinct features about the preparation method. Firstly, there was considerable variation in the mean force values between tests. The third test had the lowest mean force of 1.81 kN, while the fourth test had the highest, being 2.9 kN, being 60% greater. Secondly, there was considerable variation in the force magnitude within each test, as shown in Figure A1.16. In most cases the standard deviation of the force was large, it being 33.6% of the mean force in the second test. Moreover, there was considerable variation in the standard deviations between tests, ranging from 33.6% to 11.8% of the mean force.

The jetted tine preparation method as it was did not satisfy the objectives. Therefore the results were studied further in order to gain a greater understanding of the causes of variation in soil conditions with the purpose of refining the method by reducing the causes of variation. Further studies of the results showed four distinct characteristics common to the force profiles of all the tests, and have been highlighted in Figure A1.17. The characteristics of each zone are attributed to aspects of the preparation method, the likely causes are discussed below. The zones have been considered in descending order, since both the trolley and the vibroskid commenced their run at the far end of the soil bin, the opposite end to the passive tine.

All the results exhibit high force values in zone 'D'. Likely cause being the two jetted tines were unable to start their run at the very end of the tank, because of obstruction from the vibroskid stored at the end. Additionally, when the vibroskid was used, the vibration was turned on while the skid was at the very end of the tank, enabling the tines to penetrate to their full working depth by the time they had reached the start of the fluidised soil. Therefore the soil at the far end was not jetted yet received vibration treatment, causing it to have a high density.

Zone 'C' had a general increase in force over its length. The likely cause is the movement of the jetted soil. When the water jets on the tines were turned on the water initially rose vertically to the surface of the soil. However, as the trolley progressed along the length of the tank the line of least resistance for the jetted water was no longer vertically, but horizontally backwards into the cavity already created by the jets. The turbulent flow of water carried sand particles towards the end of the tank where they were then deposited. This process continued as the trolley advanced along the tank, depositing soil up to 2 m rearward of where it was eroded. This effect created a soil surface inclined upward towards the rear of the tank, where the jetted trolley started and the passive tine finished its run. The levelling blade was unable to fully level the soil surface since some of the soil had been shifted to the very rear of the tank, around the vibroskid, beyond the reach of the blade. As a result the working depth of the passive tine increased by about 50 mm along the length of its run, reflected by an increase in the force magnitude. Figure A1.27 shows the observed pattern of soil movement and fluidisation caused by the two jetting tines.

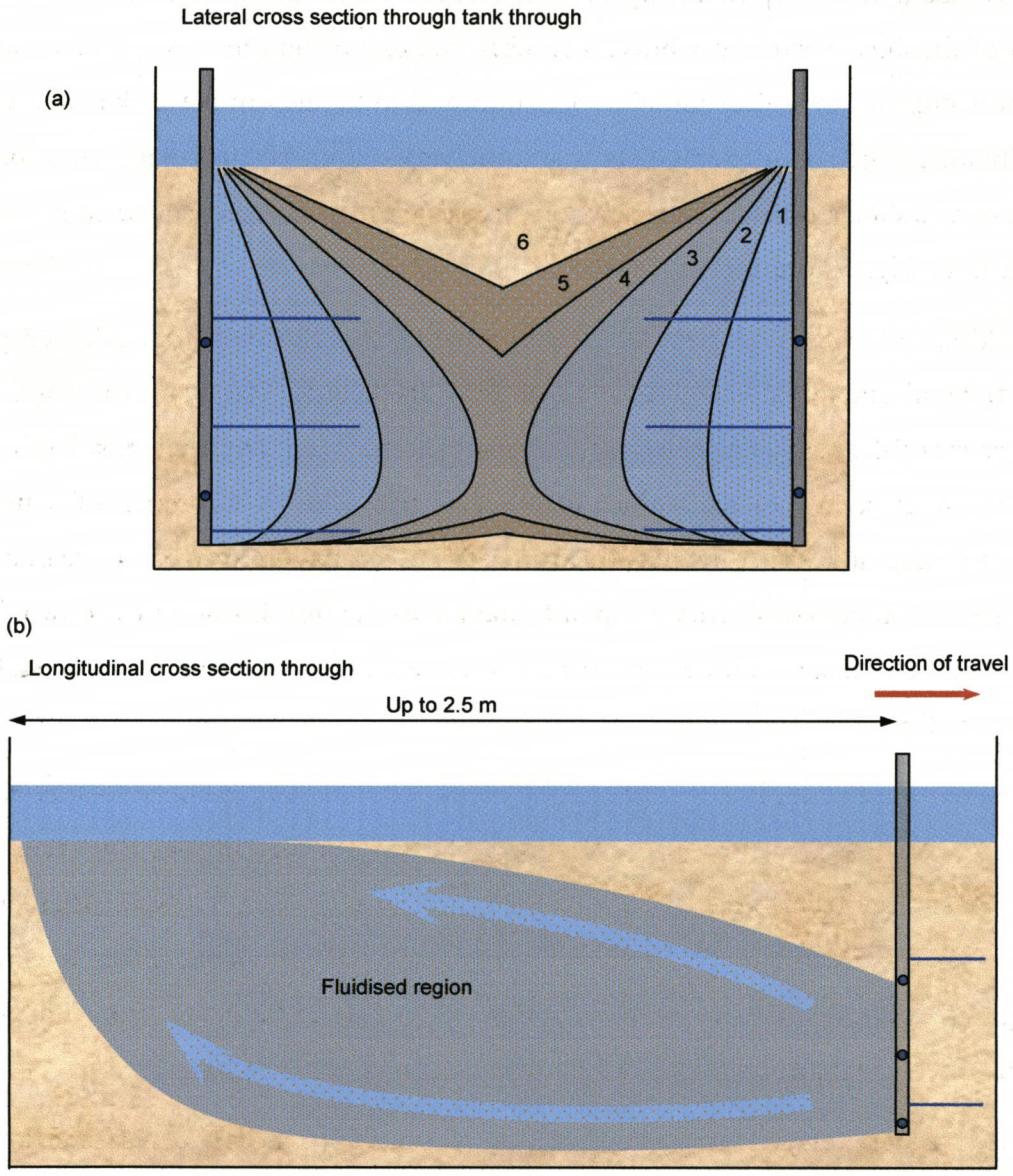

Figure A1.27 Cross sections through the tank showing the observed jetting pattern created by the jetting tines

Figure A1.27(a), displaying a section across the tank, shows that as the tines passed through the soil, the water jets initially eroded the soil immediately adjacent to them, shown as section 1. Sections 2 – 5 show the propagation of the eroded/fluidised zone as the distance rearward from the tines increased. Region 6 eventually collapsed into the cavity beneath, the sand particles then being carried with the water movement towards the rear of the tank where they were then deposited, as shown in Figure A1.27(b).

Zone 'B' had a force plateau having a higher force than the surrounding area. It was the region of the tank where the vibroskid reached the end of its run. Upon completing a run, the vibroskid was lifted out of work and moved to the rear of the tank again while still vibrating to overcome suction and frictional forces. Zone 'B' therefore had a longer period of vibration than the rest of the tank, resulting in a more consolidated soil with consequently higher forces.

Zone 'A' shows an initially very high peak in the force followed by a sudden drop. A dense zone of sand immediately surrounding the passive tine at the start of its run is the likely cause of the peak. The action of levering the tine to and fro when pushing it into the soil caused a localised consolidation in the area. Also, the absence of a trench behind the tine and the consequently restricted flow paths quite likely increased the initial suction forces considerably. Upon formation of the trench water flow down from the surface was enabled, alleviating the suction force on the tine, resulting in the sudden decrease in force.

Further tests were conducted to improve the method. Little could be done to alter zones A and D due to practical operating restrictions. The force plateau in zone B was reduced by minimising vibration time when extracting the vibroskid from the soil. Attempts to reduce the force increase within zone C were aimed at providing either a vertical passage of escape for the water from the jets or to deflect the water from travelling rearwards. The attempts are described below.

a) The inward facing jets were angled slightly forwards, to reduce the rearward flow of water, and upwards to enable the jets to erode the soil up to the surface, creating a passage for the water to escape. However, this modification was did not improve the performance.
b) Upon initiating the water jets the tines remained stationary until the sand was eroded across the full width of the tank, allowing the jetted water to flow vertically to the surface and to remain so as the tines progress along the tank, thus reducing the rearward flow of water. However, it was found that as soon as the tines progressed forwards, the soil erosion pattern reverted back to that shown in Figure A1.27.
c) Attempts to deflect the water flow sideward or upwards by placing a metal sheet in the rearward flow at a fixed distance behind the tines were ineffective.

A1.6.3Fluidisation

Investigation into the Effect of Upwash Flow Rate – Total Flow being Constant

The investigation demonstrated that greater upwash flow rates produced a weaker sand, shown by the lower mean draught forces for the higher flow rates. This is true despite the lowest flow rate having the longest upwashing duration. The strength of the soil therefore depended upon the upflow flow rate rather than the duration of the upflow period. This is in agreement with fluidizing velocity theory, that the upflow velocity determines the extent of fluidization that occurs.

The mean coefficients of variation (%CV) for the three flow rates were similar. However, there was considerable variation in the CV values between individual tests. The large CV values, especially in the third block, show considerable variation in draught force, and thus soil condition, in the tank.

It was noted during the tests that sand boils only occurred in the first 1.5 m and the very end section of the tank. This is a likely explanation for the significantly lower and more fluctuating force in that section of the tank. It was also noted that upflow water percolated through the soil along the tank centreline, where the tine had passed, more readily than through sand either side.

The investigation showed;

i. The soil condition created by the upflowing water was largely a function of the flow rate and not the endurance..
ii. There was a large variation in sand strength within the soil bin, created by the preparation method.

Investigation into the Effect of Vibration

The results, shown in Figure A1.19 and Table A1-5, show the speed of the vibrating probe did influence the strength of the sand. The slower speed (0.05 m/s) consolidated the sand to a greater extent than the faster speed, so that the mean force was 15%

greater. The forward speed of the probe can therefore be used to influence the strength of the sand.

The force characteristics of the test using the slow/fast alternating speed was very similar to that created by the fast probe speed, indicating the strength of the sand was not responsive to the speed of the vibration probe.

The shape of the force profile was similar for all the tests. The test which inserted the probe only at the midpoint of the tank did not create an uncharacteristically large force at that point, compared to the profiles of the other tests. This indicated the variation in sand strength in the soil bin was not created by the action of the vibrating probe, but by the upwash system itself.

Thus,

i. Variation in the use of the vibrating probe did not have a significant effect on the force profiles
ii. Duration of the vibrating probe in the tank influenced the mean force
iii. The upwash system created an underlying variation of soili condition in the bin.

Investigating Alternative Vibration Methods

The results of the investigation into alternative vibration methods, displayed in Figure A1.21, show the method of vibrating the sand had a significant effect on the horizontal force created on the passive tines. The forces and standard deviations of the first five tests were very similar, despite the vibration methods of being different. The coefficient of variation was lower than those in the previous investigations using upwashing. Tests 4 to 7 all used a variation of the rodding technique, yet the latter two had a considerably different force and coefficients of variation, demonstrating the method of rodding significantly influenced the sand condition created.

The force variation was not eliminated by any of the vibration methods. Figure A1.20 highlights hard and soft areas of sand common to all the tests. These underlying variations were therefore not a product of the vibration methods, but were caused by the upwashing process. Consequently the only means of reducing the underlying variation was to reduce the upwash flow rate.

Thus, the investigation showed;

i. A number of the vibration techniques produced similar soil conditions. However, the rodding method gave the greatest scope to control the sand conditions and was therefore selected to refine further.
ii. None of the vibration methods eliminated the underlying sand strength variation.
iii. A reduced upwash flow rate is required to reduce underlying variation in sand strength.

Effect of Low Upwash Flow Rate Combined with the Rodding Technique

The first test, which was the same as that used by Knight (2002) had the largest force variation, there being significantly higher forces where the rod had been used. Tests 2-5, which used the rod in a forwards and backwards motion both sides of the soil bin at close intervals, created much less force variation than test 1. The standard deviations of those tests were similar, although the mean force reduced somewhat with subsequent repetitions. Tests 6-8, using the rod on one side only, had higher mean forces than the previous tests, but force variation increased with subsequent repetitions. Tests 9-12, having a greater upwash flow rate than tests 6-8, had small force variations, and similar mean forces. Test 13, having the greatest flow rate, had a larger force variation.

Therefore, the upwash flow rate and rodding technique used in tests 9-12 were selected as an appropriate preparation method, due to the low force variability within the bin and the indication of repeatable soil conditions.

Initial Uniformity Tests

The results of the initial uniformity tests in Figure A1.24 show there was no difference between the mean forces of the replications. The standard deviation of the initial replications was small, showing uniformity of soil condition within each replication. However, the standard deviation values gradually increased with increasing repetition, having an initial coefficient of variation of 5.2 % in test 1 to 12.1 % in test 14. The

method therefore required further refinement to maintain the initially low coefficient of variation.

The increase in standard deviation values with increasing repetition is evidenced in Figure A1.23 by the force profile of Test 14 having a steeper gradient than that of Test 1, yet the mean force remains similar. The reason for the gradient change was a gradual altering of the soil depth by each repetition of the tests. The movement of the tine along the soil bin caused a shifting of sand in the direction of the tine movement, so over the course of the tests the soil depth at the start of the bin reduced and increased at the other. After the tests were completed the difference in the level of the soil surface was measure to be 0.08 m. Consequently the soil surface requires levelling as part of the preparation method.

Thus, the initial uniformity tests demonstrated the preparation method created good soil uniformity within the bin, although it decreased gradually with subsequent repetition.

Final Uniformity Tests

The results of the final uniformity tests displayed in Figure A1.26 show a significant difference in mean force between tests with the rodding process starting at the left or right hand end of the bin, the mean being 2.74 kN and 2.47 kN respectively.

The standard deviation and coefficient of uniformity was small for all the tests, the mean CU being 6.6% and 5.3% for the left and right hand tests respectively. The preparation method created adequately uniform soil conditions within the bin.

The mean force for the right hand tests was very consistent with replication, and for the left hand tests the variation was small but greater than the right hand tests. A preparation method as described in the methodology of the initial uniformity tests with the addition of the soil levelling process and rodding starting at the right hand end of the bin creates soil conditions satisfying the requirements of Section A1.1.3.

A1.7 Conclusions

1. Mechanical Methods
   a) The horizontal subsurface blade did not penetrate into the soil, making it unviable as a preparation method.

b) The vibrating tine skid proved to be inadequate at creating a uniform soil condition in the soil bin, so was not suitable.

2. Jetting Methods

The jetting methods examined did not satisfy the objectives of a soil preparation method. Further developments of jetting methods were abandoned due to time constraints.

3. Fluidising Methods

a) Fluidisation of the soil by upwashing was insufficient by itself to create a uniform soil condition.

b) A satisfactory method using partial fluidisation of the soil combined with a mechanical disturbance of the soil was development from the investigations, and is detailed in Section A1.4.3 under the initial uniformity tests..

c) The uniformity tests on the final preparation method showed an average force coefficient of uniformity of about 5 % within tests, when starting the rodding process from the right hand end of the soil bin, showing it produced adequately uniform soil conditions within the bin.

a) The soil conditions created by the final method were repeatable, the uniformity tests showing the mean soil forces having a coefficient of uniformity of 6 % between tests.

Appendix 2

Soil Properties and Experimental Technique

Contents

A2 Soil Properties and Experimental Technique

A2.1 Soil Properties

A2.1.1 Soil Particle Size Distribution

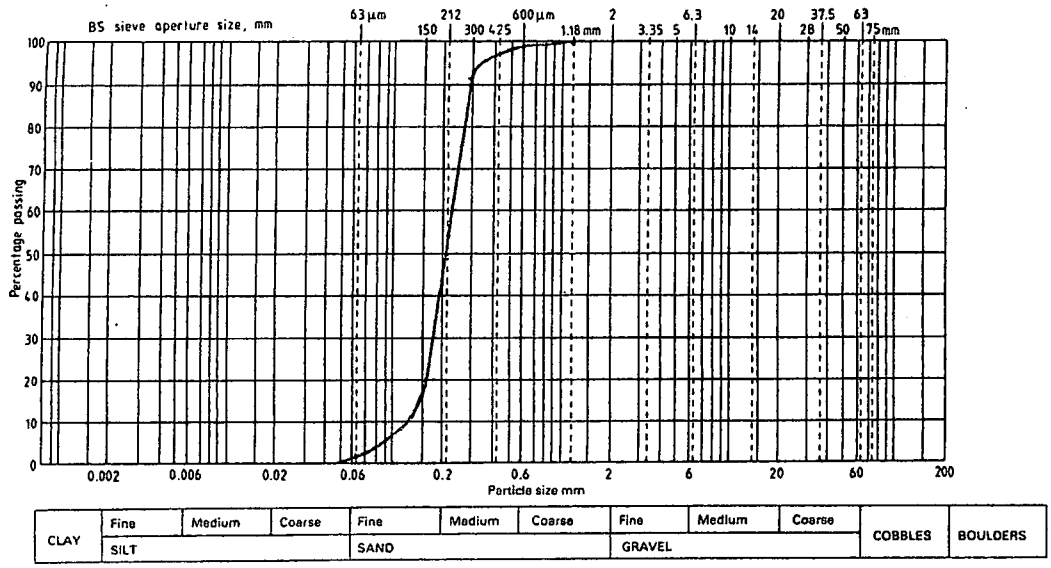

Figure A2.1 **Particle size distribution of the standard sand (SS) from Cainhoe Quarry**

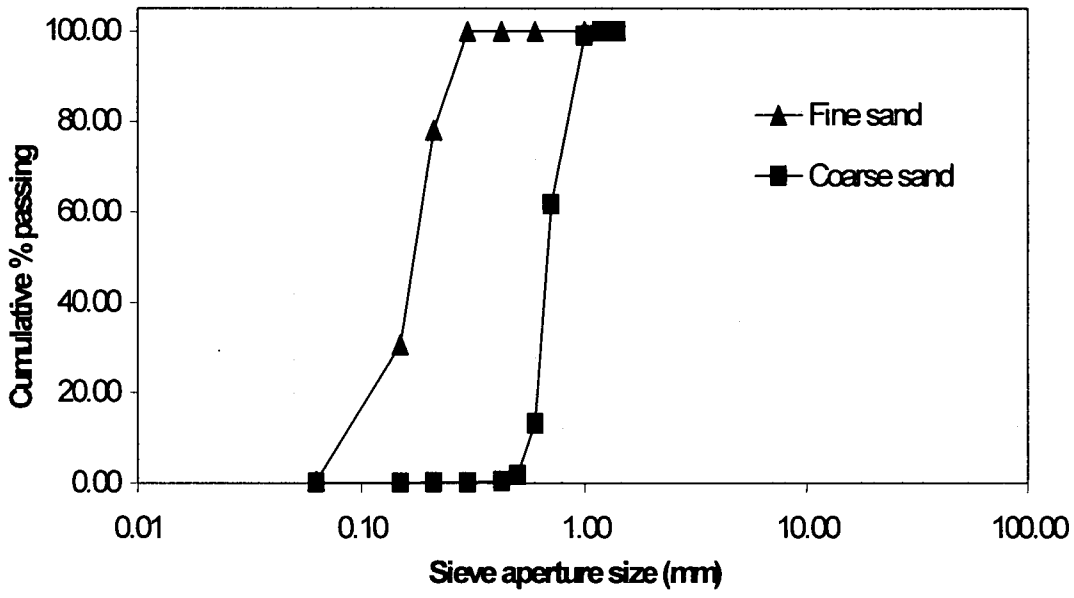

Figure A2.2 **Particle size distribution of fine and coarse sand**

Table A2-1 Hydraulic conductivity of soils

Soil Type	Particle Size (D_{50}, mm)	Hydraulic Conductivity (mm/s) [m/day]
Standard Sand (SS)	0.2	0.27 [23.28]
Fine Sand (FS)	0.15	0.24 [20.40]
Coarse Sand (CS)	0.7	4.4 [383.85]

A2.1.2 Soil Cohesion and Internal Friction Angle for Standard Sand

The soil cohesion and internal friction angle of the standard sand were measured using the annular grouser plate (bevameter) method. In situ properties of the sand in dry, damp and saturated conditions were measured. The normal stress is plot against the applied shear stress in Figure A2.3, from which the cohesion and friction angle values were determined, which are shown in Table A2-2.

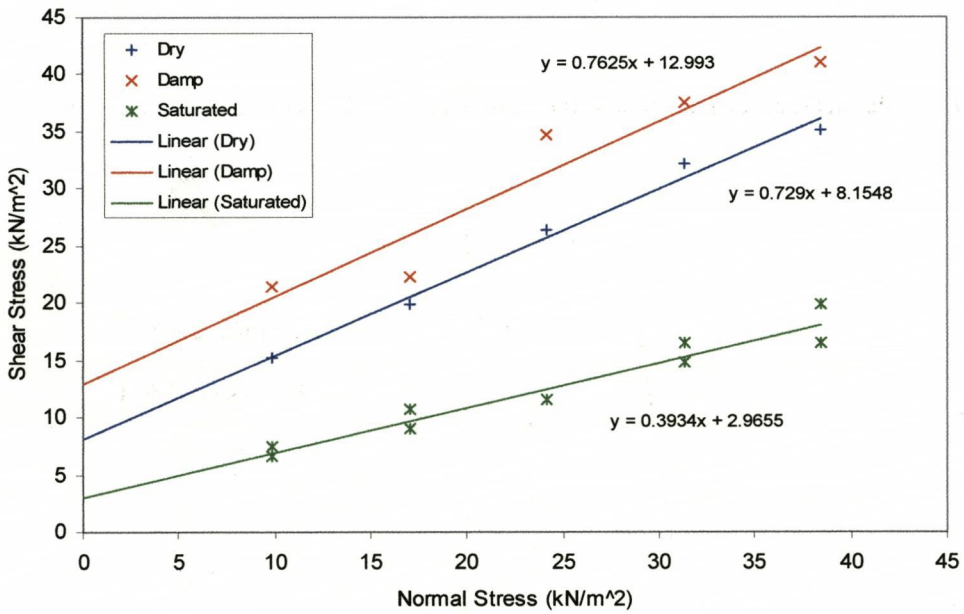

Figure A2.3 Results of bevameter tests on standard sand

Table A2-2 Values of 'c' and 'φ' for standard sand in different moisture conditions

Soil Condition	Cohesion ($kN.m^{-2}$)	Internal Friction Angle (Degrees)
Dry	8.15	36.1
Damp	12.99	37.3
Saturated	2.69	21.5

A2.2 Order of Experiments

Both the nozzle distribution and rake angle experiments of Chapter 2 were conducted in a randomised block design. The exact order of each are recorded in Table A2-3 below.

Table A2-3 Design of Nozzle Number and Rake Angle Experiment

Nozzle Distribution Exp.		
Block 1	Block 2	Block 3
3c	12b	1d
Gb	Gc	12b
3b	1c	6b
12c	3b	6c
6d	3d	12d
3d	Ga	9c
9b	Passive	3a
1c	1d	1c
12b	9d	1b
9d	6c	9d
12a	12d	Gd
Ga	9b	9b
6c	1a	6d
1d	9c	12a
12d	Gd	Passive
Gd	12c	3d
3a	Gb	3c
6b	9a	9a
9c	6d	1a
Passive	6a	12c
6a	12a	Gc
Gc	3c	6a
1a	6b	Gb
9a	1b	3b
1b	3a	Ga

Additions

6e	3f	1g
1f	1g	3g
3g	3g	1f
3f	1f	6e
1g	6e	3f

Number indictes tine number
Letter indicates jet pressure (bar)

a	1.0
b	1.5
c	2.0
d	2.5
e	0.5
f	3.0
g	3.5

Rake Angle Experiment		
Block 1	Block 2	Block 3
4a	6a	7a
VP	2b	1d
7c	8a	9b
6b	3c	3a
6a	8c	5b
3b	3a	4d
8b	5a	3d
4b	5c	1c
1b	1c	7c
4d	7d	2c
8d	3d	5d
1d	5b	6d
1a	9d	1b
9c	3b	9a
7b	6b	8a
9b	1d	FP
7d	2a	3b
3d	1a	6b
1c	4c	8d
AP	9b	5c
4c	FP	7d
6d	1b	7b
FP	2d	5a
8c	4d	8c
2b	2c	2d
6c	5d	1a
5a	8b	9d
2a	9a	2a
5d	7c	4c
8a	7b	6c
5b	VP	4a
5c	6c	VP
3a	4a	3c
9d	9c	2b
2d	8d	8b
9a	AP	4b
7a	7a	6a
3c	6d	AP
2c	4b	9c

Number indictes tine number
Letter indicates jet pressure (bar)

a	1.0
b	1.5
c	2.25
d	3.0

A2.3 Design of Uplift Plates

The size and shape of the uplift plates used in the uplift force experiments of Chapter 4 were designed to replicate those of the cavities in the static nozzle experiments. The profile of the plates therefore followed the curve generated by the equation $y = 2G\sqrt{l.x} - 2Gx$ where $G = 0.45$, l = the length of the plate and x was the distance from the end of the plate.

Two plate sizes were used, the larger (250 mm) being twice the length of the smaller (125 mm), so as to simulate different stages in the growth of the jetted cavities. The shaft lifting each plate was fixed to the plate's centre of area. The shaft was hollow so to allow water to pass down through it to the underside of the plate, alleviating suction forces as the plate was lifted through the soil. The plates, made from mild steel, were reinforced on the underside.

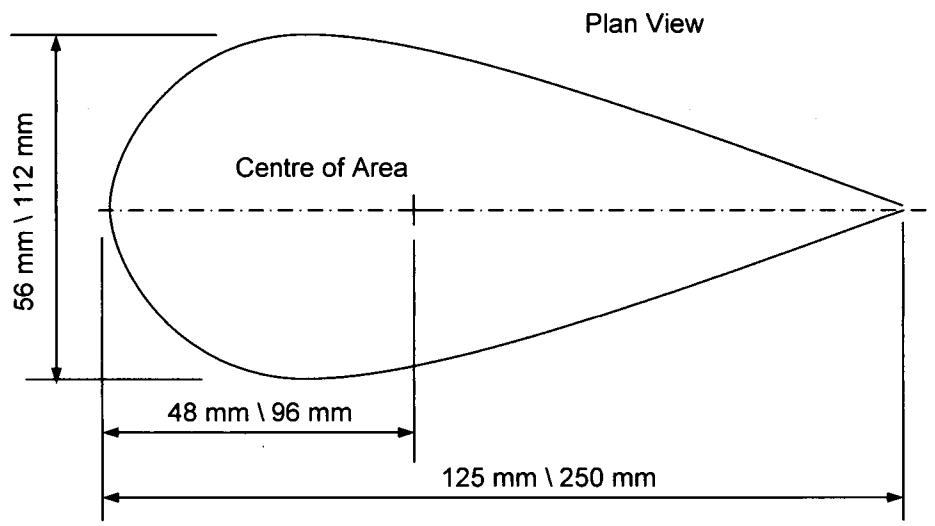

Figure A2.4 Dimensions and the profile of the two uplift plates used in Chapter 4

A2.4 Concentration of Potassium Permanganate Dye

The required concentration of potassium permanganate dye was calculated in order to ensure the jet flow was visible on the video of the single half nozzle experiments of Chapters 4 and 5. Figure 4.9 shows the arrangement of fluid system used.

Trials were conducted in which it was found that 0.2 grams of potassium permanganate crystals per litre of water were required to give the water jet sufficient colour to distinguish it on video.

Endurance of 19 litre capacity dye reservoir tank, assuming an output flow of 1 l/m, is 19 minutes. Assuming an average water jet flow rate through the nozzle is 0.3 l/s (18 l/min), then total volume of flow through nozzle in 19 minutes is 342 litres. Mass of potassium permanganate dye crystals required in the dye tank is thus 0.2 * 342 = 68.4 grams.

Appendix 3

Calibration of Equipment

Contents

A3 Appendix 2

A3.1 Calibration of Transducers used in Jet Assisted Tine Experiments

A3.1.1 Calibration of Extended Octagonal Ring Transducer Experiments

The horizontal force (Fx), vertical force (Fz) and moment measured by the Extended Octagonal Ring Transducer (EORT) was calibrated *in situ*. The horizontal and vertical forces were calibrated in separate tests, measurements from both tests were used to calibrate the moment.

A diagram of the apparatus used for calibrating the horizontal force is shown in Figure A3.1 (a). Force from weights was applied to the EORT through a cable on a pulley system. Due to friction in the pulley bearings the force applied to the EORT was less than the value of the weights. Therefore a calibrated force cell was attached to the EORT, through which the force from the cable acted, giving a direct measurement and readout of the applied force at the EORT. The signal from the EORT was measured and amplified using the Flyde data acquisition module and DasyLab software described in Section 2.5.1 of Chapter 2.

Weights were loaded and unloaded in eight 196 N (20 kg) increments, from zero to 1570 N and repeated four times. In separate tests, a 4905 N load was applied, also repeated three times.

A diagram of the apparatus used for calibrating the vertical force is shown in Figure A3.1 (b). The results for the horizontal, vertical and moment are shown in Figure A3.2.

The calibration constants were;

$$Fx = 0.7832 \times \text{Voltage}$$

$$Fz = 0.7818 \times \text{Voltage}$$

$$\text{Moment} = 0.1064 \times \text{Voltage}$$

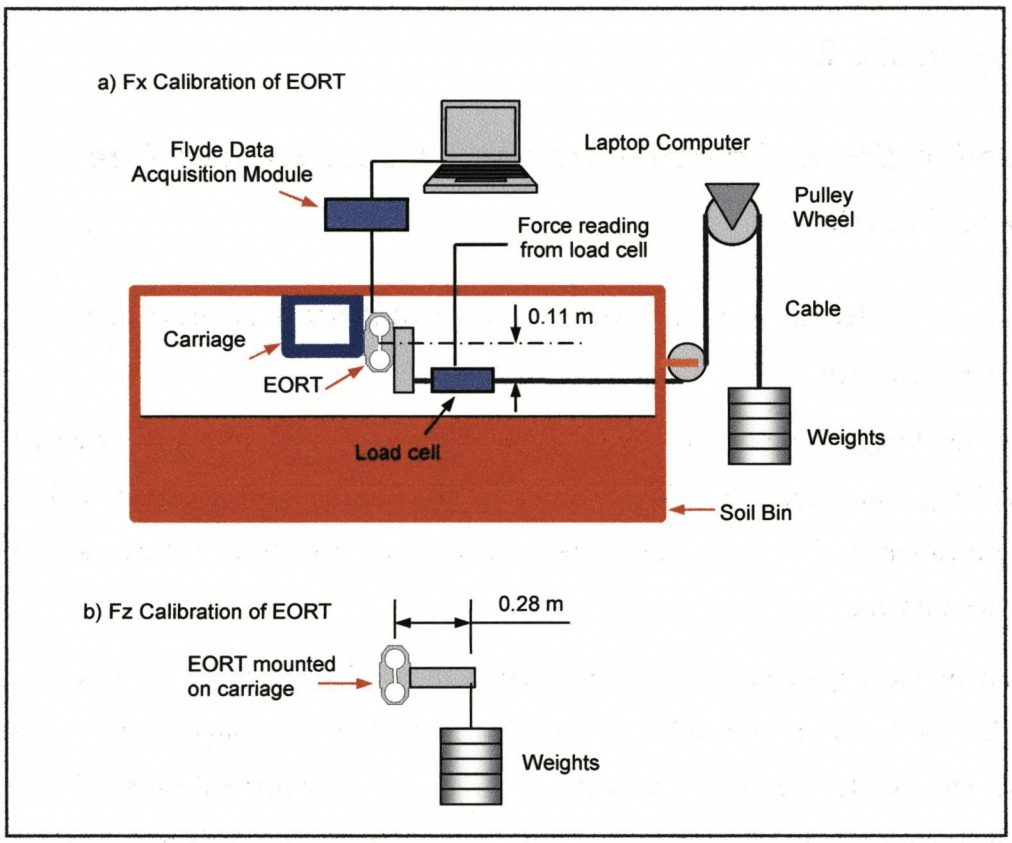

Figure A3.1 Equipment and method of EORT calibration

a) Calibration Fx EORT

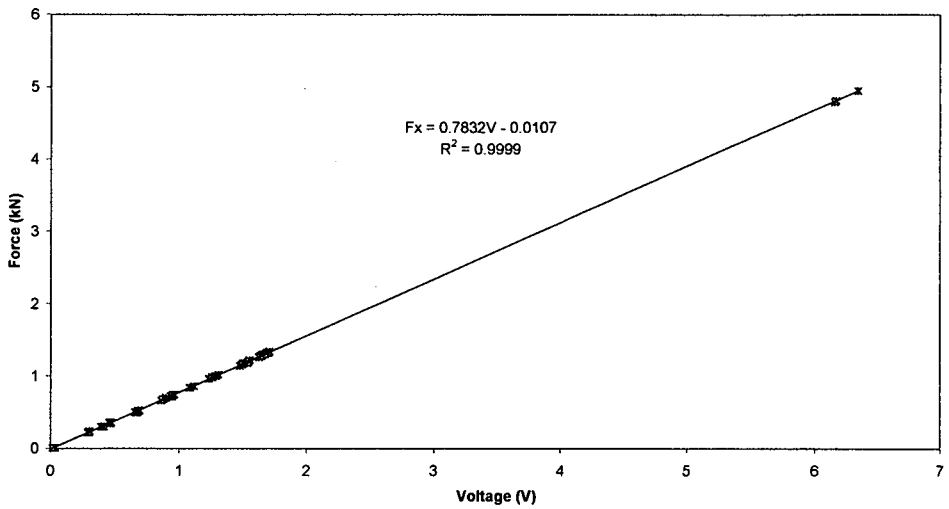

b) Calibration of Fz EORT

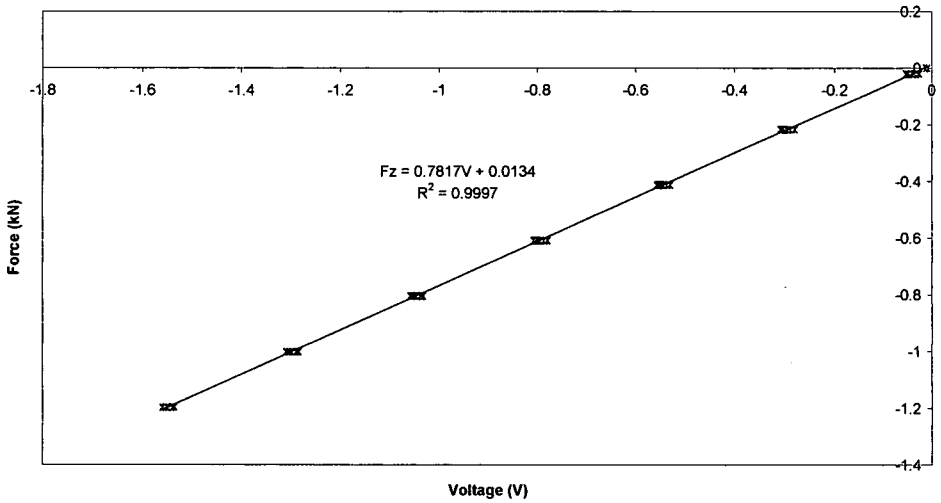

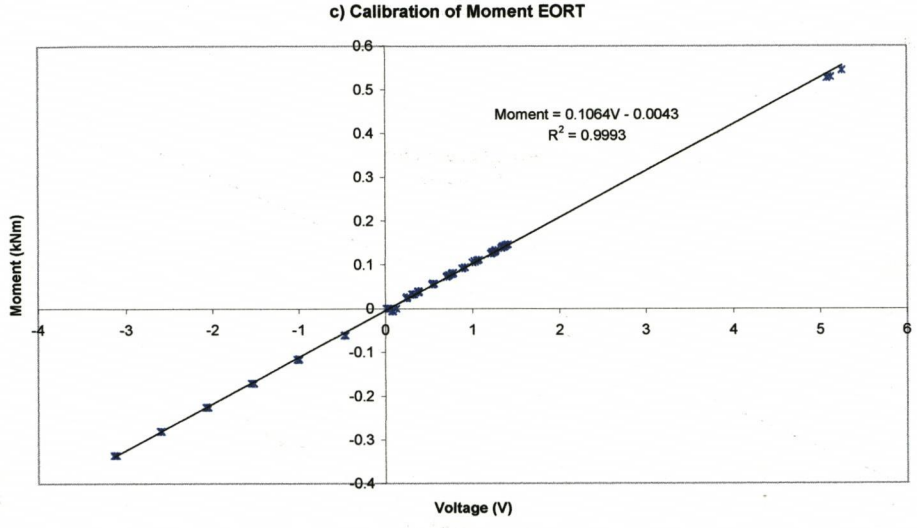

Figure A3.2 Calibration results of Fx, Fz and moment for the EORT

A3.1.2 Calibration of Flow Sensor

The flow transducer was a Danfoss Magflo® Flowmeter, Type MAG 5000. The supply voltage was 12V and the magnitude of the output voltage corresponded directly to the units of flow selected on the flow sensor.

A3.1.3 Calibration of Pressure Sensor

The calibration details supplied by the manufacturer for the pressure transducer, type Applied Measurements, P805C9-20Bar, are;

Pressure rating = 10 barg

Zero output = 0.037mV @ 24V DC

Full scale output = 4.997V DC

Calibration constant = $2.0012V-7.4*10^{-5}$

A3.1.4 Calibration of Carriage Velocity

The velocity of the carriage was measured using a proximity sensor positioned next to a drive sprocket for the carriage system.

Chain pitch = 25.4 mm

Carriage velocity (m/s) = frequency*0.0254

A3.1.5 Calibration of Ceramic Pressure

The ceramic pressure sensors (type Applied Measurements Limited PT18-50barg) were calibrated according to the method described in Section 3.5.1 of Chapter 3. The results of the calibrations for each sensor are shown in Figure A3.3 and Figure A3.4, where P1 is the uppermost sensor on the tine and P5 the lowest.

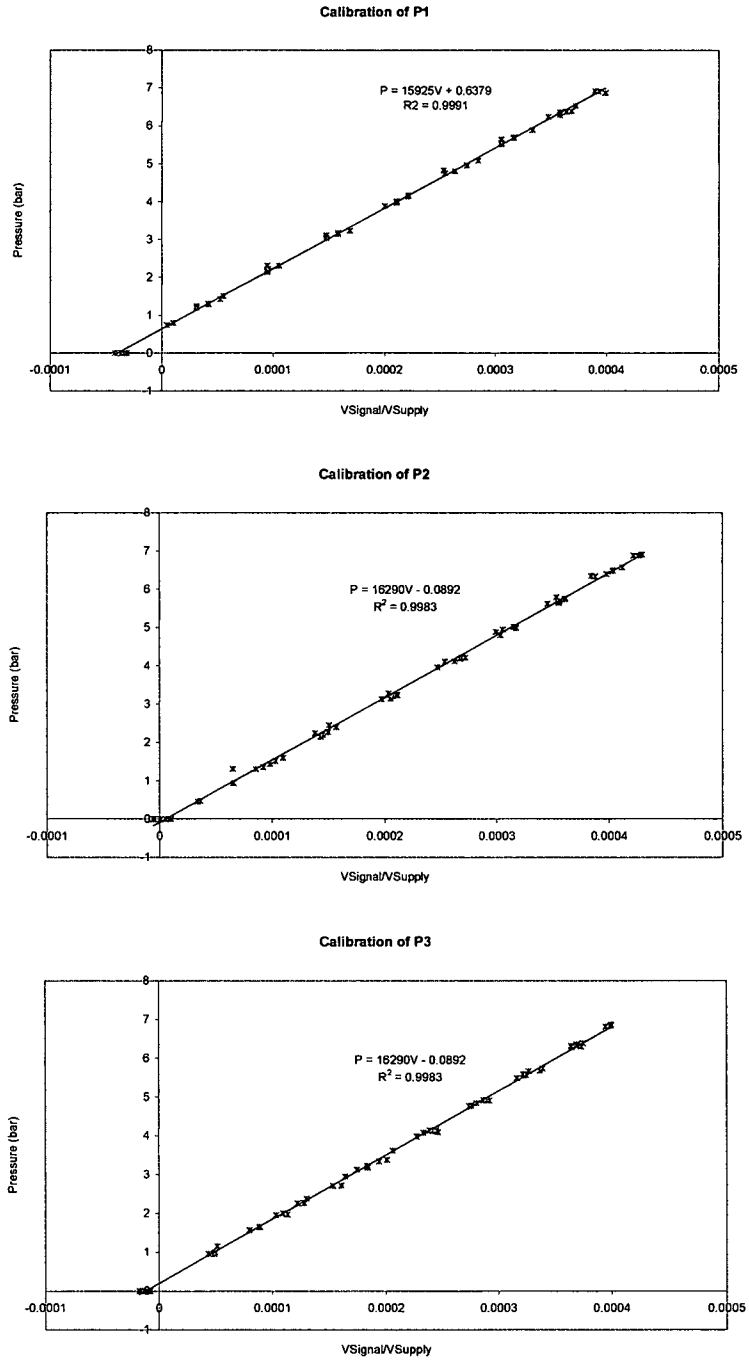

Figure A3.3 Calibration results for ceramic pressure sensors P1 to P3

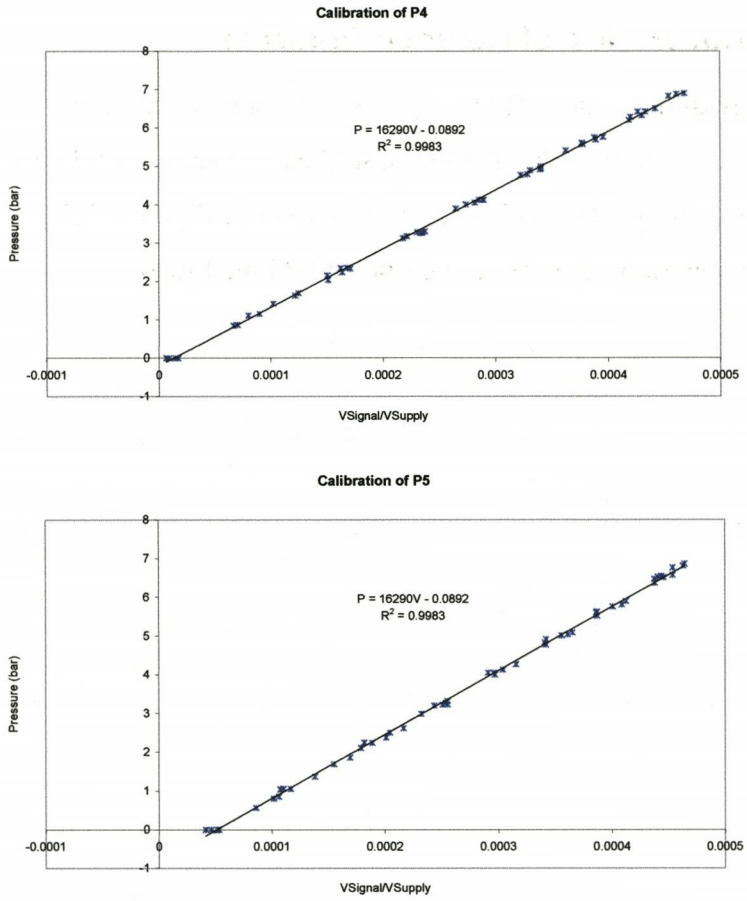

Figure A3.4 Calibration results for ceramic pressure sensors P4 and P5

A3.2 Calibration of Transducers used in Uplift Force Experiments

A3.2.1 Calibration of Extended Octagonal Ring Transducer

The Extended Octagonal Ring Transducer (EORT) used in the uplift force experiments of Chapter 4 was calibrated *in situ*. The output signal of the EORT was amplified and recorded using the Flyde data acquisition module and DasyLab software while loads were applied in the Fx axis. The test was replicated three times. Results are shown in Figure A3.5. The calibration constant is;

$$Fx = 189.13 \times Voltage$$

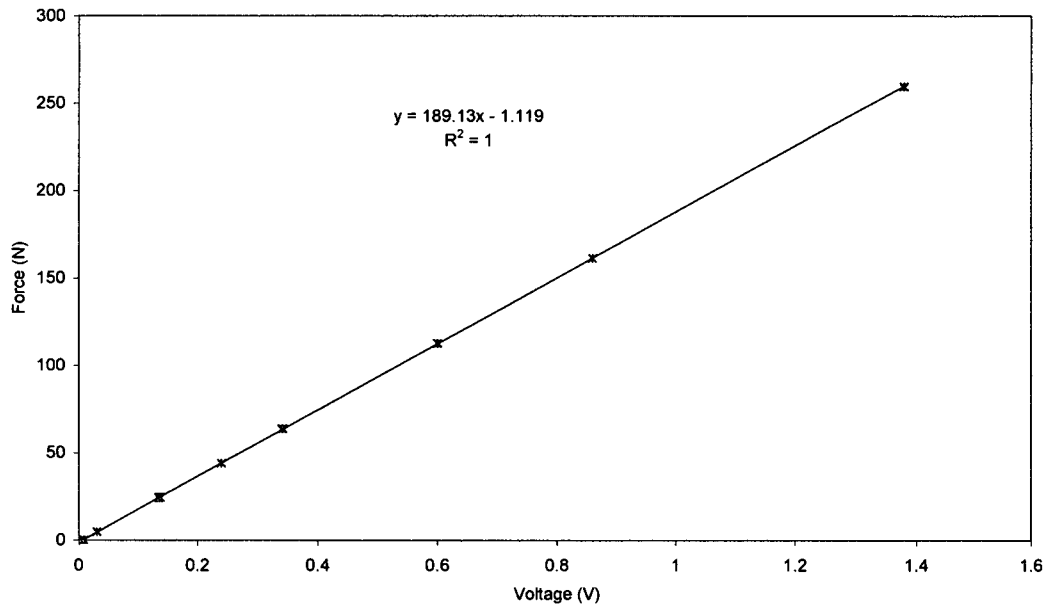

Figure A3.5 Calibration results of EORT used in uplift force experiments

A3.2.2 Calibration of Stringpot Potentiometer

The stringpot potentiometer, which measured the vertical displacement of the uplift plate, was calibrated by incrementally changing the displacement while recording the voltage output. This was repeated three times. Results of the calibration are in Figure A3.6, and the calibration was measure as;

$$Displacement = -265.47 \times V = 243.19$$

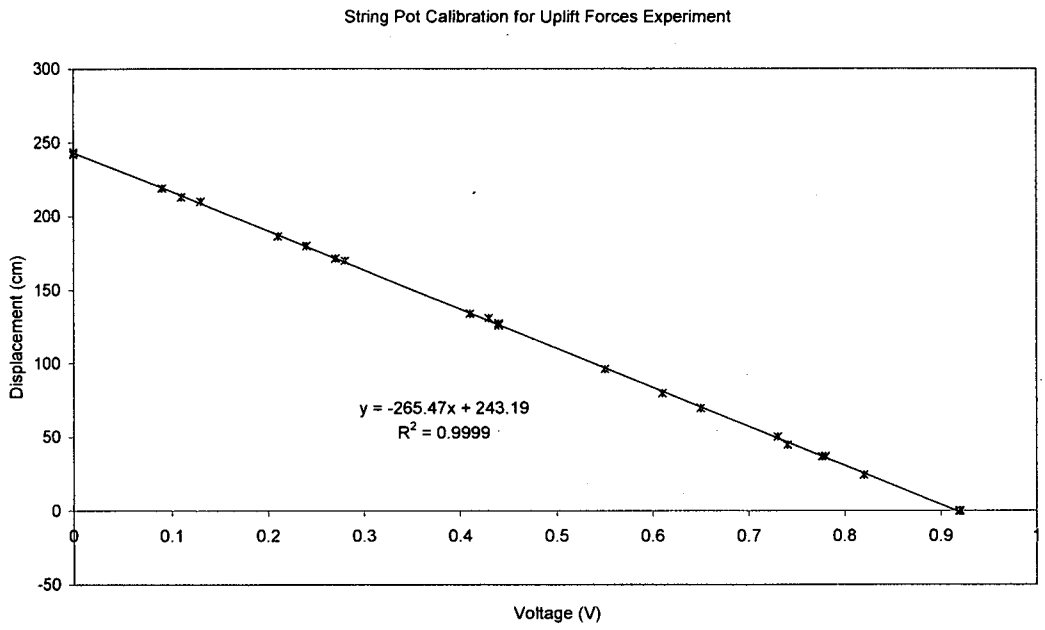

Figure A3.6 Calibration results for the stringpot potentiometer used in the uplift experiments

A3.3 Refractive Index of Glass Windows used in Single Nozzle Experiments

A3.3.1 Refractive Index of Glass Window in Static Nozzle Experiments

The refractive index of the glass window used in the static nozzle experiment was determined by measurement of the angles of incidence and refraction of a laser beam shone at the window, as shown in Figure A3.7. The results shown in Table A3-1 are plot as $\sin\theta_1$ against $\sin\theta 2$ in Figure A3.8, the gradient of 1.54 being the refractive index of the glass (n_2).

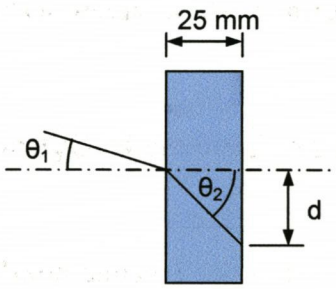

$n_1.\sin\theta_1 = n_2.\sin\theta_2$

$\theta_2 = \tan^{-1}(d/25)$

$n_2 = \sin\theta_1/\sin\theta_2$

Figure A3.7 Determination of refractive index

Table A3-1 Measurements of refractive index for window in static nozzle experiments

θ_1	d (mm)	θ_2	$\sin\theta_1$	$\sin\theta_2$
0	0	0	0.00	0.00
20	6	13.5	0.34	0.23
30	8	17.7	0.50	0.30
40	11	23.7	0.64	0.40
50	13.5	28.4	0.77	0.48
60	17.5	35.0	0.87	0.57
68	20	38.7	0.93	0.62

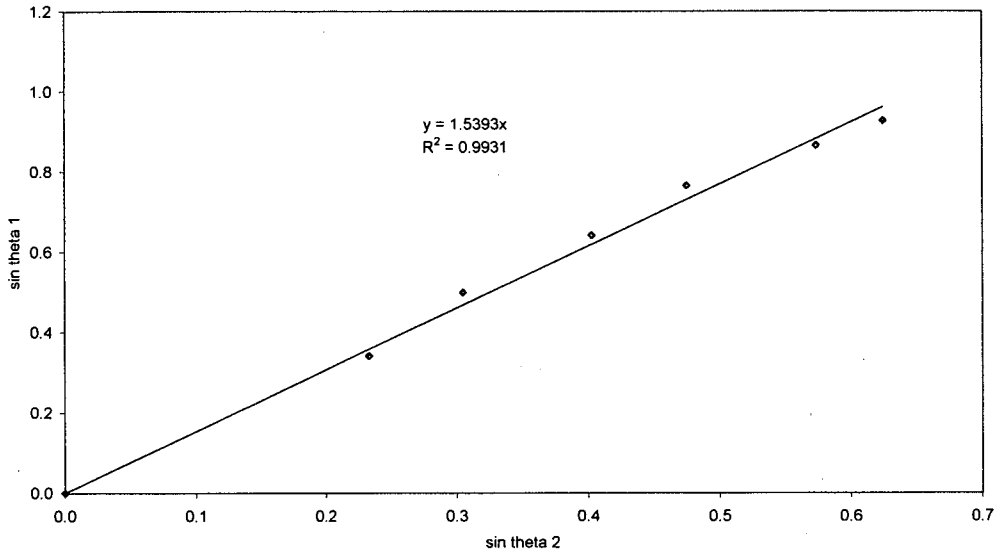

Figure A3.8 **Refractive index determined as gradient of $\sin\theta_1$ against $\sin\theta_2$**

A3.3.2 Refractive Index of Glass Window in Dynamic Nozzle Experiments

The refractive index of the glass window used in the dynamic nozzle experiments of Chapter 5 differed to the static nozzle experiments due to the use of extra sheets of glass (giving a thickness of 44.15 mm) and a layer of oil between them. The refractive index was determined in the same way, the results are shown in Table A3-2 and Figure A3.9 shows the refractive index to be 1.47.

Table A3-2 **Measurements of refractive index for window in dynamic nozzle experiments**

θ_1	d (mm)	θ_2	$\sin\theta_1$	$\sin\theta_2$
0	0	0	0.00	0.00
10	5	6.5	0.17	0.11
20	11	14.0	0.34	0.24
30	16	19.9	0.50	0.34
40	22	26.5	0.64	0.45
50	26.5	31.0	0.77	0.51
55	29	33.3	0.82	0.55
60	31	35.1	0.87	0.57
65	35	38.4	0.91	0.62
69	38	40.7	0.93	0.65

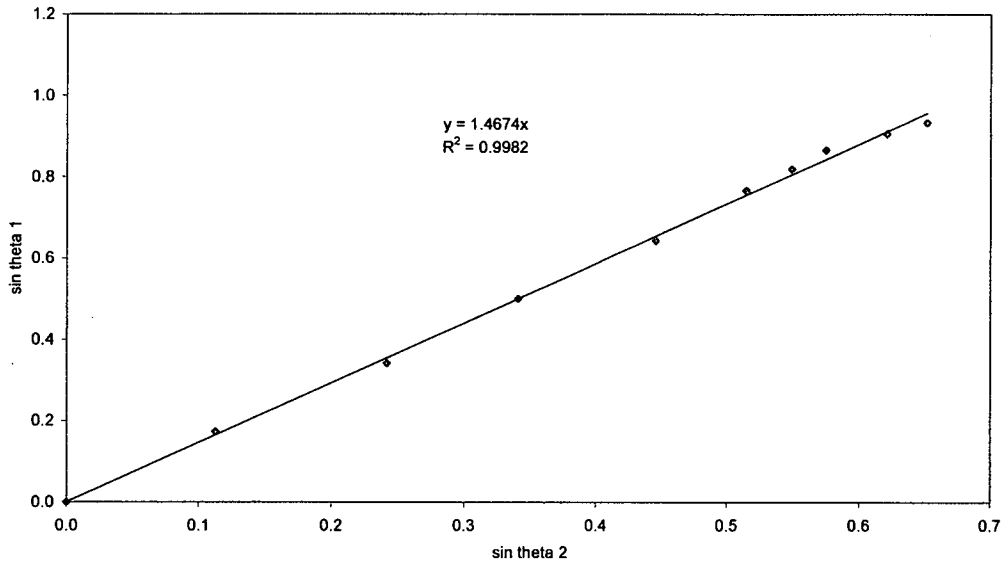

Figure A3.9 Refractive index of thick window determined as gradient of $\sin\theta_1$ against $\sin\theta_2$

Appendix 4

Experimental Results

Contents

A4 Experimental Results

A4.1 Results of the Nozzle Distribution Experiments

Table A4-1 Tabulated results of the nozzle distribution experiments

	Horizontal Force (kN)				Vertical Force (kN)				Moment (kN.m)			
Experiment	R1	R2	R3	Mean	R1	R2	R3	Mean	R1	R2	R3	Mean
1a	3.9871	4.0773	4.3280	4.1285	0.3651	0.3675	0.4101	0.3809	1.0811	1.0817	1.0801	1.0810
1b	3.3772	3.6437	2.7754	3.2664	0.3161	0.3554	0.2960	0.3225	1.0802	1.0882	1.0814	1.0833
1c	2.9339	3.2553	2.9001	3.0301	0.2885	0.3254	0.3106	0.3082	1.0707	1.0819	1.0810	1.0779
1d	3.1504	2.3813	2.8821	2.7379	0.3152	0.2540	0.2982	0.2891	1.0840	1.0815	1.0822	1.0826
1f	3.6548	2.6427	2.3553	3.0176	0.3751	0.2926	0.3022	0.3233	2.0024	1.5145	1.6214	1.7127
1g	2.6278	2.7205	2.3527	2.7337	0.3118	0.2954	0.2999	0.3023	1.6141	1.5536	1.5225	1.5634
3a	2.6459	2.5933	3.1311	2.8568	0.2411	0.2293	0.2865	0.2523	1.0831	1.0869	1.0842	1.0847
3b	1.4424	1.4550	2.0254	1.6409	0.1235	0.1186	0.1775	0.1399	0.8183	0.8246	1.0505	0.8978
3c	1.1674	1.2032	1.1539	1.1748	0.1002	0.0931	0.0961	0.0964	0.6676	0.6788	0.6568	0.6677
3d	0.6263	0.7938	0.8901	0.7700	0.0543	0.0673	0.0702	0.0639	0.3635	0.4569	0.5067	0.4424
3f	0.6204	0.6254	0.7570	0.6552	0.0579	0.0475	0.0616	0.0557	0.3059	0.3490	0.4026	0.3626
3g	0.4625	0.3857	0.5054	0.4845	0.0460	0.0338	0.0411	0.0403	0.2644	0.2212	0.3409	0.2755
6a	0.6413	1.6493	1.8953	1.3953	0.0508	0.1146	0.1186	0.0947	0.4675	0.9304	0.9379	0.7786
6b	0.1413	0.2030	0.2180	0.1894	0.0052	0.0220	0.0238	0.0170	0.0808	0.1219	0.1299	0.1109
6c	0.0992	0.0720	0.0743	0.0819	0.0034	0.0101	0.0061	0.0065	0.0543	0.0408	0.0417	0.0456
6d	0.0757	0.0822	0.0837	0.0805	0.0054	0.0095	0.0070	0.0073	0.0424	0.0462	0.0474	0.0453
6e	3.2600	3.0693	3.1312	3.1535	0.3135	0.2507	0.2480	0.2707	1.7614	1.6975	1.7138	1.7242
9a	1.0172	2.5430	1.7086	1.7579	0.0560	0.1726	0.1421	0.1236	0.5922	1.0668	1.0041	0.8877
9b	2.6684	3.1159	1.0302	2.2715	0.2178	0.2544	0.0789	0.1837	0.9098	1.0805	0.5936	0.8613
9c	1.4118	0.0695	0.4551	0.6455	0.1124	0.0110	0.0352	0.0529	0.8158	0.0361	0.2494	0.3671
9d	0.0559	0.0631	0.0565	0.0575	0.0091	0.0061	0.0052	0.0068	0.0287	0.0282	0.0286	0.0285
12a	0.5640	2.8524	1.0304	1.4823	0.0249	0.1932	0.0809	0.0930	0.3204	1.0849	0.6109	0.6721
12b	0.0862	0.1150	0.2194	0.1402	0.0073	0.0058	0.0200	0.0110	0.0471	0.0633	0.1156	0.0753
12c	2.0851	0.0739	0.0884	0.7508	0.1609	0.0075	0.0015	0.0566	1.0009	0.0432	0.0510	0.3650
12d	0.0651	0.0712	0.0733	0.0699	-0.0011	0.0054	0.0001	0.0015	0.0351	0.0401	0.0410	0.0387
ga	2.6585	2.4976	2.7856	2.7139	0.2301	0.2098	0.2342	0.2247	1.0670	1.0817	1.0807	1.0765
gb	1.6614	2.0812	2.1736	2.0387	0.1479	0.1739	0.1757	0.1669	1.0266	1.0697	1.0695	1.0553
gc	1.1147	1.1909	1.3404	1.3153	0.0895	0.0989	0.1273	0.1052	0.6329	0.6802	0.9208	0.7446
gd	0.9612	0.8057	0.8799	0.8159	0.0826	0.0776	0.0862	0.0755	0.5605	0.4700	0.3935	0.4747
Passive	6.6288	6.5970	6.5231	6.5830	0.6964	0.7004	0.7985	0.7318	1.0820	1.0803	1.0806	1.0810

Table A4-2 Tabulated results of the nozzle distribution experiments

	Flow Rate (l/s)				Jet Pressure (bar)				Tine Speed (m/s)			
Experiment	B1	B2	B3	Mean	B1	B2	B3	Mean	B1	B2	B3	Mean
1a	0.9666	0.9515	0.9742	0.9641	1.0409	1.0006	1.0482	1.0299	0.2795	0.2797	0.2825	0.2806
1b	1.1485	1.1648	1.1619	1.1584	1.4831	1.5348	1.5355	1.5178	0.2806	0.2821	0.2840	0.2822
1c	1.2790	1.2773	1.2781	1.2782	1.9995	2.0214	2.0007	2.0072	0.2794	0.2806	0.2837	0.2812
1d	1.3712	1.3734	1.3866	1.3771	2.4853	2.4926	2.5291	2.5023	0.2791	0.2834	0.2837	0.2820
1f	1.4765	1.4675	1.4669	1.4703	3.0286	3.0000	2.9888	3.0058	0.3256	0.3012	0.3000	0.3090
1g	1.5601	1.5539	1.5524	1.5521	3.4994	3.5285	3.4983	3.5087	0.2975	0.2989	0.3008	0.2991
3a	0.9690	0.9580	0.9679	0.9650	1.0479	1.0129	1.0391	1.0333	0.2800	0.2845	0.2831	0.2825
3b	1.2003	1.1695	1.1870	1.1856	1.5729	1.5098	1.5376	1.5401	0.2813	0.2833	0.2879	0.2842
3c	1.3365	1.3406	1.3453	1.3408	1.9750	2.0369	2.0369	2.0162	0.2810	0.2862	0.2892	0.2855
3d	1.4522	1.4396	1.4411	1.4443	2.5264	2.4883	2.4750	2.4965	0.2833	0.2852	0.2888	0.2858
3f	1.5419	1.5275	1.5349	1.5348	3.0228	2.9738	2.9906	2.9958	0.3031	0.3042	0.3079	0.3050
3g	1.6326	1.6312	1.6255	1.6298	3.5179	3.5349	3.5161	3.5230	0.3124	0.3073	0.3076	0.3091
6a	1.0008	0.9778	0.9931	0.9906	1.0568	1.0643	1.0626	1.0679	0.2844	0.2853	0.2881	0.2860
6b	1.2207	1.2181	1.2167	1.2185	1.5377	1.5335	1.5126	1.5279	0.2823	0.2887	0.2870	0.2860
6c	1.4131	1.3890	1.4014	1.4011	2.0448	2.0027	1.9928	2.0135	0.2835	0.2876	0.2873	0.2862
6d	1.5686	1.5575	1.5658	1.5639	2.5271	2.5214	2.5345	2.5277	0.2835	0.2877	0.2903	0.2872
6e	0.6957	0.6819	0.6919	0.6899	0.9707	0.9659	0.9796	0.9687	0.3094	0.2994	0.3001	0.3029
9a	0.9465	0.8913	0.9376	0.9251	1.2273	1.9263	1.4118	1.5218	0.2817	0.2840	0.2885	0.2847
9b	1.0476	1.0522	1.1647	1.0882	2.4365	2.5114	1.9415	2.2965	0.2802	0.2820	0.2888	0.2837
9c	1.1940	1.3956	1.3866	1.3254	2.3886	2.0190	2.1440	2.1839	0.2826	0.2878	0.2859	0.2854
9d	1.5680	1.5590	1.5664	1.5645	2.5392	2.5168	2.5270	2.5276	0.2851	0.2880	0.2894	0.2875
12a	1.0096	0.8734	0.9888	0.9573	1.0353	2.1682	1.2872	1.4969	0.2843	0.2836	0.2884	0.2854
12b	1.2595	1.2448	1.2391	1.2478	1.5599	1.5741	1.5469	1.5603	0.2849	0.2859	0.2873	0.2860
12c	1.1943	1.4488	1.4455	1.3628	2.5588	2.1116	2.0368	2.2358	0.2801	0.2878	0.2915	0.2865
12d	1.6070	1.6139	1.6143	1.6117	2.5272	2.5256	2.5268	2.5265	0.2838	0.2879	0.2874	0.2864
ga	1.0097	0.9951	0.9900	0.9982	1.0907	1.0634	1.0624	1.0722	0.2805	0.2826	0.2867	0.2833
gb	1.2212	1.2032	1.2099	1.2114	1.5533	1.5249	1.5375	1.5386	0.2808	0.2848	0.2874	0.2843
gc	1.4086	1.4134	1.3997	1.4072	2.0664	2.0808	2.0304	2.0592	0.2843	0.2841	0.2880	0.2855
gd	1.5701	1.5699	1.5708	1.5703	2.5165	2.5384	2.5396	2.5315	0.2828	0.2857	0.2893	0.2860
Passive	0.0000	0.0000	0.0000	0.0000	0.0004	0.0079	0.0025	0.0036	0.2700	0.2709	0.2716	0.2708

A4.2 Results of the Rake Angle Experiments

Table A4-3 Tabulated results of the rake angle experiments

	Horizontal Force (kN)				Vertical Force (kN)				Moment (kN.m)			
Exp.	B1	B2	B3	Mean	B1	B2	B3	Mean	B1	B2	B3	Mean
1a	3.670	3.971	3.763	3.801	-1.141	-1.234	-1.184	-1.180	2.109	2.274	2.147	2.177
1b	4.794	2.568	2.429	3.264	-1.453	-0.918	-0.933	-1.101	2.749	1.497	1.445	1.897
1c	2.814	3.544	2.148	2.835	-0.801	-1.105	-0.797	-0.835	1.685	2.084	1.309	1.692
1d	2.710	2.792	3.707	3.070	-0.819	-0.898	-1.240	-0.986	1.654	1.677	2.196	1.842
2a	5.114	3.418	2.108	3.547	-1.424	-1.049	-0.798	-1.090	2.899	1.951	1.233	2.028
2b	3.535	3.625	1.861	3.007	-1.070	-1.101	-0.707	-0.959	2.035	2.114	1.119	1.756
2c	4.073	2.839	1.800	2.904	-1.189	-0.895	-0.715	-0.933	2.395	1.702	1.120	1.739
2d	3.671	1.893	1.441	2.335	-1.072	-0.646	-0.523	-0.747	2.172	1.140	0.914	1.409
3a	3.642	3.909	3.670	3.740	-1.111	-1.170	-1.130	-1.137	2.049	2.214	2.076	2.113
3b	2.737	2.665	1.415	2.272	-0.863	-0.855	-0.533	-0.750	1.608	1.576	0.838	1.341
3c	2.299	2.643	1.405	2.116	-0.753	-0.835	-0.532	-0.707	1.295	1.518	0.842	1.218
3d	1.806	1.998	1.739	1.848	-0.644	-0.664	-0.601	-0.636	1.102	1.183	1.045	1.110
FP	6.663	7.282	5.314	6.420	-1.709	-1.797	-1.664	-1.723	3.635	3.913	2.885	3.478
4a	4.591	3.688	3.464	3.914	0.409	0.340	0.210	0.320	2.498	1.998	1.876	2.124
4b	2.789	3.150	3.079	3.006	0.102	0.205	0.109	0.138	1.546	1.734	1.669	1.649
4c	3.324	2.023	2.189	2.512	0.151	0.028	0.079	0.086	1.838	1.119	1.209	1.389
4d	1.621	2.042	1.802	1.822	0.016	0.053	0.071	0.047	0.920	1.148	1.024	1.031
5a	3.499	2.973	2.423	2.965	0.297	0.194	0.182	0.224	1.881	1.598	1.359	1.613
5b	2.630	1.438	0.927	1.665	0.207	0.111	0.025	0.114	1.477	0.819	0.535	0.944
5c	1.137	0.790	0.588	0.838	0.067	0.061	0.054	0.061	0.682	0.481	0.361	0.508
5d	0.580	0.662	0.455	0.566	0.041	0.032	0.051	0.041	0.334	0.401	0.283	0.339
6a	3.517	3.973	3.979	3.823	0.311	0.342	0.301	0.318	1.955	2.132	2.107	2.065
6b	2.525	2.248	1.776	2.183	0.226	0.195	0.121	0.180	1.445	1.254	0.979	1.226
6c	0.793	0.598	0.774	0.722	0.152	0.082	0.077	0.104	0.424	0.328	0.434	0.395
6d	0.646	0.566	0.516	0.576	0.112	0.067	0.011	0.063	0.342	0.316	0.305	0.321
VP	6.503	6.123	6.137	6.254	0.773	0.741	0.606	0.707	3.476	3.227	3.235	3.313
7a	4.573	3.695	3.812	4.026	2.459	1.964	2.076	2.166	3.632	2.898	3.002	3.177
7b	3.328	3.142	2.549	3.006	1.783	1.783	1.409	1.658	2.572	2.618	2.085	2.425
7c	1.323	2.686	1.575	1.861	0.854	1.550	0.941	1.115	1.220	2.296	1.324	1.613
7d	2.387	1.748	1.663	1.933	1.440	1.087	0.957	1.155	2.100	1.508	1.418	1.675
8a	2.438	2.129	1.886	2.151	1.497	1.310	1.158	1.321	1.978	1.646	1.587	1.737
8b	0.776	1.160	1.092	1.010	0.488	0.736	0.715	0.646	0.591	0.874	0.849	0.772
8c	0.624	0.687	0.427	0.580	0.536	0.493	0.209	0.413	0.540	0.533	0.246	0.440
8d	0.660	0.400	0.537	0.533	0.455	0.302	0.354	0.370	0.524	0.312	0.394	0.410
9a	4.063	3.789	3.166	3.673	2.182	2.080	1.697	1.986	3.117	2.964	2.429	2.837
9b	2.795	2.313	1.471	2.193	1.673	1.416	0.932	1.340	2.231	1.857	1.180	1.756
9c	1.036	0.509	0.793	0.779	0.694	0.335	0.527	0.519	0.809	0.410	0.605	0.608
9d	0.792	0.686	0.626	0.701	0.545	0.494	0.407	0.482	0.611	0.551	0.473	0.545
AP	6.102	5.437	6.720	6.086	2.953	2.729	3.151	2.944	4.661	4.091	4.910	4.554

Table A4-4 Tabulated results of the rake angle experiments

Exp.	Flow (l/s)				Pressure (bar)				Speed (m/s)			
	B1	B2	B3	Mean	B1	B2	B3	Mean	B1	B2	B3	Mean
1a	0.862	0.808	0.813	0.828	1.109	1.807	1.855	1.590	0.280	0.306	0.275	0.287
1b	1.039	1.090	1.085	1.071	1.560	1.614	1.598	1.591	0.276	0.310	0.276	0.287
1c	1.284	1.280	1.278	1.281	2.296	2.283	2.271	2.283	0.286	0.300	0.279	0.288
1d	1.419	1.421	1.422	1.421	3.063	3.038	3.022	3.041	0.281	0.306	0.276	0.288
2a	0.931	0.951	0.944	0.942	1.058	1.124	1.117	1.099	0.282	0.304	0.279	0.288
2b	1.159	1.140	1.140	1.146	1.602	1.581	1.572	1.585	0.293	0.294	0.281	0.289
2c	1.347	1.349	1.346	1.347	2.269	2.298	2.297	2.288	0.291	0.309	0.276	0.292
2d	1.503	1.496	1.495	1.498	3.035	3.039	3.055	3.043	0.290	0.312	0.280	0.294
3a	0.921	0.915	0.907	0.914	1.136	1.083	1.048	1.089	0.295	0.297	0.276	0.289
3b	1.116	1.111	1.121	1.116	1.579	1.547	1.582	1.569	0.279	0.306	0.279	0.288
3c	1.357	1.346	1.348	1.350	2.315	2.261	2.287	2.288	0.288	0.299	0.281	0.283
3d	1.526	1.507	1.514	1.515	3.044	3.019	3.032	3.032	0.287	0.307	0.280	0.291
FP	0.000	0.000	0.000	0.000	0.001	0.000	-0.002	0.000	0.271	0.278	0.272	0.274
4a	0.894	0.888	0.892	0.891	1.119	1.079	1.104	1.101	0.273	0.272	0.275	0.273
4b	1.076	1.086	1.077	1.080	1.567	1.590	1.577	1.578	0.279	0.275	0.280	0.278
4c	1.262	1.258	1.250	1.257	2.278	2.296	2.268	2.281	0.285	0.309	0.275	0.290
4d	1.406	1.385	1.391	1.388	3.086	3.036	3.018	3.047	0.282	0.311	0.280	0.291
5a	0.946	0.925	0.965	0.946	1.095	1.046	1.093	1.078	0.289	0.302	0.276	0.289
5b	1.156	1.157	1.165	1.159	1.581	1.582	1.577	1.580	0.290	0.308	0.280	0.293
5c	1.344	1.340	1.343	1.342	2.293	2.260	2.310	2.288	0.294	0.294	0.279	0.289
5d	1.491	1.486	1.483	1.487	3.044	3.028	3.029	3.034	0.295	0.313	0.278	0.296
6a	0.885	0.885	0.894	0.888	1.077	1.103	1.100	1.093	0.277	0.292	0.279	0.283
6b	1.073	1.080	1.104	1.086	1.500	1.584	1.611	1.565	0.277	0.308	0.276	0.287
6c	1.315	1.309	1.309	1.311	2.292	2.321	2.310	2.308	0.291	0.276	0.279	0.282
6d	1.475	1.458	1.459	1.464	3.044	3.038	3.057	3.046	0.291	0.280	0.278	0.283
VP	0.000	0.000	0.000	0.000	-0.013	-0.001	0.001	-0.004	0.269	0.270	0.270	0.270
7a	0.861	0.856	0.870	0.862	1.117	1.068	1.103	1.096	0.289	0.274	0.275	0.279
7b	1.060	1.067	1.053	1.060	1.555	1.613	1.533	1.567	0.281	0.311	0.276	0.289
7c	1.242	1.233	1.233	1.236	2.292	2.289	2.303	2.294	0.279	0.311	0.281	0.290
7d	1.375	1.369	1.369	1.371	3.048	3.029	3.097	3.058	0.285	0.305	0.276	0.289
8a	0.913	0.934	0.925	0.924	1.166	1.184	1.172	1.174	0.290	0.299	0.278	0.289
8b	1.114	1.116	1.107	1.112	1.556	1.565	1.559	1.560	0.281	0.312	0.282	0.292
8c	1.304	1.311	1.301	1.305	2.242	2.286	2.270	2.266	0.290	0.305	0.280	0.292
8d	0.000	1.454	1.444	1.449	3.062	3.086	3.040	3.063	0.284	0.279	0.278	0.280
9a	0.889	0.887	0.887	0.888	1.143	1.156	1.127	1.142	0.288	0.306	0.276	0.290
9b	1.081	1.089	1.094	1.088	1.604	1.619	1.590	1.604	0.282	0.310	0.279	0.291
9c	1.318	1.318	1.312	1.316	2.280	2.296	2.283	2.286	0.284	0.278	0.279	0.280
9d	1.464	1.466	1.457	1.462	3.069	3.040	3.028	3.046	0.287	0.310	0.281	0.296
AP	0.000	0.000	0.001	0.000	0.000	0.002	0.009	0.004	0.274	0.271	0.269	0.271

A4.3 Results of the Soil Pressure Profile Experiments

Table A4-5 Tabulated results of the soil pressure profile experiments of Chapter 3

	Measured by EORT			Measured by ceramic pressure sensors					
	Horizontal Force (kN)	Vertical Force (kN)	Moment (kN.m)	Sensor	Start Zero (bar)	End Zero (bar)	Dynamic (bar)	Net Pressure Start (bar)	Net Pressure End (bar)
Test 0				P1	0.000	-0.014	0.027	0.027	0.041
Zero	0.176	0.019	0.005	P2	-1.193	-0.623	1.671	2.864	2.294
Dynamic	5.659	0.646	2.639	P3	-0.246	-3.812	2.751	2.998	6.564
Difference	5.483	0.627	2.634	P4	0.909	0.072	13.027	12.118	12.955
S.Deviation	0.392	0.030	0.000	P5	0.037	-0.090	14.403	14.366	14.493
Test 1				P1	0.000	-0.007	0.041	0.041	0.048
Zero	0.153	0.016	0.004	P2	-0.895	-0.317	1.765	2.660	2.081
Dynamic	5.493	0.631	2.623	P3	0.983	-3.575	2.608	1.624	6.183
Difference	5.340	0.616	2.619	P4	0.821	-0.368	11.639	10.817	12.006
S.Deviation	0.426	0.026	0.043	P5	-0.004	-0.011	13.739	13.743	13.750
Test 2				P1	-0.021	-0.051	0.036	0.057	0.087
Zero	0.149	0.021	0.006	P2	-0.235	-0.501	1.880	2.115	2.381
Dynamic	5.627	0.637	2.639	P3	-0.162	-4.189	1.962	2.124	6.151
Difference	5.478	0.616	2.633	P4	1.123	0.583	13.060	11.937	12.477
S.Deviation	0.332	0.031	0.001	P5	-0.037	-0.070	14.398	14.435	14.467
Test 3				P1	-0.007	-0.034	0.090	0.097	0.124
Zero	0.130	0.022	0.006	P2	-0.243	-0.138	2.707	2.950	2.845
Dynamic	6.547	0.686	2.639	P3	0.314	-4.578	2.611	2.297	7.189
Difference	6.417	0.664	2.633	P4	1.501	0.223	14.350	12.849	14.127
S.Deviation	0.584	0.036	0.000	P5	-0.008	-0.147	16.374	16.382	16.521
Test 4				P1	-0.007	-0.031	0.148	0.155	0.179
Zero	0.175	0.038	0.010	P2	0.116	0.005	2.827	2.711	2.822
Dynamic	6.799	0.735	2.639	P3	2.005	-1.352	6.006	4.000	7.358
Difference	6.624	0.697	2.629	P4	0.192	0.004	13.748	13.556	13.745
S.Deviation	0.471	0.043	0.000	P5	-0.068	-0.133	17.282	17.350	17.415
Test 5				P1	-0.009	0.337	0.091	0.100	-0.247
Zero	0.149	0.017	0.005	P2	0.359	-0.434	2.758	2.399	3.192
Dynamic	5.537	0.644	2.638	P3	2.470	-1.488	5.630	3.160	7.118
Difference	5.388	0.627	2.634	P4	0.910	4.448	11.791	10.881	7.343
S.Deviation	0.275	0.030	0.004	P5	-0.112	-0.636	14.650	14.762	15.286
Test 6				P1	0.000	-0.025	0.089	0.089	0.114
Zero	0.174	0.015	0.004	P2	0.394	0.345	2.733	2.340	2.389
Dynamic	5.483	0.656	2.624	P3	2.250	0.891	6.867	4.617	5.976
Difference	5.309	0.641	2.620	P4	1.763	0.670	11.609	9.847	10.939
S.Deviation	0.407	0.033	0.045	P5	-0.018	-0.170	13.211	13.229	13.381

Test 5 gave erroneous measurements at the end of test.
Test 6 P3 data is questionable because of odd characteristics as the tine reached the end of its run.

A4.4 Results of the Static Nozzle Experiments

A4.4.1 Jet flow rate and pressure Results

Table A4-6 Tabulated results of the jet flow rate and pressure for the static nozzle experiments in standard, fine and coarse sand

Standard Sand

	Time (s)	Design flow rate (m/s) 25	50	75	100	125	150	175	200	250	300	350	400	450
Flowrate (m/s)	0.28	12.6	44.7	197.8	69.7	82.5	146.8	51.4	120.5	229.6	82.2	119.0	222.3	459.1
	0.48	113.3	219.1	190.7	171.1	178.6	164.5	90.9	207.6	128.1	77.7	173.2	307.3	353.7
	1.00	10.5	41.3	86.2	72.6	103.9	123.9	135.3	169.5	259.3	85.7	281.8	356.3	404.5
	2.00	17.8	54.4	72.4	95.7	129.6	141.9	155.0	152.7	266.0	97.6	321.9	372.3	413.1
	0-2s average	38.6	74.1	97.1	101.5	124.2	138.3	125.5	177.7	219.8	85.2	268.0	333.8	411.7
	2-20 mean	**18.3**	**53.5**	**77.3**	**98.2**	**128.9**	**154.1**	**166.0**	**202.8**	**257.9**	**202.7**	**324.0**	**375.1**	**418.9**
Pressure (bar)	0.28	2.15	1.37	1.31	2.56	2.91	3.26	3.63	3.52	2.78	3.52	4.63	4.68	5.27
	0.48	1.42	1.00	1.07	1.91	2.27	2.56	2.67	2.88	2.43	3.25	4.00	4.38	5.27
	1.00	0.76	0.63	0.76	1.22	1.59	1.79	2.03	2.20	2.18	2.73	3.19	4.14	5.24
	2.00	0.35	0.37	0.54	0.71	1.09	1.19	1.31	1.69	2.05	2.53	3.21	4.09	5.44
	0-2s average	0.37	0.73	0.86	1.10	1.46	1.68	2.22	2.38	2.26	2.33	3.68	4.28	5.46
	2-20 mean	**0.17**	**0.23**	**0.39**	**0.46**	**0.82**	**0.91**	**0.96**	**1.43**	**2.02**	**2.53**	**3.21**	**4.07**	**5.43**

Fine Sand

	Time (s)	Design flow rate (m/s) 50	100	150	250	400
Flowrate (m/s)	0.20	30.0	30.4	144.6	226.7	406.6
	0.48	0.9	175.1	45.8	318.5	369.4
	1.00	61.4	75.0	117.7	234.1	375.9
	2.00	47.0	36.2	143.5	247.9	378.9
	0-2s average	37.3	100.3	123.6	264.4	381.7
	2-20 mean	**50.1**	**99.5**	**147.9**	**247.7**	**376.9**
Pressure (bar)	0.28	2.22	2.41	2.61	2.77	4.28
	0.48	1.58	1.01	1.66	2.42	4.25
	1.00	0.91	1.34	1.90	2.17	4.26
	2.00	0.40	0.93	1.02	2.03	4.22
	0-2s average	1.12	1.51	1.55	2.35	4.26
	2-20 mean	**0.27**	**0.56**	**0.85**	**1.95**	**4.26**

Coarse Sand

	Time (s)	Design flow rate (m/s) 50	100	150	200	250	300	400
Flowrate (m/s)	0.20	0.18	0.55	0.20	174.2	260.3	403.2	
	0.48	0.17	0.53	0.82	155.3	311.4	411.3	
	1.00	0.19	0.51	0.78	152.3	259.2	413.2	
	2.00	0.20	0.44	0.75	152.2	248.8	413.6	
	0-2s average	0.18	0.52	0.79	155.7	266.2	423.7	
	2-20 mean	**0.20**	**0.42**	**0.75**	**146.5**	**245.9**	**398.2**	
Pressure (bar)	0.28	0.18	0.55	0.86	1.95			
	0.48	0.17	0.53	0.82	2.00			
	1.00	0.19	0.51	0.78	2.15			
	2.00	0.20	0.44	0.75	2.25			
	0-2s average	0.18	0.52	0.79	2.26			
	2-20 mean	**0.20**	**0.42**	**0.75**	**2.62**			

A4.4.2 Measured Cavity Dimensions

Table A4-7 Tabulated results of cavity length and depth from static nozzle experiments in standard sand

STANDARD SAND

		Flow rate (ml/s) [Design/Measured]														
		25	50	75	100	125	150	175	200	250	300	350	400	450		
	Time (s)	18.3	53.5	77.3	98.2	128.9	154.1	166.0	202.8	257.9	202.7	324.0	375.1	418.9		
Length	0.24	72.8	67.3	67.5	80.5	73.6	89.1	87.6	83.4	81.3	89.4	85.2	87.5	94.3		
	0.48	88.8	89.0	96.8	96.5	98.6	106.8	100.5	106.6	112.5	104.4		113.8	121.1		
	1	108.7	103.9	106.5	122.8	124.2	128.7	135.0	136.3	135.7	138.1	150.4	151.7	158.1		
	2	121.5	121.9	127.7	141.0	151.7	161.5	159.6	165.3	171.3	172.6	185.9	190.2	200.2		
	4	135.1	138.7	148.4	168.6	182.3	199.5	194.1	198.5	223.2	232.6	233.4	254.1	266.4		
	6	143.8	151.7	169.7	190.2	208.1	221.0	217.6	237.5	258.0	263.1	273.1	291.9	305.3		
	8	147.4	160.2	184.4	207.0	227.0	243.4	245.2	261.7	276.9	294.1	303.9	325.9	340.2		
	10	152.2	165.1	197.6	217.3	248.7	258.2	269.1	284.4	296.8	317.9	324.4	348.5	373.5		
	12	152.3	167.0	204.8	223.3	256.6	270.3	272.7	297.0	313.3	332.1	338.0	366.7	400.3		
	16	152.6	175.0	217.0	229.7	273.9	287.1	289.6	319.9	346.8	359.5	371.3	398.6	439.2		
	20	152.3	177.1	220.6	234.0	284.5	295.5	305.2	339.8	364.2	381.3			464.2		
	22				235.2											
	24		179.7	227.1							14 seconds	355.5	385.8	420.4		
	30	139.8														
Depth	0.24	31.5	33.9	27.6	34.6	36.1	40.3	40.0	35.4	35.3	39.2	35.4	35.3	40.6		
	0.48	38.9	34.3	36.3	40.0	43.4	41.5	41.3	43.3	42.6	42.0		49.9	50.4		
	1	48.4	41.7	43.6	54.3	50.7	51.8	56.9	54.1	57.5	58.8	63.6	65.8	73.5		
	2	53.2	47.3	51.7	65.5	64.7	70.6	70.1	70.8	77.5	82.8	84.1	90.4	99.5		
	4	66.6	59.4	72.5	79.9	89.1	94.3	96.6	101.0	114.7	115.4	137.2	133.1	167.4		
	6	68.1	68.4	88.8	97.6	113.1	128.7	127.4	132.9	148.6	155.1	174.8	177.8	192.0		
	8	67.4	75.9	104.0	111.4	142.0	154.3	155.4	156.7	178.0	190.7	210.5	212.5	222.3		
	10	73.1	85.4	118.4	126.2	165.9	174.7	168.5	178.6	208.7	220.6	237.3	244.5	249.9		
	12	81.0	102.0	134.5	139.2	173.5	194.9	185.4	197.0	221.1	255.6	275.8	278.4	287.2		
	16	100.5	129.3	173.1	173.3	215.4	242.7	229.0	254.8	288.6	370.3	360.7	372.2	367.8		
	20	109.2	170.3	224.9	205.0	328.0	316.2	325.1	360.4	393.0	369.0			374.0		
	22				220.3											
	24		227.9	253.3							14 seconds	363.4	319.0	327.7		
	30	167.7														

Table A4-8 Tabulated results of cavity length and depth from static nozzle experiments in fine sand

FINE SAND

		Flow rate (ml/s) [Design/Measured]				
		50	100	150	250	400
	Time (secs)	50.1	99.5	147.9	247.7	376.9
Length	0.24	78.4	86.8	77.2	78.5	82.4
	0.48	97.4	105.0	104.3	103.1	103.1
	1	116.9	126.1	126.0	132.0	143.8
	2	136.5	151.4	157.4	168.2	187.9
	4	155.5	183.4	184.2	216.4	246.8
	6	168.9	202.9	211.1	252.7	292.4
	8	174.9	218.1	235.4	280.5	323.9
	10	180.4	229.9	253.6	302.0	354.0
	12	185.1	240.8	268.0	320.5	373.0
	16	191.5	252.3	293.2	349.1	404.9
	20	194.1	260.5	305.5	369.4	
	22				378.4	
	24			314.1		
	26	205.7				
	28		269.7			
Depth	0.24	31.1	35.1	35.8	31.3	35.1
	0.48	39.6	40.1	39.3	41.4	45.7
	1	43.5	51.6	50.0	51.2	60.1
	2	51.8	57.7	66.0	66.2	82.2
	4	63.6	76.1	80.4	97.7	118.5
	6	72.7	88.9	99.3	129.6	151.5
	8	83.5	104.9	119.4	158.0	184.2
	10	90.3	121.9	142.3	182.7	220.0
	12	102.1	133.7	149.7	207.2	246.2
	16	122.2	168.9	180.8	244.7	321.2
	20	163.9	197.2	205.9	273.5	
	22				293.8	
	24			238.8		
	26	234.8				
	28		266.9			

Red font indicates cavities that had entered the third stage of cavity development, breaking upwards towards the soil surface

Table A4-9 Tabulated results of cavity length and depth from static nozzle experiments in coarse sand

COARSE SAND

		Flow rate (ml/s) [Design/Measured]				
		50	100	150	250	400
	Time (secs)	53.1	98.9	146.5	245.9	398.2
Length	0.24	23.0	47.3	48.1	97.2	99.4
	0.48	30.1	48.8	50.1	106.4	112.4
	0.72	36.9	48.7	51.3	103.3	115.5
	1.0	35.3	48.7	50.2	104.0	117.2
	1.48	36.3	48.4	50.6	108.1	122.3
	2.0	37.0	49.0	50.3	107.4	125.0
	4.0	38.6	50.2	51.1	109.4	
	8.0	41.5				
	18.0					131.1
Depth	0.24	14.6	18.2	18.7	28.9	34.3
	0.48	18.8	18.5	21.7	29.9	32.3
	0.72	19.2	17.7	20.9	31.2	33.6
	1.0	18.8	17.0	19.3	27.4	39.6
	1.48	18.5	16.4	18.9	30.0	31.8
	2.0	17.4	17.6	16.6	29.2	35.9
	4.0	19.8	21.2	16.8	29.5	
	8.0	19.6				
	18.0					36.8

A4.4.3 Calculation of the Surface Area of a Cavity

In Chapter 4 the cavity created by a static nozzle internal to the sand was found to take the approximate form $y = 2G\sqrt{l.x} - 2G.x$ [Eq 4.15]. The surface area is thus given by the integral $A = \int_{x_1}^{x_2} 2\pi.\left(2G\sqrt{lx} - 2Gx\right)\sqrt{1 + \frac{G^2 l}{x} - \frac{4G^2\sqrt{l}}{\sqrt{x}} + 4G^2}.dx$ [Eq. 4.29]. It was not possible to solve this integral algebraically, so a numerical solution was found using a scientific calculator, as detailed in Section 4.7.1 G of Chapter 4. Numerically determined surface areas, assuming a G value of 0.45, are shown against the corresponding cavity length values in Table A4-10 below. Figure A4.1 shows that the surface area can be closely approximated as the length squared (l^2).

Table A4-10 Results of calculated surface area corresponding to cavity length

Cavity Length (mm)	Surface Area (mm^2)	Length^2 (mm^2)
0	0	0
10	103.7	100
30	933.2	900
50	2592.3	2500
70	5080.9	4900
90	8399.1	8100
110	12546.8	12100
130	17524.1	16900
150	23330.8	22500
170	29967.2	28900
190	37433.0	36100
210	45728.5	44100
230	54853.4	52900
250	64807.9	62500
270	75591.9	72900
290	87205.5	84100
310	99648.6	96100

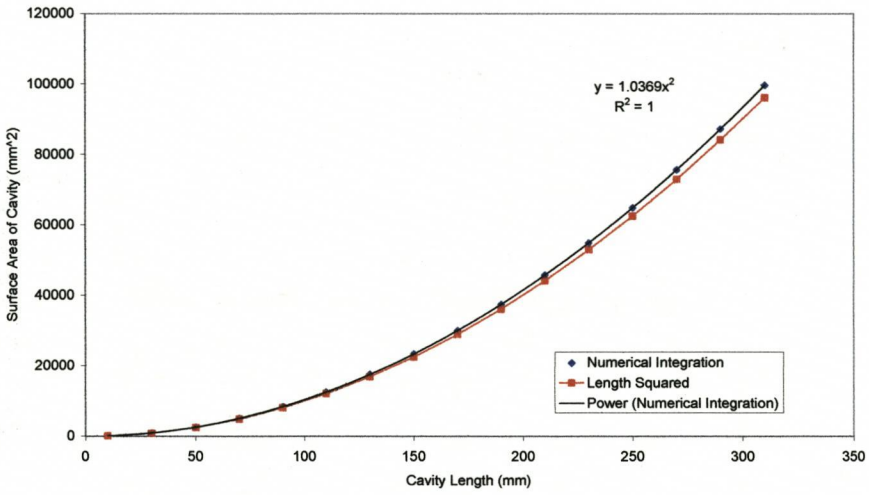

Figure A4.1 Comparison of numerically determined surface area against cavity length and approximating curve of length^2

A4.4.4 Plots of Cavities Profiles created by Static Nozzles

18.3 ml/s

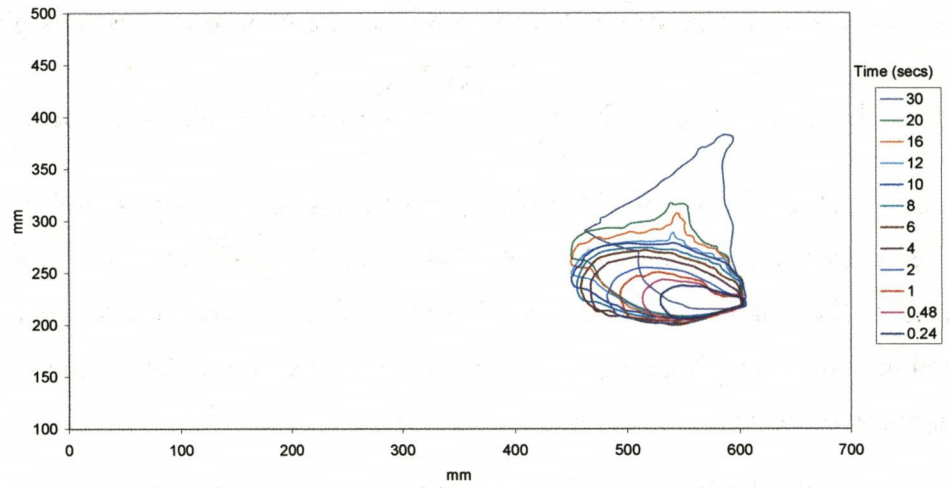

53.5 ml/s

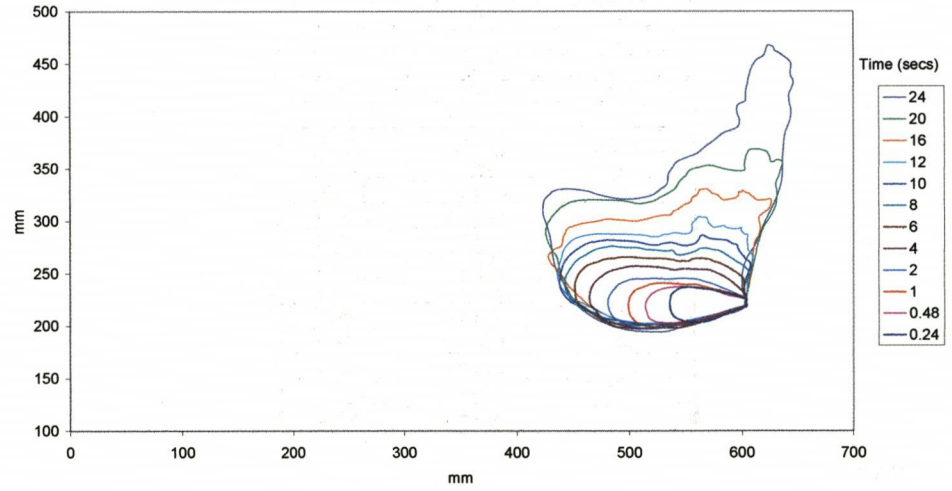

77 ml/s

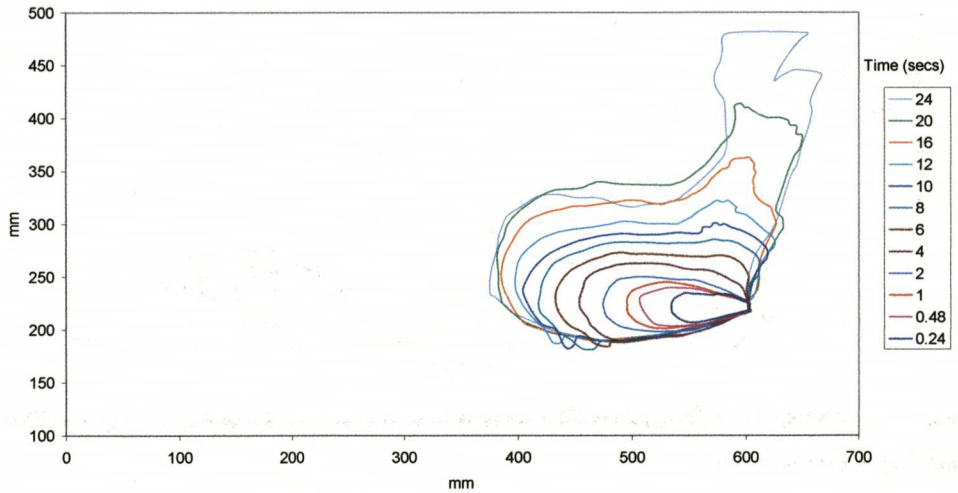

98 ml/s

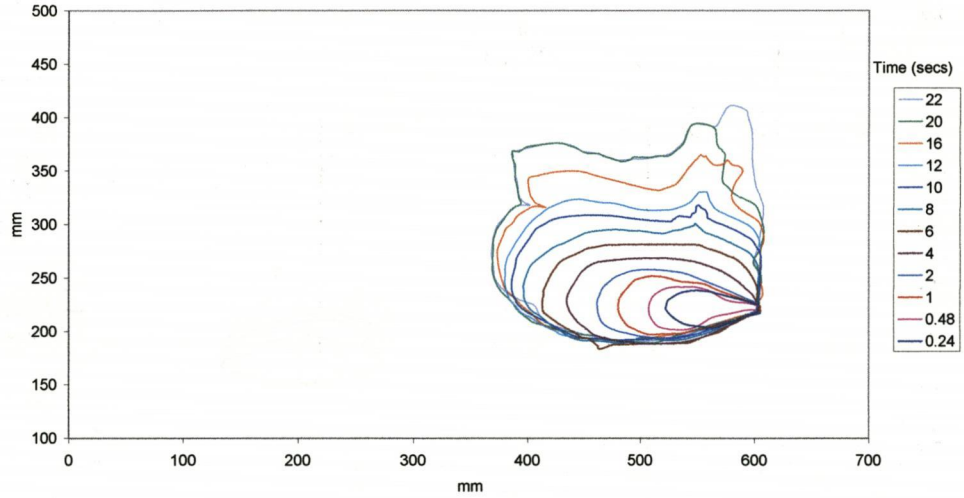

129 ml/s

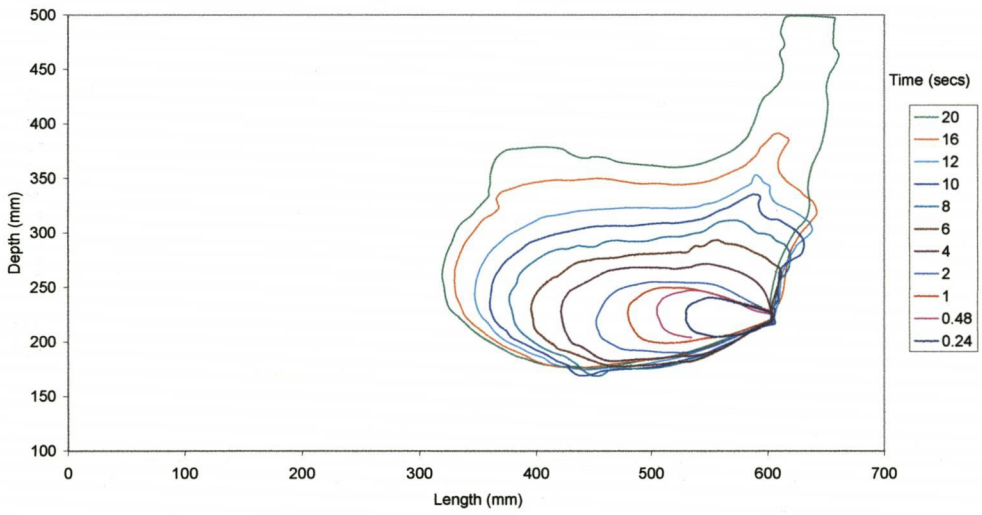

154 ml/s

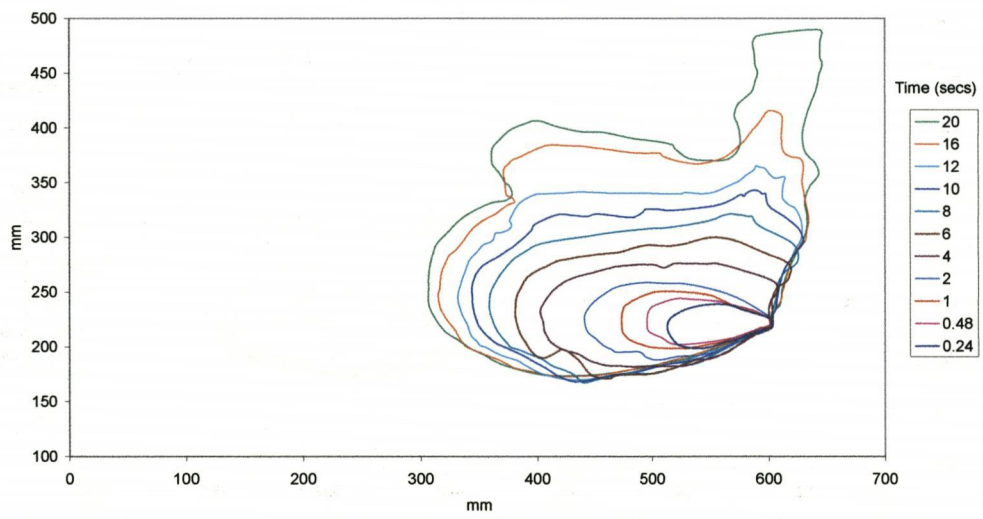

166 ml/s

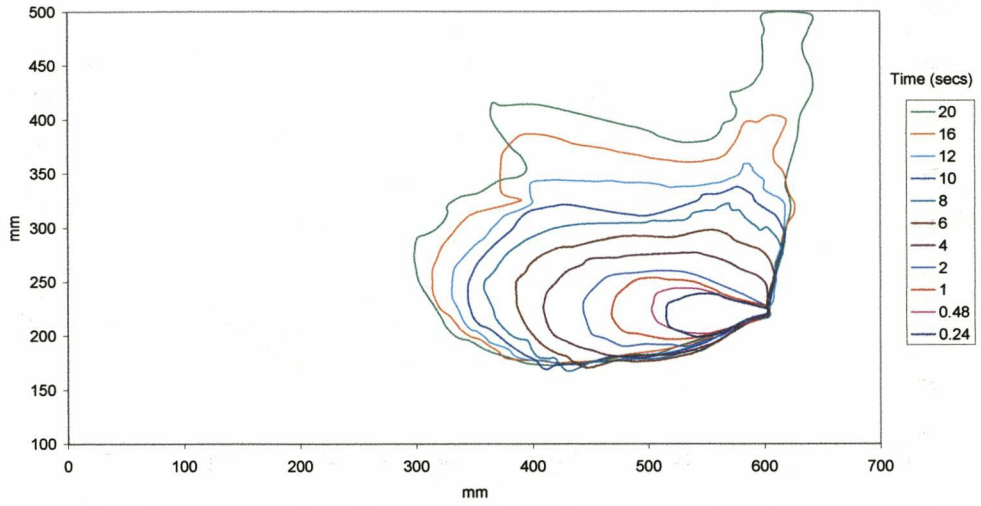

203 ml/s

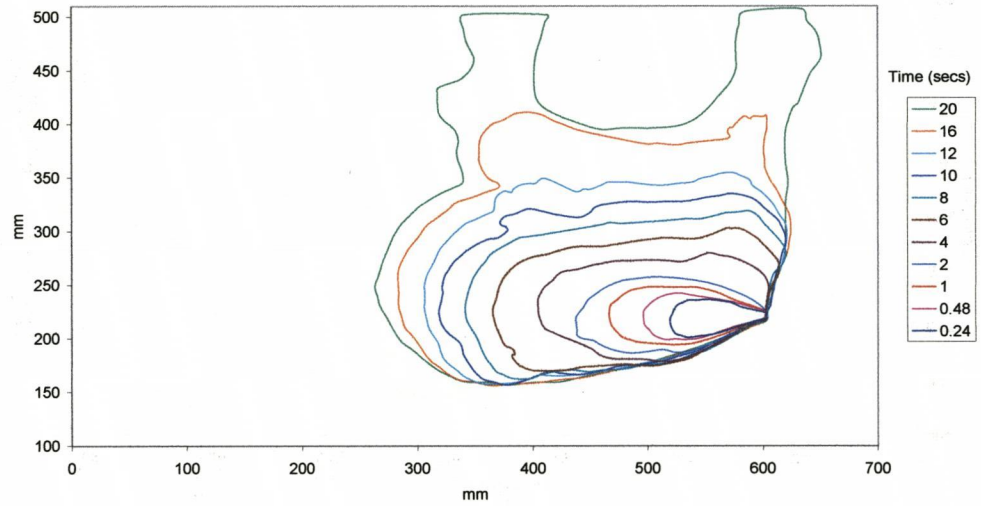

258 ml/s

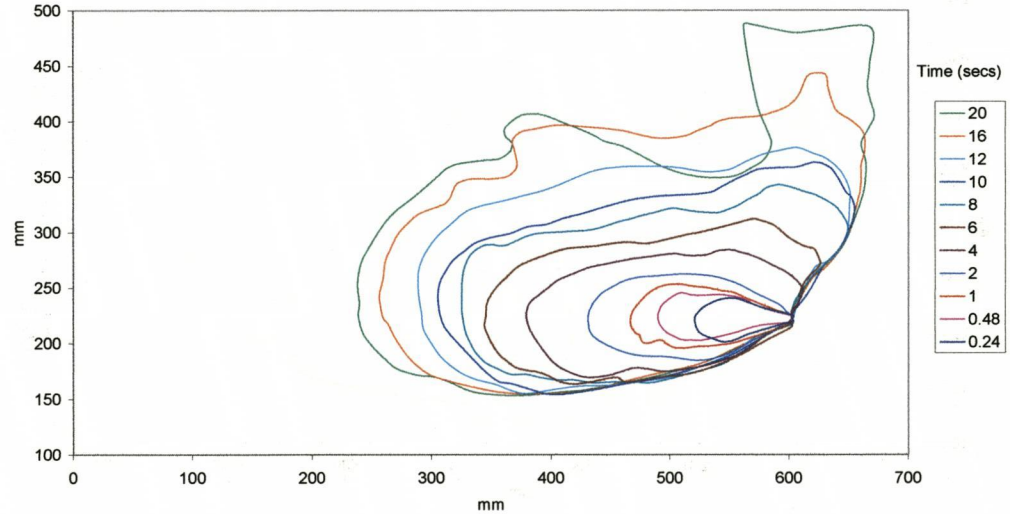

300 ml/s

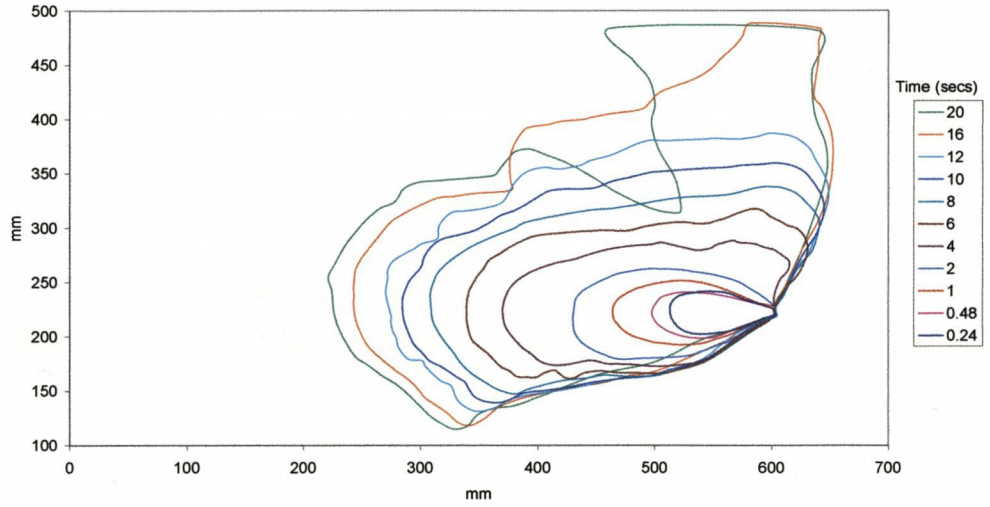

324 ml/s

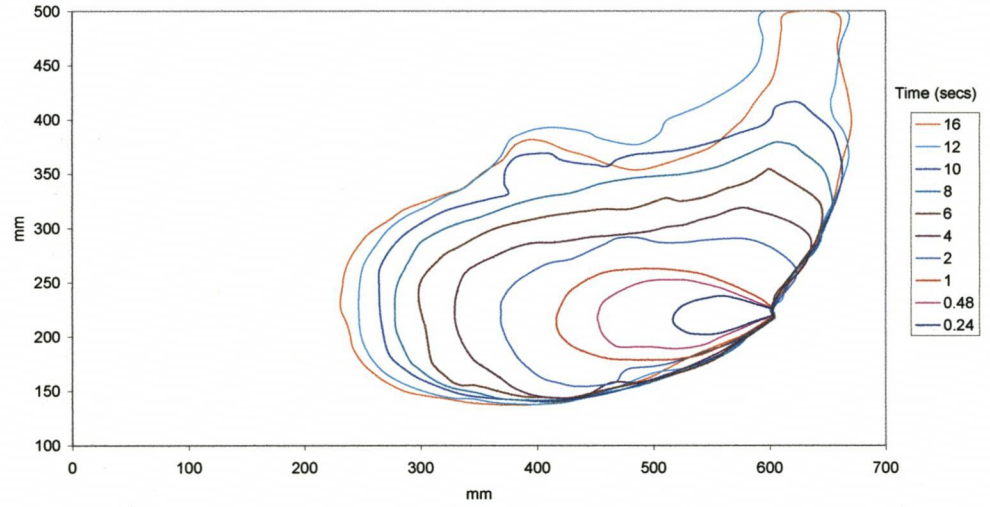

375 ml/s

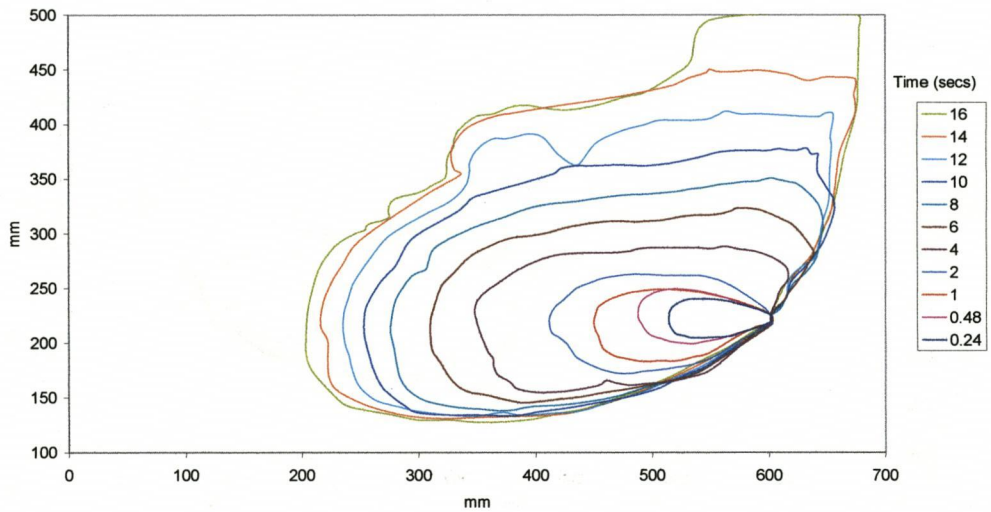

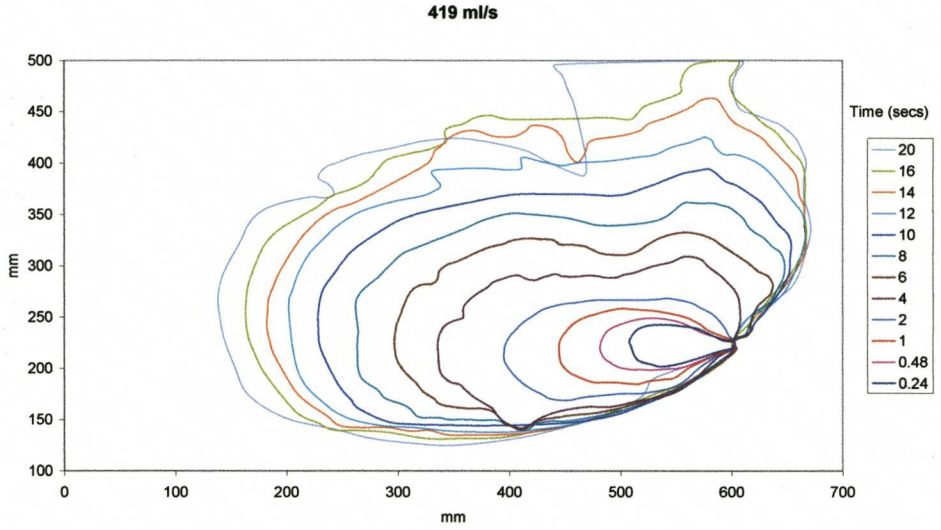

Figure A4.2 Profile of cavities created in standard sand by the thirteen flow rates in the static nozzle experiments

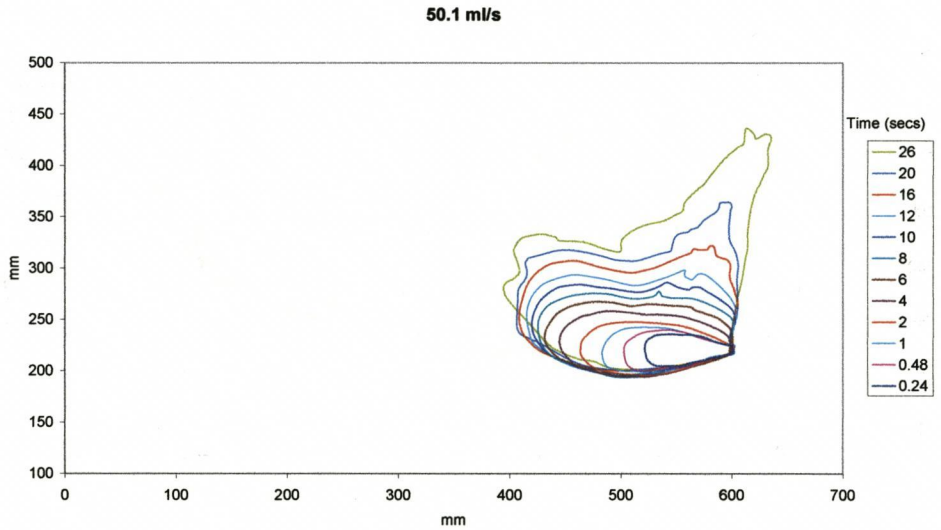

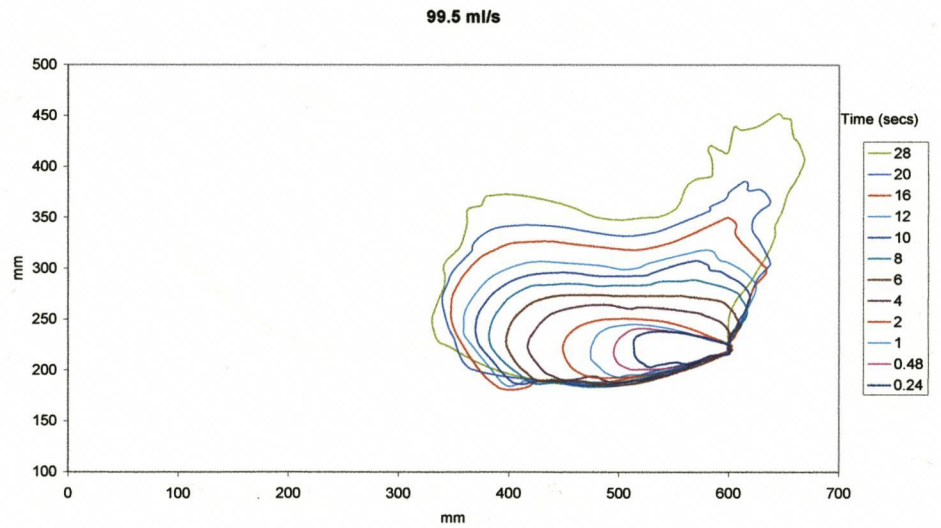

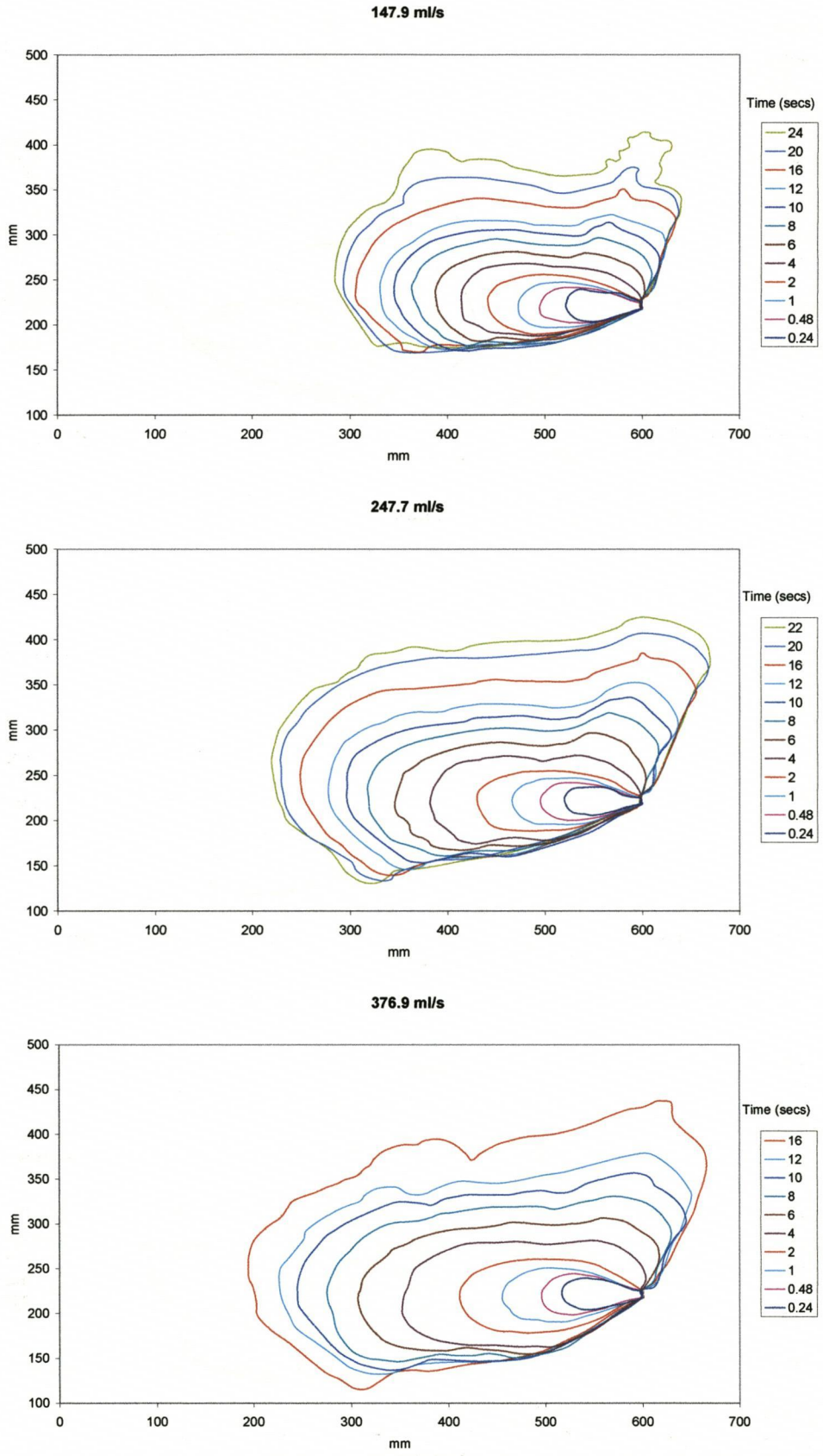

Figure A4.3 Profile of cavities created in fine sand by the five flow rates in the static nozzle experiments

53 ml/s

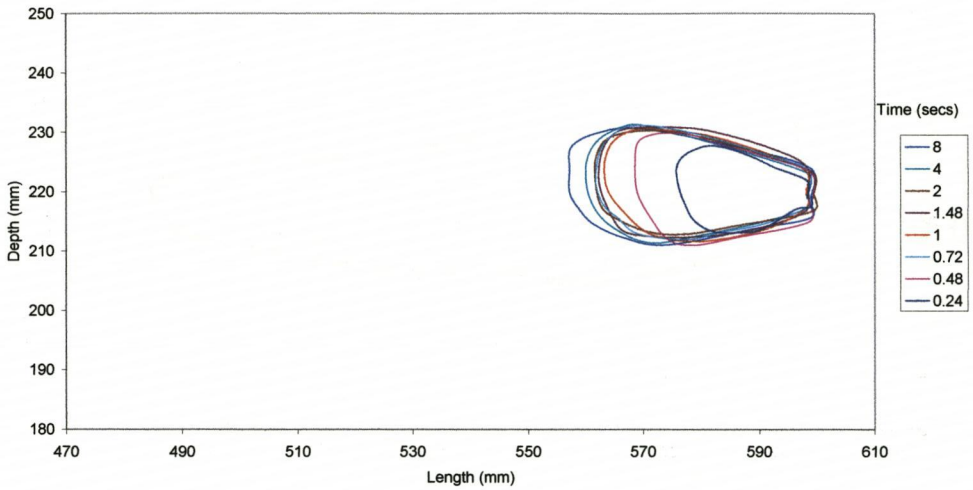

99 ml/s

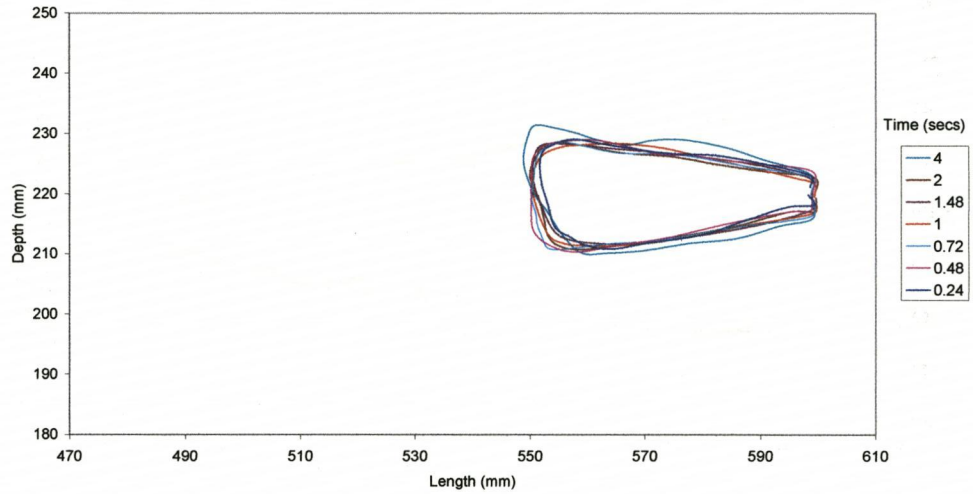

147 ml/s

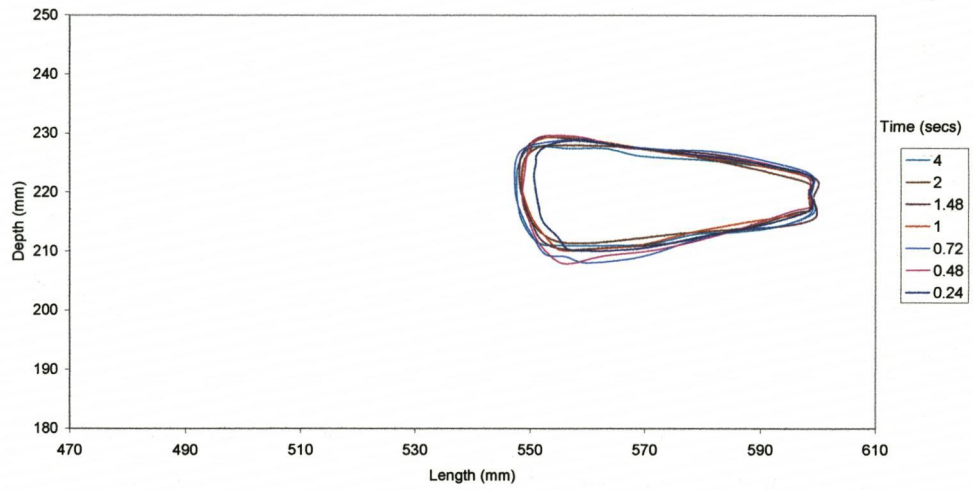

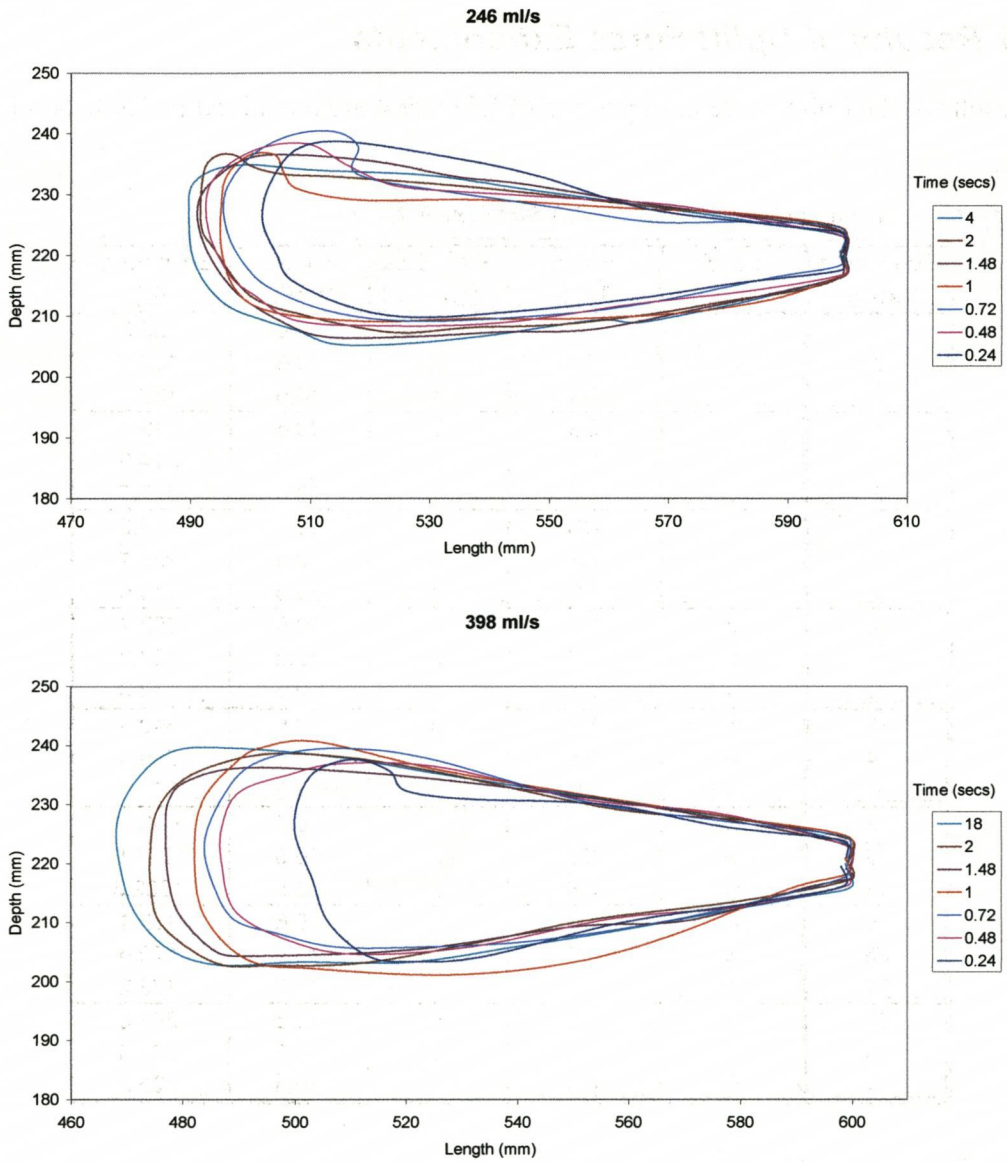

Figure A4.4 Profile of cavities created in coarse sand by the five flow rates in the static nozzle experiments

A4.5 Results of Uplift Force Experiments

The results of the uplift force experiments of Chapter 4 are contained in Table A4-11 below.

Table A4-11 Tabulated results of the uplift force experiments

Experiment Number	Sand Dry/Wet	Sand Type	Plate Size Lare/Small	Velocity (mm/s)	Uplift Force (N)
1	d	SS	s	10.6	109.3
2	d	SS	s	10.6	136.1
3	d	SS	s	10.5	136.1
4	d	SS	L	10.6	219.4
5	d	SS	L	10.5	214.0
6	d	SS	L	10.5	233.7
7	d	CS	s	10.6	119.2
8	d	CS	s	10.5	155.1
9	d	CS	s	10.6	170.5
10	d	CS	L	10.5	202.4
11	d	CS	L	10.5	223.2
12	d	CS	L	10.6	272.3
13	w	SS	s	10.5	843.8
14	w	SS	s	10.5	769.8
15	w	SS	s	10.5	801.9
16	w	SS	L	10.6	1247.1
17	w	SS	L	10.5	1277.6
18	w	SS	L	10.5	1282.3
19	w	CS	s	10.6	172.1
20	w	CS	s	10.6	170.6
21	w	CS	s	10.6	153.2
22	w	CS	L	10.5	291.3
23	w	CS	L	10.5	331.0
24	w	CS	L	10.5	325.2

A4.6 Dynamic Nozzle Experimental Results

Table A4-12 Tabulated results of the jet flow rate and pressure for the dynamic nozzle experiments

Speed (mm/s)	Flow rate (ml/s)	Pressure (bar)
7.5	211.5	2.499
18.9	213.4	2.514
33.1	213.7	2.550
34.5	211.4	2.523
48.5	214.0	2.517
57.0	214.0	2.534
82.5	211.9	2.539
89.8	211.7	2.518
101.5	214.3	2.535
Mean	212.9	2.526

A4.6.1 Dimensions of Cavities created by Dynamic Nozzles

Table A4-13 Tabulated results of the dynamic nozzle cavity lengths

	CAVITY LENGTH (mm)								
	Nozzle Speed (mm/s) [Design/Measured]								
	10	20	30	40	50	60	80	90	100
Frame No.	7.5	18.9	33.1	34.5	48.5	57.0	82.5	89.8	101.5
1	256.5	207.2	192.1	208.0	189.3	171.9	144.0	175.8	163.5
2	249.8	201.0	188.2	191.5	164.1	162.4	128.0	141.1	128.5
3	247.4	201.6	179.2	167.0	146.7	140.6	126.0	127.7	113.7
4	254.2	196.0	169.1	164.5	129.4	124.9	98.5	109.8	97.4
5	258.2	200.5	161.8	150.0	129.4	118.7	99.0	90.2	86.8
6	268.2	196.6	163.0	156.0	121.5	117.6	97.0	89.6	84.6
7	275.0	198.2	152.3	145.5	117.6	113.7	99.5	91.3	86.2
8	268.8	203.3	149.0	148.0	118.7	118.7	99.5	88.5	87.4
9	276.6	202.2	152.3	145.0	127.1	115.9	92.5	90.2	79.0
10	282.0	197.1	152.3	151.0	126.6	115.4	97.5	87.4	80.0
11	238.0	194.3	146.2	142.0	120.4	114.8	96.0	84.6	67.0
12	189.8	189.3	149.0	148.0	125.4	116.5	86.0	87.9	64.0
13		161.3	138.9	139.0	124.9	115.4	88.0	81.2	57.8
14					122.1	115.4	85.5	75.0	59.0
Mean	263.7	198.9	151.6	147.2	123.9	116.2	94.5	87.9	85.9

Red numbers denote cavities not in dynamic equilibrium and were thus not used in further analysis

Table A4-14 Tabulated results of the dynamic nozzle cavity depth, r_a and r_b

	CAVITY DEPTH ra (mm)								
	Nozzle Speed (mm/s) [Design/Measured]								
	10	20	30	40	50	60	80	90	100
Frame No.	7.5	18.9	33.1	34.5	48.5	57.0	82.5	89.8	101.5
1	207.4	97.6							
2	219.1	95.4							
3		109.2							
4		107.1			84.6		48.2		65.3
5	172.1	101.2	98.0	84.5	65.8	65.9	45.8	53.1	41.0
6	169.7	95.5	82.3	79.0	53.7	49.7	43.7	43.6	40.1
7	175.3	94.3	78.8	67.7	52.7	45.5	41.3	39.5	34.3
8	177.9	88.9	70.9	64.9	48.8	44.1	39.3	34.8	34.5
9	182.1	92.3	68.4	67.3	45.4	44.3	37.1	31.4	30.0
10	180.8	97.8	61.8	63.0	47.3	46.4	36.0	29.4	34.2
11		98.7	61.6	65.6	47.5	44.2	32.8	34.8	
12		97.1	59.4	60.2	50.9	44.9	34.6	37.1	
13			69.9	59.5	50.2	44.7	35.0	35.0	
14					49.9	45.9	38.5		
Mean	176.3	97.9	69.1	64.0	49.6	45.5	39.3	35.7	35.7
	CAVITY DEPTH rb (mm)								
1	-11.9	-46.2							
2	-23.5	-53.4							
3	-30.7	-43.2							
4	-33.6	-44.1			-40.3		-33.5		-33.2
5	-32.0	-50.8	-36.1	-39.2	-43.1	-35.9	-31.0	-29.5	-32.7
6	-25.6	-50.4	-44.1	-42.0	-42.1	-38.5	-31.5	-32.7	-32.2
7	-27.4	-53.3	-43.0	-42.7	-43.1	-40.1	-30.7	-30.2	-28.1
8	-28.7	-50.4	-43.7	-42.8	-38.5	-39.4	-28.9	-28.6	-30.1
9	-24.9	-49.7	-46.1	-44.8	-41.6	-38.6	-30.2	-30.6	-6.9
10	-23.1	-51.5	-45.4	-43.8	-37.6	-35.8	-28.5	-21.9	-6.5
11		-50.6	-42.9	-41.8	-39.8	-39.6	-20.8	-8.6	
12		-49.4	-46.3	-41.1	-39.6	-35.7	-23.1	-5.9	
13			-44.7	-42.2	-38.5	-36.3	-15.7	-6.5	
14					-42.6	-37.8	-27.2		
Mean	-26.2	-49.4	-43.6	-42.3	-40.6	-37.8	-27.4	-21.6	-31.2

A4.6.2 Plots of Cavities Profiles created by Dynamic Nozzles

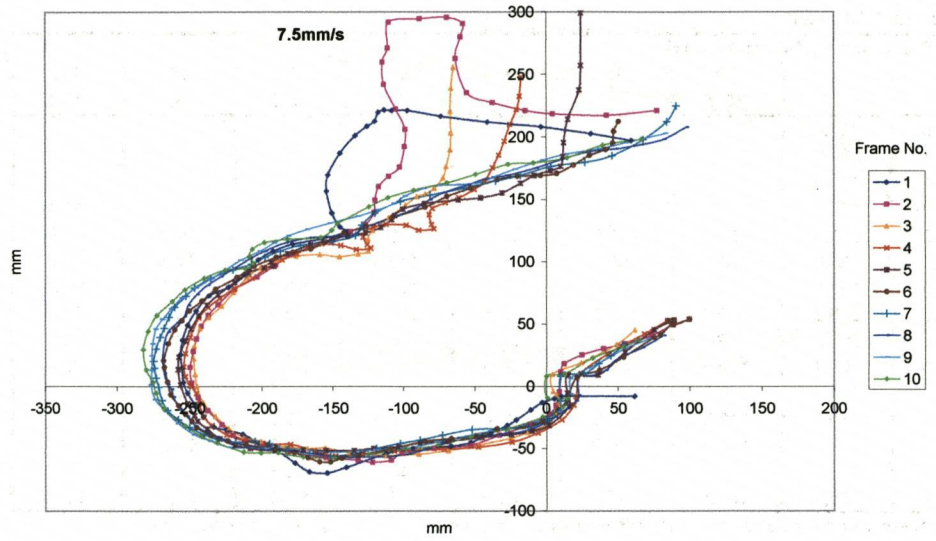

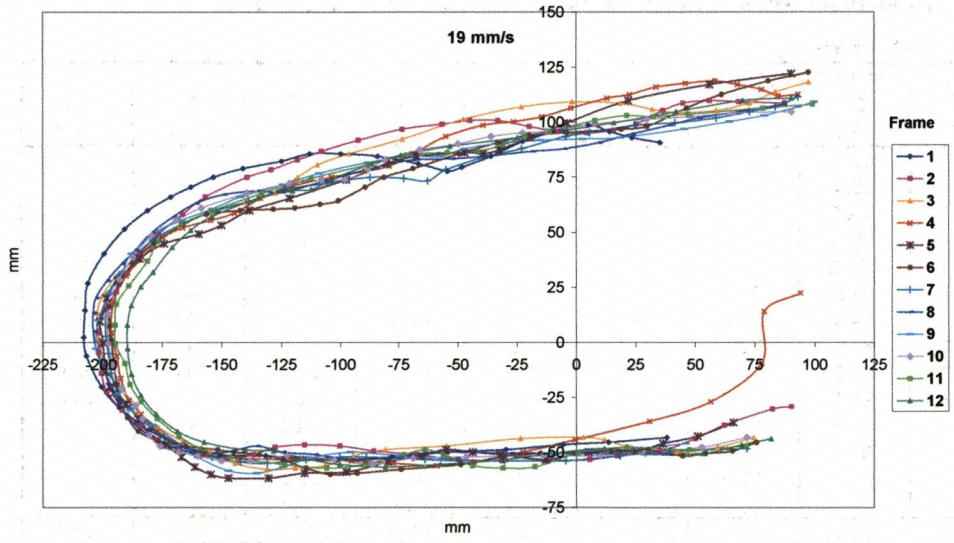

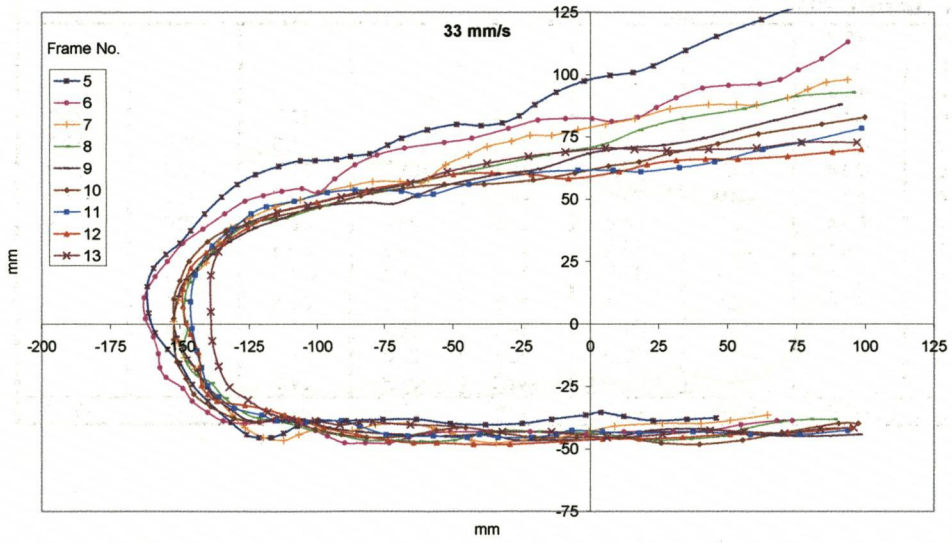

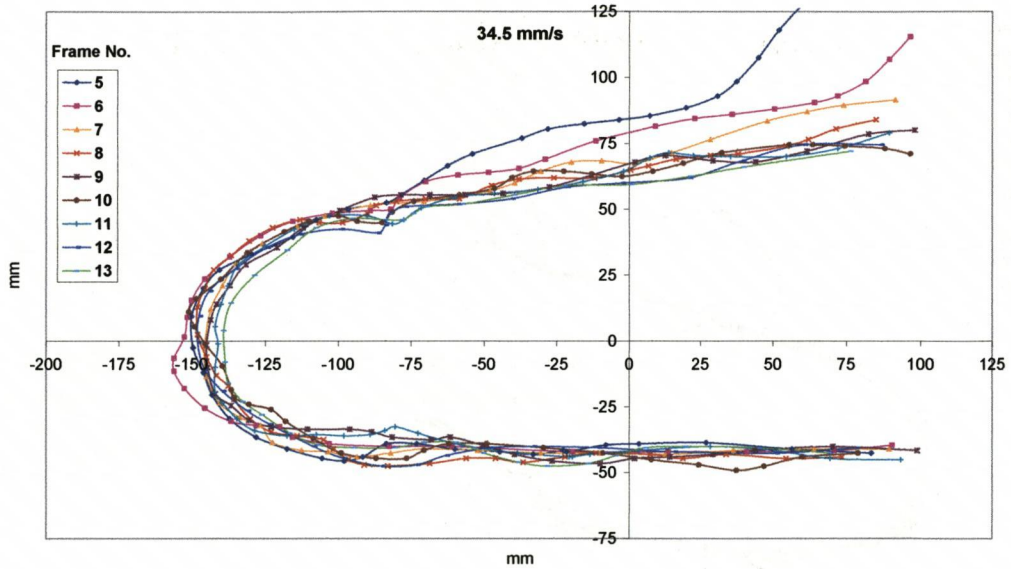
34.5 mm/s
Frame No.
5
6
7
8
9
10
11
12
13
mm
mm

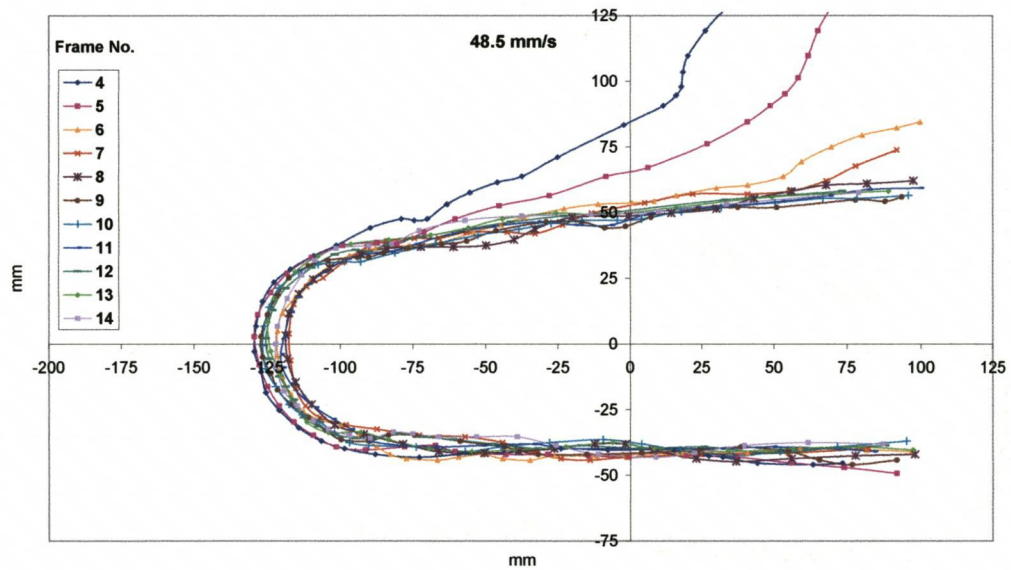
48.5 mm/s
Frame No.
4
5
6
7
8
9
10
11
12
13
14
mm
mm

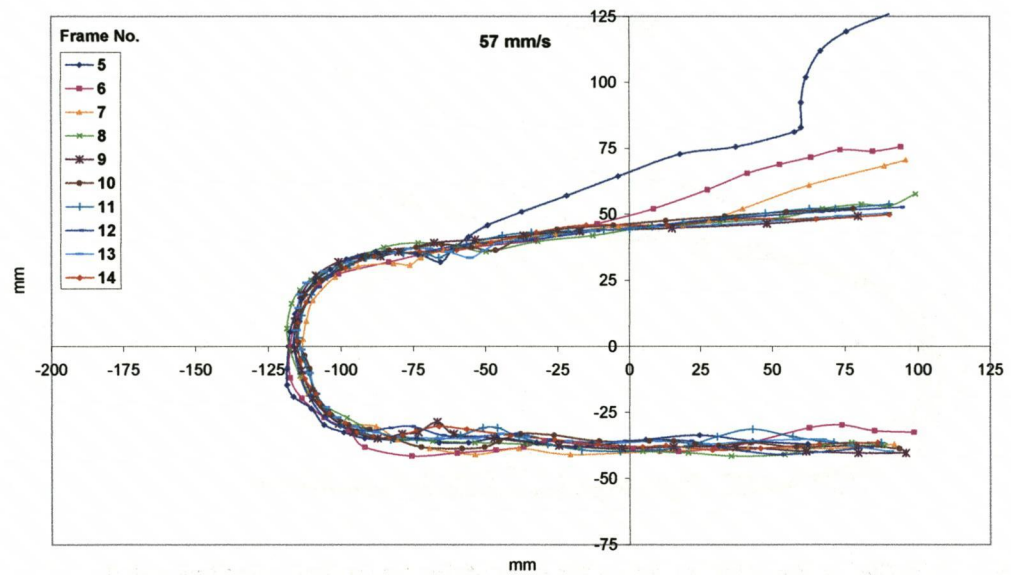
57 mm/s
Frame No.
5
6
7
8
9
10
11
12
13
14
mm
mm

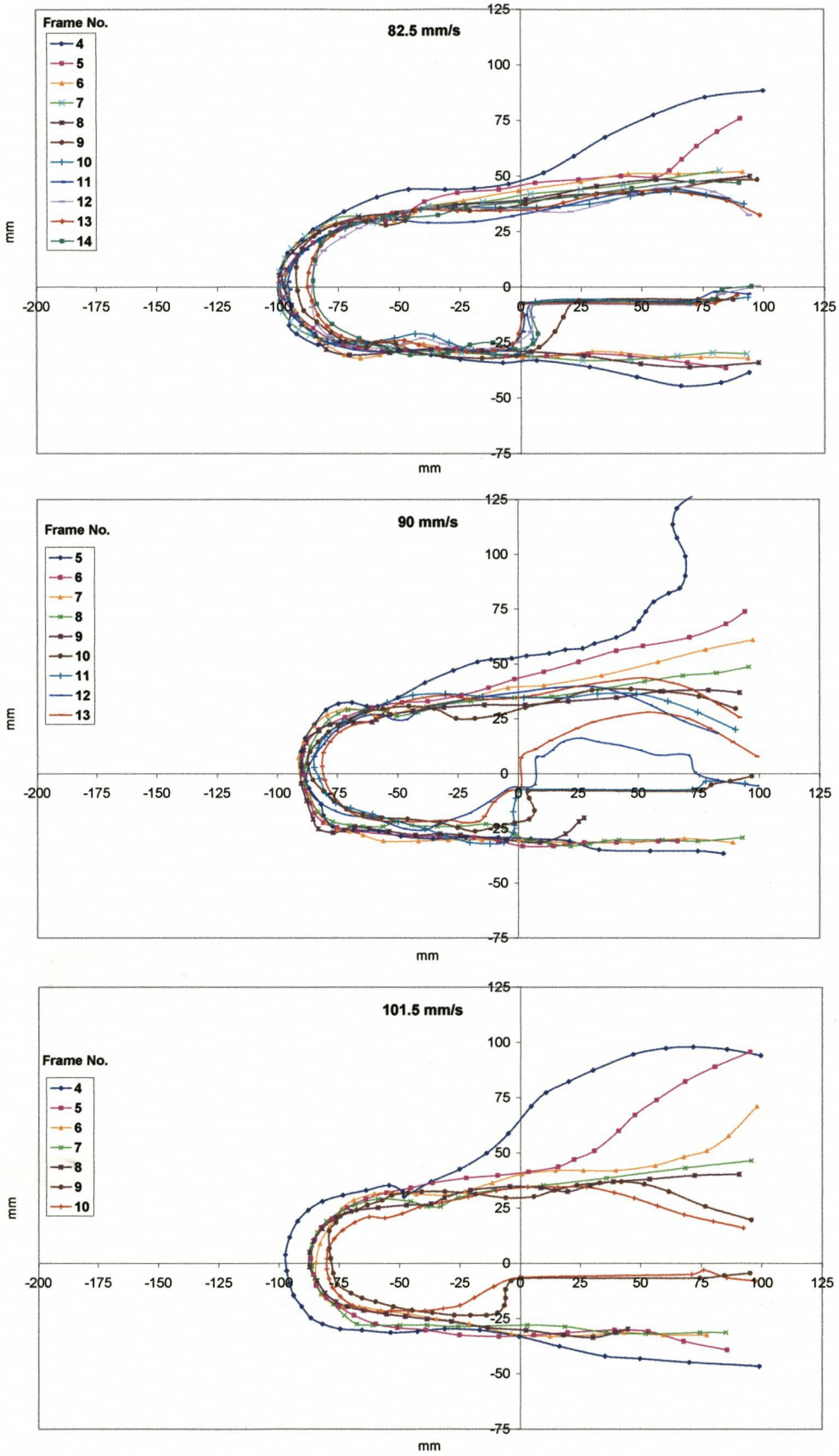

Figure A4.5 Profiles of the cavities created for each of the nine nozzle velocities tested

Appendix 5

Design Drawings

Contents

A5.1 Design Drawings of Tines used in Nozzle Distribution Experiments

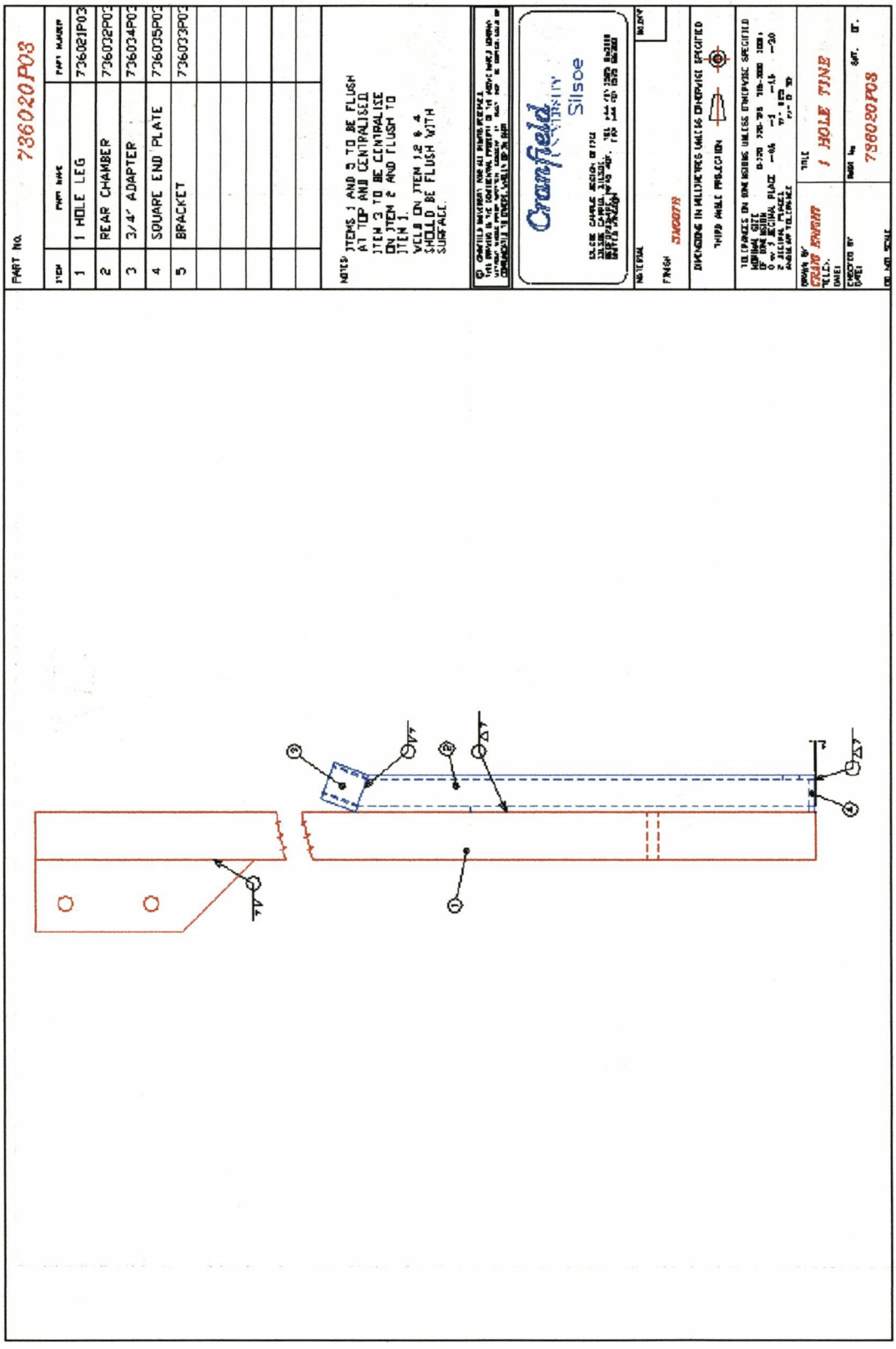

PART No. 736022P03

ITEM	PART NAME	PART NUMBER
1	3 HOLE LEG	736021P03
2	REAR CHAMBER	736032P03
3	3/4" ADAPTER	736034P03
4	SQUARE END PLATE	736035P03
5	BRACKET	736033P03

NOTES: ITEMS 1 AND 5 TO BE FLUSH AT TOP AND CENTRALISED.
ITEM 3 TO BE CENTRALISE ON ITEM 2 AND FLUSH TO ITEM 1.
WELD ON ITEM 1 & 4 SHOULD BE FLUSH WITH SURFACE.

Cranfield UNIVERSITY Silsoe

MATERIAL

FINISH ZINDOTE

THIRD ANGLE PROJECTION

DRAWN BY CRAIG KNIGHT

TITLE: 3 HOLE TINE

PART No. 736022P03

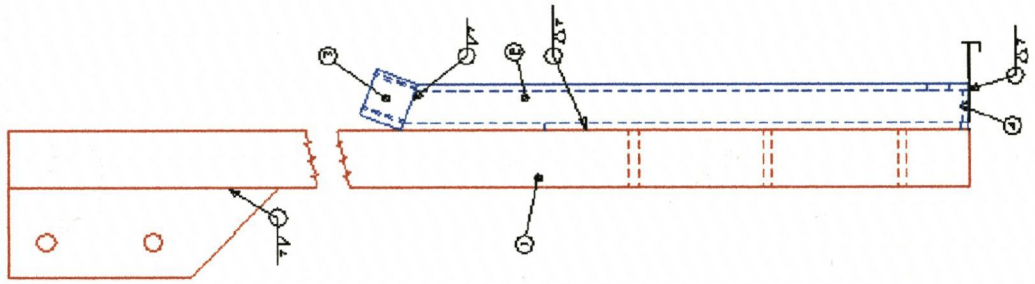

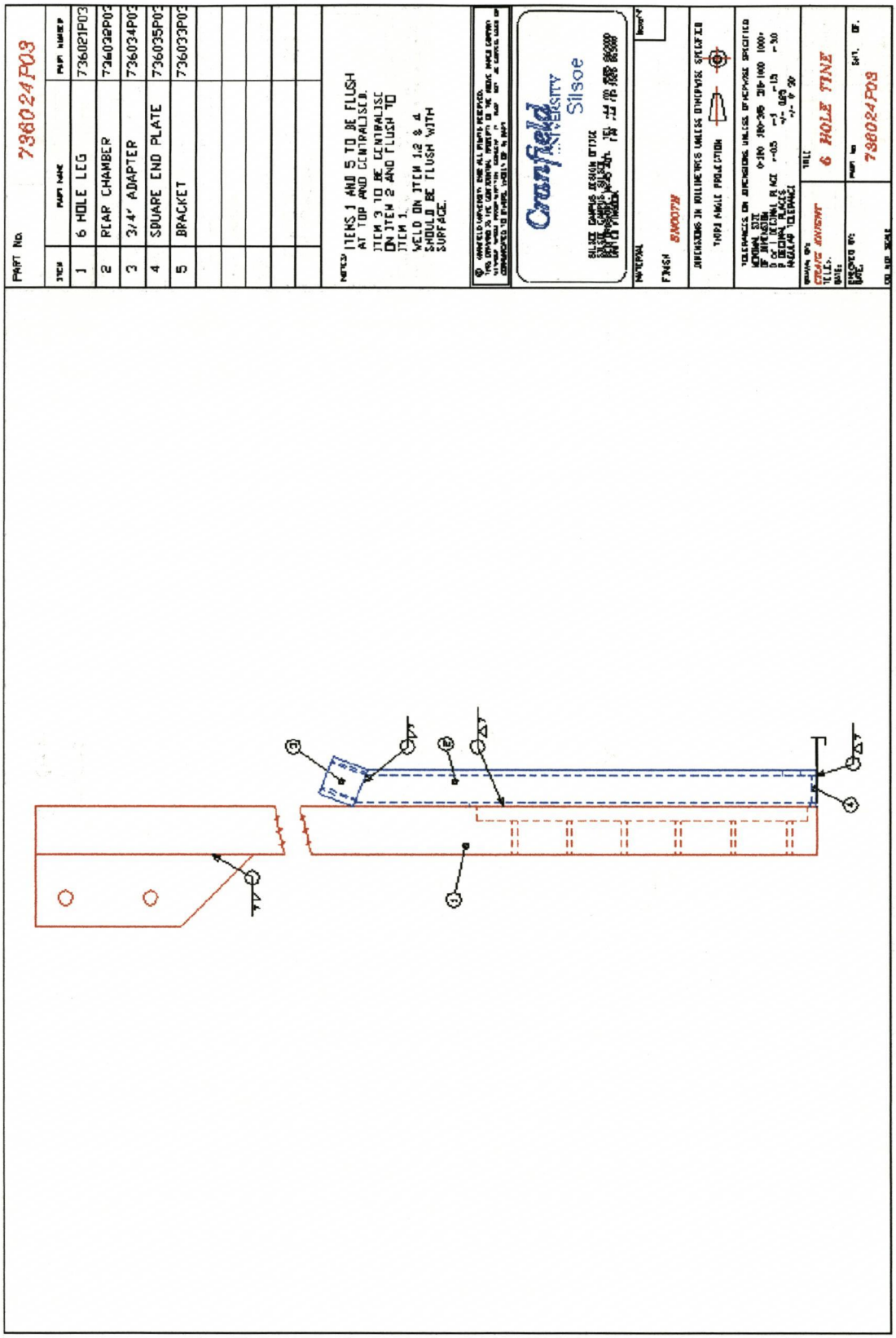
PART No. 7360024P03
ITEM
PART NAME
PART NUMBER
1 6 HOLE LEG 7360021P03
2 REAP CHAMBER 7360032P03
3 3/4" ADAPTER 7360034P03
4 SQUARE END PLATE 7360035P03
5 BRACKET 7360033P03
NOTES: ITEMS 1 AND 5 TO BE FLUSH AT TOP AND CENTRALISED. ITEM 3 TO BE CENTRALISE ON ITEM 2 AND FLUSH TO ITEM 1. WELD ON ITEM 1,2 & 4 SHOULD BE FLUSH WITH SURFACE.
Cranfield University Silsoe
MATERIAL
FINISH SMOOTH
DIMENSIONS IN MILLIMETRES UNLESS OTHERWISE SPECIFIED
THIRD ANGLE PROJECTION
TOLERANCES ON DIMENSIONS UNLESS OTHERWISE SPECIFIED
NOMINAL SIZE 0-120 120-315 315-1000 1000+
2 DECIMAL PLACES +/-0.05 +/-0.1 +/-0.15
ANGULAR TOLERANCE +/- 0° 30' +/- 0° 15' +/- 0° 30'
DRAWN
CRAIG KNIGHT
TITLE
6 HOLE TINE
CHECKED
DATE
PART No. 7360024P03
SCALE 1:2 SHT. OF.

PART No. 736026P03
ITEM
PART NAME
PART NUMBER
1 9 HOLE LEG 736021P03
2 REAR CHAMBER 736032P03
3 3/4" ADAPTER 736034P03
4 SQUARE END PLATE 736035P03
5 BRACKET 736033P03
NOTES ITEMS 1 AND 5 TO BE FLUSH AT TOP AND CENTRALISED ON ITEM 2 AND FLUSH TO ITEM 1. ITEM 3 TO BE CENTRALISE WELD ON ITEM 1& 4 SHOULD BE FLUSH WITH SURFACE.
Cranfield UNIVERSITY Silsoe
MATERIAL
FINISH
DRAWN BY CRAIG KNIGHT
DATE:
DESIGNED BY
DATE
TITLE 9 HOLE TINE
PART No. 736026P03
SHT. OF.

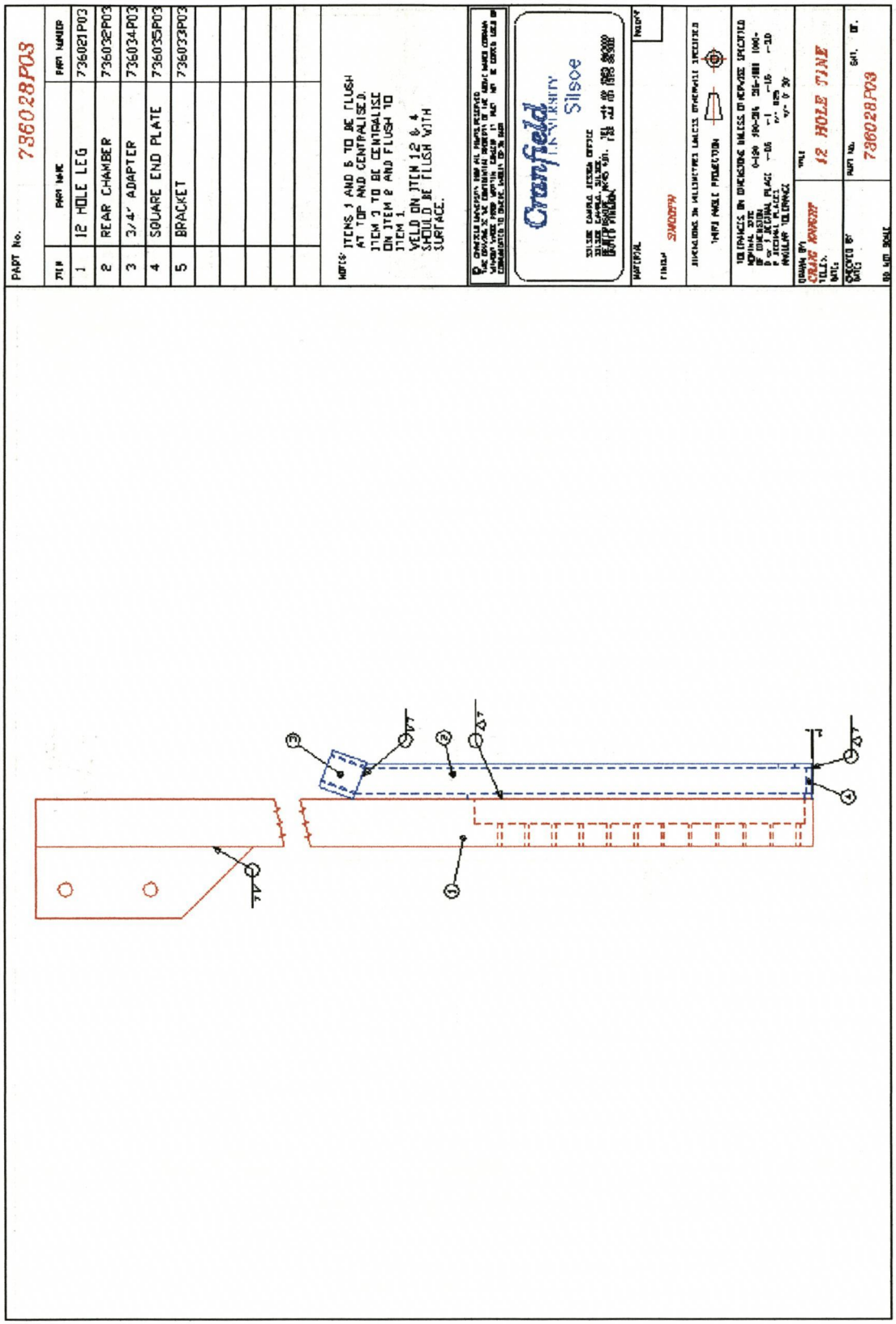
PART No. 736028P03
ITEM | PART NAME | PART NUMBER
1 | 12 HOLE LEG | 736021P03
2 | REAR CHAMBER | 736032P03
3 | 3/4" ADAPTER | 736034P03
4 | SQUARE END PLATE | 736035P03
5 | BRACKET | 736033P03
NOTES: ITEMS 1 AND 5 TO BE FLUSH AT TOP AND CENTRALISED. ITEM 2 TO BE CENTRALISE ON ITEM 2 AND FLUSH TO ITEM 1. WELD ON ITEM 12 & 4 SHOULD BE FLUSH WITH SURFACE.
Cranfield UNIVERSITY Silsoe
MATERIAL
FINISH
DRAWN BY
CHECKED BY
DATE
12 HOLE TINE
PART No. 736028P03
SCALE
SHEET OF

PART No 736028P03
ITEM
PART NAME
PART NUMBER
1 12 CLUSTER LEG 736011P03
2 REAR CHAMBER 736012P03
3 3/4" ADAPTER 736014P03
4 SQUARE END PLATE 736015P03
5 BRACKET 736013P03
NOTES ITEMS 1 AND 5 TO BE FLUSH AT TOP AND CENTRALISED. ITEM 3 TO BE CENTRALISE ON ITEM 2 AND FLUSH TO ITEM 1. WELD ON ITEM 1,2 & 4 SHOULD BE FLUSH WITH SURFACE.
Cranfield UNIVERSITY Silsoe
MATERIAL
FINISH
DRAWN BY CRAIG KNIGHT
DATE
CHECKED BY
DATE
TITLE 12 HOLE TINE
PART No. 736028P03
SIZE
SCALE

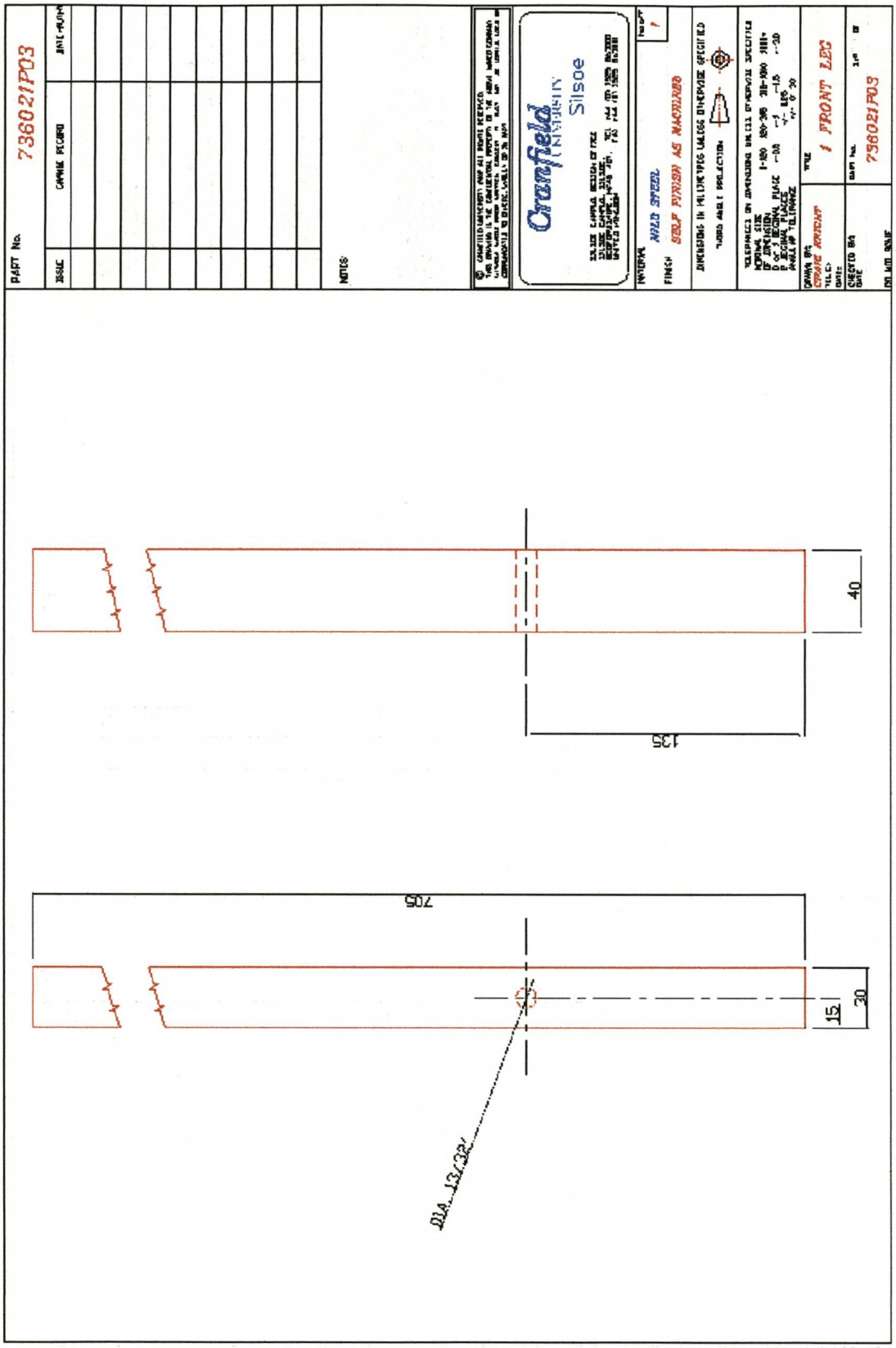
PART No.
736021P03
ISSUE
CHANGE RECORD
DATE/INITIALS
NOTES
Cranfield UNIVERSITY
Silsoe
MATERIAL
MILD STEEL
FINISH
SELF FINISH AS MACHINED
DIMENSIONS IN MILLIMETRES UNLESS OTHERWISE SPECIFIED
THIRD ANGLE PROJECTION
DRAWN BY
CRAIG KNIGHT
CHECKED BY
DATE
TITLE
1 FRONT LEG
DWG No.
736021P03
705
40
135
30
15
DIA 13/32"

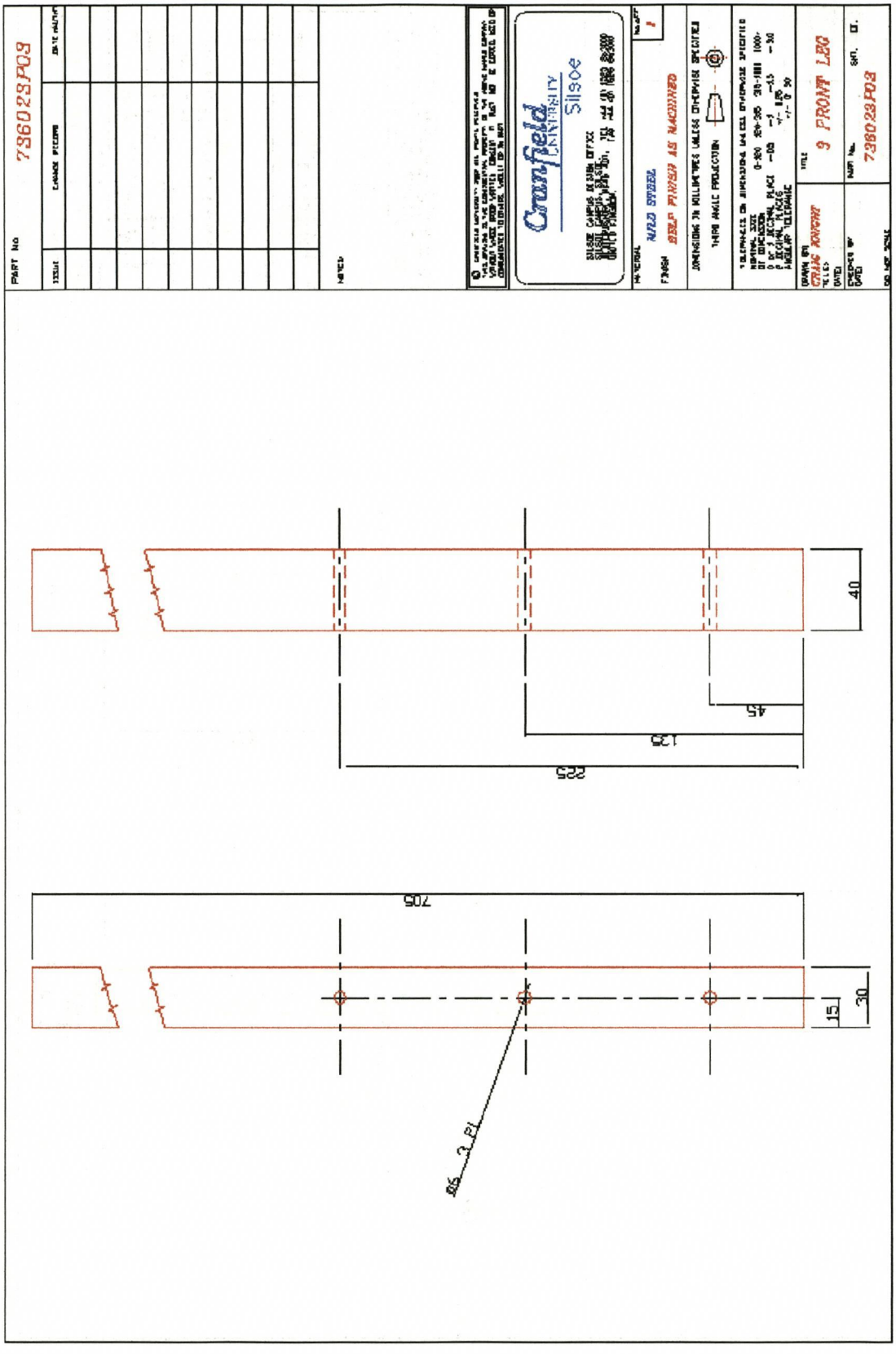
PART No
7360 23 P03
Cranfield UNIVERSITY Silsoe
MATERIAL
MILD STEEL
FINISH
SELF FINISH AS MACHINED
TITLE
9 POINT LEG
PART No.
7360 23 P03
225
123
45
40
205
30
15
Ø6 3 PL

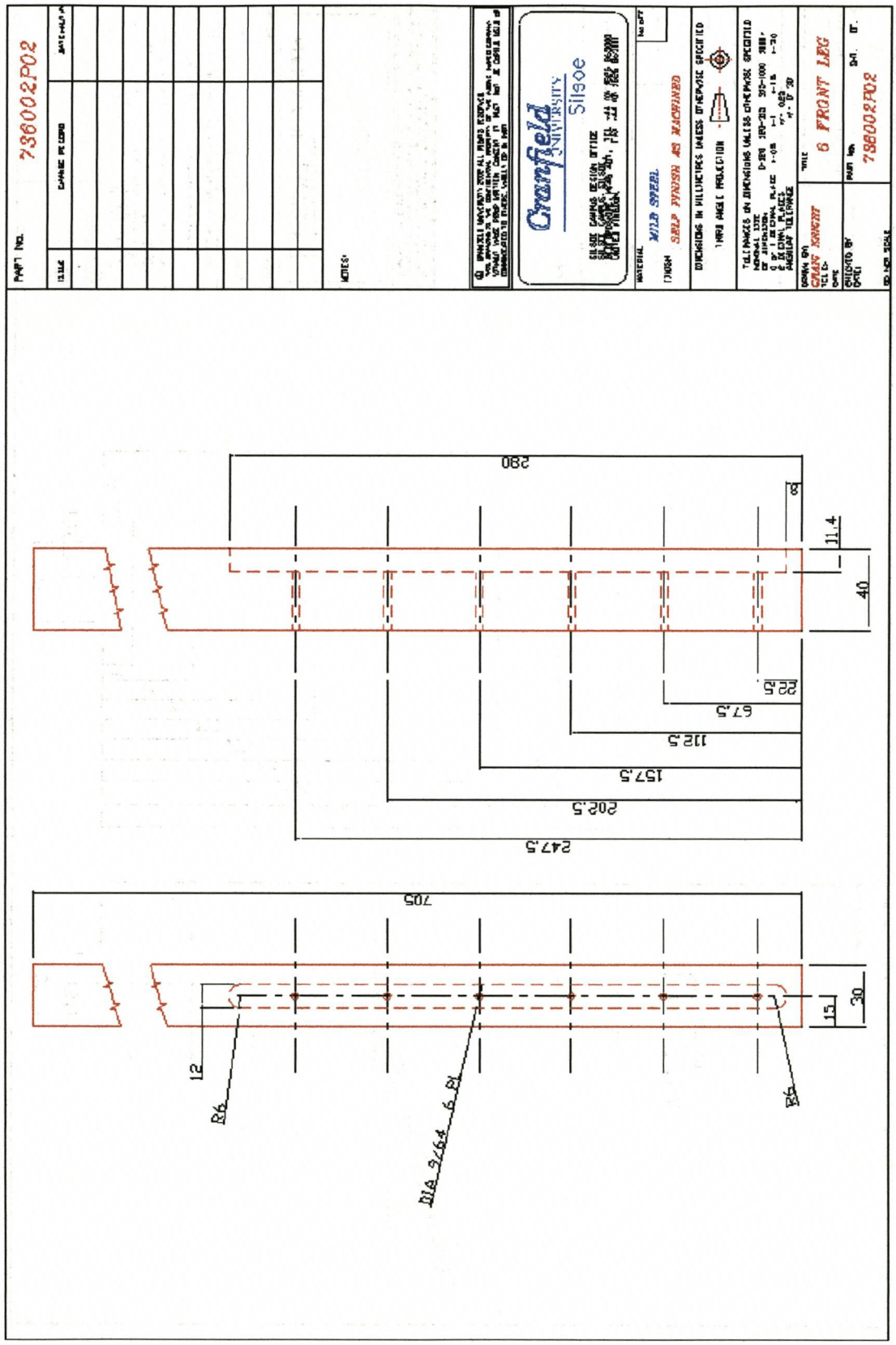
PART No. 786002P02
NOTES:
Cranfield UNIVERSITY Silsoe
MATERIAL MILD STEEL
FINISH SHOT BLASTED AS MACHINED
DIMENSIONS IN MILLIMETRES UNLESS OTHERWISE SPECIFIED
THIRD ANGLE PROJECTION
TOLERANCES ON DIMENSIONS UNLESS OTHERWISE SPECIFIED
DRAWN BY CRAIG KNIGHT
TITLE 6 FRONT LEG
PART No. 786002P02
280
80
11.4
40
22.5
67.5
112.5
157.5
202.5
247.5
705
15
30
12
R6
DIA 9.764 6 PL
R5

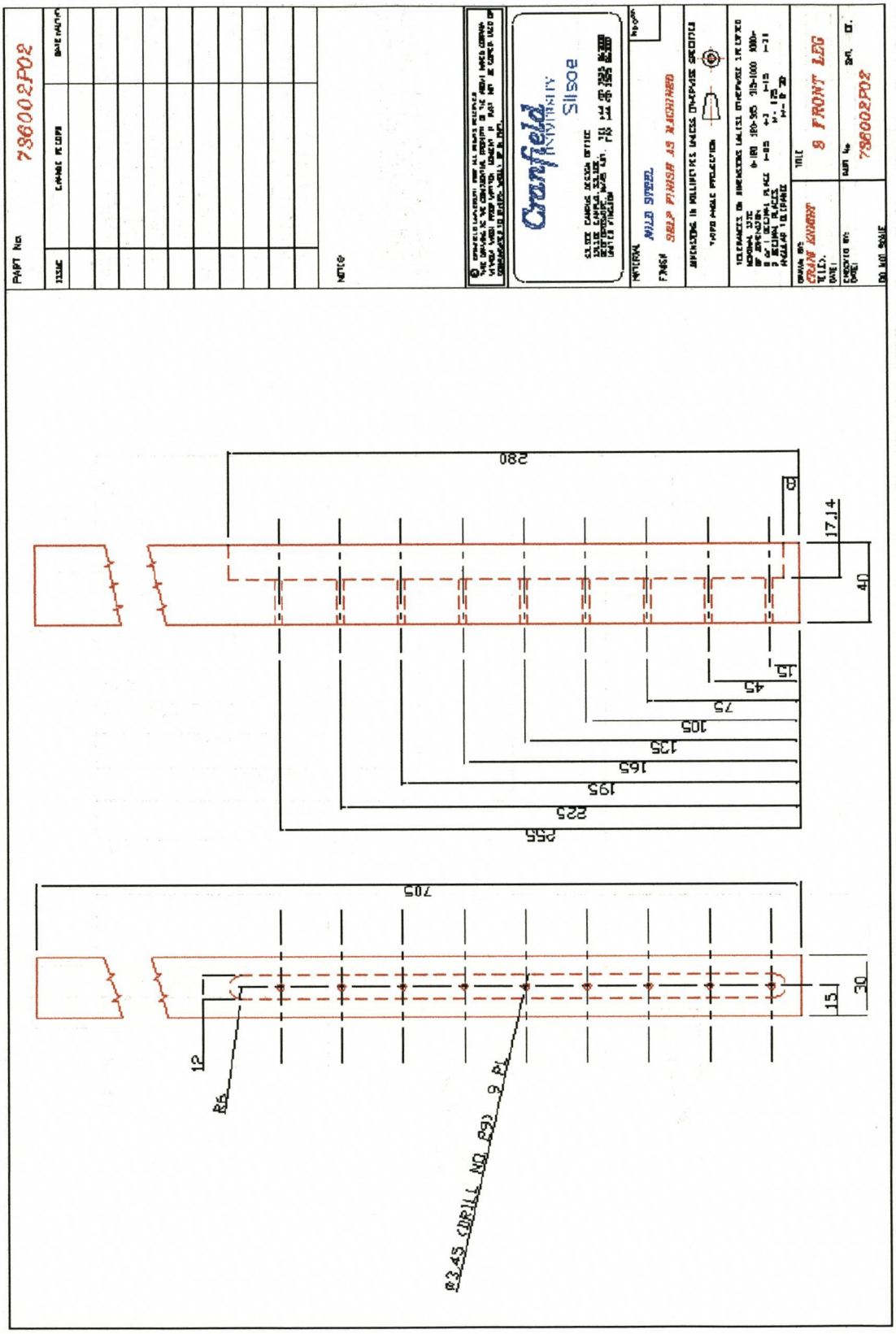
PART No: 736002P02
NOTES:
Cranfield UNIVERSITY Silsoe
MATERIAL: MILD STEEL
FINISH: SHOT BLAST AS MACHINED
TITLE: S FRONT LEG
DRAWN BY: CRAIG KNIGHT
DATE:
DWG No: 736002P02
DO NOT SCALE
280
17.14
40
15
45
75
105
135
165
195
225
255
705
12
R6
Ø3.45 (DRILL NO 29) 2 PL
15
30

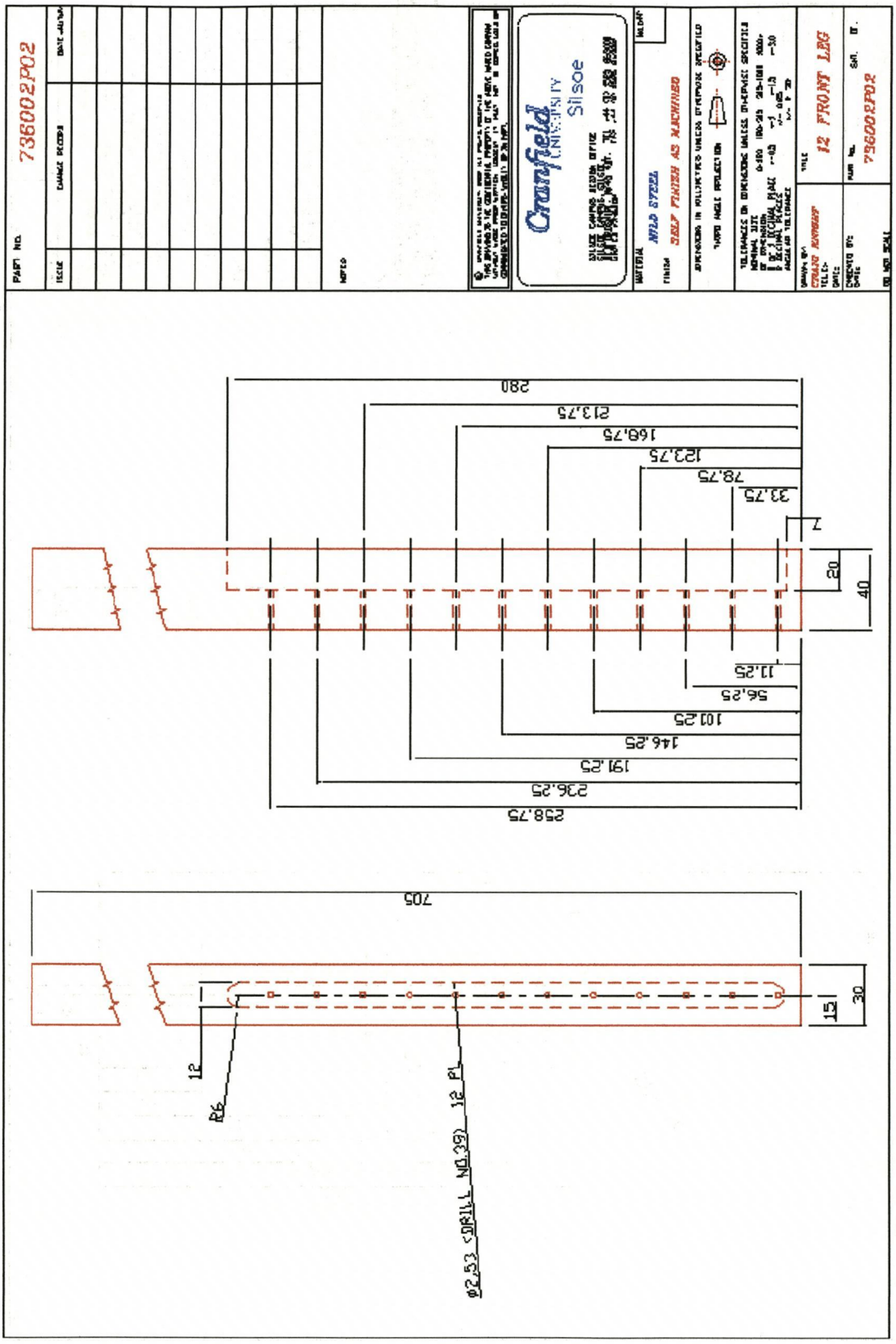
PART NO. 736002P02
ISSUE
DATE AMENDED
NOTES
Cranfield
UNIVERSITY
Silsoe
MATERIAL MILD STEEL
FINISH SELF FINISH AS MACHINED
TITLE 12 FRONT LEG
DRAWN BY CRAIG KNIGHT
DATE
DRAWING NO. 736002P02
SCALE
DIMENSIONS IN MILLIMETRES UNLESS OTHERWISE SPECIFIED
THIRD ANGLE PROJECTION
280
213.75
168.75
123.75
78.75
33.75
7
20
40
11.25
56.25
101.25
146.25
191.25
236.25
258.75
705
30
15
12
R6
12 PL
Ø2.53 <DRILL NO.39>

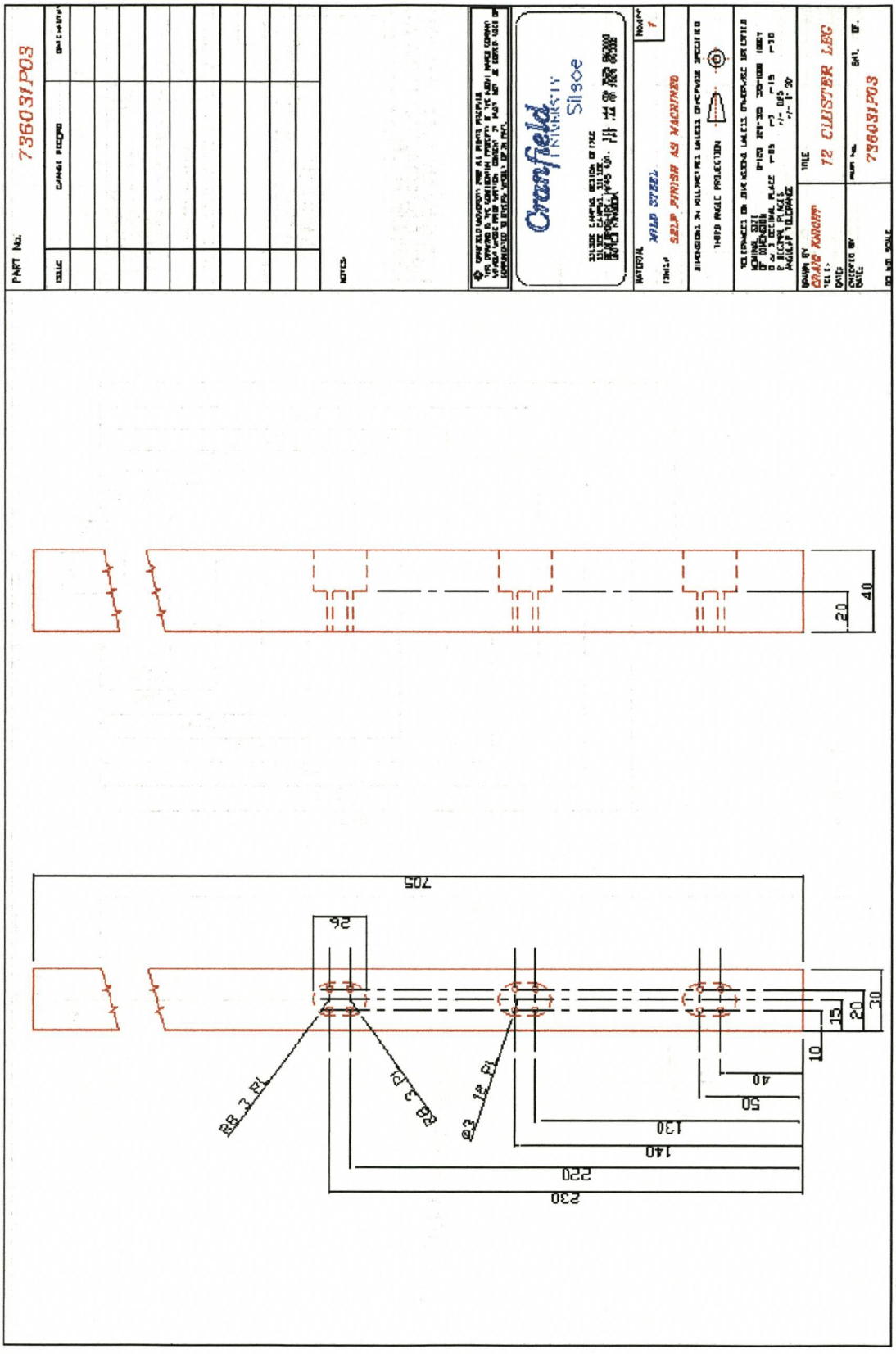
PART No. 736031P03
Cranfield UNIVERSITY Silsoe
MATERIAL MILD STEEL
FINISH SELF FINISH AS MACHINED
TITLE 12 CLUSTER LBG
DRAWN BY CRAIG KNIGHT
736031P03
705
26
RB 3 PL
RB 3 PL
Ø3 12 PL
230
220
140
130
50
40
10
15
20
30
20
40

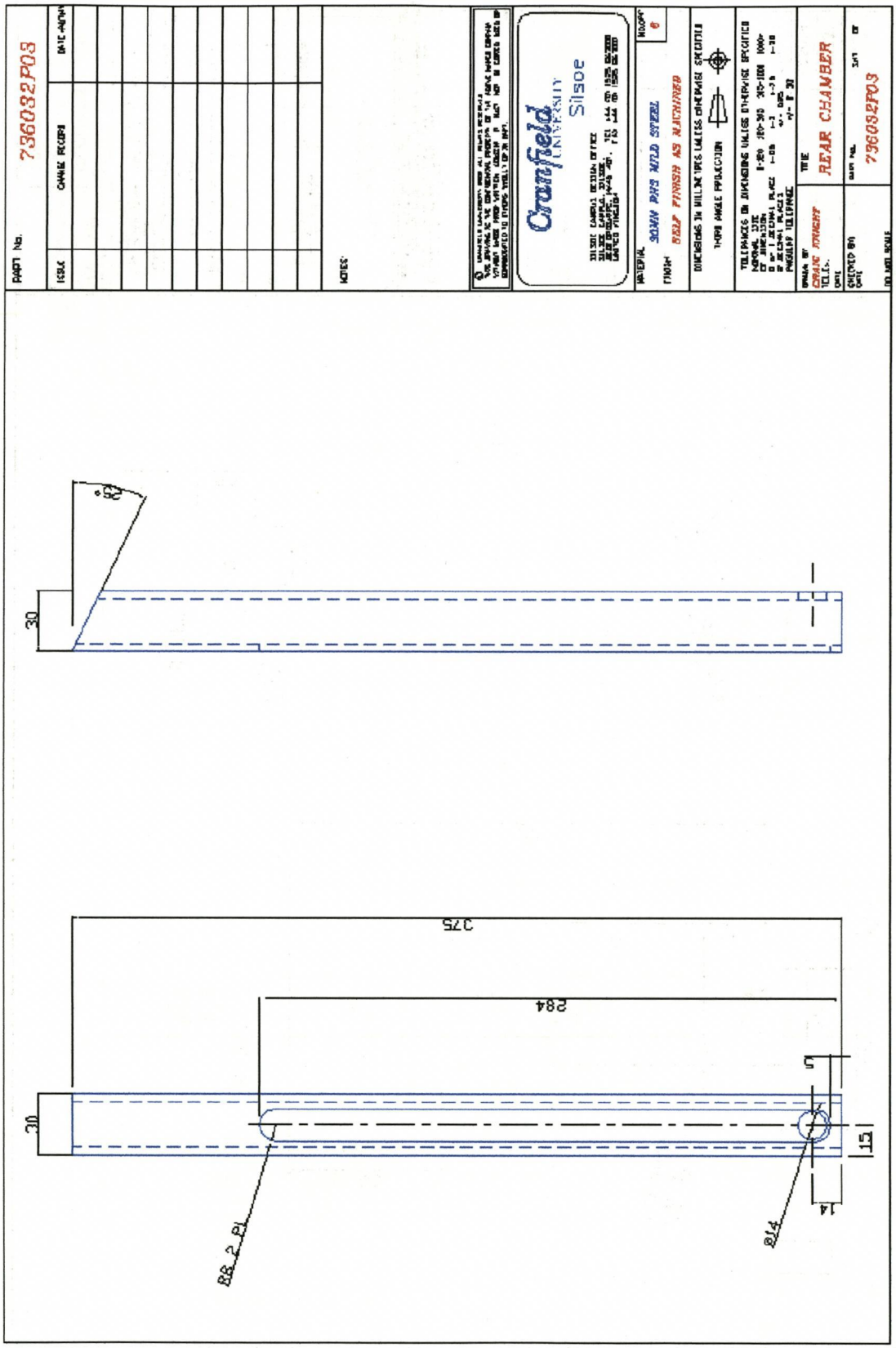
PART No. 736032P03
ISSUE
CHANGE RECORD
DATE-AUTH
NOTES:
Cranfield UNIVERSITY
Silsoe
MATERIAL
MILD STEEL
FINISH
AS MACHINED
DIMENSIONS IN MILLIMETRES UNLESS OTHERWISE STATED
TITLE
REAR CHAMBER
DRAWN BY
CRAIG KNIGHT
DATE
CHECKED BY
DATE
DRAWING No.
736032P03
SIZE
A4
SCALE
30
82
275
284
30
15
14
88.2 PCD
Ø14

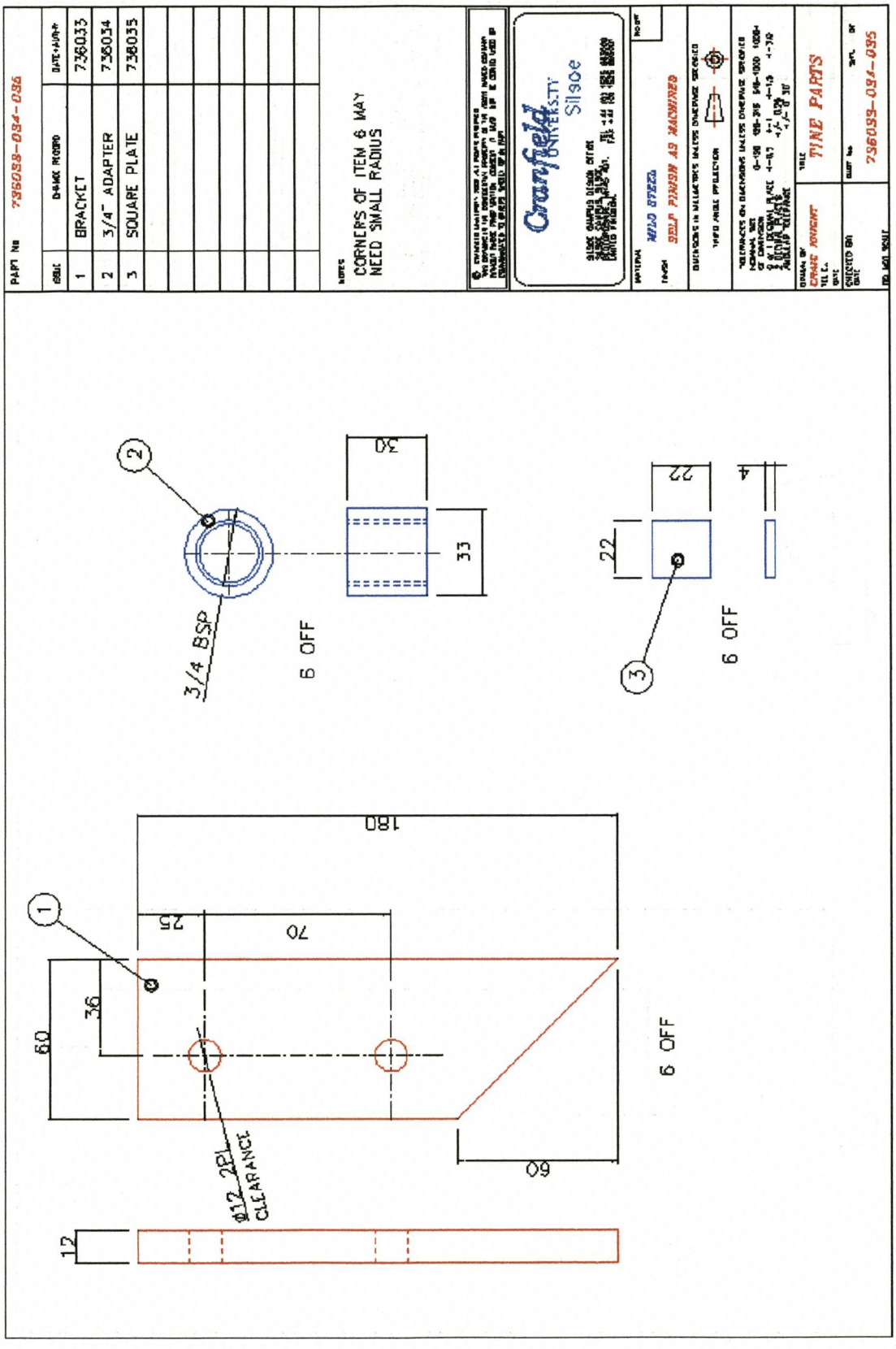
PART No 736038-034-036
ISSUE
DRAWING NUMBER
DATE ISSUED
1 BRACKET 736033
2 3/4" ADAPTER 736034
3 SQUARE PLATE 736035
NOTES
CORNERS OF ITEM 6 WAY
NEED SMALL RADIUS
Cranfield UNIVERSITY Silsoe
MATERIAL MILD STEEL
FINISH SELF FINISH AS MACHINED
TITLE TINE PARTS
DRAWN BY CRAIG KNIGHT
736033-034-035
2
3/4 BSP
6 OFF
30
33
3
22
22
4
6 OFF
1
180
25
70
36
60
Ø12 2PL CLEARANCE
60
12
6 OFF

A5.2 Design Drawings of Tines used in the Rake angle Experiments

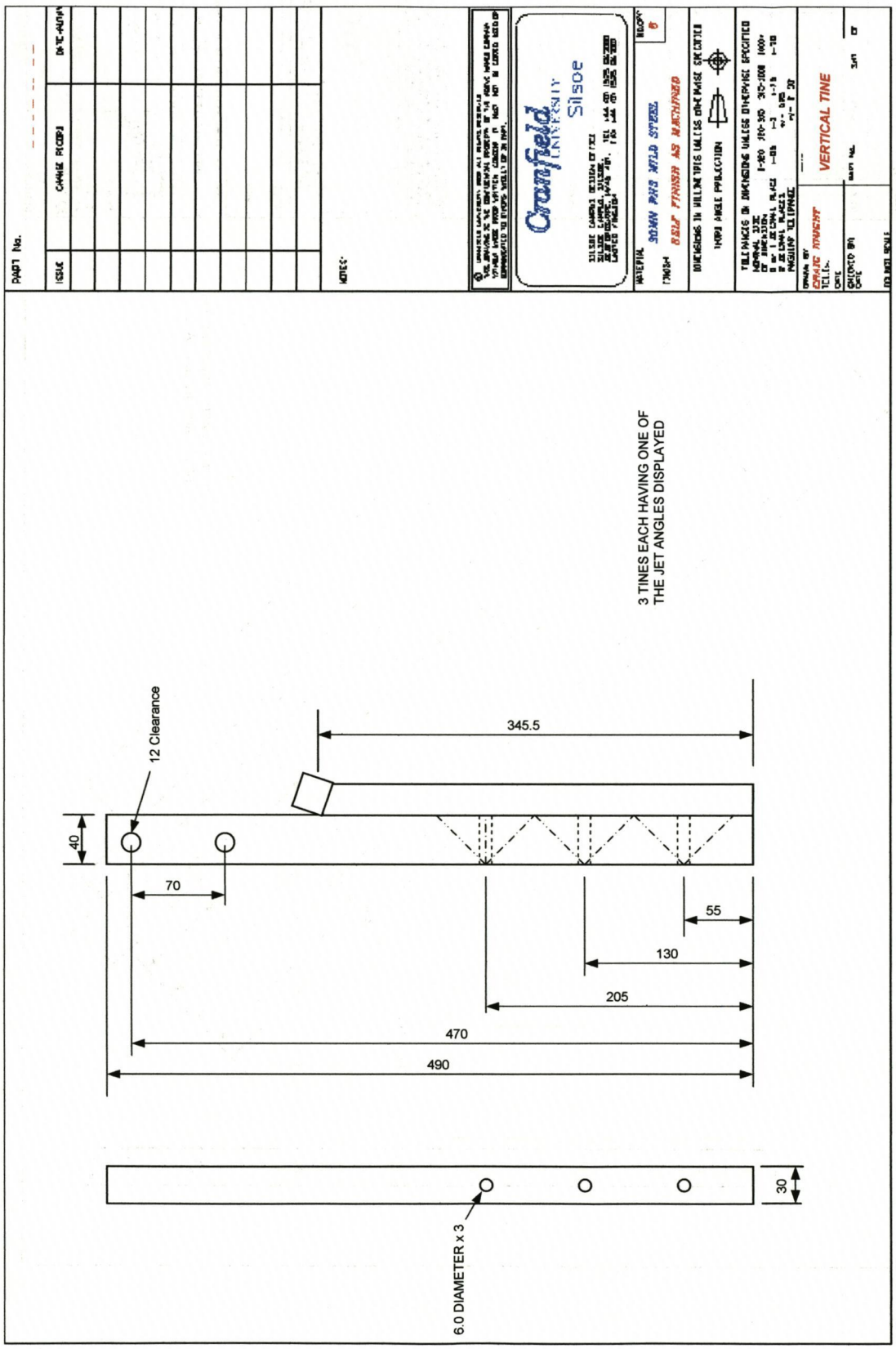

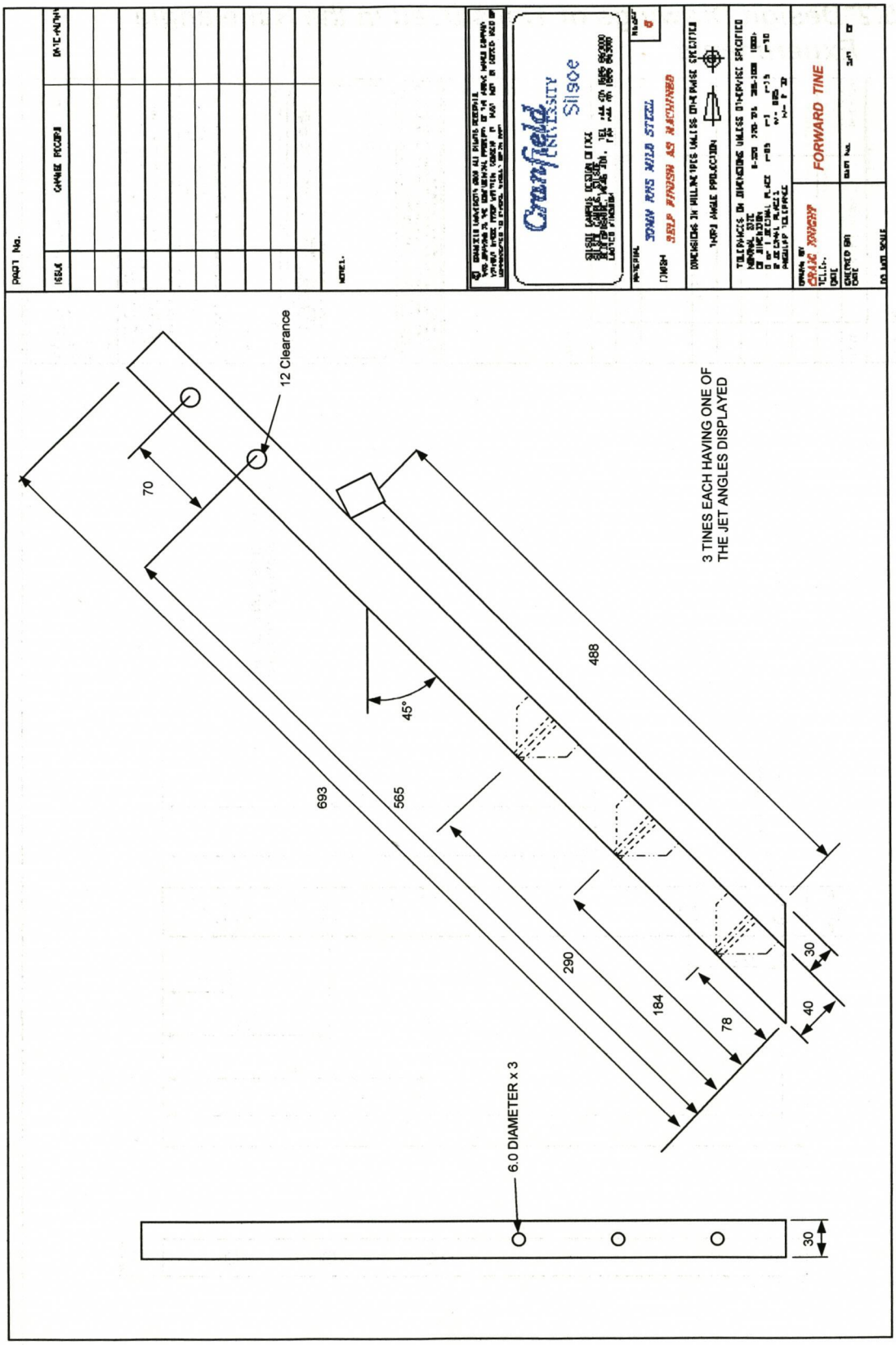
12 Clearance
70
45°
693
565
488
290
184
78
30
40
30
6.0 DIAMETER x 3
3 TINES EACH HAVING ONE OF
THE JET ANGLES DISPLAYED
FORWARD TINE
Cranfield
UNIVERSITY
Silsoe

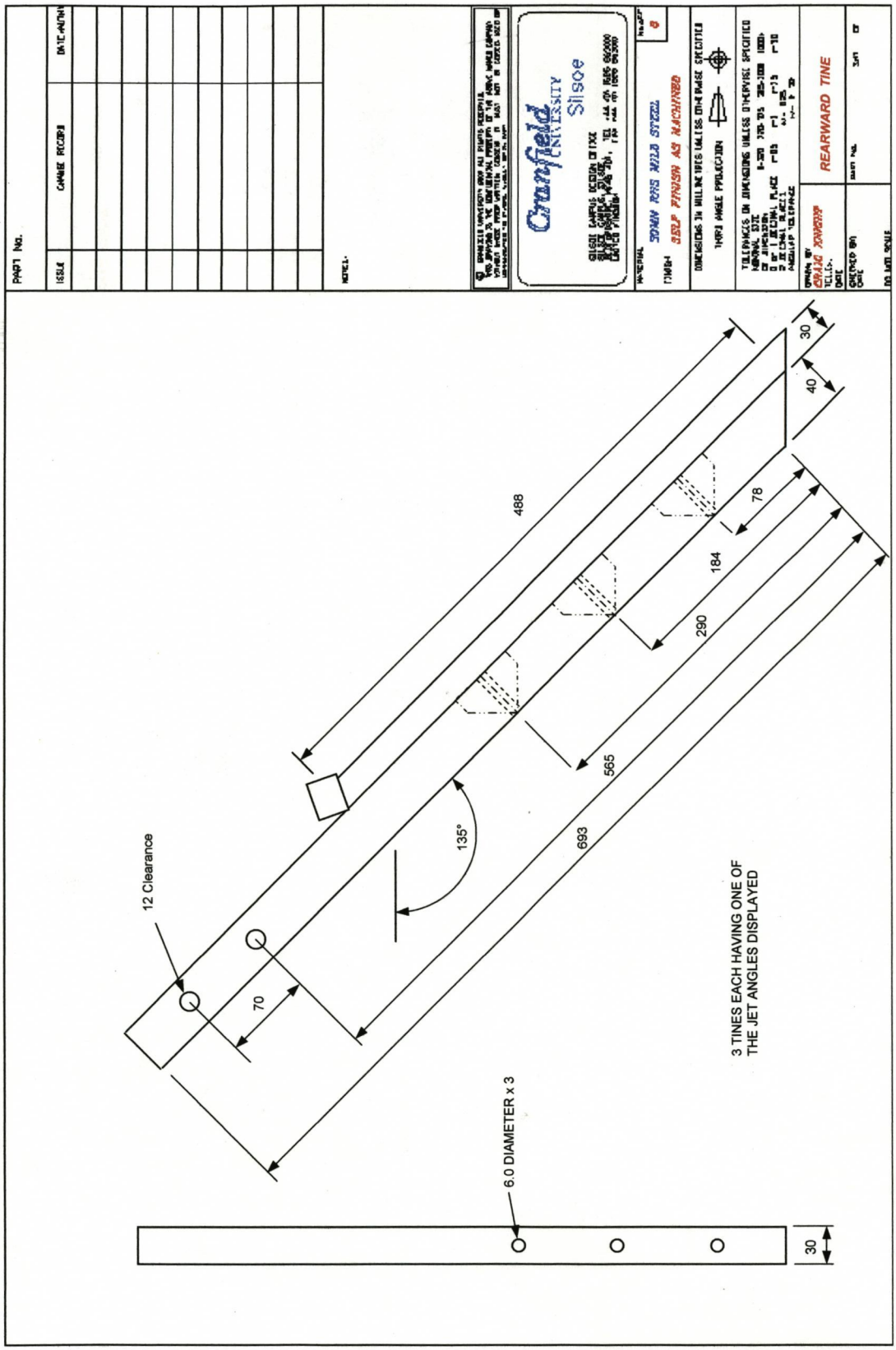
PART No.
ISSUE
CHANGE RECORD
DATE-AUTH
NOTES:
Cranfield
UNIVERSITY
Silsoe
SILSOE CAMPUS, BEDFORD, MK45 4DT
MATERIAL
SPRING ROHS MILD STEEL
FINISH
SELF FINISH AS MACHINED
DIMENSIONS IN MILLIMETRES UNLESS OTHERWISE SPECIFIED
THIRD ANGLE PROJECTION
TOLERANCES ON DIMENSIONS UNLESS OTHERWISE SPECIFIED
DRAWN BY
CRAIG KNIGHT
TITLE
REARWARD TINE
DATE
CHECKED BY
DATE
DRAWING No.
SIZE
SHEET
OF
DO NOT SCALE
12 Clearance
70
135°
488
693
565
290
184
78
40
30
30
6.0 DIAMETER x 3
3 TINES EACH HAVING ONE OF
THE JET ANGLES DISPLAYED